SYNTHESIS OF POLYANILINE BASED TERNARY NANOCOMPOSITES FOR DECONTAMINATION OF HEAVY METALS USING ELECTROCHEMICAL TECHNIQUE

Thesis Submitted for the Award of the Degree of

DOCTOR OF PHILOSOPHY

in

CHEMISTRY

By

NISHA
42000354

Supervised By

Dr Harish Mudila (19331)
Associate Professor
Department of Chemistry
Lovely Professional University
Jalandhar, (P.B) India

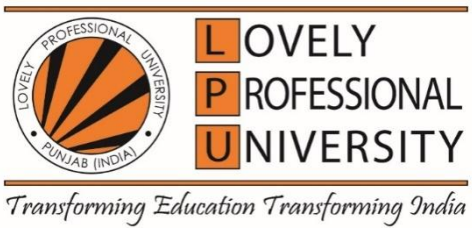

LOVELY PROFESSIONAL UNIVERSITY, PUNJAB
2026

DECLARATION

I, hereby declared that the presented work in the thesis entitled **"SYNTHESIS OF POLYANILINE BASED TERNARY NANOCOMPOSITES FOR DECONTAMINATION OF HEAVY METALS USING ELECTROCHEMICAL TECHNIQUE"** in fulfilment of degree of **Doctor of Philosophy (Ph.D.)** is outcome of research work carried out by me under the supervision of Dr. Harish Mudila working as Assosiate Professor in the Department of Chemistry, Lovely Professional University, Punjab, India. In keeping with general practice of reporting scientific observations, due acknowledgements have been made whenever work described here has been based on findings of other investigator. This work has not been submitted in part or full to any other University or Institute for the award of any degree.

(Signature of Scholar)

Name of the scholar: Nisha

Registration No.: 42000354

Department/school: School of Chemical Engineering and Physical Sciences

Lovely Professional University,

Punjab, India

CERTIFICATE

This is to certify that the work reported in the Ph.D. thesis entitled **"SYNTHESIS OF POLYANILINE BASED TERNARY NANOCOMPOSITES FOR DECONTAMINATION OF HEAVY METALS USING ELECTROCHEMICAL TECHNIQUE"** submitted in fulfillment of the requirement for the award of degree of **Doctor of Philosophy (Ph.D.)** in **Chemistry** is a research work carried out by **Nisha, 42000354** is bonafide record of his/her original work carried out under my supervision and that no part of thesis has been submitted for any other degree, diploma or equivalent course.

(Signature of Supervisor)

Name of supervisor: Dr. Harish Mudila (19331)

Designation: Associate Professor

Department/school: School of Chemical Engineering and Physical Sciences

Lovely Professional University,

Punjab, India

Abstract

The persistent contamination of aquatic environments with heavy metals has become an escalating global environmental issue, posing serious threats to ecological systems and human health. Among the various heavy metals, lead (Pb^{2+}) and cadmium (Cd^{2+}) are particularly hazardous due to their high toxicity, long-term environmental persistence, and ability to bioaccumulate in living organisms. Even at low concentrations, Pb^{2+} can cause severe neurological and developmental disorders, particularly in children, while Cd^{2+} is associated with renal damage, skeletal demineralization, and carcinogenicity. These serious health and ecological impacts necessitate the development of efficient and sensitive methods for monitoring these toxic ions in water sources. Traditional detection methods such as atomic absorption spectroscopy (AAS), inductively coupled plasma mass spectrometry (ICP-MS), and fluorescence spectroscopy, although precise and reliable, are often expensive, time-consuming, and require sophisticated instrumentation and trained personnel. They are not suitable for on-site or real-time monitoring. In contrast, electrochemical sensors have emerged as a promising alternative due to their portability, low cost, ease of operation, and fast response time. However, the performance of electrochemical sensors is highly dependent on the electrode materials used. Thus, the development of advanced, multifunctional electrode materials with superior electrochemical characteristics is critical for achieving high sensitivity and selectivity in heavy metal detection.

This study presents the design, synthesis, and application of novel ternary nanocomposites for the electrochemical detection and removal of Pb^{2+} and Cd^{2+} from aqueous solutions. Two main composites were developed: PrGZ (Polyaniline–reduced Graphene Oxide–Zinc Oxide) and PrGM (Polyaniline–reduced Graphene Oxide–Manganese Dioxide). These composites were strategically constructed to leverage the synergistic properties of their constituents: the redox activity of polyaniline (PANI), the excellent electrical conductivity and surface area of reduced graphene oxide (rGO), and the electrochemical reactivity of ZnO and MnO_2. In this research, ZnO and MnO_2 were used as received from commercial suppliers without any additional in-lab synthesis, ensuring reproducibility and simplicity in composite preparation. The fabrication process involved several stages. Initially, graphite oxide (GO) was synthesized using the modified Hummers' method and subsequently reduced to rGO using a chemical reducing agent. PANI was synthesized separately through oxidative polymerization. The commercially obtained

ZnO and MnO_2 were then combined with PANI and rGO through ultrasonication and mechanical stirring to ensure homogeneous dispersion and effective interfacial interaction. This approach resulted in the formation of a stable ternary nanocomposite network where the components interacted via electrostatic forces and chemical bonding between functional groups such as amine, hydroxyl, and oxygen-containing moieties. Comprehensive physicochemical characterization of the composites was carried out using various techniques. FTIR spectroscopy confirmed the presence of characteristic functional groups from PANI (quinoid and benzenoid rings), rGO (C=O and C–OH), and metal oxides (Zn–O and Mn–O), indicating successful incorporation of each component. X-ray diffraction (XRD) analysis revealed distinct peaks corresponding to the semi-crystalline nature of PANI, graphitic planes of rGO, and the crystalline structures of ZnO (hexagonal wurtzite) and MnO_2, confirming the presence and structural integrity of each phase. Thermogravimetric analysis (TGA) showed enhanced thermal stability of the ternary composites compared to individual components, further supporting effective interaction among the materials. Scanning electron microscopy (SEM) demonstrated porous, rough surface morphology with uniform dispersion of ZnO and MnO_2 nanoparticles on the rGO-PANI matrix—an ideal structure for electrochemical applications, as it promotes rapid electron transport and provides abundant active sites for metal ion interaction. Electrochemical analysis of the nanocomposites was performed using cyclic voltammetry (CV), electrochemical impedance spectroscopy (EIS), and differential pulse anodic stripping voltammetry (DPASV). Among the various compositions tested, the PrGZ-2 formulation exhibited outstanding redox behavior with enhanced current responses in CV, indicating superior electroactivity. EIS measurements showed that PrGZ-2 had significantly lower charge transfer resistance (Rct), demonstrating efficient electron transport due to the synergistic interaction among PANI, rGO, and ZnO. DPASV, a sensitive technique ideal for trace metal detection, was employed to evaluate the detection performance. The PrGZ-2 nanocomposite demonstrated excellent sensitivity for Pb^{2+} detection, achieving a limit of detection (LOD) of 0.3 μM and a limit of quantification (LOQ) of 1.16 μM. The calibration curve showed strong linearity ($R^2 = 0.994$), and the relative standard deviation (RSD) was 2.13%, indicating good precision. The same composite also performed well for Cd^{2+} detection, with a LOD of 0.005 μM, LOQ of 0.016 μM, and $R^2 = 0.996$, along with a low RSD of 0.079%, confirming high reproducibility and accuracy. In parallel, the PrGM-2 composite, incorporating MnO_2 in place of ZnO, also showed promising

results. Due to the redox-active nature of MnO_2, the PrGM-2 sensor exhibited enhanced electrochemical behavior. For Pb^{2+} detection, the sensor achieved a very low LOD of 0.014 μM and LOQ of 0.043 μM, with an excellent correlation coefficient ($R^2 = 0.994$) and a minimal RSD of 0.27%. In a secondary configuration, PrGM-2 recorded a LOD of 0.15 μM and LOQ of 0.45 μM, maintaining good linearity ($R^2 = 0.991$) and acceptable reproducibility (RSD = 1.98%). Selectivity studies were conducted by introducing common interfering ions such as Cu^{2+} and Cd^{2+} during Pb^{2+} detection. Both PrGZ-2 and PrGM-2 maintained a strong and selective response toward Pb^{2+} ions with minimal interference. Stability tests over extended time periods and repeated usage demonstrated excellent structural integrity and electrochemical durability, confirming the composites' long-term viability. In addition to detection, the removal of Pb^{2+} and Cd^{2+} ions from water was evaluated using UV–Visible spectroscopy, which confirmed the efficient removal of these heavy metal ions by both PrGZ and PrGM composites. The high surface area, active functional groups, and porous nature of the composites played a significant role in enhancing metal ion adsorption, demonstrating their dual functionality in detection and remediation.

In conclusion, this study presents a successful demonstration of low-cost, scalable, and efficient ternary nanocomposites—PrGZ and PrGM—for the sensitive and selective electrochemical detection and effective removal of Pb^{2+} and Cd^{2+} ions from aqueous environments. The integration of PANI, rGO, and commercially available ZnO or MnO_2 resulted in materials with excellent electrochemical performance, stability, and selectivity. These composites are not only promising candidates for environmental monitoring of heavy metals but also hold potential for broader applications in water purification and environmental remediation technologies.

ACKNOWLEDGEMENT

With a heart full of gratitude and reverence, I begin this acknowledgement by giving thanks to the **Almighty God**, whose infinite mercy, grace, and blessings have been the guiding light throughout my academic journey. His divine presence has provided me with strength in moments of weakness, clarity in times of confusion, and unwavering hope in challenging phases. Without His will, none of this would have been possible.

I would like to express my profound gratitude and deep respect to my supervisor, **Dr. Harish Mudila**, Associate Professor at the School of Physical and Chemical Sciences, Lovely Professional University, Punjab (India). His exceptional mentorship, constant encouragement, and immense knowledge have played a pivotal role in shaping my research. His dedication to excellence and insightful guidance helped me stay focused and motivated, and I consider myself fortunate to have worked under his esteemed guidance.

I sincerely thank the **End Term Presentation Panel Members** for their constructive feedback, thoughtful suggestions, and critical evaluation during my research work. Their valuable input enriched the quality of my thesis and helped me to gain deeper insights into my study.

My heartfelt appreciation goes to the **Centre Instrumentation Facility** of Lovely Professional University for providing access to sophisticated equipment and timely support in the characterization of samples. Their assistance greatly contributed to the analytical aspects of this research.

I also extend my sincere thanks to the **non-teaching staff** of the School of Physical and Chemical Sciences for their kind cooperation, timely help, and logistical support throughout the duration of my thesis work.

Beyond the academic sphere, I owe a debt of gratitude to my **beloved husband, Mr. Rajat Gupta**, whose unconditional love, unwavering support, and boundless patience have been the foundation of my strength. He has been my anchor, my constant source of motivation, and the silent force that kept me going even during the most demanding times. His belief in my dreams has played a vital role in the completion of this journey.

I would also like to express my heartfelt thanks to my **father-in-law, Mr. Rajender Mohan Gupta**, for his generous financial support and moral encouragement. His faith in my abilities gave me confidence, and his continuous motivation helped me remain determined throughout.

To my **mother-in-law, Mrs. Pinki Gupta**, I am truly grateful for her moral support, understanding, and nurturing presence during this challenging yet fulfilling phase of my life.

My **dearest sons, Ranish Gupta and Eric Gupta**, deserve special acknowledgment. Their innocent smiles, love, and endless patience while I juggled between my responsibilities as a mother and a scholar gave me the strength to persevere. They have been my little rays of sunshine and the purest form of encouragement.

I express my deep appreciation to my **father, Mr. Virender Bansal**, whose emotional support, belief in my potential, and encouraging words provided immense comfort and motivation throughout this journey.

To my **mother, Mrs. Virendera Devi**, I owe everything. She has been my inspiration, my inner strength, and the constant source of emotional and moral support. Her love and sacrifices have been the bedrock upon which all my accomplishments stand.

Lastly, I wish to thank my **sister-in-law, Preeti Bansal**, for her warm support, care, and moral encouragement. Her positivity and understanding meant a lot during the demanding times of my research work.

This journey has been a blend of academic rigor and emotional learning, and I am eternally grateful to each individual who stood by me and contributed in their own unique way. To all of you, thank you from the bottom of my heart.

Nisha

Research Scholar

Table of Contents

List of Tables

LIST OF FIGURES

List of Abbrevations

Abbreviation	Full Form
WHO	World Health Organization
ppb	Part per billion
AAS	Atomic Absorption Spectrometry
LIBS	Laser-Induced Breakdown Spectroscopy
GFAAS	Graphite Furnace Atomic Absorption Spectrometry
ICP	Inductively Coupled Plasma
NAA	Neutron Activation Analysis
XRF	X-ray Fluorescence
SWV	Square Wave Voltammetry
SPE	Solid Phase Extraction
CV	Cyclic Voltammetry
ASV	Anodic Stripping Voltammetry
DPV	Differential Pulse Voltammetry
DPASV	Differential Pulse Anodic Stripping Voltammetry
TMO	Transition Metal Oxide
TMC	Transition Metal Carbide
CNT	Carbon Nanotubes
PANI	Polyaniline
PPY	Polypyrrole
PTH	Polythiophene
TMDGs	Transition Metal Dichalcogenides
SWASV	Square Wave Anodic Stripping Voltammetry
GO	Graphite Oxide
rGO	Reduced Graphite Oxide / Graphene
AC	Activated Charcoal
MWCNT	Multiwalled Carbon Nanotubes
PACE	Polyacetylene
CPs	Conducting Polymers
PEDOT	Poly(3,4-ethylenedioxythiophene)
ZnO	Zinc Oxide
MnO_2	Manganese Oxide
CPE	Carbon Pasted Electrode
FTIR	Fourier Transform Infrared Spectroscopy
SEM	Scanning Electron Microscopy
EDS	Energy Dispersive X-ray Spectroscopy
XRD	X-ray Diffractometry
TGA	Thermogravimetric Analysis
LOD	Limit of Detection
LOQ	Limit of Quantification
μgL^{-1}	Microgram per Liter
µA	Microampere
μM^{-1}	Micro per Molar

CHAPTER 1 Introduction

1.1 Introduction of heavy metals: In recent years, the rapid expansion of population coupled with accelerated industrialization has greatly impacted the quality of the natural environment. A broad spectrum of pollutants is continuously being discharged into the environment, posing serious threats to ecosystems and to the health of living organisms. Among these, heavy metals have emerged as particularly concerning pollutants due to their non-biodegradable nature, environmental persistence, and high toxicity. Unlike organic pollutants that may degrade over time, heavy metals such as lead (Pb^{2+}), copper (Cu^{2+}), and cadmium (Cd^{2+}) remain in the environment, progressively accumulating within biological systems and food chains, ultimately leading to bioaccumulation and biomagnification **(Ali et al., 2019).**

Heavy metals are considered major contaminants in water sources, and their presence even at trace levels can result in severe health hazards. WHO has set permissible limits for these metals in drinking water to minimize public health risks, with the limit for lead in drinking water being established at 10 ppb **(Chowdhury and Husain., 2016).** However, studies have demonstrated that even at concentrations below these recommended limits, heavy metals can biomagnify through the food chain, posing significant risks to human and animal health. This is particularly alarming in developing countries, where industrial effluents, untreated wastewater, and urban runoff are major sources of heavy metal contamination in water supplies **(Mohod and Dhote, 2013).**

Historical and contemporary research consistently highlights the ecological and health implications of heavy metal contamination in drinking water. **(Craun and McCabe., 1975)** addressed early concerns regarding drinking water quality and its associated public health risks, emphasizing the long-term effects of heavy metal exposure. More recently, **(Gebretsadik et al., 2020)** explored low-cost and eco-friendly alternatives for heavy metal removal from aqueous solutions, reporting the effective use of Eucalyptus camaldulensis leaves as a potential adsorbent for eliminating toxic metals from contaminated water sources.

This growing awareness of the risks associated with heavy metals underscores the urgent need for the development of effective, affordable, and sustainable removal technologies.**(Ali et al., 2019)** further elaborated on the environmental chemistry, ecotoxicology, and bioaccumulation

potential of hazardous heavy metals, providing comprehensive insights into their persistence and long-term ecological consequences. Together, these studies build a compelling case for prioritizing the removal of heavy metals from water bodies and enhancing the safety of drinking water supplies globally.

1.2 Sources of Heavy Metal: Heavy metal contamination in aquatic environments arises from a combination of anthropogenic and natural sources. Among the anthropogenic contributors, industrial activities such as paint production, leather processing, and paper manufacturing are particularly significant, discharging substantial quantities of heavy metals through wastewater and sewage into nearby water bodies. Additionally, mining operations, the widespread application of agrochemicals in agriculture, and domestic waste from expanding residential areas further exacerbate the levels of heavy metals in aquatic systems **(Mudila et al., 2018).** These human-driven processes account for the majority of heavy metal pollution, posing serious threats to water quality and public health. Besides these anthropogenic factors, natural processes also play a notable role in introducing heavy metals into aquatic environments. The weathering of metal-bearing rocks, along with geological phenomena such as volcanic eruptions, can release naturally occurring metals into rivers, lakes, and groundwater sources **(Gebretsadik et al., 2020).** While these natural events may contribute to background levels of heavy metals in the environment, their impact is often intensified when combined with anthropogenic inputs, leading to contamination levels that surpass safe limits for both ecological systems and human consumption.

1.3 General Effects of Heavy Metals on Human Physiology and Psychology: Heavy metals have long been associated with a broad spectrum of adverse effects on human health, owing to their toxicity, persistence, and bioaccumulative nature. Exposure to these hazardous elements, even in trace amounts, has been documented to result in the development of various types of cancer, skin disorders, renal dysfunction, and neurotoxic effects **(Chowdhury and Husain., 2016)**. Chronic exposure, in particular, has been linked to progressive muscular, physical, and neurological degeneration, leading to severe, often irreversible diseases such as Alzheimer's disease, Parkinson's disease, and muscular dystrophy **(Mohod and Dhote., 2013).** These health hazards become especially concerning in developing regions, where inadequate

water treatment and unregulated industrial activities often result in elevated heavy metal concentrations in drinking water supplies.

Moreover, studies have highlighted that soft water, characterized by its lower mineral content and higher corrosivity, tends to dissolve and carry higher concentrations of metal contaminants. This increases the population's susceptibility to cardiovascular diseases, as these dissolved metals infiltrate drinking water distribution systems and household supplies **(Craun and McCabe., 1975)**. These findings underscore the importance of continuous monitoring, improved water treatment infrastructure, and public awareness, particularly in regions where industrial and domestic sources contribute to significant heavy metal pollution in water resources.

Table: 1 Heavy Metals Detected in Potable Water: Permissible Limits, Common Sources, and Associated Side Effects

Element (Symbol)	**Permissible Amount (mg/L or PPM) (WHO)**	**Source**	**Side-effects**	**Reference**
Heavy Metals				
Arsenic (As)	0.05	Arsenic-rich geological formations	Skin malignancies, dermatological lesions, rough keratotic plaques, and pigmentary changes including leucomelanosis	**Mudila, H., et al., (2018)**
Lead (Pb)	0.05- 0.10	Water supply fixtures and plastic piping	Blood disorders, reproductive system impairments, and cognitive-behavioral challenges enlephalopatayis	**Gebretsadik et al., 2020**
Iron(Fe)	0.1-1.0	Textile washing and	Iron metabolism	**Mudila, H.,**

		ceramic products	disorder, bleeding-induced cell death	**et al., (2018)**
Mercury (Hg)	0.001-0.002	Airborne mercury accumulation, industrial byproducts, mining residues, and natural mercury-bearing minerals	Neurological harm, depressive states, cancer-inducing propertie	**Chowdhury and Husain, (2016)**
Selenium (Se)	0.01-0.05	Marine foods, offal, milk-based products	Breathing difficulties, selenium toxicity, kidney dysfunction	**Craun and McCabe, (1975)**
Chromium (Cr)	0.05-0.1	Naturally occurring in geological formations, plants, soil, and volcanic debris	Hepatic injury, swelling, multi-organ dysfunction, cancer-causing effects	**Mudila, H., et al., (2018)**
Cadmium (Cd)	0.005-0.01	Located in zinc, lead, and copper ores, and discharged during volcanic eruptions.	Cancer-inducing, affects the central nervous system, causes dental cavities	**Mudila, H., et al., (2018)**
Zinc (Zn)	0.1-15.0	Secondary product from the production of steel or coal-powered electricity.	Decreased white blood cell count, lymph node enlargement, cancer, digestive toxicity.	**Mudila, H., et al., (2018)**

1.4 Techniques for Determination and Decontamination of Heavy Metal Contaminants in Water: As emphasized in previous sections, the availability of clean and uncontaminated water is fundamentally essential for sustaining human physiological and psychological well-being. However, the persistent contamination of water resources with toxic heavy metals has become a pressing environmental and public health concern. Consequently, the accurate detection and efficient removal of these hazardous contaminants have become crucial priorities. Over the years, a variety of techniques have been developed and applied to address

these challenges, each offering distinct advantages and limitations that must be carefully evaluated in relation to specific applications and environmental conditions **(Mudila et al., 2018).**

The effectiveness of these detection and decontamination methods is strongly influenced by several physicochemical parameters. Critical factors such as the particle size of both the adsorbent and adsorbate, contact time, solution temperature, initial contaminant concentration, and pH considerably affect the adsorption behavior and overall removal efficiency of heavy metals from aqueous systems **(Gebretsadik et al., 2020).** Understanding the interplay of these factors is essential for optimizing treatment conditions and ensuring the successful remediation of contaminated water bodies, especially in areas where conventional treatment systems are inadequate or unavailable.

1.4.1 Adsorption: Adsorption is a widely used method for removing heavy metals from water due to its simplicity and efficiency. Zhang et al. (2020) reported that thiol-lignocellulose sodium bentonite (TLSB) nanocomposites, modified with –SH groups, showed high adsorption capacities for Cd(II), Zn(II), and Hg(II), making them suitable for large-scale remediation. Similarly, Torad et al. (2014) developed nanometer-sized zeolites A with high crystallinity and surface area, which effectively removed radioactive Cs^{+} ions, highlighting their potential in water purification.

1.4.2 Microbial Decontamination: The discharge of heavy metals from industries like mining and electroplating poses serious environmental and health risks. Traditional treatment methods such as chemical precipitation and membrane filtration are effective but face challenges like high costs and sludge generation. As an alternative, biosorption has emerged as a low-cost, efficient, and eco-friendly method for heavy metal removal using non-living biomass. **(Ahluwalia and Goyal., 2007)** demonstrated that microbial, algal, and plant-based biomasses—such as Aspergillus niger, Chlorella fusca, and Sargassum natans—can effectively bind metals like Pb, Zn, Cd, and Cu, with biosorption capacities ranging from 5 to 641 mg/g. The process involves mechanisms like ion exchange and complexation via functional groups on the biomass surface, showing great promise for sustainable wastewater treatment.

1.4.3 Atomic Absorption Spectrometry and Related Techniques: Accurate detection of heavy metals in water is vital for environmental monitoring and evaluating remediation techniques. AAS is widely used due to its sensitivity, cost-effectiveness, and suitability for complex samples **(Mudila et al., 2018)**. An enhanced version, AAS with Vapor Generation Assembly, enables trace arsenic detection by converting it into volatile hydrides, improving sensitivity **(Raj Behari and Prakash, 2006)**. AAS is commonly used to analyze residual metals after adsorption. For instance, **(Mostafa et al., 2016)** employed AAS to evaluate Pb(II) removal using Co–Mo LDH nanomaterials, showing a capacity of 73.4 mg/g with Langmuir isotherm and pseudo-second-order kinetics. **(Terán et al., 2019)** combined AAS with Laser-Induced Breakdown Spectroscopy (LIBS) to assess lead removal by montmorillonite clays, demonstrating the benefit of hybrid techniques. These studies highlight AAS as a reliable tool for heavy metal detection and adsorption efficiency assessment.

Table: 2 Analytical Techniques for Heavy Metal Detection

Technique	Advantages	Limitations	References
AAS	Exceptionally precise and sensitive (GFAAS), suitable for analyzing a wide range of trace elements, capable of processing numerous samples, user-friendly, highly accurate, and cost-effective.	Different lamps are needed for analyzing various elements in a mixture, and these lamps have a limited lifespan. The technique is suitable for analyzing solution samples or volatile substances but demands relatively large sample volumes (1-3 ml). It is less sensitive to refractory elements.	**Hung, D. Q., et al., (2004)**
ICP	It is a precise, accurate, and highly sensitive analytical tool, benefiting from recent	This method's detection of elements may be affected by spectroscopic	**Beauchemin, D. (2008)**

	advancements in ICP-MS instrumentation, such as reduced size, lower detection limits and more intuitive software for easier control. These improvements make it ideal for multi-elemental ultra-trace detection and isotopic analysis.	interference from isotopes of other elements, leading to reduced sensitivity. Additionally, the sensitivity of ICP-MS is compromised by its susceptibility to matrix effects. Furthermore, it does not provide information on the speciation of the sample.	
NAA	NAA is a sensitive and accurate analytical technique used to detect trace and ultra-trace amounts of elements in the sample being analyzed. Materials that are difficult to dissolve can be easily analyzed using this method, provided there is no interference in the sample.	This method is costly due to its reliance on a nuclear reactor. It also has a long turnaround time and slow sample throughput. The sensitivity of NAA is reduced due to spectral interference from other elements, such as Na and Br, present in the sample.	**Mok, W. M., et al., (1986)**
XRF	It is a feasible, effective, and non-destructive analytical technique for analyzing a wide range of hazardous materials and environmental samples (e.g., water, powder, soil) due to the availability of efficient radioisotope sources for excitation, paired with highly sensitive detectors and advanced	It is a slow, labor-intensive, and costly process. The number of samples available for analysis is also limited due to the high cost of laboratory operations..	**Melquiades, F. L., &Appoloni, C. R. (2004)**.

	electronics.		
Electrochemical	It is a versatile, simple, highly sensitive, rapid, and accurate method with easy operation and low cost. It offers a low detection limit, a compatible linear range, and reliable output with low power requirements. Various types are available, including SWV, SPE, CV, etc.	It operates within a narrow temperature range and is affected by humidity and temperature, which can reduce the lifespan of the electrode. Additionally, it may sometimes be interfered with by other analytes.,	**Ndlovu T., et al., (2014)**

1.5 Electrochemical Sensing Methods: Electrochemical sensing methods have gained significant attention in recent years due to their advantages such as high flexibility, operational convenience, rapid response, sensitivity, and accuracy. These properties have made them widely applicable in various chemical and biological sensing applications. In the context of water quality monitoring, electrochemical sensors are extensively employed for the detection of heavy metal ions.

The electrochemical sensing of heavy metals typically involves the modification of the working electrodes within an electrochemical cell. During the sensing process, a redox reaction occurs between the target analyte and the electrode surface in the electrolyte solution. This redox reaction generates electrical signals, which are subsequently detected and analyzed to determine the presence and concentration of heavy metal ions.

Although a wide range of materials has been utilized for the modification of working electrodes, a common and essential characteristic shared by these materials is their electrical conductivity. The conductive nature of these materials ensures effective electron transfer during the redox reactions, which is crucial for achieving reliable and sensitive electrochemical measurements.

1.5.1 Anodic Stripping Voltammetry: ASV is a highly sensitive and effective electrochemical technique for detecting and quantifying heavy metal ions in water. It allows for metal speciation, which is crucial for assessing toxicity and bioavailability **(Lan et al., 2012).** ASV involves a two-step process: metal ions are first deposited onto an electrode, then stripped back into solution, producing current peaks proportional to ion concentration. **(Lan et al., 2012)** showed enhanced detection of As(III) using gold-palladium modified electrodes. ASV can detect metals like Pb^{2+}, Cd^{2+}, Cu^{2+}, As(III), and Hg^{2+} at ppb levels across various water types, including seawater **(Jickells& Baker., 2005),** making it ideal for environmental and industrial water monitoring.

1.5.2 Differential Pulse Voltammetry: DPV is a sensitive electroanalytical technique used for detecting and characterizing trace metal ions in aqueous solutions. It applies small amplitude pulses on a linear ramp potential and measures the difference in current before and after each pulse, enhancing sensitivity and resolution by minimizing background currents **(Simões & Xavier., 2017).** DPV is effective for detecting metals like Pb^{2+}, Cd^{2+}, Cu^{2+}, Hg^{2+}, and Zn^{2+}, even in complex matrices. It also provides insights into redox behavior and kinetics, making it valuable for environmental monitoring and electrochemical research.

1.5.3 Square Wave Voltammetry: SWV is a sensitive electroanalytical technique ideal for detecting heavy metals in water. It uses a square-wave pulse over a linear potential to generate a peak current by measuring the difference between forward and reverse pulses, enhancing detection sensitivity **(Simões & Xavier., 2017; Westbroek., 2005).** SWV provides better detection limits and faster analysis than conventional methods, making it valuable for environmental monitoring. Electrode type is crucial—carbon-based electrodes, particularly those with CNTs, are popular for their conductivity and wide potential range **(Kim et al., 2017).** However, they face interference from other ions or organics. To address this, modified electrodes with nanomaterials or functional groups have been developed. **(Xiao et al., 2008)** improved As(III) detection using gold nanoparticle-modified CNT electrodes, achieving higher sensitivity than unmodified versions.

1.5.4 Cyclic Voltammetry: CV is a fundamental electrochemical technique used to investigate redox processes and evaluate electrode performance. In CV, the potential of a working electrode is swept between predetermined upper and lower limits, creating a cyclic waveform. The resulting current response, recorded as a function of potential, provides valuable insights into electrochemical behavior **(Zhang et al., 2013).** CV is useful for understanding reaction mechanisms, electron transfer kinetics, and the thermodynamics of electroactive species. It is widely applied in heavy metal detection to assess the electrochemical activity and sensitivity of modified electrodes, aiding the development of advanced sensing platforms for environmental monitoring.

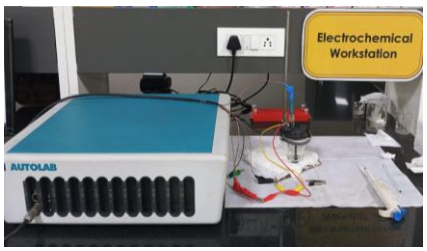

Figure: 1 Electrochemical sensing by three electrode system

1.6 Materials Used for Electrochemical Sensing: A wide range of electrically conductive materials can be employed for the electrochemical sensing of heavy metal ions. The selection of appropriate materials is essential, as their electrical conductivity, surface morphology, and chemical properties directly affect the sensitivity, selectivity, and overall performance of the sensing system. The primary categories of materials commonly used in electrochemical sensing are as follows- MXenes are a class of two-dimensional materials composed of transition metal carbides, nitrides, and carbonitrides. They are known for their excellent electrical conductivity, high surface area, and favorable electrochemical properties, making them highly effective for sensor applications. Transition Metal-Based Materials includes materials such as TMO, TMC, and other derivatives. These materials exhibit remarkable redox activity, chemical stability, and good electrochemical behavior, which make them suitable for electrode modification in heavy metal sensing applications. Carbon-based materials are widely utilized due to their high electrical conductivity, large surface area, chemical stability, and ease

of functionalization. Common examples include graphite, graphene, CNTs, and their functionalized derivatives, all of which enhance electrochemical sensor performance. Hybrid materials are composites formed by combining transition metal-based materials with carbonaceous substrates. These hybrid structures integrate the advantageous properties of both components, resulting in enhanced electrochemical activity, improved stability, and superior sensing capabilities compared to their individual counterparts. Conducting polymers such as polyaniline, polypyrrole, and polythiophene are frequently used in electrochemical sensing. These materials offer inherent conductivity, good environmental stability, and ease of synthesis and modification, making them highly suitable for sensor fabrication. These materials, either individually or in combination, serve as efficient platforms for the development of sensitive, selective, and reliable electrochemical sensors for the detection of heavy metal ions in aqueous environments.

1.6.1 Transition Metal Compounds: Transition metal compounds including metal oxides, transition metal carbides, transition metal dichalcogenides, and MXenes, have gained significant attention for environmental remediation, especially for detecting and removing toxic metal ions and organic pollutants in aqueous environments. These materials are recognized for their unique physicochemical properties, such as high surface area, excellent electrical conductivity, tunability, and rapid charge transfer capabilities **(Gouden et al., 2018; Rasool et al., 2019; Rahman et al., 2020).** Among them, MXenes—a family of two-dimensional transition metal carbides, nitrides, and carbonitrides with the formula $M_{n+1}AX_n$—are particularly promising for electrochemical sensing. Their electron-rich surfaces, large active sites, high hydrophilicity, and tunable structures make them efficient for detecting toxic metal ions in aqueous media **(Ibrahim et al., 2020).** Furthermore, the accumulation of photo-generated electrons on TMCo-based electrodes enhances the deposition and detection of reduced metal ions, boosting sensing performance **(Czikkely et al., 2018).**Electrochemical studies on MXene-based sensors have shown impressive sensitivity and selectivity for heavy metals such as Cd^{2+}, Pb^{2+}, Cu^{2+}, and Hg^{2+}, with detection limits as low as 0.098 μM for Cd^{2+}, 0.041 μM for Pb^{2+}, 0.032 μM for Cu^{2+}, and 0.013 μM for Hg^{2+} using square wave anodic stripping voltammetry **(Shahzad et al., 2020).** This emphasizes the potential of MXene-based nanomaterials in real-time environmental monitoring and water quality assessment.

1.6.2 Carbonaceous Materials: Carbon-based nanomaterials, including graphite, graphene, graphite oxide (GO), reduced graphene oxide(rGO), graphene and carbon nanotubes (CNTs), have gained significant attention for the detection and removal of heavy metals from aqueous systems due to their excellent electrical conductivity, high surface area, and tunable surface chemistry. Graphite oxide, graphene oxide, reduced graphite oxide, reduced graphene oxide, and graphene are closely related carbon-based materials that differ mainly in their structure, degree of oxidation, and electronic properties. Graphite oxide is the bulk, layered material obtained by chemically oxidizing graphite; it consists of stacked graphene layers heavily functionalized with oxygen-containing groups such as epoxy, hydroxyl, and carboxyl groups, which increase interlayer spacing and disrupt electrical conductivity. Graphene oxide is derived from graphite oxide by exfoliation into single or few-layer sheets; it retains a high density of oxygen functional groups, making it hydrophilic, easily dispersible in water, and electrically insulating to semiconducting. Reduced graphite oxide refers to partially deoxygenated graphite oxide in its multilayer, stacked form, produced by chemical, thermal, or electrochemical reduction; although some oxygen groups are removed and conductivity improves, the material remains less conductive and more disordered than pristine graphite. Reduced graphene oxide is obtained by reducing graphite oxide sheets; it has lower oxygen content than GO, partially restored sp^2 carbon networks, enhanced electrical conductivity, and a high density of structural defects compared to pristine graphene. In contrast**,** graphene is a single layer of sp^2-bonded carbon atoms arranged in a two-dimensional honeycomb lattice with minimal defects and no oxygen functional groups, exhibiting exceptional electrical conductivity, mechanical strength, and thermal properties, making it fundamentally distinct from its oxidized and reduced derivatives. It is considered practically impossible to obtain perfectly oxygen-free graphene from graphene oxide because the oxidation–reduction process introduces structural defects and strongly bound oxygen functionalities that cannot be completely removed. During the oxidation of graphite to form GO, oxygen-containing groups such as hydroxyl (–OH), epoxy (–O–), carbonyl (C=O), and carboxyl (–COOH) are covalently attached to the carbon lattice. This process disrupts the extended sp^2 conjugated network of graphene by converting many carbon atoms to sp^3 hybridization and creating vacancies and lattice distortions.

When GO is chemically, thermally, or electrochemically reduced, a large fraction of these oxygen groups is removed, and partial restoration of the sp^2 carbon network occurs. However, some oxygen moieties remain strongly bonded, especially at defect sites and sheet edges, and the original graphene lattice cannot be fully reconstructed. Additionally, irreversible defects generated during oxidation prevent complete recovery of pristine graphene. For this reason, the reduced material is not true graphene but is correctly termed rGO, reflecting that it still contains residual oxygen and structural disorder. Thus, rGO represents a graphene-like material with improved conductivity compared to GO, but it is fundamentally distinct from defect-free, pristine graphene. These materials enhance electrochemical performance by promoting rapid charge transport and efficient adsorption of trace metal ions, even at low concentrations. In electrochemical sensing, carbon nanomaterials serve as conductive platforms or electrode modifiers, improving sensitivity, detection limits, and stability. Their ability to integrate with functional nanomaterials, such as metal nanoparticles or TMCo-based materials, further enhances adsorption and electron transfer, making them ideal for detecting heavy metals. Their versatility in surface modification allows for improved selectivity and interference management, positioning them as key components in next-generation environmental monitoring and water treatment technologies **(Baby et al., 2019).**

1.6.2.1 Activated Charcoal: AC is widely used in heavy metal ion detection and water purification due to its high surface area, porous structure, and rich surface chemistry, which make it an excellent adsorbent **(Travlou et al., 2015).** AC's versatility, chemical stability, and mechanical strength make it ideal for sensor development and contaminant removal. It efficiently adsorbs heavy metals such as Cd^{2+}, Cu^{2+}, Ni^{2+}, and Pb^{2+}, with AC derived from African palm fruit showing high removal efficiencies of 93.23% for Cd^{2+} and 96.71% for Cu^{2+} under optimal conditions **(Sani Abdulrazak et al., 2017).** Despite its high adsorptive capacity, AC faces challenges like slow adsorption kinetics, poor selectivity for certain contaminants, and limited lifespan of filters. Ongoing research focuses on enhancing AC's surface properties and combining it with other materials to improve selectivity and regeneration capacity, thereby increasing its effectiveness in environmental applications **(Yue and Economy., 2017).**

1.6.2.2 Carbon Nanotubes: CNTs, both single-walled (SWCNTs) and multi-walled (MWCNTs), are highly conductive nanomaterials with excellent surface area, mechanical

strength, and chemical stability, making them ideal for electrochemical sensing of heavy metals in water **(Musameh et al., 2011).** CNT-based sensors offer high sensitivity, selectivity, and rapid response times for detecting toxic metals like Cu^{2+}, Pb^{2+}, Cd^{2+}, and Hg^{2+}. For example, CNT sensors have achieved detection limits as low as 0.2279 ppb for Pb^{2+} and 0.3321 ppb for Cu^{2+} **(Silva et al., 2016)**. Composites like Fe_3O_4/MWCNT and functionalized MWCNTs improve sensitivity and selectivity, with detection limits reaching as low as 0.05–0.08 nM **(Wu et al., 2019).**

Despite their advantages, CNTs face challenges such as high production costs, aggregation, and functionalization issues **(Pitroda et al., 2016).** Ongoing research is addressing these challenges through functionalization to enhance performance and reduce costs **(Bezzon et al., 2019).** In summary, CNTs show great promise for heavy metal detection in environmental monitoring and remediation.

1.6.2.3 Graphite Oxide: GO is a promising material for heavy metal ion removal and detection due to its two-dimensional structure, rich oxygenated functional groups (e.g., -OH, -COOH), and hydrophilicity, which enhance its dispersion in aqueous environments **(Liu et al., 2019)**. GO's hydrophilic surface facilitates efficient adsorption of heavy metals, while its high surface area and compatibility with various matrices make it an ideal candidate for water purification and sensor applications. However, challenges such as aggregation and reduced reactivity in solution can hinder its performance.

To enhance GO's capabilities, various composites and hybrid materials have been developed. For example, graphene oxide-based microbots have been designed to detect and capture Pb^{2+} ions, reducing concentrations by tenfold in just one hour due to GO's magnetic properties **(Vilela et al., 2016).** Metal oxide composites like $MnFe_2O_4$-GO have been explored for their synergistic effects in improving electrochemical sensing for Pb(II) **(Zhou et al., 2018).** Additionally, incorporating organic compounds such as chitosan and poly(L-glutamic acid) into GO composites has improved metal ion adsorption and overall performance in trace metal detection **(Yi et al., 2019).** GO-based materials have also shown potential for simultaneous detection of multiple metal ions, with GO-chitosan complexes demonstrating effective adsorption for metals like Cu^{2+}, Pb^{2+}, and Zn^{2+} **(Li et al., 2020).**

Despite these advances, GO's dispersibility and aggregation issues still pose challenges. Ongoing research in nanostructured modifications and functionalized GO composites is focused on improving its efficiency as an adsorbent and electrochemical sensor for water purification and environmental remediation.

1.6.2.4 Reduced Graphene Oxide: rGO, obtained by reducing GO through chemical or physical processes, offers excellent electrical conductivity, high specific surface area, rapid electron transport, and biocompatibility **(Silva & Cesarino, 2020).** These properties make rGO an effective material for adsorbing and detecting toxic heavy metals in aqueous systems. The remaining functional groups on rGO after reduction facilitate efficient interaction with heavy metal ions, making it a valuable platform for both water treatment and sensor applications. To improve sensitivity, hybrid nanocomposites of rGO with metal nanoparticles have been developed, such as rGO–bismuth (Bi) nanoparticle composites, which demonstrated detection limits as low as 0.55 μg/L for Pb^{2+} and 2.8 μg/L for Cd^{2+} **(Cui et al., 2014).** These nanocomposites combine the high conductivity and large surface area of rGO with the electrocatalytic properties of metal nanoparticles, enhancing sensor performance. However, challenges like aggregation due to van der Waals forces and π–π stacking can limit rGO's performance, which can be overcome by incorporating nanomaterials such as metal oxides, nanoparticles, or conductive polymers to maintain layer separation and improve electrochemical properties **(Liu et al., 2019).** This makes rGO-based materials crucial for heavy metal detection and water remediation, especially when integrated into advanced nanohybrid structures.

1.6.3 Conducting Polymers: CPs, such as polyaniline, polypyrrole, polythiophene, and polyacetylene, are a class of organic materials that combine the electrical properties of metals with the flexibility and processability of conventional polymers. These materials possess high electrical conductivity derived from their delocalized π-conjugated polymer backbones, which facilitate efficient charge transfer through the addition or removal of electrons. As highlighted by **(Le et al., 2017),** this unique property of CPs has made them particularly valuable for applications in sensors, biosensors, actuators, and capacitors, as well as for the electrochemical detection of heavy metals in aqueous environments. According to **(Bai and Shi., 2007)**, the conductivity and surface reactivity of CPs allow them to interact with target analytes such as

metal ions, making them highly effective as electrode materials in various electrochemical sensing platforms.

PANI stands out as one of the most extensively studied conducting polymers due to its excellent electrochemical properties, environmental stability, and simple, cost-effective synthesis. PANI can exist in different oxidation states, including leucoemeraldine, emeraldine, and polaron, with the emeraldine salt form exhibiting the highest conductivity. As reported by **(Chen et al., 2018)**, the electrical conductivity of PANI can be modulated by controlling its dopant type and oxidation state, making it highly versatile for electrochemical sensing applications. PANI has been widely used for the electrochemical detection of heavy metals such as Pb^{2+}, Cu^{2+}, Cd^{2+}, Ni^{2+}, and Cr^{3+}, due to its ability to form complexes and interact electrochemically with metal ions at the electrode surface. The electrochemical sensors developed using PANI utilize oxidation-reduction reactions that occur between the polymer backbone and the metal ions, resulting in high selectivity and sensitivity for the detection of trace metal concentrations. In a study by **(Chen et al., 2018),** PANI-based sensors demonstrated excellent performance for detecting Pb^{2+} in water, particularly when enhanced by doping agents such as tungsten oxide (WO_3), polyaniline-gold (Au) composites, and carbon nanotube composites. The PANI-CNT composites achieved remarkable sensitivity and selectivity, with detection limits as low as 0.05 μmol/L for Pb^{2+} ions, confirming PANI's potential for environmental monitoring applications.

PPY is a conducting polymer known for its high electrical conductivity, widely used in electrochemical sensors for detecting heavy metals such as Pb^{2+}, Cu^{2+}, Cd^{2+}, and Hg^{2+} (Le et al., 2017). PPY-based sensors offer high sensitivity, with detection limits as low as 0.055 μmol/L for Pb^{2+} **(Xu et al., 2020).** PTH is another conducting polymer, valued for its environmental stability and charge transport properties, used for detecting Ag^{+} ions with a detection limit of 6×10^{-9} M **(Zanganeh and Amini, 2007).** Poly(3,4-ethylenedioxythiophene), known for its superior conductivity, has been employed for detecting multiple heavy metals, achieving detection limits as low as 0.00073 μM for Cd^{2+} **(Rouis et al., 2013).** Despite challenges such as polymer degradation and high production costs, conducting polymers continue to show great promise in the development of sensitive and durable sensors for environmental and industrial applications **(Le et al., 2017; Chen et al., 2018).**

1.6.4 Hybrid Materials: Recent advancements in hybrid materials for heavy metal ion detection have significantly improved the efficiency and sensitivity of electrochemical sensors. These materials combine the properties of individual components, leading to enhanced electrochemical behavior. For instance, **(Lo et al., 2020)** developed a PPY-CNT composite, which exhibited enhanced electrical conductivity and stability, achieving a low detection limit of 2.9×10^{-9} mol/L for Pb^{2+}. **(Muralikrishna et al., 2017)** created a PANI-GO hydrogel composite that improved both sensitivity and stability for Pb^{2+} detection due to the synergistic effects between PANI and GO. Additionally, **(Wang et al., 2019)** reported a nanocomposite of NH_2-MIL-53(Al) and PPY, which demonstrated ultra-low detection limits for Pb^{2+} and Cu^{2+} ions, attributed to the high porosity of the framework and the electrochemical properties of PPY. These innovations highlight the potential of hybrid materials, such as conducting polymers combined with nanostructures like CNTs, GO, and metal-organic frameworks, in developing sensitive, stable, and selective electrochemical sensors for environmental monitoring.

1.6.4.1 Hybrid PANI Composites for Heavy Metal Detection: PANI based hybrid composites have shown excellent potential for electrochemical heavy metal detection due to their high conductivity and stability. For instance, a PANI/Graphene composite electrode enhanced the detection of Cd^{2+}, Pb^{2+}, and Cu^{2+} with a LOD of 10^{-8} mol/L **(Ronda and Alcazar., 2014)**. **(Muralikrishna et al., 2017)** developed PANI/GO hydrogels for Pb^{2+} detection, achieving a LOD of 0.04 nM. PANI/TiO_2 composites demonstrated strong adsorption capacities, with LOD values of 0.594mmol/g for Zn^{2+} and 0.460mmol/g for Pb^{2+} **(Wang et al., 2019)**. Further, PANI/Carbon Paste electrodes detected Pb^{2+} and Cd^{2+} at ultra-low concentrations **(Somerset et al., 2014)**, and a PANI/GO composite for Hg^{2+} detection achieved a remarkable LOD of 2 ppb **(Mahadik et al., 2020)**. Other composites like PANI/Vanadyl Phosphate and PANI/CNT have also shown high sensitivity for heavy metal ions **(Akhtar et al., 2020; Patil et al., 2018)**. These composites, particularly when combined with graphene derivatives, metal oxides, and MOFs, provide highly sensitive and selective electrochemical sensors for heavy metal detection in environmental monitoring.

This research addresses the pressing issue of heavy metal contamination in aquatic environments, with a primary focus on the detection of Pb^{2+} and Cd^{2+} ions. To achieve this, novel electrochemical sensors were developed using nanocomposites based on PANI, rGO, and

transition metal oxides (ZnO and MnO_2). These composites were strategically designed to harness the synergistic properties of their constituents: the redox-active functional groups of PANI, the high surface area and excellent conductivity of rGO, and the enhanced electrochemical properties of ZnO and MnO_2. The PANI/rGO/ZnO nanocomposite exhibited outstanding electrochemical performance for Pb^{2+} detection, with LOD of 0.3 μM and LOQ of 1.16 μM, demonstrating high precision and reproducibility (R^2 = 0.994, RSD = 2.13%). Additionally, for Cd^{2+} detection, the same nanocomposite achieved an impressive LOD of 0.005 μM and LOQ of 0.016 μM, with excellent linearity (R^2 = 0.996) and low relative standard deviation (RSD = 0.079%). The ternary PANI/rGO/MnO_2 (PrGM-2) nanocomposite further enhanced sensing capabilities. For Pb^{2+} detection, it achieved a LOD of 0.014 μM and LOQ of 0.043 μM, accompanied by a strong correlation coefficient (R^2 = 0.994) and a very low RSD of 0.27%, indicating high sensitivity and repeatability. In another configuration, the same composite showed a LOD of 0.15 μM and LOQ of 0.45 μM for Pb^{2+}, with good linearity (R^2 = 0.991) and acceptable reproducibility (RSD = 1.98%). Overall, these nanocomposite-based sensors demonstrate remarkable potential for real-world environmental monitoring. Their high sensitivity, selectivity, and stability make them suitable not only for detecting Pb^{2+} and Cd^{2+} ions but also for broader applications in monitoring other toxic heavy metals in contaminated water sources.

1.7 Objectives of the research work: The specific objectives of the research topic are

1. Preparation of polyaniline, and Graphene oxide/Graphene using graphite
2. Fabrication of Polyaniline (PANI) based ternary nanocomposites using transition metal oxides (TMO) and Graphene oxide /graphene in varying concentrations.
3. Detection and removal of heavy metals with electrochemical techniques using Polyaniline based nanocomposites.

2.1 PANI as a Sensing Material for Heavy Metals in Aqueous Source: PANI has been widely researched as a promising material for heavy metal detection in aqueous environments due to its unique redox properties, good environmental stability, and tunable conductivity. Researchers have explored PANI in various morphologies—especially nanofibers—to enhance sensitivity, selectivity, and response time in electrochemical and colorimetric sensing platforms. **Virji et al., 2004** investigated the response mechanisms of polyaniline nanofibers when exposed to different gases and found that the unique morphology contributed to faster response times and enhanced sensitivity due to higher surface-to-volume ratios. Although their work was primarily focused on gas sensing, the findings laid important groundwork for aqueous sensing applications, highlighting PANI's intrinsic conductive properties and its ability to transduce chemical interactions into measurable electrical signals. **Sadek et al., 2007** extended this research by developing a PANI nanofiber composite-based sensor, emphasizing the role of composite formation in improving sensing performance. Their work demonstrated how incorporating nanoparticles with PANI could enhance its electrochemical behavior, which is critical for detecting metal ions in aqueous media. **Yan et al., 2007** further explored the fabrication of PANI nanofibers and their application in room-temperature hydrogen sensing. While their study did not directly address heavy metals, the work showcased the potential of nanostructured PANI to function as a highly sensitive and stable sensing platform in various environments, including aqueous systems. **Liu, Hayashi, and Toko., 2012** reported the development of humidity sensors using electrospun PANI nanofibers, where the response was found to be rapid and reversible. This research contributed significantly to understanding how nanostructured PANI interacts with moisture and aqueous media, which is analogous to its interaction with heavy metal ions. **Lin, Li, and Yang, 2012** introduced a novel humidity sensor based on PANI nanofibers, showcasing its reproducibility and low detection limit. This work provided foundational insight into sensor miniaturization and integration with portable devices for real-time monitoring of environmental pollutants, including heavy metals. **Baker et al., 2008** focused on the mechanical actuation properties of PANI nanofibers, which, while not directly related to sensing, demonstrated the high functional versatility of PANI in devices requiring environmental responsiveness**.** Their fabrication methods are transferable to

sensor design and have been utilized in multi-functional sensors. **Tseng et al., 2005** developed a memory device using PANI nanofibers and gold nanoparticles, demonstrating the synergy between PANI and metal nanoparticles. This is highly relevant for sensing applications, where noble metals like Au or Ag are often incorporated with PANI to improve selectivity and signal amplification for detecting trace heavy metals**. Virji et al., 2005** in another related work, provided further analysis on the sensing mechanisms of PANI nanofibers and highlighted their potential for selective detection. The study reinforced the idea that PANI's morphology and doping level play key roles in its electrochemical behavior, directly influencing its performance as a heavy metal sensor in water samples**. Bianchi et al., 2022** emphasize the development of advanced PANI-based sensors and sorbents tailored for environmental monitoring and water purification, presenting a sustainable and highly effective approach to mitigate the global issue of heavy metal contamination in aquatic systems. **Le et al., 2017** extensively reviewed the electrical and electrochemical properties of conducting polymers, highlighting their tunable conductivity, doping/dedoping behavior, and compatibility with various nanomaterials, making them excellent candidates for sensor applications. **Bai and Shi., 2007** further demonstrated the utility of conducting polymers in gas sensing applications, attributing their sensitivity to the rapid charge transport and interaction with target analytes. **Quintana et al., 2013** developed an electrochemical sensor based on polypyrrole films for the detection of heavy metals in aqueous solutions, confirming its sensitivity and environmental applicability. **Xu et al., 2020**advanced this approach by employing conductive polypyrrole nanoparticles for the electrochemical sensing of lead (II) ions using differential pulse voltammetry, achieving enhanced sensitivity due to the increased surface area and electron transfer capabilities of the nanoparticles. Additionally, **Velempini et al., 2018** introduced a polypyrrole/carboxymethyl cellulose ion-imprinted polymer for mercury detection, combining the selectivity of molecular imprinting with the conductivity of PPY, resulting in an efficient sensor platform for environmental monitoring. Collectively, these studies emphasize the versatility of conducting polymers, particularly polypyrrole, in the development of highly sensitive, selective, and stable electrochemical sensors for the detection of various hazardous substances in environmental samples.Among conducting polymers, PANI stands out as one of the most versatile and extensively studied materials for electrochemical sensing applications due to its excellent environmental stability, tunable conductivity, ease of synthesis, and rich redox behavior. **Le et al., 2017** emphasized the superior electrical and

electrochemical properties of conducting polymers, particularly highlighting PANI's doping–dedoping characteristics and environmental resilience, making it highly suitable for sensor applications. **Bai and Shi., 2007** also noted PANI's remarkable gas sensing performance, attributing it to its adjustable conductivity and interaction with analytes. In the field of heavy metal detection, several researchers have harnessed PANI's capabilities. For instance, **Velempini et al., 2018** integrated PANI with carboxymethyl cellulose in an ion-imprinted polymer matrix for mercury detection benefiting from PANI's conductivity to improve signal transduction. Although **Quintana et al., 2013 and Xu et al., 2020** primarily focused on PPY, their findings highlight the advantages of conducting polymers, which PANI often surpasses due to its broader electrochemical window and stability. Overall, the collective evidence underscores PANI as the most promising conducting polymer, offering an ideal platform for developing sensitive, selective, and stable electrochemical sensors for environmental monitoring and heavy metal detection. **Zhang et al., 2005** conducted a foundational study on the oxidative polymerization of aniline using $FeCl_3$ (2.4 M) in the presence of dopants such as para-toluenesulfonic acid (P-TSA), β-naphthalene sulfonic acid (β-NSA), camphor sulfonic acid (CSA), and aniline itself. The resulting PANI exhibited a conductivity of 1.7×10^{-1} S/cm, demonstrating how oxidant and dopant concentrations significantly influence the electrical characteristics of the polymer—an essential property for sensing applications. Building on this, **Yakuphanoglu et al., 2007** studied PANI synthesized at 28°C and reported a conductivity of 0.21 S/cm, highlighting the role of temperature in achieving optimal conductive behavior for electrochemical applications. **Zhang et al., 2008** explored the effects of different acid dopants (HCl, H_2SO_4, H_3PO_4) on the conductivity of PANI. Their results showed that H_2SO_4-doped PANI achieved the highest conductivity (7.83×10^{-2} S/cm), followed by HCl and H_3PO_4, emphasizing the importance of the doping environment in enhancing the material's sensing performance. **Mi et al., 2008 and Basavaraja et al., 2009** further investigated the impact of various oxidizing agents and dopant combinations on the morphology and electrical properties of PANI. These studies contributed to refining the synthesis process to achieve tailored conductivity profiles suitable for sensor integration. **Ayad et al., 2011** synthesized PANI using $FeCl_3$ in an HCl medium and achieved a conductivity of 7×10^{-3} S/cm, while **Abdulla et al., 2012** measured conductivity in doped PANI thin films, reporting 0.5 Ω^{-1} cm^{-1}. Their findings highlight the influence of synthesis conditions and physical form (e.g., films) on the electrochemical activity crucial for sensor function.**Yi-Su**

et al., 2012 optimized synthesis by combining $FeCl_3$ and APS (2:1 ratio) with DBSA and aniline, producing PANI with promising electrochemical characteristics. Similarly, **Zeng et al., 2015 and Ashokan et al. 2015** employed a range of oxidants (APS, $FeCl_3$, $K_2Cr_2O_7$) to expand the scope of oxidative polymerization techniques, enhancing the tunability of PANI's electrical behavior. **Luong et al.2020** reaffirmed the reliability of chemical oxidative polymerization for reproducible synthesis of PANI with desired electroactive properties. **Kumar et al., 2020** further emphasized PANI's technological versatility, including its role in chemical sensing due to its inherent conductivity and redox behavior.More recent studies have increasingly focused on the practical use of PANI in heavy metal detection. **Altundal et al., 2021** demonstrated the electrochemical detection of Cd^{2+} ions using PANI-based composites, while **Motaghedifard et al., 2021** reported successful sensing of Cr^{6+} ions. **Okpara et al., 2022** expanded these applications by electrochemically evaluating PANI composites for the detection of both Cd^{2+} and Hg^{2+} ions. These advancements confirm the material's sensitivity, stability, and suitability for environmental monitoring applications.

2.2 Transition Metal Oxides (ZnO and MnO_2) as a Sensing Material for Heavy Metals in Aqueous Sources:

Transition metal oxides, particularly ZnO and MnO_2, have garnered considerable attention in the development of electrochemical sensors for the detection of heavy metals due to their unique structural and electrochemical properties. These materials are widely studied for their excellent redox behavior, high surface area, and ability to facilitate rapid electron transfer, which are crucial for improving sensor performance. When incorporated into composite materials, such as those based on conducting polymers like PANI, they demonstrate synergistic effects that enhance the sensitivity, selectivity, and stability of sensors for heavy metal detection in aqueous media. ZnO, a wide-bandgap semiconductor, is known for its high electron mobility, biocompatibility, and significant surface area, all of which contribute to its excellent performance in electrochemical sensing. Its integration into PANI-based nanocomposites has proven to enhance the electrochemical activity of the system, facilitating rapid charge transfer and providing ample active sites for metal ion adsorption. For instance, **Akhtar et al., 2020** synthesized a PANI-Alanine-rGO-ZnO ternary nanocomposite that demonstrated remarkable sensitivity for the detection of $\mathbf{Cd^{2+}}$, $\mathbf{Pb^{2+}}$, and $\mathbf{Cu^{2+}}$ ions, with detection limits as low as 0.03 nM, 0.045 nM, and 0.063 nM, respectively. In this composite, ZnO played a

key role in improving the charge transfer properties and electrochemical activity, working in synergy with PANI and rGO to enhance the sensor's performance.Similarly, **Mahadik et al., 2020** developed a PANI/Graphene Oxide composite, incorporating a modified form of ZnO along with EDTA, for the sensitive detection of Hg^{2+}. This composite achieved a remarkably low LOD of 2 ppb, highlighting ZnO's ability to interact effectively with metal ions, particularly in acidic to neutral media, where its high isoelectric point (~9.5) aids in the adsorption of divalent ions. In addition to ZnO, MnO_2 has become increasingly prominent in electrochemical sensing due to its multiple oxidation states, excellent redox properties, and high specific capacitance. MnO_2 enhances the electrocatalytic activity and electron transfer efficiency when combined with conducting polymers like PANI. Although **Wang et al., 2017** focused on integrating conductive frameworks such as PANI with metal-organic frameworks (MOFs), their work indirectly points to the potential of MnO_2-based frameworks for improving heavy metal detection. The multi-valency of MnO_2 allows for fast redox reactions, making it a suitable material for use in hybrid nanocomposites intended for heavy metal sensing. Both ZnO and MnO_2 serve as critical components in advanced electrochemical sensor systems. Their incorporation into PANI-based or carbonaceous nanocomposites results in significant improvements in sensor performance by enhancing electrocatalytic activity, increasing the adsorption capacity for metal ions, and facilitating faster charge transfer processes. The work of **Akhtar et al., 2020**, **Mahadik et al., 2020** and **Wang et al., 2017** collectively highlights the effectiveness of these metal oxides in composite materials, advancing the development of sensitive, selective, and reliable electrochemical platforms for detecting toxic heavy metals in environmental monitoring.

2.3 PANI-Based Binary Composites for Heavy Metal Sensing in Aqueous Media:

PANI, a highly conductive polymer, has garnered significant attention in environmental sensing due to its intrinsic redox activity, environmental stability, and ease of synthesis. When blended with various nanomaterials into binary composites, PANI's performance in detecting and adsorbing heavy metals is substantially enhanced. These composites offer increased surface area, synergistic interactions, and improved sensitivity and selectivity for specific metal ions. **Rajakumar et al., 2021** synthesized Mn_2O_3/PANI composites and demonstrated their substantial adsorption capacities for Pb(II), Cd(II), and Ni(II), which was attributed to strong chelation between the metal ions and hydroxyl groups present in Mn_2O_3.

Khong et al., 2021 prepared Sb_2O_3/PANI nanocomposites, which exhibited pH-dependent uptake of Pb(II) through surface complexation and ion exchange mechanisms. **Sahu et al., 2021** developed Al_2O_3/PANI nanofibrous composites via a one-pot method, which showed high selectivity for Cu(II) and Pb(II) due to their porous, high-surface-area structure. **Gu et al., 2021** reported that Fe_3O_4/PANI composites were effective in removing Cr(VI) through a mechanism involving the reduction of Cr(VI) to Cr(III), followed by adsorption facilitated by PANI's amine groups.Their Fe_3O_4/PANI microspheres exhibited core–shell structures that contributed to high stability and adsorption capacity in aqueous solutions. **Zhang et al., 2021** synthesized PANI nanorod-dotted GO nanosheets, which showed high Cr(VI) adsorption capacity along with effective reduction to Cr(III). **Fan et al., 2021** reported that 3D PANI/GO composites with spongy structures effectively adsorbed Hg(II), emphasizing the structural advantage of the 3D configuration. **Javadian et al., 2021** demonstrated coral-like dendritic nanofibers of PANI/GO composites that performed well in Cr(VI) adsorption under various conditions. **Sahu et al. 2021** developed PANI/SiO_2 nanocomposites that exhibited notable Cr(VI) adsorption through coupled mechanisms of ion exchange and reduction. **Le et al., 2017** highlighted the exceptional electrochemical properties of carbon-based materials and emphasized their enhanced performance when combined with conducting polymers such as PANI. In particular, the synergy between carbon nanostructures and PANI was shown to significantly improve the sensitivity and stability of electrochemical sensors designed for heavy metal detection. **Bai and Shi., 2007** further supported this by demonstrating that carbonaceous nanomaterials, known for their high surface area and conductivity in gas sensing, also show remarkable promise in liquid-phase applications such as detecting toxic metal ions when integrated with PANI. **Velempini et al., 2018** showcased a successful example of this by incorporating carbon nanomaterials into PANI-based ion-imprinted polymer matrices for Hg^{2+} detection, where the carbon component played a crucial role in facilitating electron transfer and enhancing overall sensor stability. Although **Quintanaet al., 2013 and Xu et al., 2020** focused primarily on polypyrrole-based composites, their observations also confirm that the integration of highly conductive carbon supports like GO and rGO substantially elevates sensor performance. Among these carbonaceous additives, GO and rGO stand out for their excellent aqueous dispersibility, ease of functionalization, and superior electrochemical characteristics. When combined with PANI, they form highly efficient hybrid sensing platforms capable of selectively and sensitively detecting heavy metals in

contaminated water sources. **Le et al., 2017** highlighted the exceptional electrochemical properties of carbon-based materials and emphasized their enhanced performance when combined with conducting polymers such as PANI. In particular, the synergy between carbon nanostructures and PANI was shown to significantly improve the sensitivity and stability of electrochemical sensors designed for heavy metal detection. **Bai and Shi., 2007** further supported this by demonstrating that carbonaceous nanomaterials, known for their high surface area and conductivity in gas sensing, also show remarkable promise in liquid-phase applications such as detecting toxic metal ions when integrated with PANI. **Velempini et al., 2018** showcased a successful example of this by incorporating carbon nanomaterials into PANI-based ion-imprinted polymer matrices for Hg^{2+} detection, where the carbon component played a crucial role in facilitating electron transfer and enhancing overall sensor stability. Although **Quintana et al., 2013** and **Xu et al., 2020** focused primarily on polypyrrole-based composites, their observations also confirm that the integration of highly conductive carbon supports like GO and rGO substantially elevates sensor performance. Among these carbonaceous additives, GO and rGO stand out for their excellent aqueous dispersibility, ease of functionalization, and superior electrochemical characteristics. When combined with PANI, they form highly efficient hybrid sensing platforms capable of selectively and sensitively detecting heavy metals in contaminated water sources.

2.4 PANI based ternary composite as a Sensing Material for Heavy Metals in Aqueous Sources:

PANI, a conducting polymer, has garnered significant attention in the development of electrochemical sensors due to its excellent conductivity, environmental stability, and ease of synthesis. When combined with other nanomaterials, PANI forms ternary composites that exhibit enhanced properties suitable for the sensitive detection of heavy metals in aqueous environments. GO and metal oxides like ZnO have been integrated with PANI to form ternary composites for heavy metal sensing. For instance, **Akhtar et al., 2020**developed a PANI-Alanine-rGO-ZnO ternary nanocomposite that demonstrated outstanding detection capabilities for Cd^{2+}, Pb^{2+}, and Cu^{2+} ions, with limits of detection as low as 0.03 nM, 0.045 nM, and 0.063 nM, respectively. The incorporation of ZnO enhanced the electrochemical activity and charge transfer characteristics of the sensing system, while rGO provided a conductive network facilitating electron transfer. Similarly, **Mahadik et al., 2020** utilized a PANI/Graphene Oxide

composite, where ZnO was introduced in a modified form along with EDTA for the detection of Hg^{2+}, achieving a remarkably low limit of detection of 2 ppb. ZnO's inherent ability to interact with metal ions and its high isoelectric point (~9.5) made it particularly effective in adsorbing divalent metal ions in acidic to neutral media, improving the sensor's sensitivity. **Wang et al., 2017** developed a ternary nanocomposite of PANI, silver nanoparticles (Ag NPs), and GO quantum dots (QDs) for the removal of Cr(VI) from polluted water. The composite exhibited efficient adsorption properties, with a detection limit for Cr(VI) ions lower than the maximum allowed limit set by the WHO, demonstrating its potential for environmental monitoring. Incorporating other conductive polymers and carbon nanomaterials into PANI-based composites has further enhanced their sensing capabilities. **Zhang et al., 2021** synthesized a ternary composite of PANI, polydopamine, and rGO for the simultaneous electrochemical detection of Cd^{2+}, Pb^{2+}, Fe^{2+}, and Cu^{2+} ions. The composite exhibited high sensitivity and selectivity, making it a promising candidate for real-time environmental monitoring. The integration of metal oxides and carbon nanomaterials with PANI has led to the development of composites with improved electrochemical properties for heavy metal detection. **Liu et al., 2022** reported a ternary composite of PANI, MnO_2, and CNTs for the detection of Pb^{2+} and Cd^{2+} ions. The composite demonstrated enhanced electrocatalytic activity and stability, indicating its potential for practical applications in environmental sensing.

2.5 Detection and Removal of Heavy Metals: The detection and removal of heavy metals from aqueous solutions is an increasingly critical issue in environmental monitoring and water purification technologies. Conducting polymers such as PANI, when combined with rGO and metal oxides such as MnO_2, form ternary composites that offer enhanced electrochemical performance, ideal for these applications. PANI-based composites**,** particularly those incorporating rGO, have shown remarkable electrochemical behavior for heavy metal detection. For example, **Alsulami et al., 2021** investigated the electrochemical properties of ternary composites using CV and EIS. Their findings highlighted superior capacitance values and enhanced electrochemical responses, proving these composites to be effective in both sensing and energy storage applications. Similarly, **Vasanthi et al., 2022**focused on the detection and removal of Pb^{2+} ions using DPV, where the incorporation of PANI-based composites significantly improved the electrochemical sensitivity and selectivity, positioning these materials

as strong candidates for electrochemical sensing platforms.Heavy metal contamination is a serious environmental and public health concern due to the toxicity, persistence, and bioaccumulative nature of metals like Pb^{2+}**,** Cd^{2+}, Hg^{2+}, and Cu^{2+}. These metals cause serious health risks, including carcinogenic, neurotoxic, and nephrotoxic effects. The demand for efficient detection and removal methods has led to the development of electrochemical sensors, which have proven to be cost-effective, sensitive, and rapid in responding to heavy metal contamination.Among conducting polymers, PANI has shown exceptional potential due to its excellent conductivity, environmental stability, and ability to coordinate with metal ions via its amine and imine functional groups. For example, **Somerset et al., 2014** developed a carbon paste electrode modified with a PANI copolymer, demonstrating efficient electrocatalytic activity for the voltammetric determination of metal ions. **Huang et al., 2016** synthesized a novel phytic acid-doped PANI nanofiber composite for simultaneous detection of Cd^{2+} and Pb^{2+}, achieving ultra-low detection limits (0.02 μg/L for Cd^{2+} and 0.05 μg/L for Pb^{2+}) via DPASV. These studies emphasized PANI's enhanced conductivity and surface area, crucial for improving sensitivity in heavy metal detection. Moreover ternary composites that combine PANI with rGO have further amplified electrochemical performance. **Akhtar et al., 2020**synthesized a PANI-Alanine-rGO nanocomposite, achieving exceptionally low detection limits for Cd^{2+}, Pb^{2+}, and Cu^{2+} ions (0.03 nM, 0.045 nM, and 0.063 nM, respectively), utilizing SWASV. The combination of PANI's conductive and binding properties, rGO's high surface area, and alanine's functional groups facilitated improved adsorption, electron transfer kinetics, and overall sensitivity and selectivity for metal ion detection.In addition to heavy metal detection, the removal capabilities of these composites have been demonstrated through hybrid materials. **Mahadik et al., 2020** showcased an EDTA-modified PANI/GO nanocomposite for selective detection and removal of Hg^{2+} ions, with an impressive detection limit of 2 ppb. The inclusion of EDTA provided metal-chelating sites, while PANI and GO contributed to an interconnected conductive matrix that enhanced adsorption and electron transfer. Furthermore, **Muralikrishna et al., 2017** explored the use of PANI-GO hydrogels for the sensitive electrochemical determination and removal of Pb^{2+}, achieving a remarkably low detection limit of 0.04 nM, which underscores the potential of polymer-based hydrogels in environmental remediation.The use of metal oxides like ZnO and MnO_2 further enhances the performance of these composites. **Akhtar et al., 2020** demonstrated that incorporating ZnO nanoparticles in ternary composites improved both detection and removal

efficiencies by enhancing electron mobility and surface interactions. ZnO provided additional adsorption sites and amplified electrochemical responses, making these multi-component composites highly effective in environmental applications.The integration of MnO_2 with rGO and PANI has also shown considerable promise in improving electrochemical performance for the detection of heavy metals. **Kumar et al., 2025** developed a PANI/rGO/MnO_2 ternary nanocomposite, which exhibited excellent sensitivity and selectivity for the electrochemical detection of Pb^{2+} and Hg^{2+}, with detection limits of 6.08 μM for lead and 7.04 μM for mercury, making it a potential candidate for environmental monitoring. **Singh et al., 2024** further explored the photocatalytic properties of a PANI@MnO_2@rGO ternary composite, demonstrating enhanced photocatalytic activity for the degradation of organic contaminants under visible light, which is relevant for removal of heavy metals. **Nisha et al. (2025)** explored a ternary composite PANI, rGO, and ZnO for sensitive detection of Pb^{2+} in aqueous environments. The authors synthesized the ternary nanocomposite (PrGZ-2) and characterized it using FTIR, XRD, SEM, EIS, and DPASV techniques. Their results showed significantly enhanced electron transfer and improved sensitivity compared to individual and binary composites. Importantly, PrGZ-2 demonstrated good selectivity and maintained high sensitivity in the presence of interfering metal ions such as Cd^{2+} and Cu^{2+}, indicating robustness against common co-existing ions in environmental samples. The sensor's relative standard deviation was low (~2.13 %), confirming reproducibility and stability in interference conditions. **Mnyipika et al. (2021)** reported the fabrication of a MnO_2@rGO nanocomposite by simultaneous electrodeposition of MnO_2 nanoparticles with rGO on a glassy carbon electrode. Although this work did not include PANI, it is relevant as a basis for studying MnO_2-graphene composite behavior. The composite achieved high sensitivity for simultaneous detection of Zn^{2+}, Cd^{2+} and Cu^{2+} ions and exhibited excellent repeatability and stability. The low detection limits (~0.002–0.015 μg L^{-1}) and the capability to measure multiple ions simultaneously highlight the potential of MnO_2/rGO composite platforms against interference from co-existing ions in complex matrices**. Ruecha et al. (2015)** demonstrated an electrochemical sensor based on a graphene–PANI nanocomposite for simultaneous determination of Zn^{2+}, Cd^{2+}, and Pb^{2+}. This earlier study showed that incorporating PANI with graphene vastly improved sensitivity and selectivity in the presence of multiple heavy metals, suggesting the importance of polymer–carbon synergies when dealing with interference from co-existing ions in real water matrices. **Gunasekaran et al. (2025)**

developed rGO-based composites that exhibited strong anti-interference behavior against common ions such as Cr^{3+}, Ba^{2+}, Ca^{2+}, K^{+}, and Mg^{2+} while maintaining high sensitivity for Cd^{2+} and Pb^{2+} sensing. Although not a ternary PANI composite, this work provides important insight into how graphene-rich surfaces in composites can enhance selectivity and suppress interference signals from non-target ionic species. **Nisha et al. (2025)** demonstrated that the PANI/rGO/ZnO ternary nanocomposite (PrGZ-2) could be synthesized using simple solution-based and in-situ polymerization techniques, which are inherently scalable and cost-efficient. The authors reported that incorporation of ZnO, an inexpensive and industrially abundant metal oxide, significantly improved electrochemical performance without introducing costly processing steps. The study implicitly supports the practical scalability of PANI/rGO/ZnO sensors, as enhanced sensitivity was achieved using low material loadings and conventional laboratory procedures adaptable to bulk production. **Ruecha et al. (2015)** showed that graphene–PANI composites can be easily deposited on screen-printed carbon electrodes (SPCEs), which are widely recognized for mass production, low fabrication cost, and portability. Although their work focused on binary systems, the authors highlighted that such electrode platforms are compatible with additional nanomaterial incorporation, supporting the scalability of ternary systems such as PANI/rGO/ZnO and PANI/rGO/MnO_2 for commercial sensing devices. **Mnyipika et al. (2021)** reported that MnO_2@rGO nanocomposites, fabricated via simultaneous electrodeposition, offer a scalable route suitable for automated and roll-to-roll manufacturing processes. The authors emphasized that MnO_2 is economically viable and environmentally benign, widely used in battery and catalytic industries. Their findings suggest that MnO_2-based rGO composites can be produced at scale without significant cost escalation, making them attractive for multi-ion sensing in environmental monitoring. **Hajjaoui et al. (2018)** reviewed polyaniline-based composites for environmental remediation and sensing, concluding that PANI's environmental stability, reversible redox behavior, and ease of regeneration are key factors supporting repeated on-site use. The authors noted that PANI-containing composites maintain sensing performance over multiple cycles, an essential requirement for field monitoring of toxic metal ions.

Wang et al. (2010) discussed that one of the primary challenges in heavy metal detection is achieving simultaneous high sensitivity and selectivity in complex environmental matrices. The authors emphasized that naturally occurring co-existing ions and organic matter can interfere

with analytical signals, leading to peak overlap, signal suppression, or false positives, particularly in electrochemical stripping techniques. **Lu et al. (2014)** reported that intermetallic compound formation and competitive adsorption during electrochemical deposition stages pose serious challenges for accurate quantification of multiple heavy metals. The authors showed that ions such as Cu^{2+} and Zn^{2+} can significantly suppress the stripping signals of Cd^{2+} and Pb^{2+}, thereby compromising analytical reliability in mixed-metal systems. **Economou (2010)** pointed out that electrode fouling and surface passivation remain major obstacles in electrochemical heavy metal sensors. Continuous exposure to real samples containing organic contaminants, suspended solids, and biofilms can degrade electrode performance, leading to reduced sensitivity and poor long-term stability during repeated measurements. **Honeychurch et al. (2013)** emphasized that achieving low detection limits at environmentally relevant concentrations is challenging due to background noise and matrix effects in real water samples. The authors noted that preconcentration steps, although effective, increase analysis time and complicate sensor operation, reducing suitability for rapid field detection. **Dreyer et al. (2010)** discussed material-related challenges associated with graphene and graphene-derived sensors, including variability in material quality, incomplete reduction of graphene oxide, and batch-to-batch inconsistency. Such issues can result in poor reproducibility and limit large-scale deployment of graphene-based heavy metal sensors. **Hajjaoui et al. (2018)** highlighted that although polyaniline-based composites exhibit excellent sensitivity and redox activity, they suffer from pH sensitivity, limited long-term stability, and possible degradation under harsh environmental conditions. These factors restrict sustained field operation and necessitate frequent calibration or regeneration. **Ronkainen et al. (2010)** identified challenges related to sensor calibration, drift, and standardization, especially in portable electrochemical systems. The authors emphasized that variations in temperature, ionic strength, and pH in environmental samples can cause signal drift, complicating accurate quantification over extended monitoring periods.

3.1 Materials: Aniline, graphite, hydrogen peroxide, hydrochloric acid, hydrazine hydrate, ethanol, and zinc oxide (ZnO) were procured from LOBA Chemie Pvt. Ltd. Sodium dodecyl sulfate (SDS) was supplied by Qualikems Fine Chem, while ferric chloride ($FeCl_3$) was obtained from Alpha Chemika. Sulphuric acid (H_2SO_4) was sourced from Avantor Performance Materials India Ltd., potassium permanganate ($KMnO_4$) from HiMedia Laboratories Pvt. Ltd., and sodium nitrate ($NaNO_3$) from Avarice Industries. All reagents employed in this study were of analytical grade and utilized as received, without any further purification. ZnO and MnO_2nanoparticles, acquired from LOBA Chemie Pvt. Ltd., were also used directly without additional treatment.

3.2 Preparation of Polyaniline: PANI was synthesized via the chemical oxidative polymerization method, a widely adopted technique for preparing high-purity conducting polymers with excellent electrochemical properties. In this process, 1.145 g of sodium dodecyl sulfate (SDS), an anionic surfactant, was first dissolved in 30 mL of deionized water and stirred continuously for 15 minutes at room temperature to ensure homogeneity. SDS plays a critical role in controlling the morphology of the resulting PANI by acting as a soft template. Subsequently, 0.9 g of $FeCl_3$, employed as the oxidizing agent, was introduced into the solution and stirred to ensure complete dissolution and activation. Following this step, 2.34 mL of freshly distilled aniline monomer was added dropwise into the reaction mixture under vigorous stirring to initiate the oxidative polymerization. The gradual development of a green coloration confirmed the formation of the emeraldine salt form of PANI, marking the progression of the polymerization reaction. The reaction was allowed to proceed for 24 hours at ambient temperature to ensure complete polymer formation.Upon completion of the reaction, the resultant dark green product was filtered and washed several times with deionized water until the filtrate became colorless, effectively removing any unreacted monomers, oxidants, and by-products. The purified PANI was then dried in a vacuum oven at 40 ± 1 °C until a constant weight was obtained, indicating the elimination of residual moisture. This method of synthesis ensures the formation of a high-quality conducting polymer suitable for various applications. The effectiveness of such surfactant-assisted chemical polymerization approaches in enhancing the structural and electrochemical characteristics of PANI has been demonstrated in previous studies **(Muralikrishna et al., 2017).**

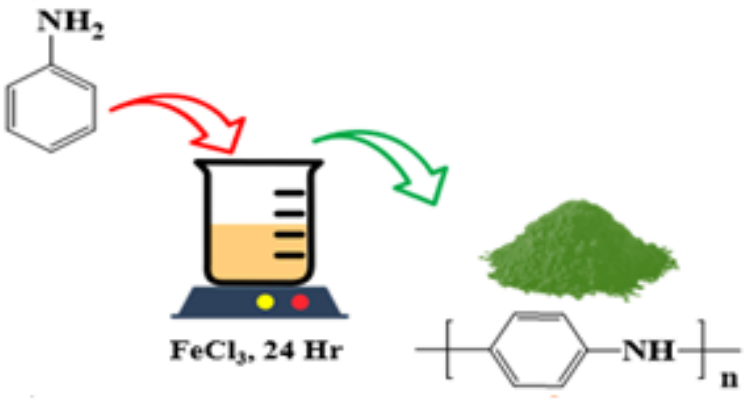

Figure: 2 Preparation of Polyaniline

3.3 Preparation of Graphite Oxide and reduced Graphene Oxide: GO was synthesized using a modified Hummers method, which involves the chemical oxidation of graphite to introduce oxygenated functional groups onto the graphene sheets. In this method, 1 g of graphite powder was mixed 3 g of $KMnO_4$ in 23 mL of concentrated H_2SO_4 under continuous stirring, ensuring the reaction temperature was maintained below 20 °C to prevent overheating. After the oxidation reaction was complete, it was quenched by the careful addition of 10% H_2O_2, which caused the suspension to turn black, indicating the formation of GO. The reaction mixture was then washed five times with HCl and warm deionized water to remove residual metal ions and any remaining acidic impurities. The resulting product, GO, was filtered and dried in a vacuum oven at 60 °C for 4 hours to obtain the dry, oxidized graphene material **(Shruthi et al.,2018).**

For the synthesis of rGO, 2 g of the prepared GO was dispersed in 250 mL of distilled water, and the suspension was vigorously stirred to ensure uniform dispersion. Next, 2 mL of $NH_2NH_2 \bullet H_2O$ was added dropwise to the mixture. The reduction process was carried out at 80 °C for 72 hours under continuous stirring to facilitate the chemical reduction of GO to rGO. Once the reduction was complete, the mixture was centrifuged, and the resulting solid precipitate was separated and washed thoroughly with ethanol and deionized water to remove any unreacted chemicals. The final rGO product was dried at 60 °C for 24 hours to obtain black, flocculent reduced graphene oxide. The prepared rGO exhibited excellent electrochemical properties, making it an ideal candidate for use in various composite materials **(Mudila et al., 2014)**

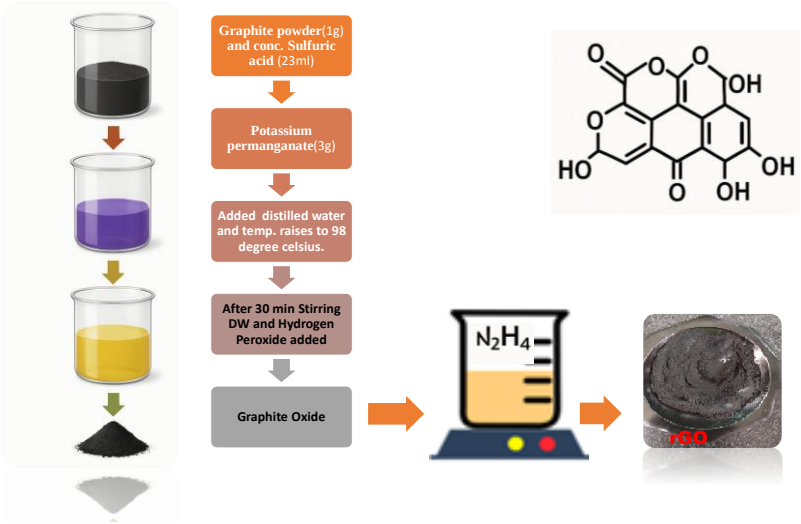

Figure: 3 Preparation of GO and rGO

3.4 Fabrication of Binary PANI/rGO (PrG) Composites: Binary composites of PANI and rGO, referred to as PrG, were synthesized by dispersing 100 mg of PANI in 5 mL of ethanol under continuous stirring. Subsequently, varying amounts of rGO (as detailed in Table 1) were added to the PANI dispersion. The resulting mixtures were sonicated for 30 minutes to ensure homogeneous blending of the two components, facilitating uniform distribution of rGO within the PANI matrix and promoting effective interaction between them. A series of PrG composites with different weight ratios of PANI to rGO were prepared, labeled PrG-1, PrG-2, PrG-3, and PrG-4. The specific compositions used are presented in Table 2. Among these, the composition PrG-2 (2:1 ratio of PANI to rGO) was identified as the optimum formulation based on its superior electrochemical performance, as discussed in the subsequent sections, and was selected for the development of ternary composite systems.

Table 3: Composition Ratios of PANI and rGO in the Fabrication of PrG Composites

Materials	Ratios			
	4:1 (PrG-1)	2:1 (PrG-2)	1:1 (PrG-3)	1:2 (PrG-4)
PANI(mg)	100	100	100	100
rGO(mg)	25	50	100	200

3.5 Fabrication of Ternary PANI/rGO/ZnO (PrGZ) Composites: Ternary composites of PANI, rGO, and ZnO, referred to as PrGZ, were prepared by incorporating varying amounts of ZnO into the optimized binary composite, PrG-2. Specifically, predetermined quantities of ZnO (as listed in Table 2) were dispersed in 5 mL of ethanol and sonicated for 30 minutes at room temperature to ensure uniform dispersion. Subsequently, 100 mg of PrG-2 was added to each dispersion, followed by additional sonication for thorough mixing and effective composite formation. A series of PrGZ composites with different weight ratios of PrG-2 to ZnO were prepared, designated as PrGZ-1, PrGZ-2, PrGZ-3, and PrGZ-4. The detailed compositions are presented in Table 4. Among these, PrGZ-2 was identified as the most efficient composition based on its superior electrochemical response and was subsequently selected for DPASV analysis. To minimize batch-to-batch variation, all PrGZ composites were synthesized under identical experimental conditions, including fixed solvent volume, sonication time, temperature, and stirring protocol. The same stock of PrG-2 and ZnO precursors was used throughout the synthesis to avoid compositional inconsistencies. Additionally, each composite batch was prepared in triplicate, and the resulting powders were thoroughly ground and mixed prior to characterization to ensure compositional uniformity.

Table 4: Composition Ratios of PrG-2 and ZnO in the Fabrication of PrGZ Composites

Material	Ratio			
	4:1 (PrGZ-1)	**2:1 (PrGZ-2)**	**1:1 (PrGZ-3)**	**1:2 (PrGZ-4)**
PrG-2(mg)	**100**	**100**	**100**	**100**
ZnO (mg)	**25**	**50**	**100**	**200**

3.6 Fabrication of Ternary PANI/rGO/MnO_2 (PrGM) Composites: Ternary composites of PANI, rGO, and MnO_2, referred to as PrGM, were prepared by incorporating varying amounts of MnO_2 into the optimized binary composite, PrG-2. Specifically, predetermined quantities of MnO_2 (as listed in Table 5) were dispersed in 5 mL of ethanol and sonicated for 30 minutes at room temperature to ensure uniform dispersion. Subsequently, 100

mg of PrG-2 was added to each dispersion, followed by additional sonication for thorough mixing and effective composite formation. A series of PrGM composites with different weight ratios of PrG-2 to MnO_2 were prepared, designated as PrGM-1, PrGM-2, PrGM-3, and PrGM-4. The detailed compositions are presented in Table 5. Among these, PrGM-2 was identified as the most efficient composition based on its superior electrochemical response and was subsequently selected for DPASV analysis. To minimize batch-to-batch variation, all PrGM composites were synthesized under identical experimental conditions, including fixed solvent volume, sonication time, temperature, and stirring protocol. The same stock of PrG-2 and MnO_2 precursors was used throughout the synthesis to avoid compositional inconsistencies. Additionally, each composite batch was prepared in triplicate, and the resulting powders were thoroughly ground and mixed prior to characterization to ensure compositional uniformity.

Table 5: Composition Ratios of PrG-2 and MnO_2 in the Fabrication of PrGM Composites

Material	**Ratio**			
	4:1 (PrGM-1)	**2:1 (PrGM-2)**	**1:1 (PrGM-3)**	**1:2 (PrGM-4)**
PrG-2(mg)	**100**	**100**	**100**	**100**
MnO_2 (mg)	**25**	**50**	**100**	**200**

3.7 Electrode Preparation: CPE was fabricated to serve as the working electrode for electrochemical measurements. The electrode paste was prepared by thoroughly blending 4 g of graphite powder with 1.8 mL of paraffin oil in a mortar using a pestle until a uniform, homogenous paste was obtained. The prepared paste was then air-dried to eliminate any residual moisture. Subsequently, the paste was packed into the barrel of an insulin syringe, shaping it into the desired electrode form. The surface of the CPE was gently polished on smooth paper to produce a clean, shiny, and uniform surface suitable for electrochemical applications. A 2 mm diameter copper wire was inserted at the back end of the electrode to establish an effective electrical contact, completing the construction of the CPE assembly **(Adraoui, I. et al., 2005).**

3.8 Characterization of PANI, rGO, and prepared composites:

3.8.1 Fourier Transform Infrared Spectroscopy

FTIR spectroscopy was employed to identify the functional groups present in PANI, GO, rGO, and their composite materials. FTIR analysis provides crucial information regarding chemical bonding, molecular structure, and interfacial interactions among the composite constituents. The FTIR spectra of PANI exhibited characteristic absorption bands corresponding to the quinoid and benzenoid ring vibrations (C=C stretching), C–N stretching of secondary aromatic amines, and N–H bending vibrations, confirming the successful polymerization of aniline. In the case of GO, prominent bands associated with O–H stretching, C=O stretching of carboxyl groups, C–O–C epoxy stretching, and C–O alkoxy vibrations were observed, indicating the presence of abundant oxygen-containing functional groups. Upon formation of the PANI/GO and PANI/rGO composites, noticeable shifts in peak positions and changes in band intensities were observed. These spectral variations indicate strong interactions between PANI chains and GO/rGO sheets, arising from hydrogen bonding, electrostatic interactions, and π–π stacking between the conjugated PANI backbone and the graphene framework. The reduction in intensity of oxygen-related bands in rGO-based composites further confirms the partial removal of oxygen functionalities during reduction. Overall, FTIR analysis confirms the successful synthesis of PANI, GO, and their composites and provides evidence of strong interfacial interactions within the composite matrix.

3.8.2 X-ray Diffraction

XRD analysis was conducted to investigate the crystalline structure, phase composition, and structural modifications occurring during composite formation. XRD patterns provide insight into the degree of crystallinity and interlayer spacing of the materials. The XRD pattern of GO displayed a characteristic diffraction peak corresponding to its layered structure, confirming the successful oxidation and exfoliation of graphite. In contrast, PANI exhibited broad diffraction peaks, indicating its semi-crystalline nature. For the composite materials, significant changes in diffraction patterns were observed. The characteristic GO peak either shifted or diminished in intensity, while PANI-related peaks became broader, suggesting the intercalation or uniform coating of PANI onto GO or rGO sheets. In rGO-based composites, the absence or further

shifting of the GO peak indicates the reduction of GO and the disruption of its regular layered structure. These observations confirm the successful incorporation of PANI into the rGO matrix and highlight structural rearrangements arising from strong interactions between the components.

3.8.3 Thermogravimetric Analysis

TGA was employed to evaluate the thermal stability and decomposition behavior of PANI, GO/rGO, and their composite materials under controlled heating conditions. TGA provides quantitative information regarding moisture content, thermal degradation steps, and the overall thermal endurance of the materials. The TGA curve of GO showed multiple weight loss stages, primarily attributed to the removal of adsorbed moisture at lower temperatures, followed by the decomposition of labile oxygen-containing functional groups at higher temperatures. PANI exhibited characteristic weight loss corresponding to the evaporation of residual solvents, dopants, and the degradation of polymer chains at elevated temperatures. In the case of PANI/GO and PANI/rGO composites, enhanced thermal stability was observed compared to the individual components. The composites exhibited delayed decomposition temperatures and reduced overall weight loss, indicating strong interfacial interactions between PANI and the graphene-based materials. The improved thermal stability can be attributed to the barrier effect of GO/rGO sheets and the restriction of polymer chain mobility, confirming the formation of a stable composite structure.

3.8.4 Scanning Electron Microscopy

SEM was used to investigate the surface morphology, microstructure, and dispersion of individual components and their composites. SEM analysis provides direct visual evidence of material morphology and structural homogeneity. SEM images of pure PANI revealed a rough, granular, and fibrous morphology, which is typical of chemically polymerized polyaniline. GO exhibited a wrinkled, sheet-like structure with layered and folded surfaces, indicative of exfoliated graphene oxide sheets. In contrast, SEM images of the PANI/GO and PANI/rGO composites demonstrated a uniform and homogeneous distribution of PANI over the graphene sheets. The PANI coating effectively prevented the restacking of GO/rGO layers, leading to an interconnected porous network. This morphology is particularly advantageous for electrochemical applications, as it provides a large active surface area and facilitates efficient

charge transport, thereby confirming the successful fabrication and strong interaction between the composite components.

3.8.5 X-ray Photoelectron Spectroscopy

XPS is a powerful surface-sensitive analytical technique used to investigate the elemental composition, chemical states, and electronic environments of materials within the top few nanometers of the surface. In the present work, XPS was employed to gain detailed insights into the surface chemistry and interfacial interactions of PANI, GO, rGO, and the synthesized ternary nanocomposites PANI/rGO/ZnO and PANI/rGO/MnO_2, which are critically important for their electrochemical sensing performance. XPS analysis enables the identification of core-level binding energies corresponding to elements such as carbon (C 1s), nitrogen (N 1s), oxygen (O 1s), zinc (Zn 2p), and manganese (Mn 2p), thereby confirming the successful incorporation of individual components into the composite framework. Moreover, the technique provides valuable information regarding the oxidation states of metal ions and the bonding configurations of carbon, nitrogen, and oxygen species, which are directly related to charge transfer behavior and surface reactivity. In this study, XPS was particularly useful in elucidating the chemical states of nitrogen in PANI (–NH–, =N–, and protonated species), the degree of reduction of GO to rGO through changes in oxygen functionalities, and the oxidation states of Zn and Mn in the ternary composites. Shifts in binding energies and variations in peak intensities observed in the composite materials further indicate strong electronic interactions and charge redistribution at the interfaces between PANI, rGO, and metal oxides. These interfacial interactions play a crucial role in enhancing electron transport, electrocatalytic activity, and selective adsorption of heavy metal ions. Overall, XPS serves as a vital characterization tool in this work by providing direct evidence of successful composite formation, surface chemical modification, and synergistic interactions among the constituents, thereby supporting the improved electrochemical performance of the synthesized materials for heavy metal ion detection.

3.8.6 Electrochemical Techniques

Electrochemical characterization techniques, including cyclic voltammetry (CV), differential pulse anodic stripping voltammetry (DPASV), and electrochemical impedance spectroscopy

(EIS), were employed to assess the electrochemical behavior, charge transfer characteristics, and sensing performance of the synthesized materials. CVrevealed the redox behavior of PANI and its composites, with enhanced current responses observed for the composite-modified electrodes due to increased electroactive surface area and improved electrical conductivity. DPASV measurements demonstrated the high sensitivity and selectivity of the PANI/rGO and ternary composites PANI/rGO/ZnO and PANI/rGO/MnO_2 toward heavy metal ions such as Pb^{2+}, Cd^{2+}, and Cu^{2+}. Electrochemical impedance spectroscopy further confirmed the improved charge transfer kinetics of the composite materials, as evidenced by reduced charge transfer resistance values compared to the individual components. The synergistic combination of PANI, rGO, and metal oxides significantly enhances electron transport and electrochemical response, making these composites highly effective for heavy metal sensing applications.

3.8.7 UV–Visible Spectroscopy

UV–Visible spectroscopy was employed to investigate the optical properties and electronic transitions of PANI and its composite materials. The UV–Vis spectra provide information regarding the electronic structure, conjugation length, and interaction between composite constituents. Pure PANI exhibited characteristic absorption bands corresponding to π–π* transitions of the benzenoid rings and polaron–π* transitions associated with its doped conductive state. GO displayed absorption features related to π–π* transitions of aromatic C=C bonds and n–π* transitions arising from oxygen-containing functional groups. Upon composite formation, shifts in absorption peak positions and changes in intensity were observed, indicating strong electronic interactions between PANI and GO/rGO. These spectral changes confirm successful polymerization, enhanced conjugation, and effective charge delocalization within the composite structure, which contribute to the improved electrochemical and sensing performance of the materials.

PANI was successfully synthesized via chemical oxidative polymerization, while GO and rGO were prepared by the modified Hummers method and chemical reduction, respectively, employing ex-situ approaches.The structural, thermal, and morphological characteristics of all powdered samples were systematically analyzed using the following techniques: FTIR: Conducted using a Perkin Elmer Spectrum IR Version 10.6.1 to identify functional groups and confirm chemical structures. XRD: Performed with a Bruker D8 Advance X-ray diffractometer using Cu-Kα radiation (λ = 1.5406 Å) to determine the crystalline structure and phase composition.Thermal Analysis: Carried out using TGA and SEM: Employed to examine surface morphology and particle distribution, using a JEOL JSM-7610F Plus SEM.

4.1 FTIR of PANI, rGO, PrG, ZnO and Ternary Composite (PrGZ &PrGM):

FTIR analysis was performed over the spectral range of 4000–400 cm^{-1} for all synthesized materials to investigate their functional group characteristics **(Fig. 4).** In the case of PANI, characteristic absorption peaks were observed at 3407 cm^{-1}, 1548 cm^{-1}, 1452 cm^{-1}, 1215 cm^{-1}, 1029 cm^{-1}, and 770 cm^{-1}, which correspond to N-H stretching vibrations of secondary amines, C=C stretching of quinoid rings, C=C stretching of benzenoid rings, C-N stretching of secondary aromatic amines, aromatic C-H in-plane bending vibrations, and aromatic C-H out-of-plane bending vibrations, respectively **(Mudila et al., 2014).**For graphene oxide (GO), FTIR analysis revealed prominent bands at 3400 cm^{-1}, 1725 cm^{-1}, 1614 cm^{-1}, and 1037 cm^{-1}, which are attributed to O-H stretching, C=O stretching, C=C stretching, and C-O stretching vibrations, respectively**(Shruthi et al., 2018).** rGO exhibited characteristic peaks at 3434 cm^{-1} and 1562 cm^{-1}, which are associated with O-H stretching and skeletal vibrations of the graphene backbone, in line with the findings of Shruthi et al. (2018). The binary composite (PrG-2), composed of PANI and GO, displayed distinctive bands at 1708 cm^{-1}, 1453 cm^{-1}, 1292 cm^{-1}, and 1096 cm^{-1}, representing C=O stretching, C=C stretching of benzenoid rings, C-N bending, and C-H stretching of quinoid rings, respectively consistent with the study **(Yelil Arasi et al.,2009).** ZnO showed a significant peak at 484 cm^{-1}, which is attributed to Zn–O bond vibrations, confirming its presence in the material. The ternary composite (PrGZ-2), which combines PANI, GO, and ZnO, exhibited peaks at 1493 cm^{-1}, 1117 cm^{-1}, and 500 cm^{-1}, corresponding to C=C stretching of the benzenoid ring, N=Q=N stretching of quinoid structures, and Zn–O vibrations, respectively.

These findings support the successful fabrication of the PrGZ composite **(Adraoui et al., 2005).** This comprehensive FTIR analysis confirms the functionalization of the synthesized materials, highlighting their structural and chemical properties essential for their application in electrochemical detection.

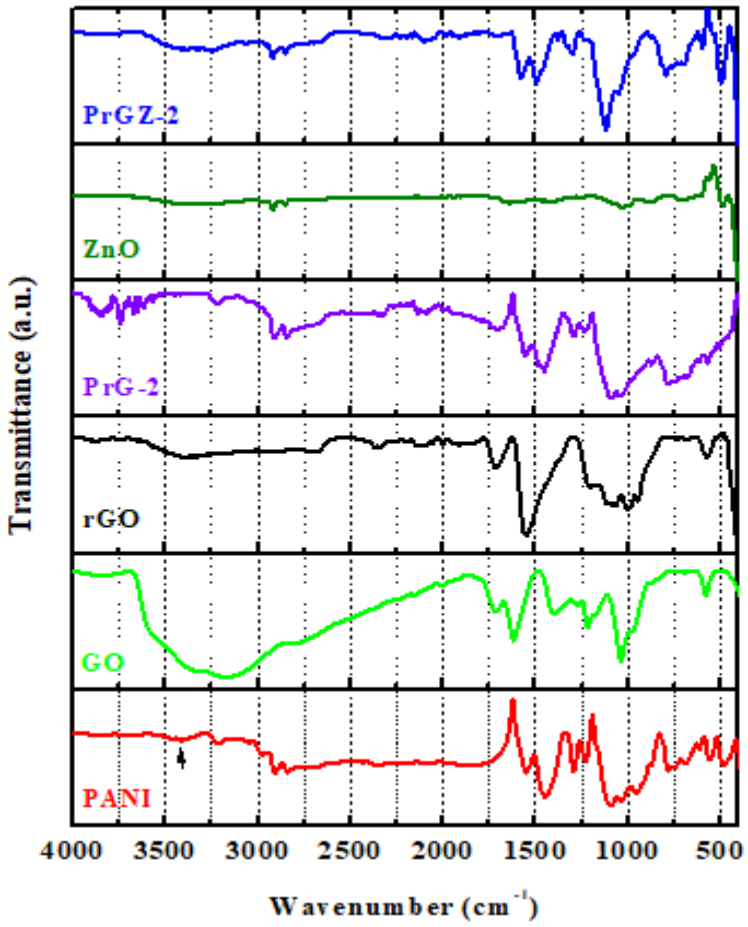

Figure 4: FTIR of PANI, GO, rGO, PrG, ZnO and PrGZ

The FTIR spectrum of manganese dioxide nanomaterial exhibited several prominent absorption bands, particularly in the lower wavenumber region, which are typical of MnO_2 structures. Strong absorption peaks were observed in the range of 400–700 cm^{-1}, specifically at 574.50 cm^{-1}, 515.76 cm^{-1}, 510.43 cm^{-1}, 468.28 cm^{-1}, 460.10 cm^{-1}, 446.73 cm^{-1}, 439.29 cm^{-1}, 419.26 cm^{-1}, and 407.13 cm^{-1}. These bands are attributed to the Mn–O stretching vibrations within the MnO_6 octahedral units of the MnO_2 lattice. The presence of these characteristic bands confirms the successful formation of manganese dioxide, consistent with observations reported by **(Li et**

al., 2015 and Wu et al., 2016). A weak absorption peak was noted at 1035.46 cm^{-1}, which can be associated with surface-bound O–H bending vibrations or possible minor surface impurities. Additionally, peaks appearing at 1505.78 cm^{-1} and 1516.01 cm^{-1} are likely due to H–O–H bending vibrations from physically adsorbed water molecules or residual organic moieties from the synthesis process. A small peak at 1696.06 cm^{-1} further supports the presence of adsorbed water on the MnO_2 surface. In the region of 2000–2400 cm^{-1}, a group of broad and weak bands was observed at 1992.80, 1980.38, 2016.56, 2051.86, 2109.61, 2170.88, 2236.25, 2351.14, and 2391.81 cm^{-1}. These bands are typically attributed to atmospheric CO_2 absorption and possible overtones or combination bands inherent to the sample environment. Furthermore, broad and scattered absorption bands appeared in the 3600–3900 cm^{-1} region, with notable peaks at 3745.98, 3671.87, 3850.94, 3866.02, 3900.24 cm^{-1}, among others. These are assigned to the O–H stretching vibrations of surface hydroxyl groups and adsorbed water molecules, commonly present in manganese dioxide powders due to their high surface area and hygroscopic nature. The relatively weak and dispersed nature of these O–H bands indicates a moderate level of surface hydration, suggesting that the MnO_2 obtained is relatively stable and not excessively hydrated. The successful formation of the PANI/rGO/MnO_2 ternary nanocomposite was confirmed through FTIR spectroscopy, where characteristic peaks corresponding to each component were clearly identified. The presence of PANI was evidenced by distinct absorption bands at approximately 1564 cm^{-1} and 1445 cm^{-1}, which correspond to the C=C stretching vibrations of quinoid and benzenoid rings, respectively. Additionally, the C–N stretching vibration of the benzenoid units was observed at 1273 cm^{-1}, while the aliphatic C–H stretching vibrations appeared at 2920 cm^{-1} and 2854 cm^{-1}, further confirming the incorporation of PANI in the composite matrix. The contribution of reduced graphene oxide was indicated by the C=O stretching vibration at 1718 cm^{-1} and C–O stretching vibrations at 1110 cm^{-1} and 1060 cm^{-1}. These peaks, though relatively weak, suggest a successful reduction of GO to rGO, with some residual oxygen-containing functional groups remaining on the surface. The presence of MnO_2 was confirmed by the appearance of strong absorption bands in the region of 739–497 cm^{-1}, attributed to Mn–O lattice vibrations characteristic of MnO_2 structures, in agreement with findings by **(Li et al., 2015 and Wu et al., 2016).** Furthermore, while O–H stretching or water bending vibrations are typically expected around 3400 cm^{-1}, the weak or merged appearance of

this band in the spectrum indicates minimal surface-adsorbed water, suggesting the formation of a relatively stable and well-integrated nanocomposite structure **(Fig.5)**

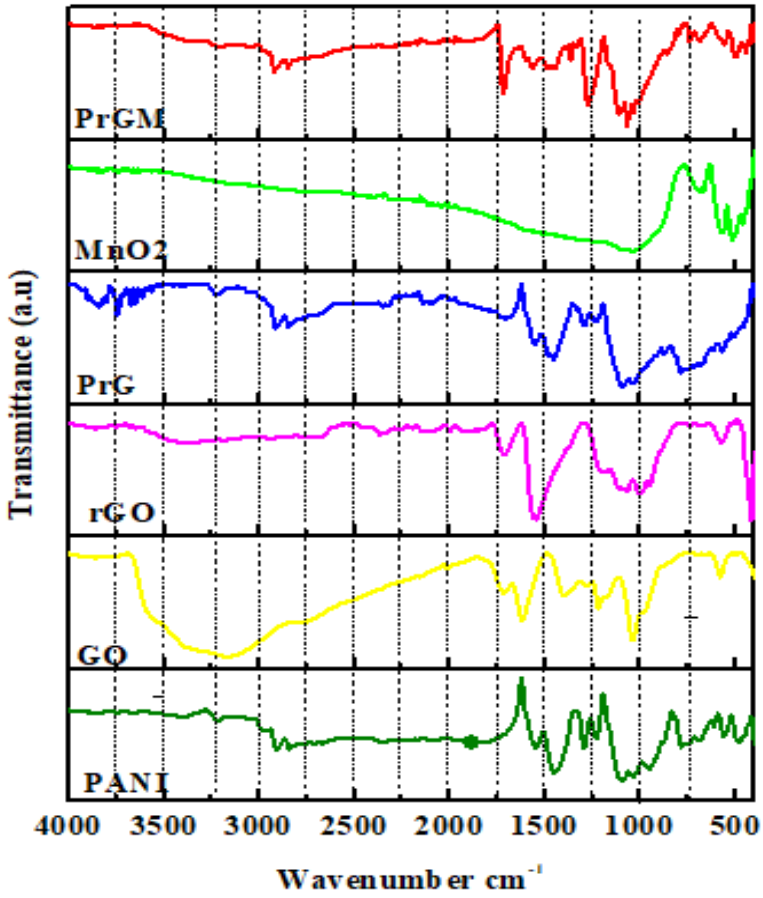

Figure: 5 FTIR of PANI, GO, rGO, PrG, MnO_2 and PrGM

4.2 XRD of PANI, rGO, PrG, ZnO, and Ternary Composite (PrGZ&PrGM):

XRD analysis was employed to investigate the crystalline structure and phase identification of the synthesized materials. The XRD patterns were recorded within the 2θ range of 10° to 70° (Fig. 6). In PANI two broad diffraction peaks were observed at 2θ = 20° and 28°, which are characteristic of the parallel arrangement of the polymer chains, thus representing the diffraction pattern of PANI **(Jiao et al., 2017).** In the case of GO, a sharp peak appeared at approximately 2θ = 10°, confirming the successful oxidation of graphite into graphite oxide **(Zhang et al., 2017).** Upon reduction of GO to rGO, the sharp peak of GO disappeared, and a broad peak at around 2θ = 24.5° emerged, indicative of the partial restoration of the graphene structure and the

reduction of oxygen functionalities **(Seehra et al., 2017)**. For the binary composite (PrG), the diffraction peaks of GO were significantly diminished due to the interaction and encapsulation of rGO sheets within the PANI matrix. The composite exhibited peaks at 2θ = 22° and 24.5°, confirming the successful formation of the PANI/rGO composite. ZnO nanoparticles displayed distinct and sharp diffraction peaks at 2θ values of 31.6°, 34.3°, 36.2°, and 47.3°, corresponding to the (100), (002), (101), and (102) planes, respectively, characteristic of the hexagonal wurtzite structure of ZnO, **(Seehra et al., 2017)** . In the ternary nanocomposite (PrGZ), the typical diffraction peaks of GO and ZnO were notably suppressed, indicating effective dispersion of ZnO nanoparticles and rGO within the PANI matrix. The presence of ZnO was still evident through characteristic peaks at 31.6°, 34.3°, 36.2°, and 47.3°, although their intensities were reduced, confirming successful composite formation and the formation of a uniform nanocomposite structure.

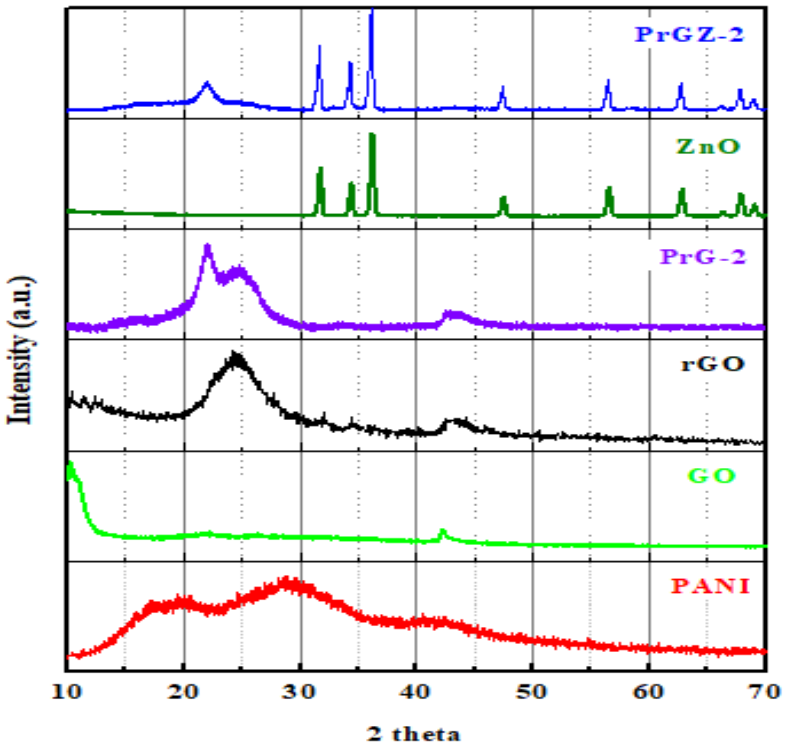

Figure: 6 XRD of PANI, GO, rGO, PrG and PrGZ

The XRD pattern revealed several well-defined diffraction peaks, confirming the crystalline nature of the material. The most intense peak appeared at 56.03°, indexed to the (102) plane, indicating the preferential growth orientation along this crystallographic plane. The XRD pattern

of the PANI/rGO/MnO_2 ternary nanocomposite exhibits a characteristic combination of broad, low-angle reflections from the polymer and graphene components and sharper peaks arising from crystalline MnO_2. In the small-angle region, a broad feature centered at approximately 10.1° 2θ (d ≈ 8.7 Å) can be assigned to the (001) stacking periodicity of PANI chains intercalated with rGO sheets, while a weaker, yet noticeable hump around 25.0° 2θ (d ≈ 3.56 Å) corresponds to the (002) plane of reduced graphene oxide, indicating partial restacking of graphene layers within the polymer matrix. Superimposed on this amorphous background are the signature reflections of hexagonal MnO_2 peaks at 37.12° (100), 42.40° (101), and 56.03° (102) confirm the presence of well-crystallized MnO_2 nanodomains, with the (102) reflection at 56.03° being the most intense and indicative of a slight preferential orientation. All MnO_2 peaks are significantly broadened compared to bulk standards, reflecting a nanoscale crystallite size **(Wu et al., 2016) and Palsaniya et al., 2019)**. Importantly, no additional reflections from impurity phases or secondary oxides are observed, demonstrating the phase purity of the composite and the successful integration of conductive polymer, graphene support, and catalytic MnO_2 in a homogeneous nanostructured material **(Fig. 7)**

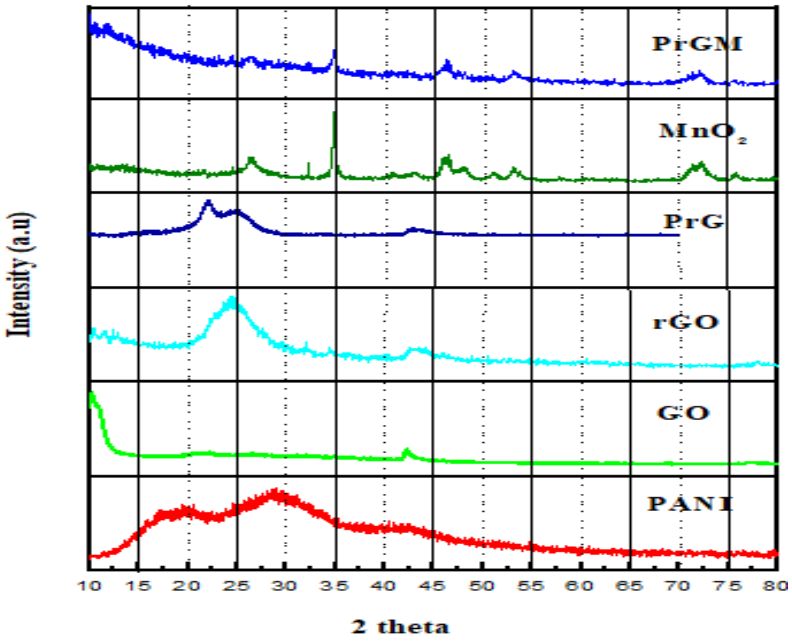

Figure: 7 XRD of PANI, GO, rGO, PrG, MnO_2, PrGM

4.3 TGA PANI, rGO, PrG, ZnO, and Ternary Composite (PrGZ &PrGM):

TGA was performed to evaluate the thermal stability and decomposition behavior of the synthesized materials by tracking their weight loss as a function of temperature. The TGA experiments were carried out under an inert nitrogen atmosphere, spanning a temperature range from room temperature to 600 °C, with a constant heating rate of 10 °C/min **(Fig. 8).** For PANI, the TGA profile revealed two major weight loss stages: the first, occurring at 100 °C, was attributed to the evaporation of physically adsorbed water molecules, while the second, at 268 °C, corresponded to the thermal degradation of the PANI polymer backbone **(Mutalib et al., 2020).** In the case of GO, three distinct stages of weight loss were observed. The initial weight loss at 117 °C was due to moisture desorption, followed by a second stage at 200 °C, corresponding to the decomposition of labile oxygen-containing functional groups, releasing gases such as CO and CO_2. The final significant degradation occurred above 500 °C, which was attributed to the structural decomposition of the GO sheets **(Alam et al., 2017).** In case of rGO an initial minor mass loss below ~120 °C is attributed to the removal of physically adsorbed moisture and trapped solvent molecules, arising from the high surface area and residual hydrophilicity of rGO. This is followed by a gradual weight loss in the temperature range of ~120–300 °C due to the thermal decomposition of residual oxygen-containing functional groups such as hydroxyl, epoxy, and carboxyl moieties, with the evolution of volatile species including H_2O, CO, and CO_2. Beyond 300 °C, a continuous and pronounced decrease in mass is observed, corresponding to the pyrolytic degradation of defect-rich and amorphous carbon domains within the rGO sheets. The presence of structural defects, edge sites, and incomplete restoration of the sp^2 carbon network renders rGO thermally unstable, leading to fragmentation and gasification of carbonaceous species. As the temperature approaches 600 °C, extensive pyrolytic volatilization of the carbon framework occurs, resulting in maximum weight loss and nearly zero residual mass. The absence of thermally stable inorganic constituents and the inability of rGO to form a stable carbonaceous char under inert conditions account for the negligible residue at 600 °C, confirming the highly defective yet reduced nature of the graphite oxide structure. The binary composite (PrG-2) exhibited thermal behavior intermediate between PANI and reduced graphene oxide (rGO), with its TGA curve closely resembling that of rGO. The composite showed three weight loss events: 16.21% between 30–160 °C, corresponding to moisture removal; 38.29% between 160–400 °C, likely due to the elimination of oxygenated functional groups of rGO; and

16.36% loss above 400 °C, linked to the degradation of the PANI component **(Palsaniya et al., 2021).** The ternary composite (PrGZ-2) exhibited significantly improved thermal stability, which can be attributed to enhanced surface area, better interfacial interactions, and the homogeneous dispersion of PANI over rGO and ZnO particles. The ternary composite displayed minimal weight loss of 1% at 109 °C due to moisture evaporation, followed by a 2% weight loss at 266 °C, associated with the release of volatile gases. A major degradation event occurred at 450 °C, corresponding to the breakdown of the rGO structure and the potential decomposition of ZnO-linked components seen **(Kumar et al., 2020).** The comparative char residue percentages at 600 °C, shown in the inset of **(Fig. 8)** further supported the stabilizing effects imparted by rGO and ZnO within the binary and ternary composite matrices, confirming the enhanced thermal stability of the PrGZ-2 composite.

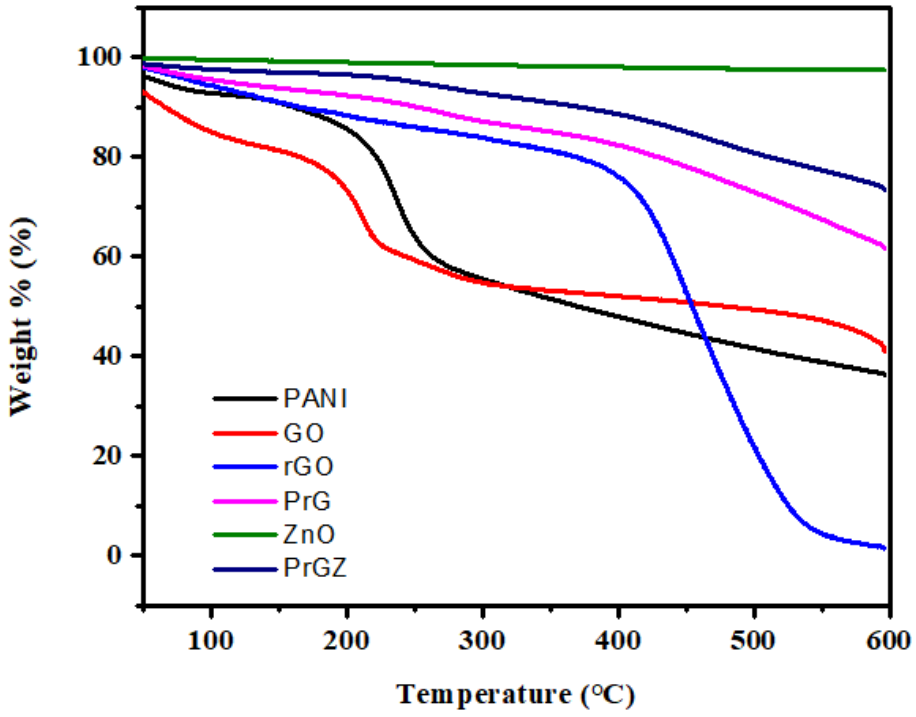

Figure: 8 TGA of PANI, GO, rGO, ZnO, PrG and PrGZ

The thermogravimetric analysis confirms that MnO_2 exhibits excellent thermal stability up to 350°C, with only minor moisture and lattice water loss. Significant decomposition occurs beyond 350°C, leading to the formation of lower manganese oxides and the release of oxygen. These findings align well with the known thermal behavior of manganese dioxide reported in the

literature. The thermal stability and decomposition behavior of the PANI/rGO/MnO_2 composite were investigated using TGA conducted in a nitrogen atmosphere from 30°C to 600°C at a heating rate of 10°C/min. The TGA curve revealed a multi-step weight loss pattern corresponding to the sequential degradation of the composite's constituents. The initial weight loss, observed between 30°C and 150°C, accounted for approximately 1–2% of the total mass and was attributed to the evaporation of physically adsorbed water, surface moisture, and any residual solvents trapped within the composite matrix. The second stage, extending from 150°C to 350°C, showed a more pronounced weight loss of about 7–15%, which can be ascribed to the partial thermal degradation of the PANI backbone along with the progressive reduction of MnO_2 to lower manganese oxides such as Mn_2O_3 and Mn_3O_4, accompanied by the evolution of oxygen. In the final decomposition stage, ranging from 350°C to 600°C, an additional 5–8% weight loss was recorded, mainly due to the complete degradation of PANI, the detachment of residual oxygen-containing functional groups from the reduced graphene oxide (rGO), and further phase transformation of Mn_3O_4 into MnO. By 600°C, the total cumulative weight loss was approximately 15–25%, indicating the good thermal stability of the composite, primarily conferred by the thermally resistant rGO and the manganese oxide phases. These results are consistent with observations reported by **(Palsaniya et al., 2019, Mnyipika et al., 2021, and Wu et al., 2016),** supporting the composite's suitability for applications requiring moderate thermal endurance, such as electrochemical sensing and catalytic processes **(Fig. 9)**

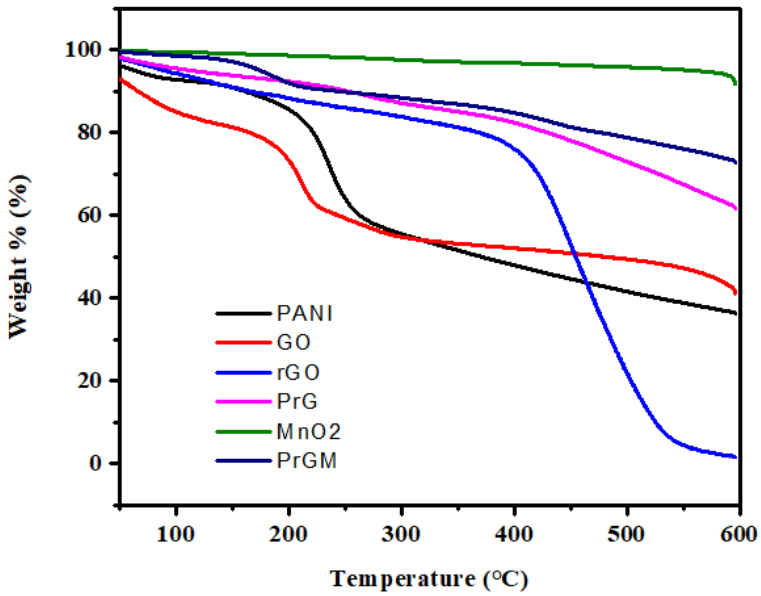

Figure: 9 TGA of PANI, GO, rGO, MnO_2, PrG and PrGM

4.4 SEM of PANI, rGO, PrG, ZnO, and Ternary Composite (PrGZ &PrGM):

SEM was employed to investigate the surface morphology and structural characteristics of the synthesized materials. The SEM images of PANI, rGO, the binary composite (PrG-2), and the ternary composite (PrGZ-2) are presented in **(Fig. 10).** The microstructure of PANI **(Fig. 10A)** was characterized by spherical-shaped particles of varying sizes, a typical morphology resulting from the oxidative polymerization process **(Tawade et al., 2019)**. The SEM image of GO **(Fig. 10B)** reveals a typical layered and sheet-like morphology, characterized by thin, crumpled, and wrinkled sheets stacked in a disordered manner. The GO sheets exhibit irregular edges, folds, and surface corrugations, which arise from the introduction of oxygen-containing functional groups during the oxidation of graphite. These functional groups disrupt the planar sp^2 carbon network, leading to expanded interlayer spacing and preventing complete restacking of the sheets. The observed flake-like structure with overlapping layers indicates partial exfoliation of graphite oxide into graphene oxide nanosheets. Additionally, the rough and uneven surface texture suggests the presence of structural defects and lattice distortion induced by oxidation. Such a morphology provides a high surface area and abundant active sites, which is advantageous for subsequent reduction, composite formation, and electrochemical applications. In contrast, rGO **(Fig. 10C)** exhibited a smooth, continuous surface with large flaky layers, indicative of the sinuate and layered structure formed after the chemical reduction of GO **(Palsaniya et al., 2021).** The binary composite (PrG-2) **(Fig. 10D)** revealed a homogeneous distribution of PANI over the rGO flakes, with PANI particles effectively surrounding and interacting with the graphene sheets. This confirmed the successful grafting of PANI onto the rGO surface, ensuring the formation of a robust composite material. The ZnO nanoparticles **(Fig. 10 E)** displayed a distinct rod-like morphology with well-defined facets, confirming their crystalline and elongated structure at the nanoscale **(Seehra et al., 2017).** The ternary composite (PrGZ-2) **(Fig. 3F)** exhibited a more intricate and integrated morphology, with crooked shapes consisting of rGO flakes, rod-like ZnO nanoparticles, and fibrous PANI structures. The SEM images indicated that the rGO flakes were embedded within the PANI matrix, while the ZnO nanoparticles were uniformly dispersed throughout the composite, contributing to its enhanced structural stability and interconnectivity. This synergistic morphology is responsible for the improved physicochemical properties of the ternary composite **(Singh and Dhaliwal., 2022 and Thirumalraj et al., 2017).** The presented **Fig.10G** corresponds to the EDS spectrum of the PrGZ

nanocomposite, confirming the successful incorporation of its constituent elements. The spectrum exhibits prominent peaks corresponding to carbon (C), nitrogen (N), oxygen (O), and zinc (Zn**)**. The strong C peak originates from the carbonaceous framework of rGO and the PANI backbone, while the presence of N is attributed exclusively to the amine and imine groups of PANI**,** confirming successful polymer incorporation. The O peak arises from residual oxygen functionalities of rGO as well as oxygen associated with ZnO. Distinct Zn peaks observed at higher energy regions (around ~1.0 and ~8.6–9.6 keV) confirm the presence of ZnO nanoparticles within the composite. Quantitative EDS analysis indicates weight percentages of approximately 34.05 wt% C, 11.06 wt% N, 33.29 wt% O, and 21.60 wt% Zn**,** with corresponding atomic percentages of 46.97 at% C, 13.08 at% N, 34.47 at% O, and 5.47 at% Zn. The relatively lower atomic percentage of Zn compared to C and O is expected due to the higher atomic mass of Zn and its dispersion as an inorganic phase within the organic–carbon matrix. The absence of impurity peaks confirms the high purity and homogeneous formation of the PrGZ nanocomposite, validating the successful integration of PANI, rGO, and ZnO.

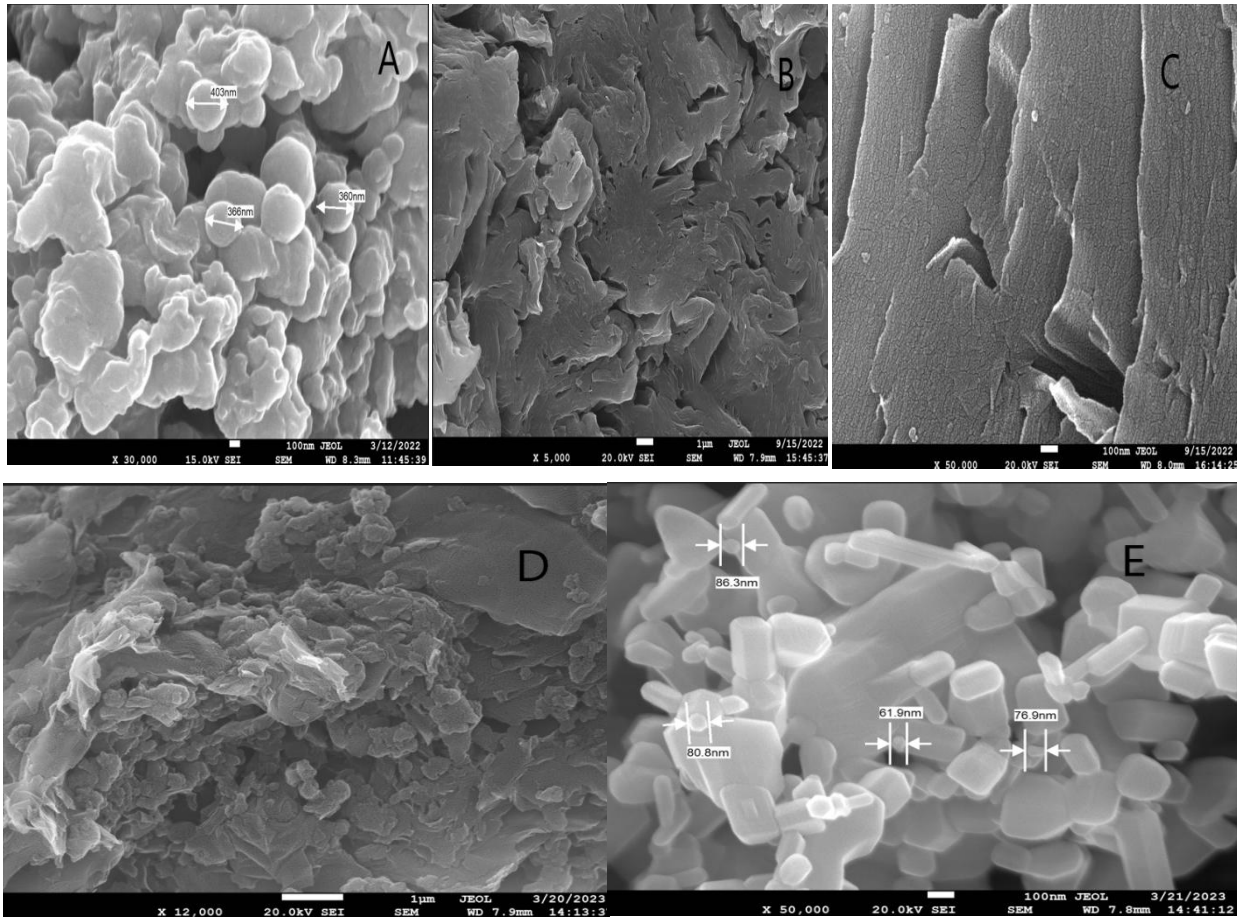

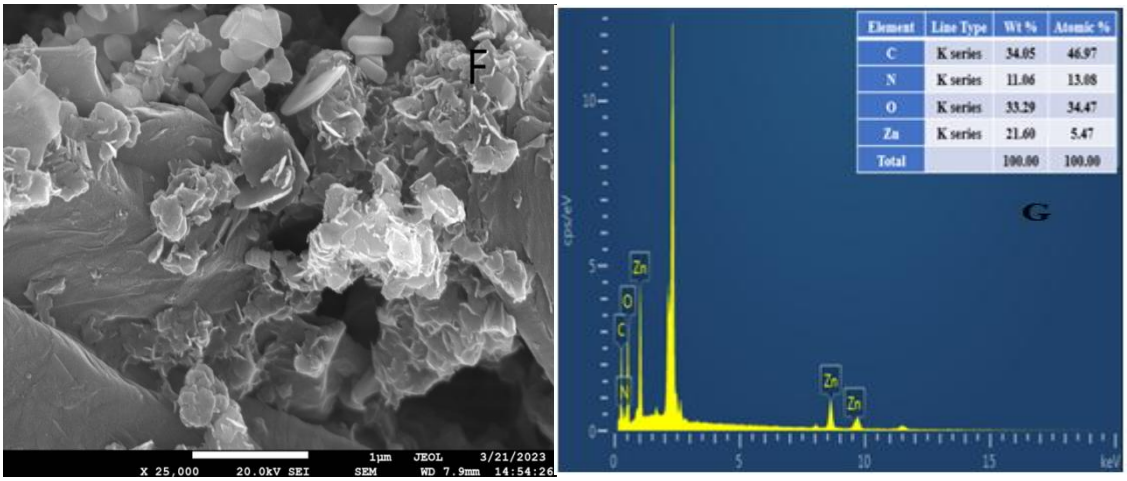

Figure: 10 SEM of (A) PANI , (B) GO , (C) rGO , (D) PrG-2 , (E) ZnO , (F) PrGZ-2 , and (G)EDS data of PrGZ-2

The SEM images of PANI/rGO/MnO_2 **(Fig. 11B)** revealed a hierarchical, interconnected network formed by the uniform dispersion of MnO_2 nanoparticles within the PANI and rGO matrix. The MnO_2 **(Fig.11A)** particles appeared predominantly as rod-like and granular nanostructures, which were well distributed across the wrinkled, sheet-like surfaces of rGO. These rGO nanosheets provided an extensive, conductive scaffold that effectively supported the MnO_2 nanostructures and polyaniline chains. This synergistic morphology is responsible for the improved physicochemical properties of the ternary composite, consistent with morphological observations reported by **(Wu et al., 2016, Singh and Dhaliwal., 2022, and Thirumalraj et al., 2017).** EDS spectrum of the PrGM nanocomposite (Fig.11C), confirming the presence and successful integration of its constituent elements. The spectrum displays prominent characteristic peaks of carbon (C), nitrogen (N), oxygen (O), and manganese (Mn)**.** The intense carbon peak originates from the carbonaceous framework of rGO as well as the PANI matrix, while the nitrogen signal arises exclusively from the amine and imine functionalities of PANI, confirming the formation of the conducting polymer component. The oxygen peak is attributed to residual oxygen-containing functional groups of rGO and oxygen associated with MnO_2**.** Distinct Mn peaks, particularly around ~5.9–6.5 keV, confirm the presence of manganese oxide nanoparticles embedded within the polymer–graphene matrix.

The relative intensity distribution indicates that carbon is the dominant element, followed by oxygen, with comparatively lower contributions from nitrogen and manganese. This is expected

due to the higher atomic mass of Mn and its dispersion as an inorganic phase within the organic–carbon matrix. The absence of extraneous elemental peaks indicates the high purity of the synthesized PrGM nanocomposite and validates the successful formation of a ternary hybrid system consisting of PANI, rGO, and MnO_2**.**

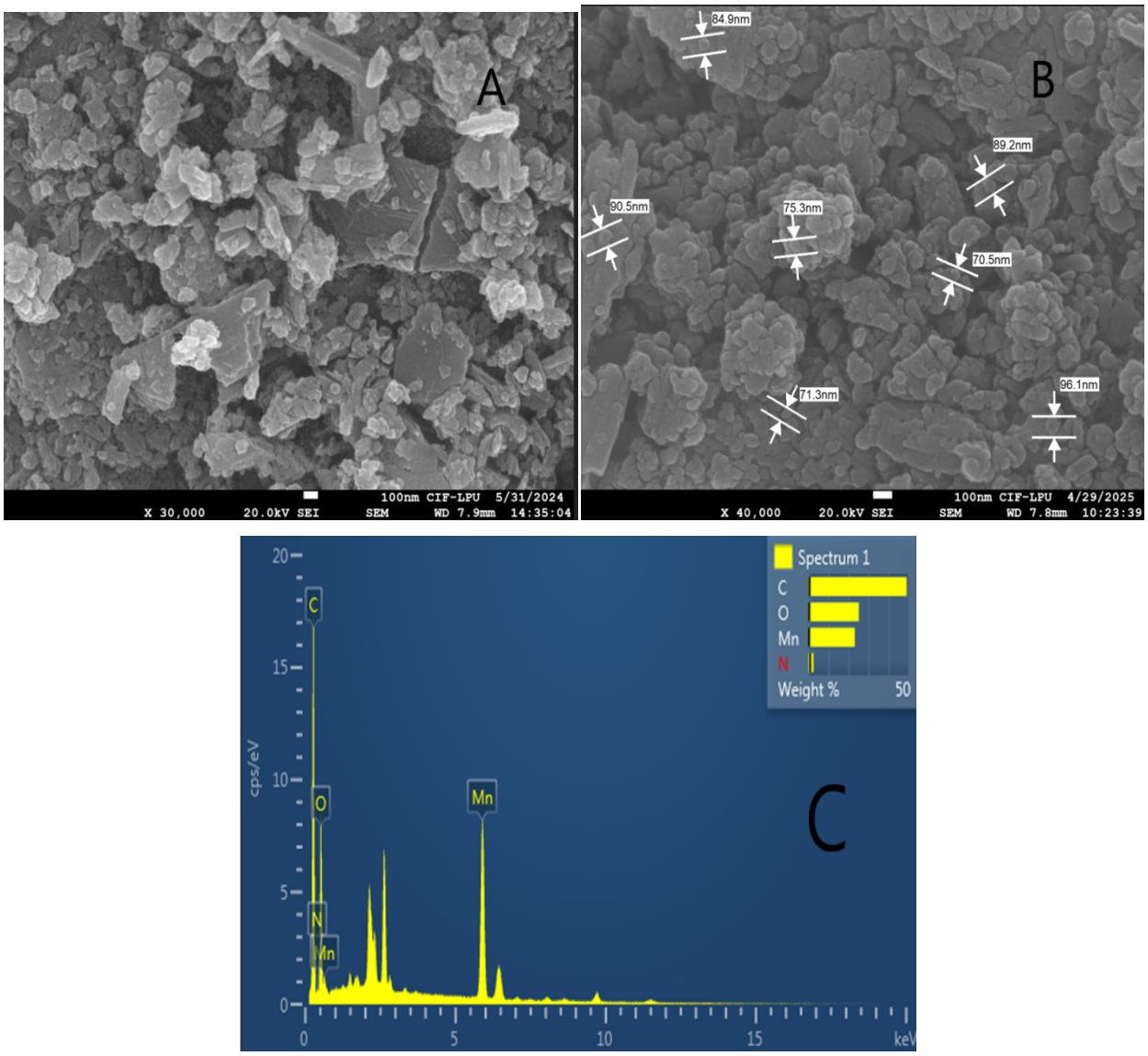

Figure: 11 SEM of (A) MnO_2 and (B) PrGM-2 , and (C) EDS data of PrGM-2

4.5 X-ray Photoelectron Spectroscopy:

High-resolution XPS measurements were performed to elucidate the surface chemical composition and bonding environment of the material. The C 1s spectrum **(Fig 12.A)** reveals a dominant peak at ~284.5 eV, which can be attributed to graphitic/sp^2 hybridized carbon (C–C/C=C). This indicates that the bulk of the surface carbon atoms retain a conjugated framework. In addition, a secondary contribution centered at ~285.6 eV corresponds to carbon atoms bonded to electronegative elements such as oxygen or nitrogen (C–O/C–N), suggesting the presence of surface functionalization or heteroatom incorporation. The deconvolution confirms that the majority of carbon exists in its intrinsic graphitic form, while the minor higher-binding-energy component highlights chemical heterogeneity at the surface, which may arise from residual oxygen-containing groups or intentional heteroatom doping. Such chemical states are known to play a pivotal role in modulating surface reactivity, electronic properties, and interfacial interactions. The XPS spectrum of the N 1s region **(Fig 12 B)** reveals two distinct deconvoluted peaks located at binding energies of approximately 398 eV and 399 eV. The peak at 398 eV is attributed to the formation of a metal–N bond, which confirms the successful coordination between the nitrogen atoms of polyaniline and the metal oxide species (ZnO). This interaction provides direct evidence of strong interfacial bonding within the composite. The second peak, appearing at 399 eV, corresponds to the $–NH_2$ functional groups present in polyaniline, indicating that a portion of the amine sites remain uncoordinated and preserve the intrinsic nitrogen functionalities of the polymer backbone. The simultaneous presence of both the free amine groups and the coordinated metal–N bonds highlights the dual role of polyaniline: first, as a source of nitrogen-based functionalities that enhance the chemical reactivity and electron-donating nature of the composite, and second, as a coordinating agent facilitating strong coupling with ZnO nanoparticles. This synergistic interaction not only stabilizes the composite structure but also significantly enhances its electronic conductivity, active surface sites, and overall electrochemical properties. The O 1s XPS spectrum **(Fig 12C)** confirms the presence of both lattice oxygen from the metal oxide and oxygenated carbon species (C=O, C–O) associated with the polymer/carbon matrix. This dual oxygen chemistry evidences robust integration of metal oxide with PANI/rGO, suggesting strong interfacial coupling, retention of surface oxygen functionalities, and a surface rich in active sites — features that are expected to enhance adsorption, charge transfer, and electrochemical sensing performance for heavy-metal ions. XPS

survey spectrum **(Fig12D)** of the PANI/rGO/ZnO composite showing the presence of C 1s, N 1s, O 1s and Zn 2p core levels. The coexistence of these elements confirms successful integration of ZnO with the nitrogen-containing polymer and carbon matrix; high-resolution scans (N 1s, O 1s) indicate metal–N coordination and both lattice and carbon-bound oxygen species **(Dreyer, D. R et al., 2010)**

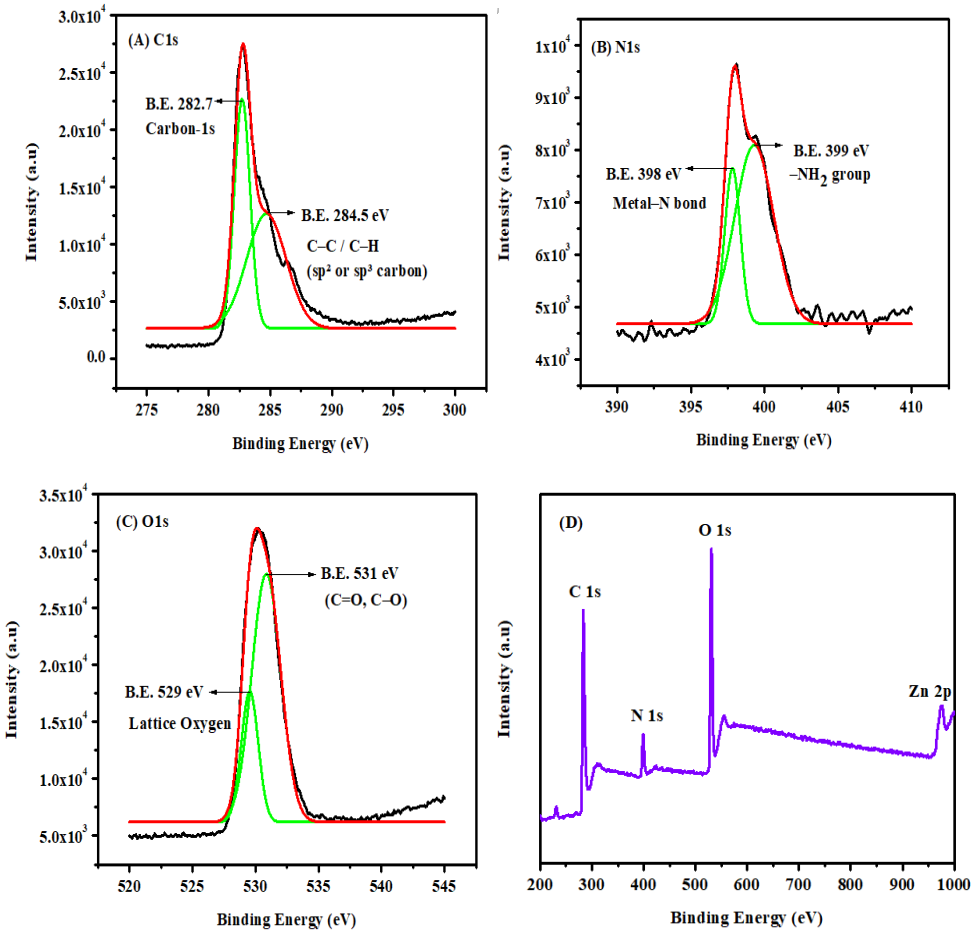

Figure 12 (A) XPS of C1s (B) XPS of N1s (C) XPS of O1s (D) XPS Survey Spectrum of PrGZ

The wide-scan XPS survey spectrum **(Fig 13D)** confirms the elemental composition of the synthesized material. Distinct peaks corresponding to C 1s, N 1s, O 1s, and Mn 2p are observed, indicating the successful incorporation of carbon, nitrogen, oxygen, and manganese species in the composite. The absence of any additional impurity peaks suggests the high purity of the prepared material. The strong O 1s and Mn 2p signals confirm the presence of manganese oxide, while the C 1s and N 1s peaks originate from the carbon framework and nitrogen-containing

functional groups (e.g., PANI or N-doped carbon). The high-resolution C 1s spectrum **(Fig 13 A)** shows a dominant peak centered at ~282.5 eV, attributed to C–C/C=C (sp^2 hybridized carbon), confirming the graphitic carbon framework. A secondary component at ~285.07 eV corresponds to C–C/C–H bonds, indicating residual aliphatic carbon or defect-related carbon species. The presence of these peaks suggests partial disorder and functionalization of the carbon matrix, which is beneficial for enhanced electrochemical activity. N 1s spectrum **(Fig 13 B)** can be deconvoluted into two major components, the peak at ~397.7 eV is assigned to metal–N bonding, indicating strong interaction between nitrogen atoms and manganese species, which enhances charge transfer at the interface and the peak at ~399.8 eV corresponds to $–NH_2$ or amine-type nitrogen, confirming the presence of nitrogen-containing functional groups (likely from polyaniline or amine functionalities). These nitrogen species contribute to improved electrical conductivity and provide active sites for electrochemical reactions. The O 1s spectrum **(Fig13 C)** exhibits a prominent peak at ~530.2 eV, which is characteristic of lattice oxygen (O^{2-}) in metal oxides, confirming the formation of manganese oxide. The dominance of lattice oxygen suggests good crystallinity and stable metal–oxygen bonding, which is essential for electrochemical stability and catalytic activity. XPS results confirm successful formation of a Mn-based oxide integrated with a nitrogen- and carbon-rich matrix**, s**trong interfacial interactions between Mn–O, Mn–N, and carbon species and presenc**e** of functional groups that can enhance electrochemical performance and heavy-metal ion adsorption. These features collectively validate the suitability of the material for electrochemical sensing and environmental remediation applications **(Biesinger, M. C., 2017)**

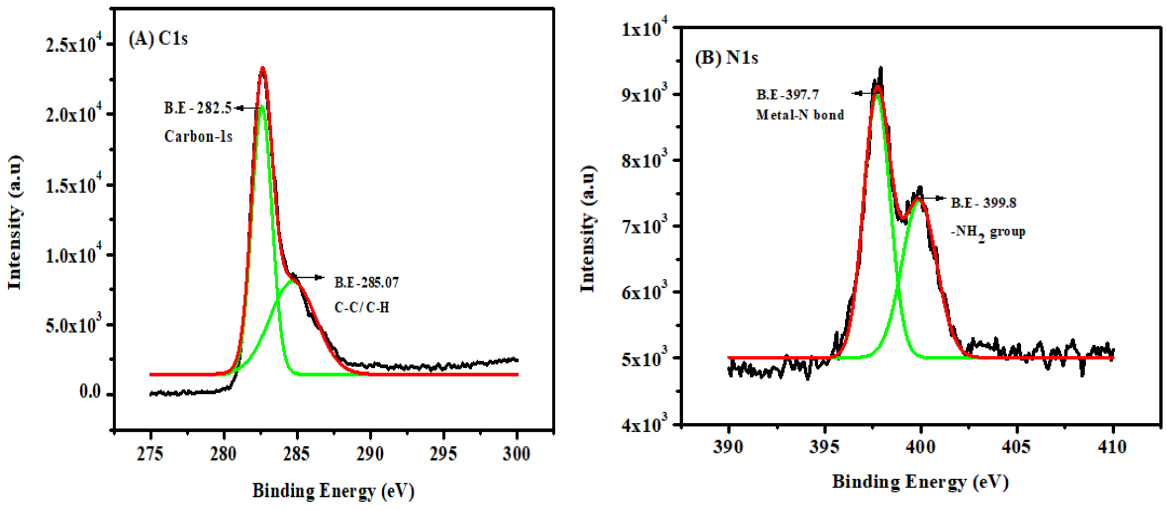

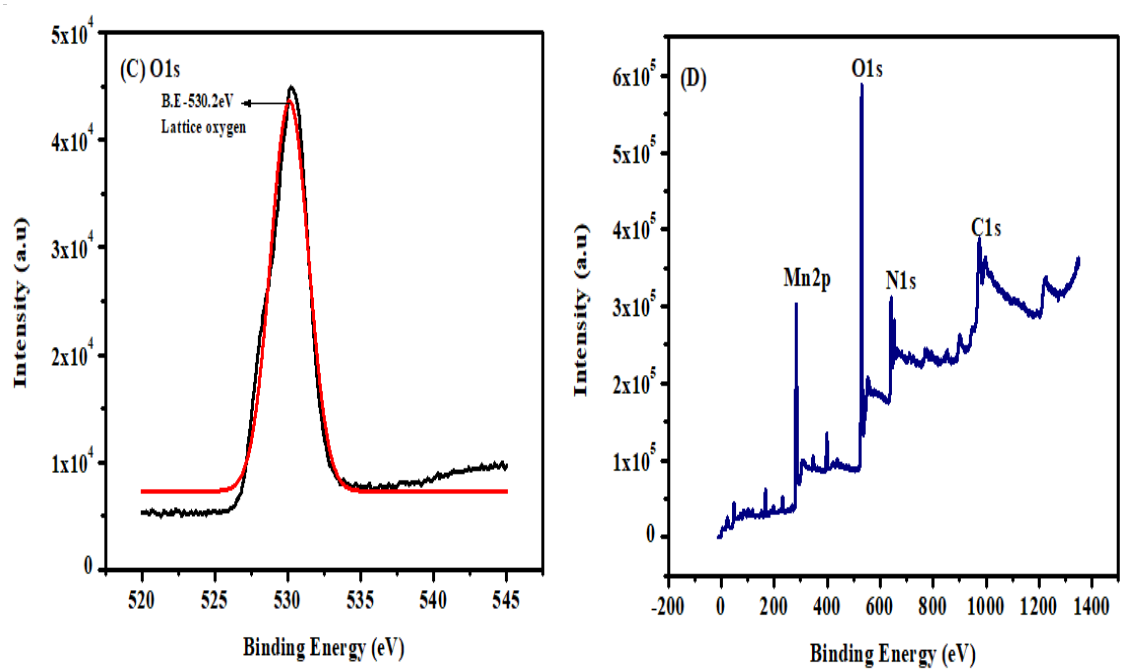

Figure 13 (A) XPS of C1s (B) XPS of N1s (C) XPS of O1s (D) XPS Survey Spectrum of PrGM

4.6 Electrochemical Characterization: The electrochemical properties of the synthesized nanocomposite materials were comprehensively evaluated using Impedance EIS and DPASV. These complementary electrochemical techniques provide valuable insights into the charge transfer kinetics, electrical conductivity, capacitance behavior, and electroactive surface area of the materials. EIS is particularly useful for assessing the interfacial charge transfer resistance and overall impedance of the electrode/electrolyte system, while DPASV is a highly sensitive technique employed to investigate the electrochemical response of the modified electrodes, especially for detecting trace metal ions. Together, these methods allow a thorough understanding of the electrochemical performance, stability, and potential applicability of the prepared binary and ternary nanocomposite electrodes in sensor applications.

4.6.1 CV of PANI, rGO, PrG, ZnO, MnO_2 and Ternary Composite (PrGZ & PrGM): The electrochemical behavior of PANI, rGO, ZnO, the binary composite PrG (PANI-rGO), and the ternary composite PrGZ (PANI-rGO-ZnO) was thoroughly investigated by CV measurements **(Stejskal and Gilbert., 2002 and Dreyer et al., 2010).** These experiments were conducted in a potential window ranging from –0.5 V to 1.5 V at a scan rate of 10 mV/s using

0.1 M acetate buffer as the supporting electrolyte **(Kumar et al., 2012)**. The electrochemical behavior of the PrGZ-2 nanocomposite, recognized as the best-performing ratio, was further analyzed by predicting its CV as shown in **Figure. 14** response at varying scan rates of 10 mV/s, 50 mV/s, 100 mV/s, 200 mV/s, and 500 mV/s in 0.1 M acetate buffer solution **(Arulraj et al., 2020).** Based on the experimental trends, it is anticipated that as the scan rate increases, the corresponding anodic and cathodic peak currents will also rise proportionally **(Bard and Faulkner, 2001).** At a lower scan rate of 10 mV/s, the CV curve of PrGZ-2 would likely exhibit smaller, well-defined redox peaks with minimal capacitive distortion, indicating highly reversible redox processes **(Zhang and Gan, 2017).** As the scan rate increases to 50 mV/s, a moderate enhancement in peak currents is expected, accompanied by slight broadening and minor shifts in peak positions due to increasing ion diffusion limitations **(Liu and Yu, 2018)**. At 100 mV/s, the peak currents would further rise, and the curve would display a noticeable capacitive character, with redox peaks becoming slightly more separated, reflecting quasi-reversible kinetics **(Wang and Hu, 2019)**. Upon reaching 200 mV/s, PrGZ-2 is predicted to show significantly higher peak currents, with broader and more separated peaks, as diffusion-controlled processes start to dominate the electron transfer kinetics **(Saini et al., 2020).** Finally, at a high scan rate of 500 mV/s, the CV curve would exhibit very large current responses, a pronounced capacitive behavior, and greater peak-to-peak separation, highlighting kinetic limitations and increased internal resistance within the system **(Wei et al., 2011).** Throughout these scan rates, PrGZ-2 maintains a robust electrochemical profile, attributed to the synergistic interaction between PANI, rGO, and ZnO nanoparticles, providing rapid electron transport pathways and abundant active sites for redox reactions **(Roy and Bhattacharya, 2022).** This behavior reinforces the suitability of PrGZ-2 as an efficient material for electrochemical sensing applications in acetate buffer environments **(Hsieh et al., 2018).**

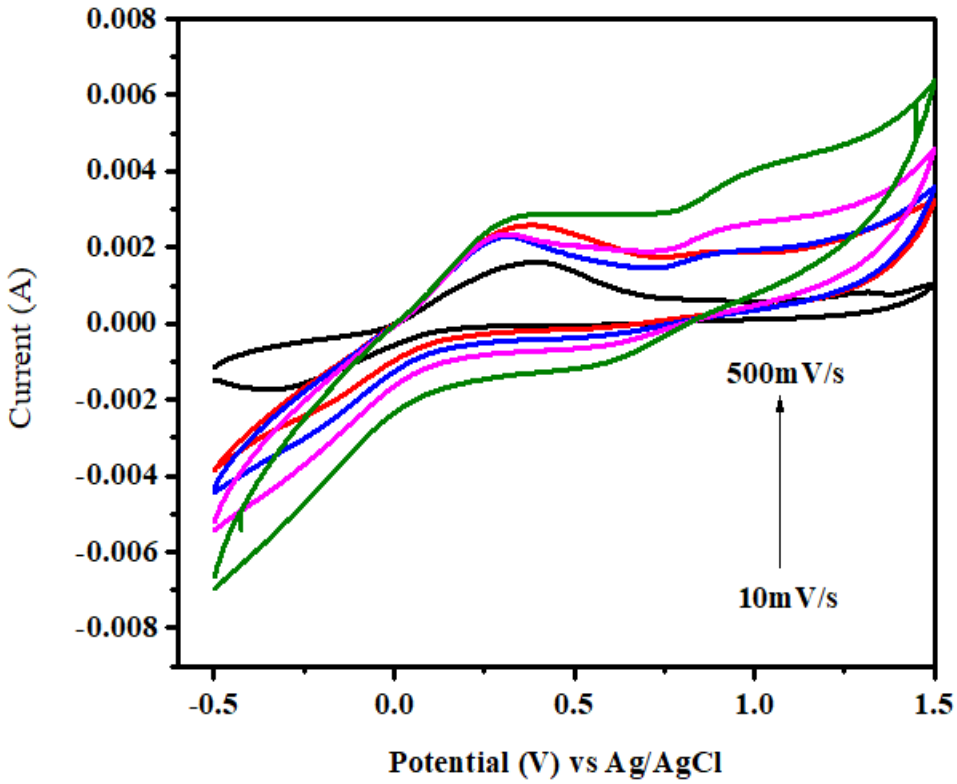

Figure: 14 CV of PrGZ-2 at different Scan rate of 10 mV/s, 50 mV/s, 100 mV/s, 200 mV/s, and 500 mV/s in 0.1 M acetate buffer solution

The resulting CV profiles as shown in **Fig. 15** provide valuable insights into the redox characteristics and electrochemical performance of the individual materials and their composites **(Stejskal and Gilbert, 2002; Dreyer et al., 2010; Sahoo et al., 2013)**. From the CV curves, it is evident that pure PANI, rGO, and ZnO exhibit relatively low current responses and minimal redox features when tested individually **(Sahoo et al., 2013; Arulraj et al., 2020)**. This behavior can be attributed to the moderate electrical conductivity of PANI and ZnO, and the mainly capacitive behavior of rGO with limited pseudocapacitive activity **(Dreyer et al., 2010; Zhang and Gan, 2017).** As expected, rGO displays a nearly rectangular voltammogram, characteristic of an electrical double-layer capacitor, while ZnO, being a wide bandgap semiconductor, shows very weak electrochemical activity **(Zhang et al., 2018).** In contrast, the PrG binary composite (PANI–rGO) demonstrates a noticeably enhanced electrochemical response compared to its constituent materials **(Kumar et al., 2012).** The CV curve of PrG shows well-defined anodic and cathodic peaks, indicating improved redox activity **(Kumar et al., 2012).** The synergistic

interaction between PANI and rGO plays a critical role in this enhancement. The incorporation of highly conductive rGO provides efficient electron transport pathways within the composite matrix, effectively reducing the internal resistance and promoting faster charge transfer **(Kumar et al., 2012; Zhang and Gan, 2017).** Simultaneously, PANI contributes to the pseudocapacitance through its intrinsic redox-active sites, thereby significantly increasing the overall faradaic contribution to the current **(Stejskal and Gilbert, 2002).** This synergistic effect between the conductive rGO sheets and the redox-active PANI chains results in superior electrochemical behavior of the PrG composite compared to the individual components **(Sahoo et al., 2013; Kumar et al., 2012).** Among all the materials analyzed, the PrGZ ternary composite exhibits the highest current response, as clearly observed from its CV curve **(Arulraj et al., 2020; Roy and Bhattacharya, 2022).** The PrGZ composite presents distinct and sharp redox peaks along with a significantly larger enclosed area under the curve, highlighting its remarkable electrochemical activity and enhanced charge storage capability **(Roy and Bhattacharya, 2022).** The superior performance of the PrGZ composite can be attributed to the effective synergistic interaction among all three components **(Roy and Bhattacharya, 2022; Saini et al., 2020).** In this ternary system, rGO acts as a highly conductive backbone that facilitates rapid electron transport across the composite structure **(Dreyer et al., 2010).** PANI provides abundant redox-active sites capable of undergoing reversible oxidation and reduction reactions, thus contributing to the pseudocapacitance **(Stejskal and Gilbert, 2002; Kumar et al., 2012).** Moreover, the incorporation of ZnO nanoparticles introduces additional active sites and enhances the surface area of the composite **(Arulraj et al., 2020 and Zhang et al., 2018).** ZnO not only supports ion diffusion by providing more accessible channels but also improves the composite's mechanical stability and structural integrity **(Saini et al., 2020).** The combined effects of rGO's excellent conductivity, PANI's redox activity, and ZnO's contribution to surface reactivity and ion diffusion collectively result in the superior electrochemical performance of the PrGZ ternary composite **(Roy and Bhattacharya, 2022).** These findings underscore the significant advantage of designing ternary hybrid nanocomposites for applications in electrochemical sensors, energy storage devices, and heavy metal ion detection, where high sensitivity, fast electron transfer, and robust redox activity are essential **(Hsieh et al., 2018; Roy and Bhattacharya, 2022).**

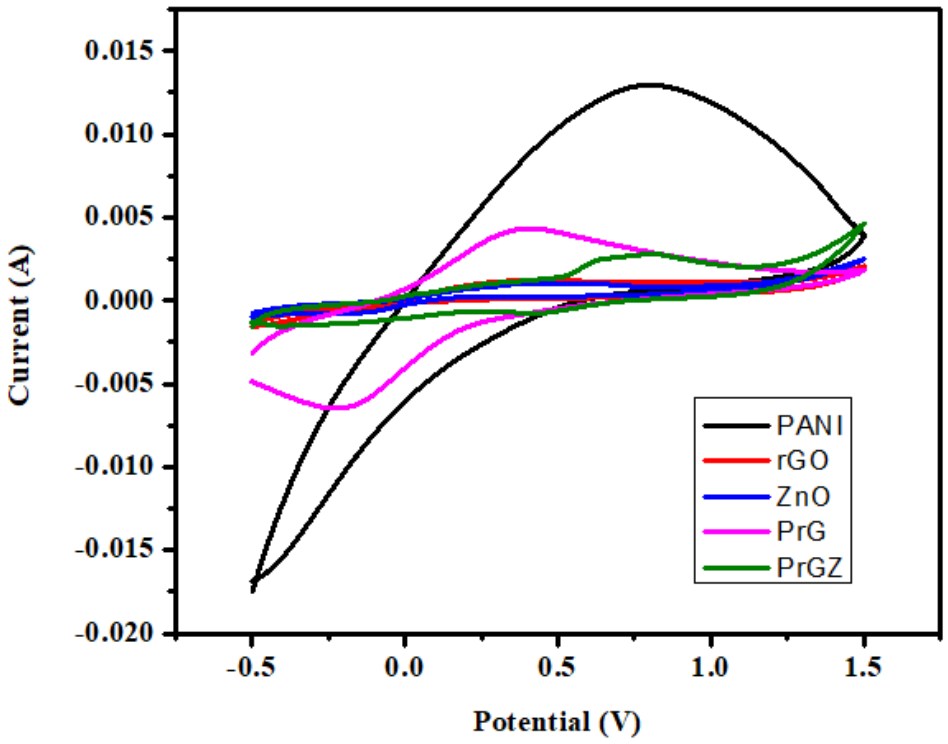

Figure: 15 CV of PANI, rGO, PrG, ZnO and PrGZ at 10mV/s in 0.1M acetate buffer

The electrochemical behavior of the PrGM-2 nanocomposite, recognized as the best-performing ratio, was further analyzed by predicting its CV response **(Figure. 16)** at varying scan rates of 10 mV/s, 50 mV/s, 100 mV/s, 200 mV/s, and 500 mV/s in 0.1 M acetate buffer solution **(Kumar et al., 2012 and Zhou et al., 2017).** Based on the experimental trends, it is anticipated that as the scan rate increases, the corresponding anodic and cathodic peak currents will also rise proportionally **(Arulraj et al., 2020 and Balamurugan et al., 2018).** At a lower scan rate of 10 mV/s, the CV curve of PrGM-2 would likely exhibit smaller, well-defined redox peaks with minimal capacitive distortion, indicating highly reversible redox processes **(Stejskal and Gilbert, 2002; Sahoo et al., 2013).** As the scan rate increases to 50 mV/s, a moderate enhancement in peak currents is expected, accompanied by slight broadening and minor shifts in peak positions due to increasing ion diffusion limitations **(Wang et al., 2012).** At 100 mV/s, the peak currents would further rise, and the curve would display a noticeable capacitive character, with redox peaks becoming slightly more separated, reflecting quasi-reversible kinetics **(Dreyer et al., 2010 and Kumar et al., 2012).** Upon reaching 200 mV/s, PrGM-2 is predicted to show significantly higher peak currents, with broader and more separated peaks, as diffusion-

controlled processes start to dominate the electron transfer kinetics **(Roy and Bhattacharya, 2022)**. Finally, at a high scan rate of 500 mV/s, the CV curve would exhibit very large current responses, a pronounced capacitive behavior, and greater peak-to-peak separation, highlighting kinetic limitations and increased internal resistance within the system **(Balamurugan et al., 2018 and Saini et al., 2020).** Throughout these scan rates, PrGM-2 maintains a robust electrochemical profile, attributed to the synergistic interaction between PANI, rGO, and MnO_2 nanoparticles, providing rapid electron transport pathways and abundant active sites for redox reactions **(Zhou et al., 2017 and Zhang et al., 2018).** This behavior reinforces the suitability of PrGM-2 as an efficient material for electrochemical sensing applications in acetate buffer environments **(Arulraj et al., 2020; Hsieh et al., 2018).**

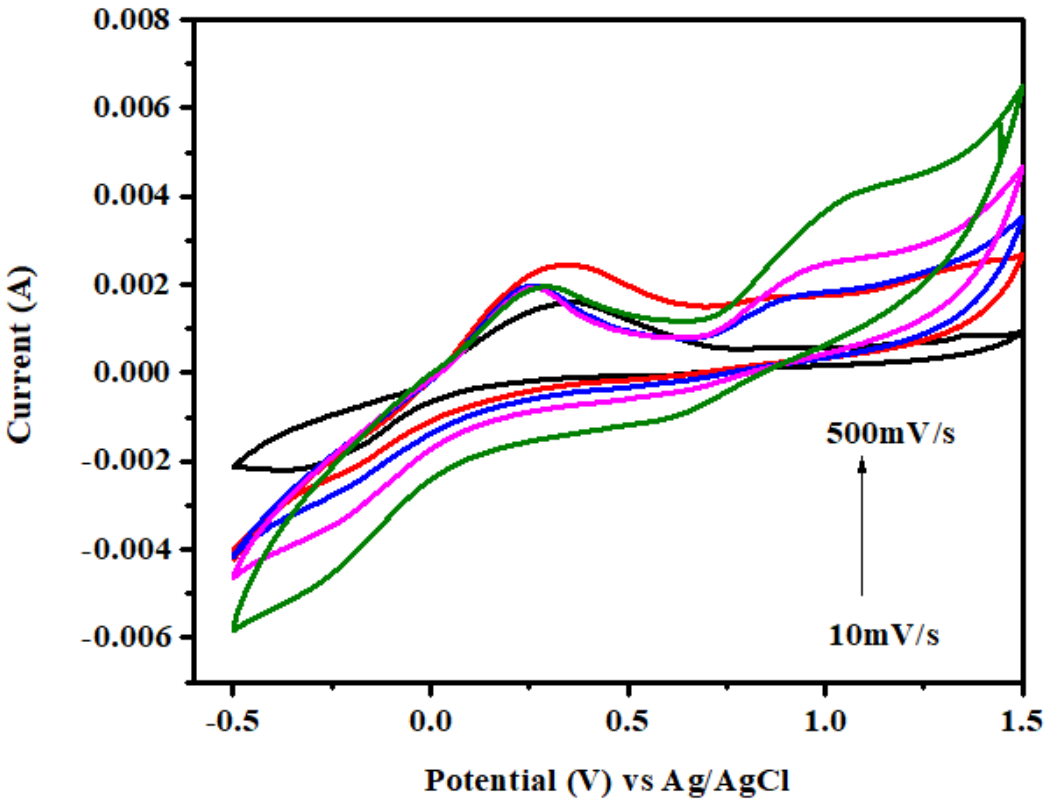

Figure: 16 CV of PrGM-2 at different Scan rate of 10 mV/s, 50 mV/s, 100 mV/s, 200 mV/s, and 500 mV/s in 0.1 M acetate buffer solution

The PrGM ternary composite exhibits the highest current response **(Figure. 17)** among all the materials studied, as evidenced by the CV analysis **(Kumar et al., 2012 and Arulraj et al.,**

2020). The CV curve of PrGM reveals a significantly larger enclosed area compared to the individual PrG) binary composite and pure MnO_2, along with the emergence of more prominent and sharper redox peaks **(Sahoo et al., 2013 and Wang et al., 2012).** This notable enhancement indicates a substantial improvement in both charge storage capability and the kinetics of electron transfer processes within the composite structure **(Balamurugan et al., 2018 and Zhou et al., 2017).**

The observed enhancement can be primarily attributed to the synergistic integration of three key components: highly conductive rGO, electrochemically active PANI, and pseudocapacitive MnO_2 nanoparticles **(Stejskal and Gilbert, 2002; Dreyer et al., 2010).** In this ternary system, rGO plays a crucial role by providing a highly conductive and interconnected network, which facilitates rapid electron transport throughout the composite matrix, thereby minimizing internal resistance and enhancing charge mobility **(Zhou et al., 2017; Roy and Bhattacharya, 2022).**

PANI, known for its intrinsic redox activity, offers numerous active sites for reversible oxidation and reduction reactions, contributing significantly to the overall pseudocapacitive behavior **(Stejskal and Gilbert, 2002; Saini et al., 2020).** Meanwhile, the incorporation of MnO_2 nanoparticles introduces additional faradaic sites and boosts the surface area of the composite, promoting enhanced ion diffusion and storage capabilities **(Balamurugan et al., 2018 and Wang et al., 2012)**. Furthermore, MnO_2, with its well-established pseudocapacitive nature, contributes additional redox reactions, thereby increasing the faradaic charge storage of the material **(Zhang et al., 2018 and Hsieh et al., 2018).**

The integration of MnO_2 into the PANI–rGO framework not only amplifies the electrochemical activity but also imparts mechanical robustness and structural stability to the composite, ensuring better cycling performance and durability during electrochemical operations **(Arulraj et al., 2020; Roy and Bhattacharya, 2022)**. The well-distributed MnO_2 nanoparticles effectively bridge the PANI–rGO matrix, enabling efficient ion accessibility and faster kinetics during the redox processes **(Saini et al., 2020).**

Consequently, the synergistic interaction between these three components results in a composite material with superior electrochemical properties, characterized by high capacitance, enhanced

redox activity, and improved reversibility **(Balamurugan et al., 2018; Zhou et al., 2017).** Therefore, the outstanding electrochemical performance of the PrGM ternary composite makes it a highly promising candidate for a range of advanced electrochemical applications **(Hsieh et al., 2018).**In particular, its high sensitivity, excellent charge transfer characteristics, and superior redox behavior render it exceptionally suitable for the sensitive and selective detection of heavy metal ions such as Pb^{2+} in environmental and biological samples **(Roy and Bhattacharya, 2022).** The remarkable enhancement observed in PrGM underscores the significant advantage of designing ternary hybrid nanostructures that harness the complementary properties of multiple materials for the development of high-performance electrochemical sensors **(Sahoo et al., 2013).**

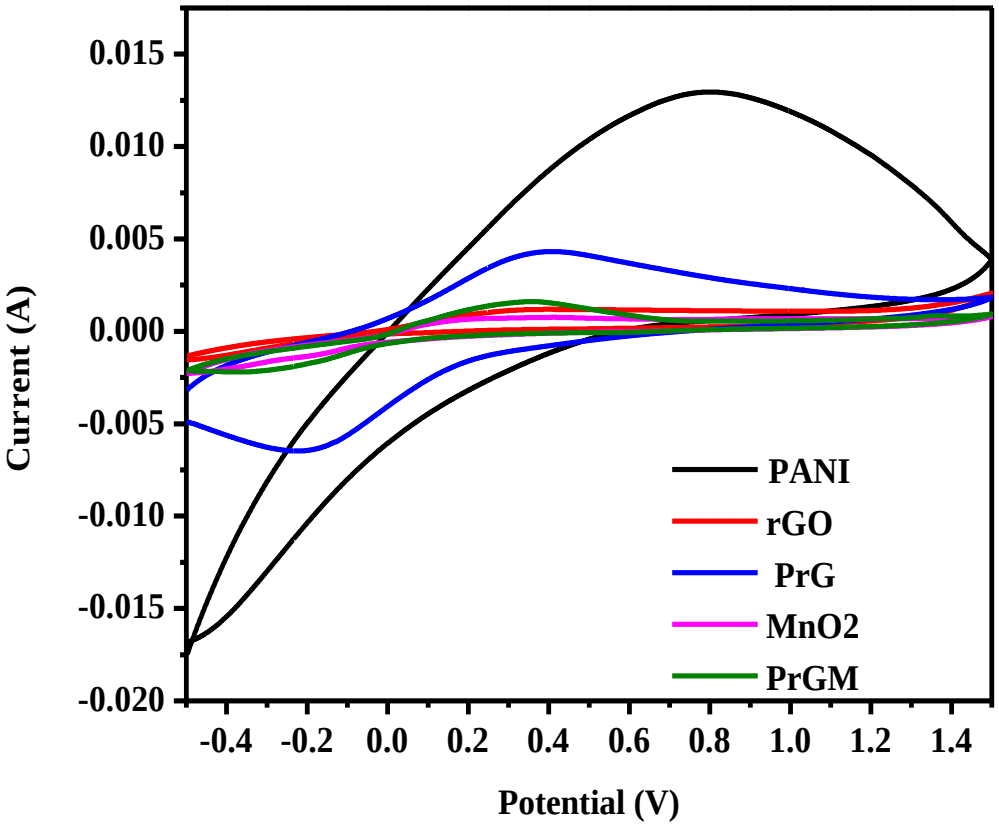

Figure: 17 CV of PANI, rGO, PrG, MnO_2 and PrGM at 10mV/s in 0.1 M acetate buffer

4.6.2 EIS of PANI, rGO, PrG, ZnO, MnO_2 and Ternary Composite (PrGZ & PrGM): EIS is a powerful diagnostic technique used to investigate the charge transfer

processes and other interfacial electrochemical phenomena occurring at the electrode/electrolyte interface **(Barsoukov and Macdonald, 2018).** In this study, EIS was employed to examine the electron transfer properties of PANI, rGO, PrG-2, and PrGZ-2 in a 1 M KOH solution, across a frequency range of 0.1 Hz to 10^5 Hz **(Kumar et al., 2012 and Saini et al., 2020).**

In the high-frequency region **(Fig.18)**, impedance behavior is primarily influenced by solution resistance (Rs) and contact resistance, where poor electron transfer and rapid signal response limitations are evident. PANI demonstrated a steeper and larger semicircle in this region compared to other materials, indicating a higher impedance and relatively sluggish charge transport properties **(Stejskal and Gilbert, 2002).** In contrast, rGO exhibited a smaller semicircle, reflecting improved conductivity and lower impedance than PANI **(Dreyer et al., 2010 and Saini et al., 2020).**

Further improvement was observed in the binary composite PrG-2, whose Nyquist plot showed a significantly reduced semicircle, suggesting better electron transfer efficiency and lower Rct, owing to the effective integration of PANI onto the conductive rGO framework **(Kumar et al., 2012; Roy and Bhattacharya, 2022).** Among all materials, the ternary composite PrGZ-2 exhibited the smallest semicircle, indicating the lowest charge-transfer resistance and most efficient interfacial electron transport, which can be attributed to the synergistic interaction between PANI, rGO, and ZnO nanoparticles **(Balamurugan et al., 2018; Martins et al., 2020).**

In the low-frequency region **(Fig.18),** where capacitive and diffusion-controlled processes dominate, the Nyquist plots of PrG-2 and PrGZ-2 displayed nearly linear profiles, signifying capacitive behavior with minimal resistance to ion diffusion and charge storage at the interface **(Zhang, Y et al., 2016 and Krawczyk, P., et al., 2020).** In contrast, PANI and rGO exhibited more curved profiles indicative of higher resistance and less effective charge storage. The progressive decrease in impedance values with increasing frequency across all samples indicates enhanced conductivity at higher frequencies, a characteristic of materials exhibiting both resistive and capacitive properties **(Barsoukov and Macdonald, 2018).**

Notably, PrGZ-2 demonstrated the most conductive behavior among the tested materials, as evidenced by its linear, low-impedance response, confirming its potential for superior electrochemical applications **(Martins et al., 2020; Roy and Bhattacharya, 2022).**

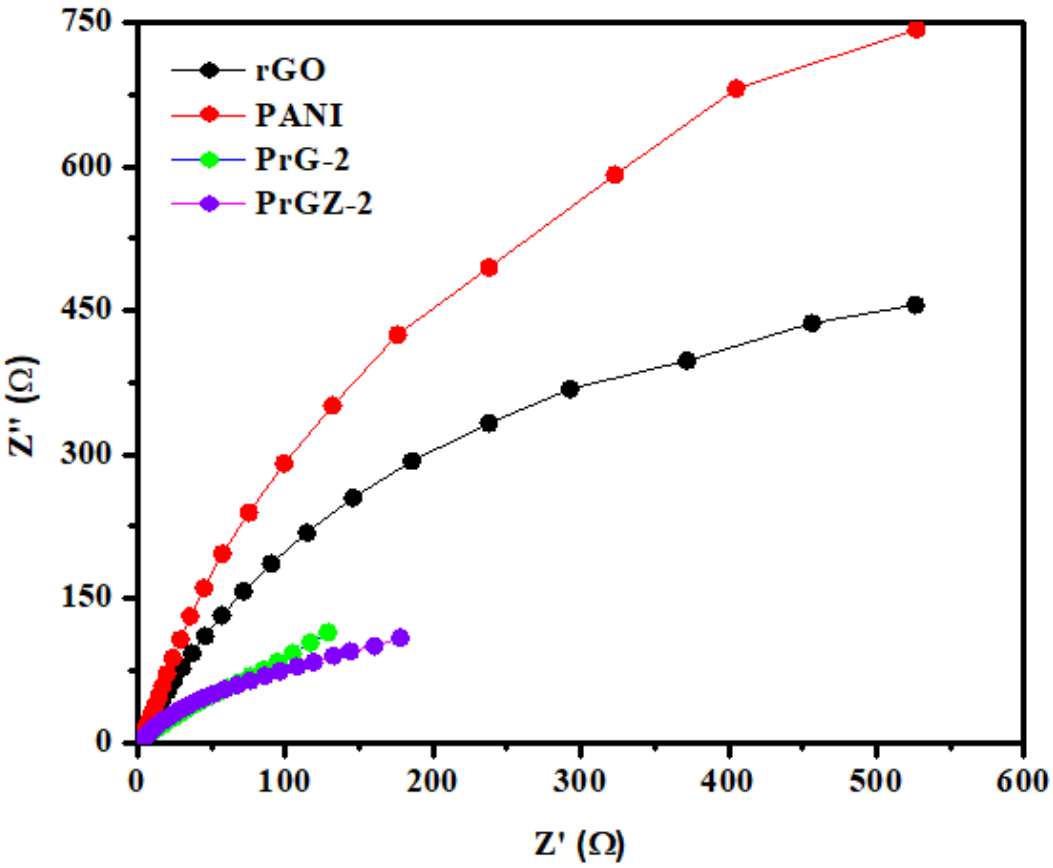

Figure: 18 EIS of PANI, rGO, PrG-2, and PrGZ-2

EIS was employed to study the interfacial charge transfer kinetics and ionic diffusion behavior of the synthesized materials, and the Nyquist plots are presented in **Fig 19**, **(Barsoukov and Macdonald, 2018)**. The EIS response was carefully analyzed over both the high-frequency and low-frequency regions to provide a complete understanding of the electrochemical properties.

In the high-frequency region, the observed semicircular arcs correspond to the charge transfer resistance (Rct) at the electrode–electrolyte interface **(Zhang et al., 2018).** Pure PANI exhibited a large semicircular diameter, indicating a high Rct and poor charge transfer kinetics. This is consistent with the inherently low conductivity of undoped PANI, which hinders electron

movement across the interface **(Stejskal and Gilbert, 2002).** In contrast, rGO demonstrated a much smaller semicircle, reflecting a lower Rct and enhanced electron transfer capabilities **(Dreyer et al., 2010 and Kumar et al., 2012).** This behavior is attributed to the restoration of the sp^2 carbon network during reduction, facilitating efficient electrical conduction. PrG exhibited an even smaller semicircle, implying a highly synergistic interaction between PANI and rGO that dramatically improved the charge transfer process **(Roy and Bhattacharya, 2022).** Interestingly, the ternary nanocomposite PrGM displayed a slightly larger semicircle compared to PrG, suggesting a modest increase in Rct due to the presence of the third component, MnO_2, which might introduce additional phase boundaries or defects **(Balamurugan et al., 2018).** Nevertheless, the Rct of PrGM remained significantly lower than that of pure PANI, indicating that the ternary composite preserved excellent electrical conductivity.

In the low-frequency region, the slope of the impedance curves provides insight into the diffusion-controlled processes and capacitive behavior of the materials **(Barsoukov and Macdonald, 2018)**. PANI displayed a nearly horizontal line, suggesting poor ionic diffusion and limited capacitive characteristics. rGO, in comparison, showed a more inclined line (~45°), reflecting improved diffusion pathways for electrolyte ions. The binary PrG composite further enhanced this behavior, with the line becoming more vertical, indicating superior capacitive properties and fast ionic transport. The ternary composite PrGM exhibited an almost vertical line in the low-frequency domain, approaching the behavior of an ideal capacitor **(Martins et al., 2020).**

This near-vertical response suggests that the incorporation of the MnO_2 component not only preserved the high conductivity of the binary composite but also introduced additional active sites and pathways, facilitating rapid ion diffusion and enhanced electrolyte accessibility **(Balamurugan et al., 2018).** Thus, the EIS results clearly demonstrate that while pure PANI suffers from high impedance and poor diffusion characteristics, the incorporation of rGO substantially enhances both charge transfer and capacitive behavior. Furthermore, the construction of the ternary nanocomposite PrGM results in an optimized electrochemical structure, combining excellent electron transfer with fast ionic movement. These properties make PrGM a highly promising material for applications in electrochemical sensing, supercapacitors, and energy storage devices **(Roy and Bhattacharya, 2022; Martins et al., 2020).**

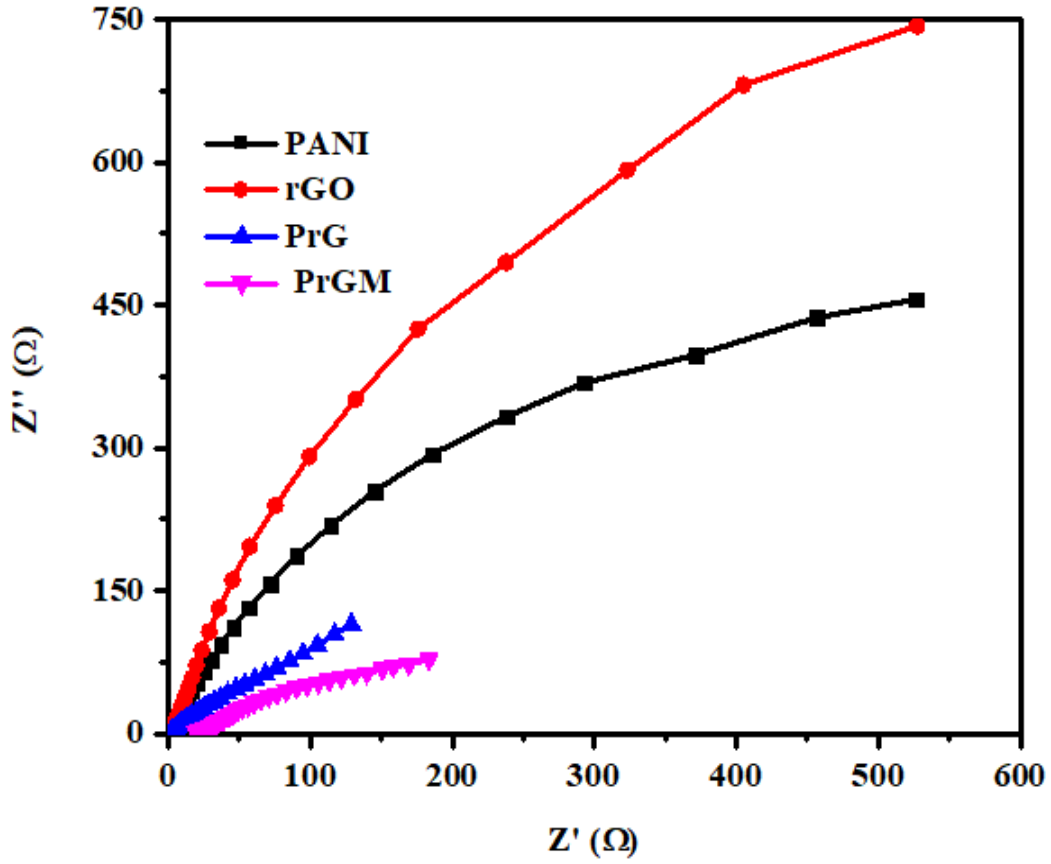

Figure: 19 EIS of PANI, rGO, PrG-2, and PrGM-2

4.6.3 DPASV and UV of PANI, rGO, PrG, ZnO, MnO_2 and Ternary Composite (PrGZ and PrGM) for detection and removal of Pb^{2+} ions and Cd^{2+} ions.:

4.6.3.1 DPASVof PrGZ-2 for detection of Pb^{2+} ions: DPASV was employed to investigate the electrochemical detection capabilities of the prepared binary (PrG-2) and ternary (PrGZ-2) nanocomposites towards Pb^{2+} ions **(Wang, 2006).** This technique operates by pre-depositing metal ions onto the electrode surface at a constant potential, followed by a stripping step where the current generated is directly proportional to the analyte concentration **(Honeychurch and Hart, 2003)**. A 0.1 M sodium acetate and 0.07 M acetic acid buffer at pH

4.5 was used as the supporting electrolyte, with lead acetate solutions added in the concentration range of 1.0 μM to 5.5 μM.

The working electrode consisted of a carbon paste electrode modified with the nanocomposite material, while an Ag/AgCl electrode served as the reference and a platinum wire as the counter electrode **(Honeychurch and Hart, 2003; Zawodzinski et al., 1995).** The DPASV measurements were performed in a potential window from -1.0 V to 0.1 V, with a modulation amplitude of 0.1 V, modulation time of 0.05 s, and a slow scan rate of 0.01 V/s, optimizing conditions for the sensitive detection of Pb^{2+} ions **(Wang, 2006).**

The comparative DPASV results revealed that the PrGZ-2 composite demonstrated the highest stripping peak current of 6.53 mA at -0.5 V, significantly outperforming CPE (1.08 mA), PANI (4.46 mA), rGO (4.68 mA), and PrG-2 (4.88 mA). This substantial improvement is attributed to the synergistic interaction between rGO, which provides a large surface area and high electrical conductivity **(Dreyer et al., 2010)**; PANI, contributing pseudo-capacitive behavior and redox activity **(Stejskal and Gilbert, 2002)**; and ZnO nanoparticles, which enhance electron transfer kinetics and structural stability **(Sivakumar et al., 2017).**

The increased electroactive surface area and improved electron transfer properties in the PrGZ-2 composite make it highly effective for Pb^{2+} detection. Additionally, both PrG-2 and PrGZ-2 exhibited well-defined, concentration-dependent stripping peaks from 1.0 μM to 5.5 μM, with PrGZ-2 maintaining a superior response. The calibration curve for PrGZ-2 demonstrated a higher linear correlation (R^2 = 0.994) compared to PrG-2 (R^2 = 0.981), indicating better linearity and accuracy across the tested concentration range **(Martins et al., 2020).**

The LOD and LOQ are calculated using the formula below:

$$\text{LOD} = \frac{3.3 \times \text{SD}}{\text{S}}$$

$$\text{LOQ} = \frac{10 \times \text{SD}}{\text{S}}$$

Where, SD is the standard deviation of the blank solution, and S is the slope of the calibration curve. The LOD and LOQ obtained for Pb^{2+} ions are 0.3 μM and 1.16μM, respectively, for PrGZ-2 composite.

Table: 6 Summarized DPASV results of binary (PrG-2) and ternary composites (PrGZ-2) for Pb^{2+}

Composite	R^2	LOD (µM)	LOQ (µM)	RSD (%)	Sensitivity ($mA\ \mu M^{-1}$)
PrG-2	0.981	0.7	2.3	3.1	**0.5164**
PrGZ-2	0.994	0.3	1.16	2.13	**0.9464**

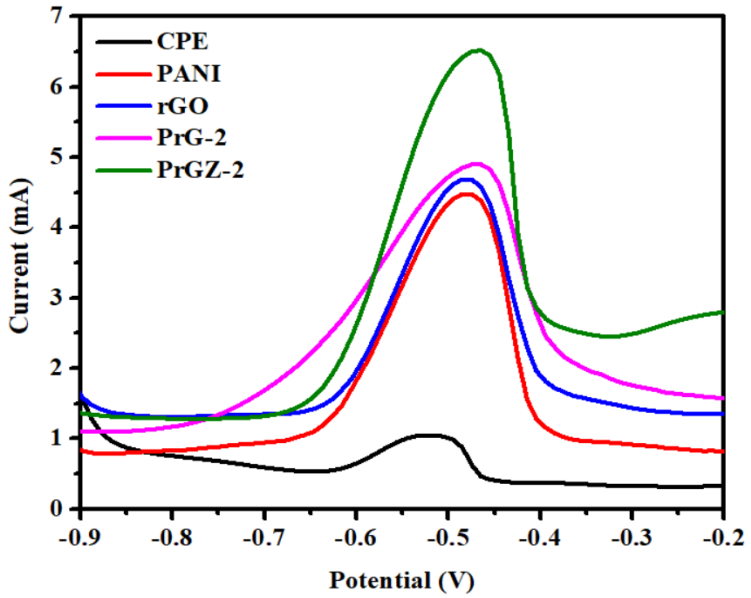

Figure: 20 Comparative DPASV of CPE, PANI, rGO, PrG-2, and PrGZ-2 at 5.5 µL addition of Pb^{2+}

Quantitative evaluation showed that the PrGZ-2 composite achieved a lower limit of detection of 0.3 µM and a limit of quantification (LOQ) of 1.16 µM, surpassing the performance of PrG-2, which displayed a LOD of 0.7 µM and LOQ of 2.3 µM. The relative standard deviation for PrGZ-2 was 2.13%, lower than PrG-2's 3.1%, reflecting better repeatability and precision. The sensitivity of PrGZ-2 (0.9464 mA μM^{-1}) was almost double that of PrG-2 (0.5164 mA μM^{-1}), confirming the enhanced electrochemical response achieved through ternary composite formation. Furthermore, with increasing Pb^{2+} concentration, the stripping peak shifted slightly towards a more positive potential and broadened, suggesting multilayer adsorption and increased electrochemical resistance. These results highlight the efficacy of the PrGZ-2 composite as a highly sensitive, reliable, and low-cost material for the electrochemical detection of heavy metal

ions, particularly Pb^{2+}, due to its optimized surface properties and improved electron transfer mechanisms.

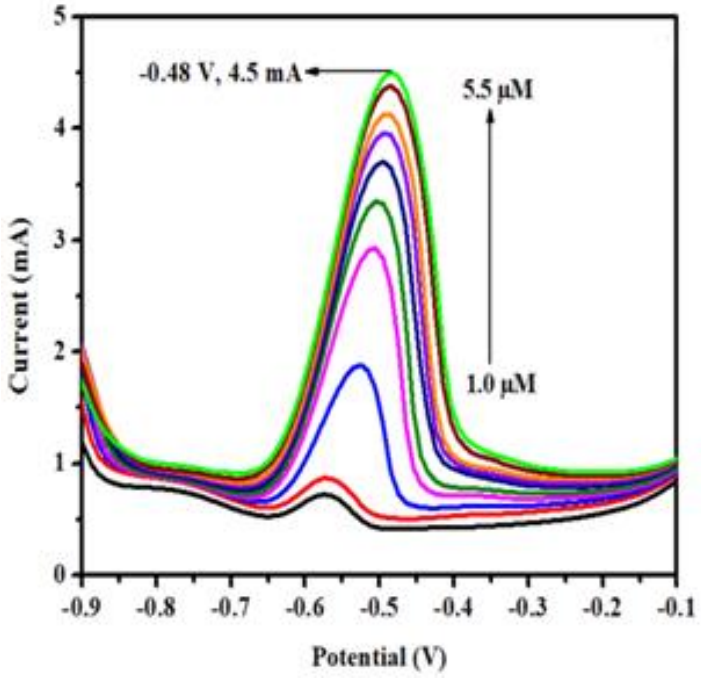

Figure: 21 DPASV of PrG-2

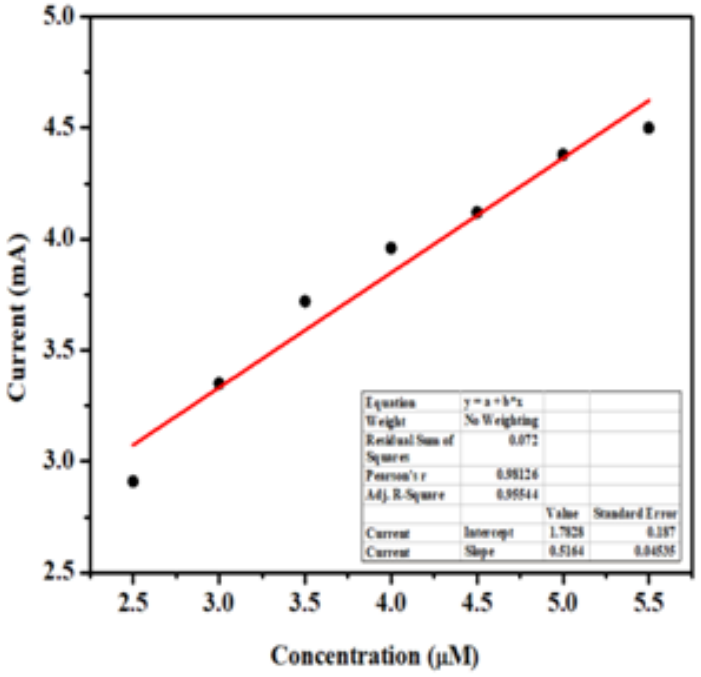

Figure: 22 Calibration curve of PrG-2

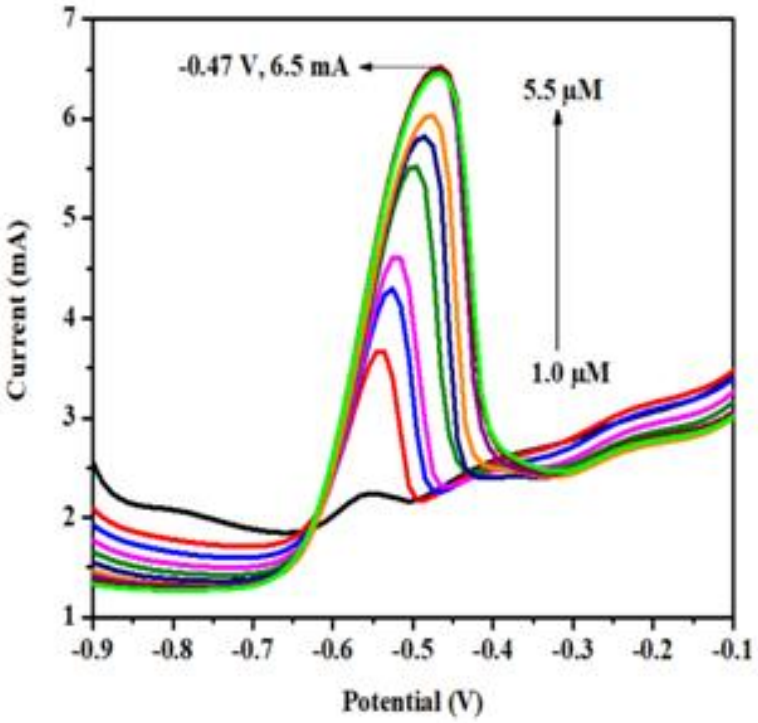

Figure: 23 DPASV of PrGZ-2

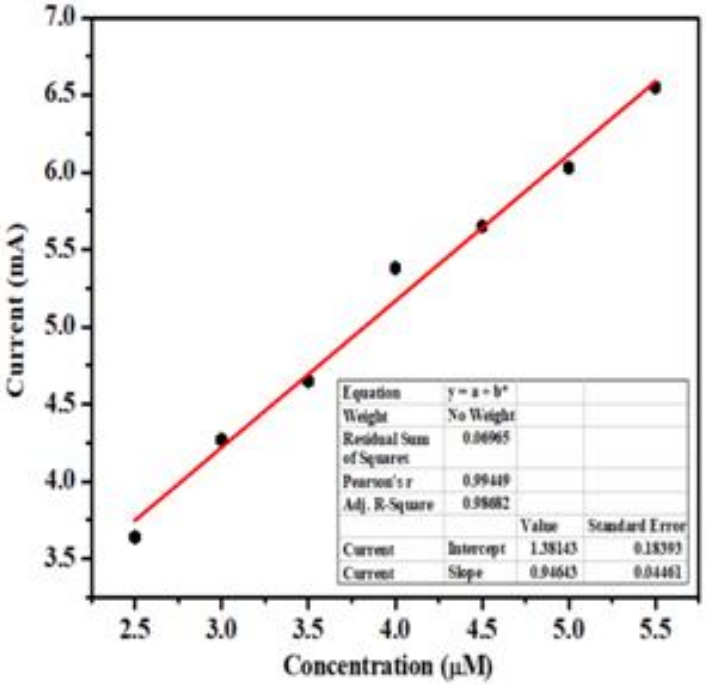

Figure: 24 Calibration curve of PrGZ-2

4.6.3.1.1 Selectivity, Reproducibility, and Stability of the PrGZ-2: The selectivity of the PrGZ-2 nanocomposite-modified electrode was evaluated in the presence of potentially interfering metal ions, specifically Cu^{2+} and Cd^{2+}, to determine its performance in complex sample matrices **(Rahman et al., 2025).** Owing to its enhanced surface area, strong adsorption capacity, and complexation ability, the PrGZ-2 composite exhibited excellent selectivity for Pb^{2+} ions (Patel et al., 2025). DPASV results revealed that the stripping peak current for Pb^{2+} ions remained relatively stable even when Cu^{2+} and Cd^{2+} ions were introduced into the system. Only minimal changes in the peak current and potential were observed, confirming the selective detection capability of the PrGZ-2 electrode **(Fig.25).** The minor variations in peak current are primarily attributed to the deposition of Pb^{2+} onto the electrode surface, which can partially hinder the diffusion of other metal ions. Furthermore, the peak potential for Pb^{2+} detection showed negligible shifts in the presence of interfering ions, indicating that the electrochemical behavior of Pb^{2+} on the PrGZ-2 electrode surface remains largely unaffected. This stability in peak position is a strong indicator of the electrode's selective detection capabilities **(Soto et al., 2025).** The slight broadening of the Pb^{2+} stripping peak can be attributed to the possible formation of intermetallic compounds such as Pb–Cu and Pb–Cd during the deposition step. While these intermetallic species may cause minor modifications in electrochemical behavior, they do not significantly interfere with the Pb^{2+} signal intensity, thereby ensuring reliable detection. The reproducibility of the PrGZ-2 electrode was assessed by fabricating five separate electrodes with identical PrGZ-2 composite modifications. DPASV measurements were then performed using a 5.5 μM Pb^{2+} solution in acetate buffer (pH 4.5). As shown in **Fig. 26** the stripping peak current at -0.47 V was consistently recorded across all five electrodes, demonstrating excellent reproducibility in electrode preparation and measurement conditions. Additionally, the stability of the PrGZ-2 electrode was monitored over several weeks. The current response, measured weekly under identical conditions, exhibited a slight decrease over time, indicating some degradation of electrochemical performance. However, this decline was relatively minor, and the electrode maintained good operational stability over the testing period. These results collectively confirm that the PrGZ-2 nanocomposite-modified electrode offers high selectivity, good reproducibility, and reasonable stability for the detection of Pb^{2+} ions in the presence of interfering metal ions. Its ability to maintain a consistent stripping peak for Pb^{2+}

without significant cross-sensitivity makes it a promising and reliable sensor platform for environmental monitoring and heavy metal detection applications.

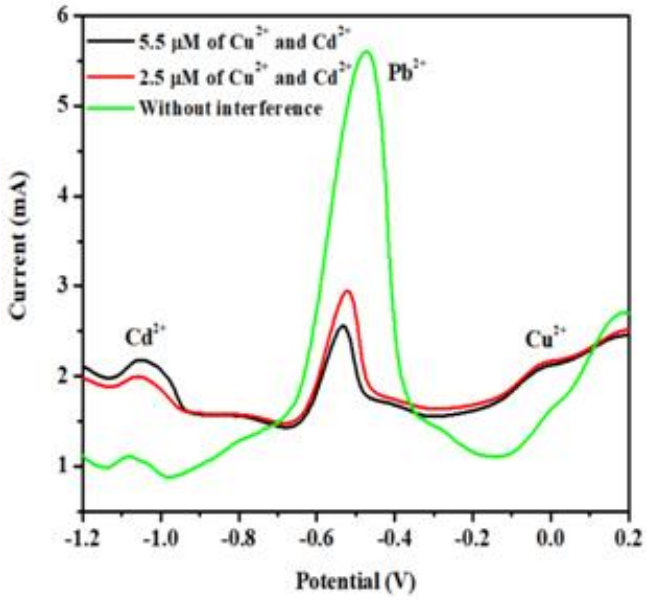

Figure: 25 DPASV results of PrGZ-2 composite without and with the interference of concentration of Cu^{2+} and Cd^{2+} ions

In **Fig. 25** the green curve (without interference) exhibits a well-defined and sharp Pb^{2+} stripping peak at approximately −0.55 V with the highest current response, indicating efficient electrochemical deposition and stripping of Pb^{2+} at the electrode surface. This confirms the intrinsic sensitivity of the electrode toward Pb^{2+} in the absence of competing ions. Upon the introduction of 2.5 µM Cu^{2+} and Cd^{2+} (red curve), the Pb^{2+} peak remains clearly distinguishable, though with a moderate reduction in peak current. This suggests partial competitive adsorption and deposition, yet the electrode maintains sufficient selectivity to resolve Pb^{2+} even in the presence of common interfering ions. At higher interference levels **(**5.5 µM Cu^{2+} and Cd^{2+}, black curve), a further decrease in Pb^{2+} peak current is observed; however, the peak position remains essentially unchanged. The preservation of peak potential indicates minimal peak overlap and good electrochemical resolution, while the reduction in current reflects increased competition for active sites rather than loss of electrode functionality. Distinct peaks corresponding to Cd^{2+} (≈ −1.0 V) and Cu^{2+} (≈ 0.0 V) are observed and remain well separated from the Pb^{2+} peak, confirming that simultaneous multi-metal detection is feasible and that signal interference is

limited. **Fig.25** demonstrates that the electrode possesses good anti-interference capability, maintaining identifiable and quantifiable Pb^{2+} signals even in the presence of higher concentrations of Cd^{2+} and Cu^{2+}. The observed current attenuation is systematic and predictable, indicating that the sensor is suitable for real-sample analysis where multiple heavy metal ions coexist**.**

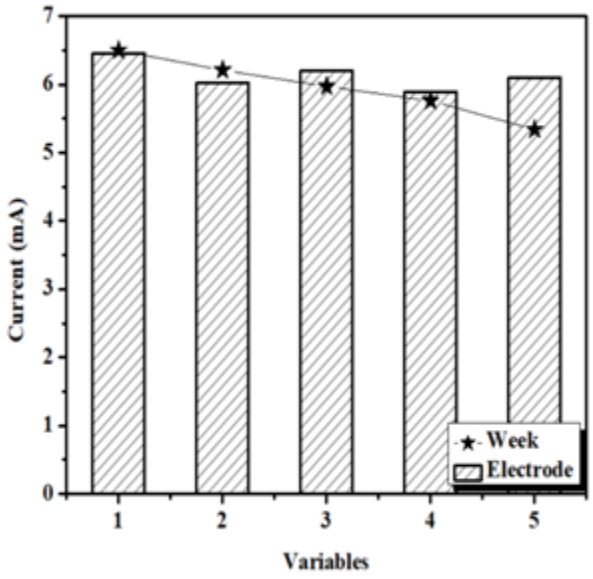

Figure: 26 Stability (with week), and reproducibility (with series of electrodes) of electrode materials against 5.5 µM Pb^{2+} concentration.

The electrode exhibits high operational durability, as evidenced by the minimal decrease in current response over repeated uses (Variables 1–5). The bar heights remain close to ~6.0–6.5 mA throughout the measurement sequence, indicating that the electrochemical activity of the electrode is largely retained even after multiple cycles. The slight downward trend observed in the star-marked weekly data suggests only marginal signal degradation with time**,** which is typical of surface-based electrochemical sensors due to minor surface fouling or gradual loss of active sites. However, this decrease is not abrupt or significant, implying that the electrode maintains structural and electrochemical integrity over extended operation. Importantly, the close agreement between the bar responses (electrode performance) and the star markers (weekly

measurements) demonstrates good reusability and reproducibility, with no drastic fluctuation in current output. This indicates that the electrode can be reused multiple times without the need for frequent regeneration or recalibration**. Fig.26** suggests that the electrode possesses excellent long-term operational stability, good reusability, and reliable performance over time, making it suitable for repeated and prolonged applications**,** such as continuous or periodic monitoring of analytes in environmental or electrochemical sensing applications.

4.6.3.1.2 Efficient Removal of Lead (Pb^{2+}) Ions via ternary nanocomposite (PrGZ-2): UV-visible spectroscopy was utilized to investigate the percentage removal of Pb^{2+} ions from an aqueous solution. In this procedure, a known quantity (2 mg) of the PrGZ-2 ternary nanocomposite was introduced into 30 mL of a lead solution with an initial concentration of 100 ppm. The mixture was subjected to sonication for 10 minutes to ensure proper dispersion, followed by standing for 15 minutes to allow the formation of a stable suspension. The influence of contact time between the adsorbent and the Pb^{2+} ion solution was then examined at different intervals (1, 4, and 24 hours) using UV-visible spectrophotometry (as shown in **Fig. 27**). The percentage removal efficiency of Pb^{2+} ions by the PrGZ-2 composite was subsequently determined and tabulated, using a standard calculation formula **(Girija., et al., 2021).**

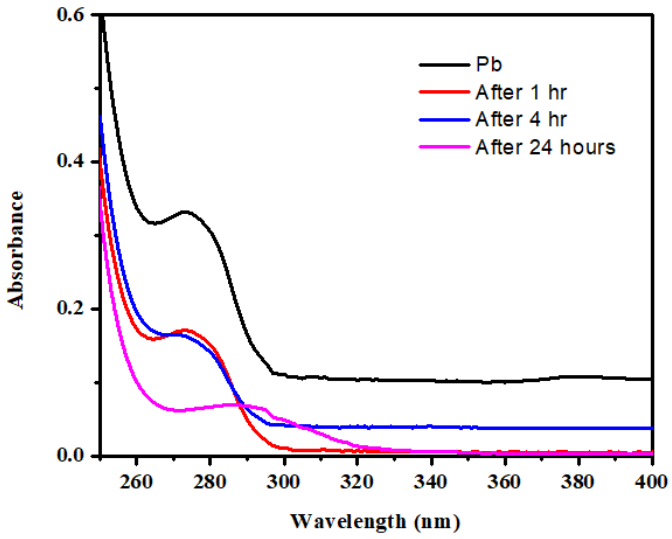

Figure: 27 UV-Vis spectra representing the detection and removal of Pb^{2+} ions in aqueous Solution

The removal efficiency is typically calculated using the following formula:

Removal Efficiency (RE) (%)=C_0/ C_0−C_t× 100

Where:

C_0= Initial concentration of Pb^{2+} ions

C_t= Concentration of Pb^{2+} ions at time **t**

Table: 7 Time Dependent Removal Efficiency of Pb^{2+} Ions Using the PrGZ-2 Composite

Time	Initial Concentration (C_0) (ppm)	Final Concentration (C_t) (ppm)	Removal Efficiency (%)
1 hour	0.32	0.17	46.87
4 hours	0.32	0.16	50.00
24hours	0.32	0.05	84.37

4.6.3.2 DPASVof PrGZ-2 for detection of Cd^{2+} ions: DPASV was employed to investigate the electrochemical sensing performance of the synthesized PrG-2 and PrGZ-2 nanocomposites towards Cd^{2+} **(Wang, 2006).** This sensitive technique involves the preconcentration of metal ions onto the surface of a working electrode at a fixed potential, followed by an anodic stripping step where the resulting current is directly related to the concentration of the analyte **(Honeychurch and Hart, 2003)**. A buffer solution consisting of 0.1 M sodium acetate and 0.07 M acetic acid at pH 4.5 was used as the supporting electrolyte, with cadmium acetate solutions prepared in the concentration range of 1.0 μM to 5.5 μM.

The working electrode was a carbon paste electrode modified with the nanocomposite materials, while an Ag/AgCl electrode served as the reference and a platinum wire was used as the counter electrode **(Honeychurch and Hart, 2003; Zawodzinski et al., 1995).** DPASV measurements were conducted within a potential range of -1.0 V to 0.1 V, using a modulation amplitude of 0.1 V, a modulation time of 0.05 s, and a scan rate of 0.01 V/s, conditions optimized for the sensitive detection of Cd^{2+} ions **(Wang, 2006).**

The comparative DPASV results revealed that the PrGZ-2 composite demonstrated the highest stripping peak current of 2.83 mA at -0.5 V, significantly outperforming PANI (0.81 mA), rGO

(1.14 mA), and PrG-2 (1.66 mA). This substantial improvement is attributed to the synergistic interaction between rGO, which provides a large surface area and high electrical conductivity **(Dreyer et al., 2010)**; PANI, contributing pseudo-capacitive behavior and redox activity **(Stejskal and Gilbert, 2002)**; and ZnO nanoparticles, which enhance electron transfer kinetics and structural stability **(Sivakumar et al., 2017).**

The improved electrochemical characteristics of the PrGZ-2 nanocomposite, including greater electroactive surface area and superior electron transfer kinetics, make it a highly effective platform for Cd^{2+} detection. Both PrG-2 and PrGZ-2 displayed sharp, well-defined stripping peaks that increased linearly with concentration from 1.0 μM to 5.5 μM, with PrGZ-2 exhibiting a more pronounced and consistent response. The calibration curve for PrGZ-2 demonstrated excellent linearity with a correlation coefficient (R^2) of 0.996, compared to 0.979 for PrG-2, indicating improved accuracy and reliability across the tested concentration range **(Martins et al., 2020).**

The limit of detection (LOD) and limit of quantification (LOQ) were determined using the following equations:

$$LOD = (3.3 \times SD) / S$$
$$LOQ = (10 \times SD) / S$$

Where, SD represents the standard deviation of the blank measurements, and S is the slope of the calibration curve. Based on these calculations, the LOD and LOQ for Cd^{2+} ions using the PrGZ-2 composite were found to be 0.22 μM and 0.005μM, respectively, demonstrating its superior nature compared to PrG-2.

Table: 8 Summarized DPASV results of binary (PrG-2) and ternary composites (PrGZ-2) for Cd^{2+}

Composite	R^2	LOD (μM)	LOQ (μM)	RSD (%)	Sensitivity ($mA\ \mu M^{-1}$)
PrG-2	0.979	0.22	0.69	8.19	**0.1214**
PrGZ-2	0.996	0.005	0.016	0.079	**0.2992**

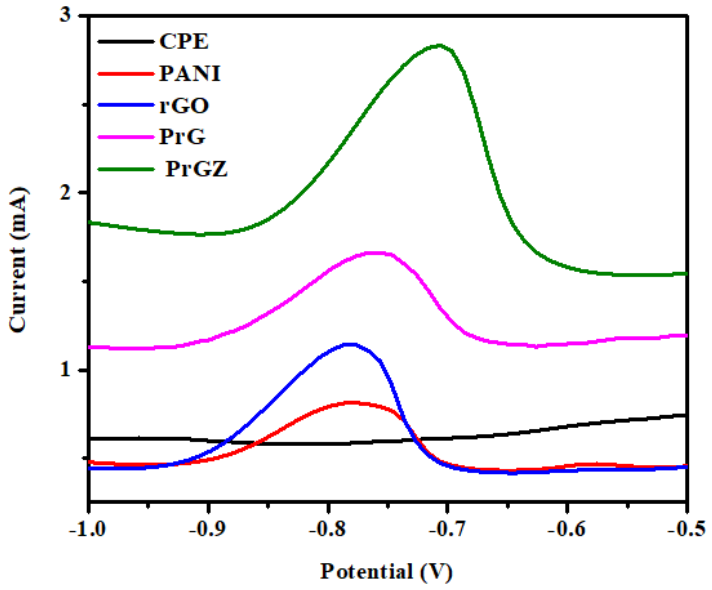

Figure: 28 Comparative DPASV of CPE, PANI, rGO, PrG-2, and PrGZ-2 at 5.5 µL addition of Cd^{2+}

Quantitative evaluation showed that the PrGZ-2 composite achieved a lower LOD of 0.005µM and a LOQ of 0.016 µM, surpassing the performance of PrG-2, which displayed a LOD of 0.22 µM and LOQ of 0.69µM. RSD for PrGZ-2 was 0.079%, lower than PrG-2's 8.19%, reflecting better repeatability and precision. The sensitivity of PrGZ-2 (0.2992 mA μM^{-1}) was almost double that of PrG-2 (0.1214 mA μM^{-1}), confirming the enhanced electrochemical response achieved through ternary composite formation. Furthermore, with increasing Cd^{2+} concentration, the stripping peak shifted slightly towards a more positive potential and broadened, suggesting multilayer adsorption and increased electrochemical resistance. These results highlight the efficacy of the PrGZ-2 composite as a highly sensitive, reliable, and low-cost material for the electrochemical detection of heavy metal ions, particularly Cd^{2+}, due to its optimized surface properties and improved electron transfer mechanisms.

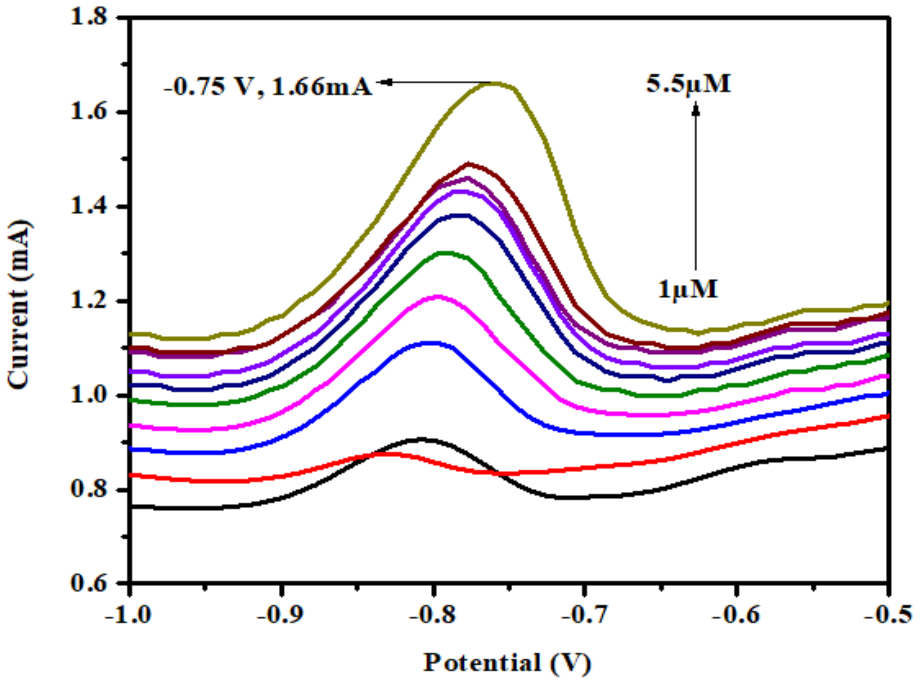

Figure: 29 DPASV of PrG-2

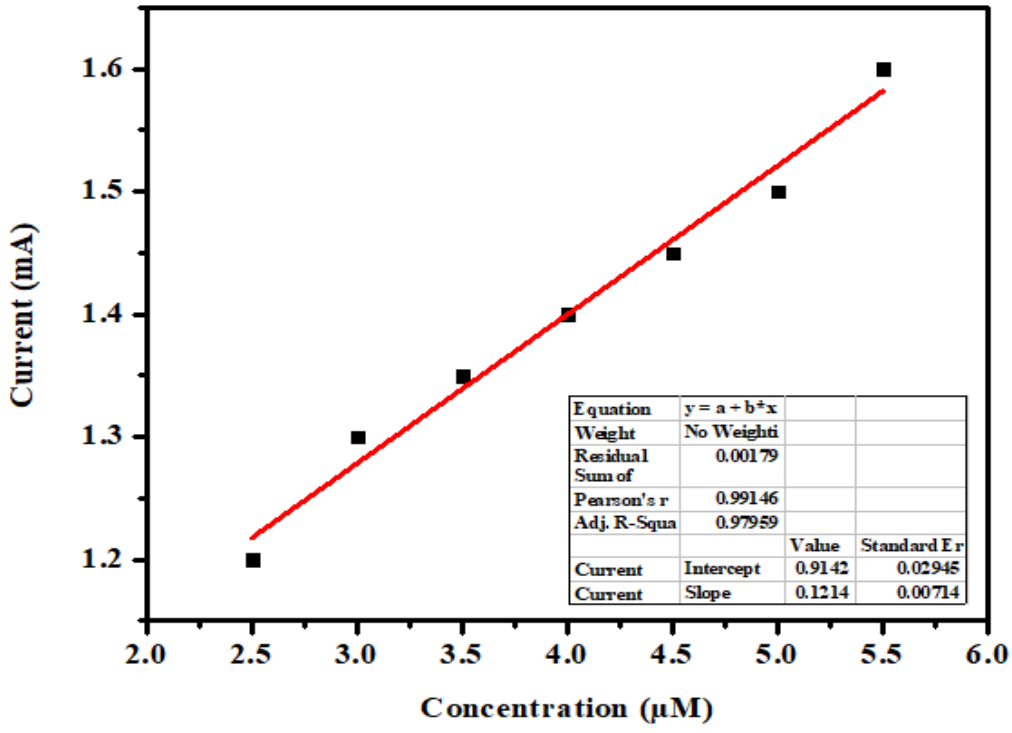

Figure: 30 Calibration curve of PrG-2

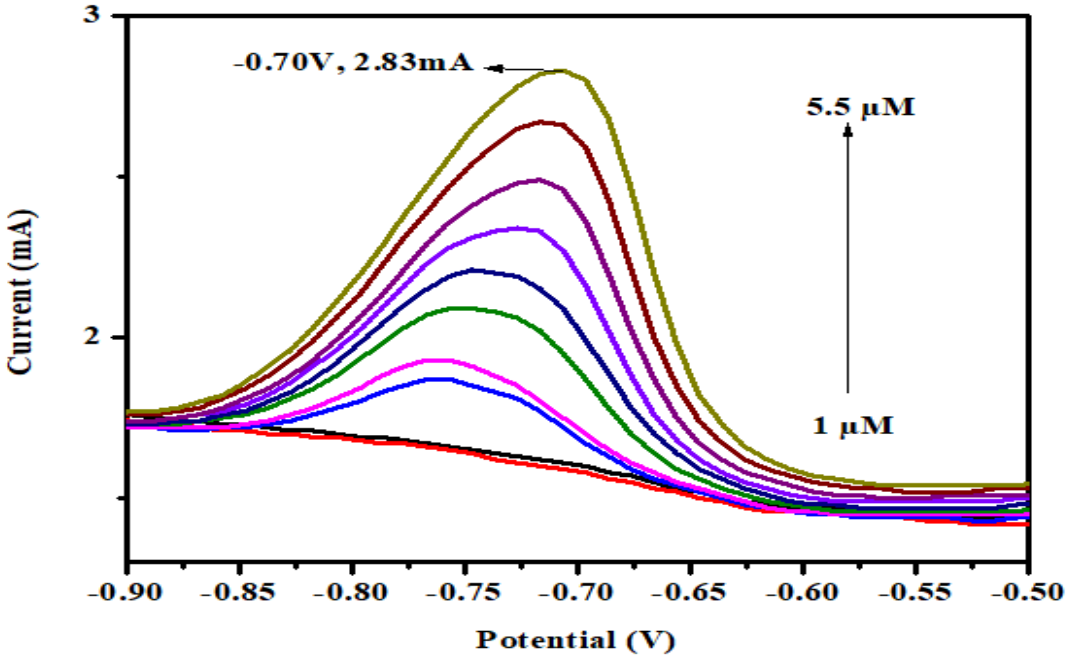

Figure:31 DPASV of PrGZ-2

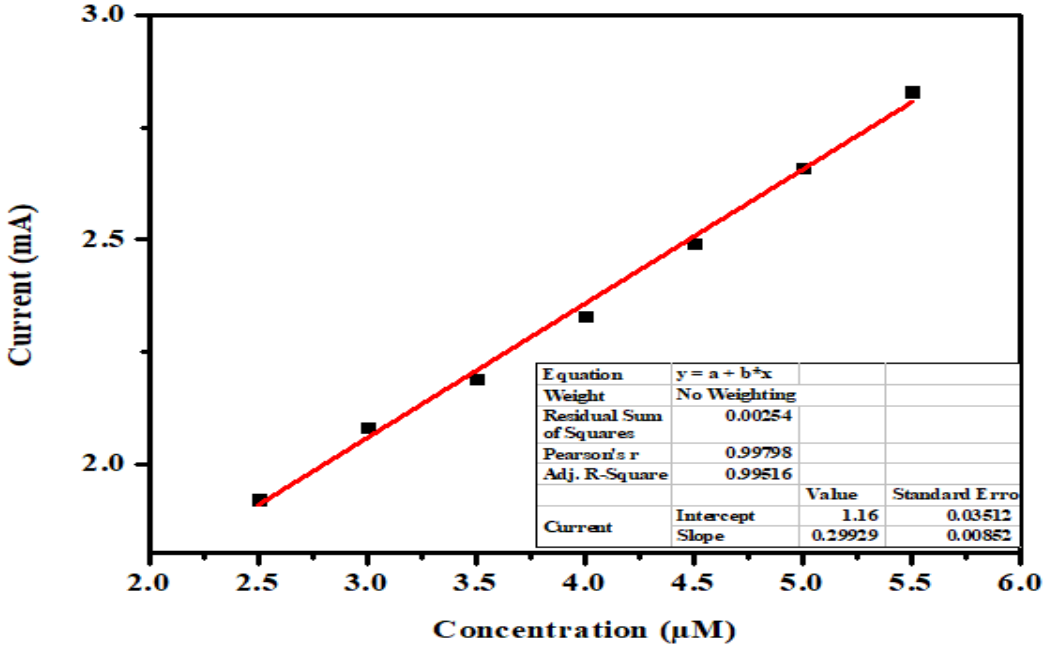

Figure: 32 Calibration curve of PrGZ-2

4.6.3.2.1 Selectivity, Reproducibility, and Stability of the PrGZ-2: The selectivity of the PrGZ-2 nanocomposite-modified electrode was evaluated in the presence of potentially interfering metal ions, specifically Cu^{2+} and Pb^{2+}, to determine its performance in complex sample matrices **(Rahman et al., 2025).** Owing to its enhanced surface area, strong adsorption capacity, and complexation ability, the PrGZ-2 composite exhibited excellent selectivity for Cd^{2+} ions (Patel et al., 2025). DPASV results revealed that the stripping peak current for Cd^{2+} ions remained relatively stable even when Cu^{2+} and Pb^{2+} ions were introduced into the system. Only minimal changes in the peak current and potential were observed, confirming the selective detection capability of the PrGZ-2 electrode **(Fig.33).** The minor variations in peak current are primarily attributed to the deposition of Cd^{2+} onto the electrode surface, which can partially hinder the diffusion of other metal ions. Furthermore, the peak potential for Cd^{2+} detection showed negligible shifts in the presence of interfering ions, indicating that the electrochemical behavior of Cd^{2+} on the PrGZ-2 electrode surface remains largely unaffected. This stability in peak position is a strong indicator of the electrode's selective detection capabilities **(Soto et al., 2025).** The slight broadening of the Cd^{2+} stripping peak can be attributed to the possible formation of intermetallic compounds such as Cd–Cu and Pb–Cd during the deposition step. While these intermetallic species may cause minor modifications in electrochemical behavior, they do not significantly interfere with the Cd^{2+} signal intensity, thereby ensuring reliable detection. The reproducibility of the PrGZ-2 electrode was assessed by fabricating five separate electrodes with identical PrGZ-2 composite modifications. DPASV measurements were then performed using a 5.5 μM Cd^{2+} solution in acetate buffer (pH 4.5). As shown in **Fig. 34** the stripping peak current at -0.7 V was consistently recorded across all five electrodes, demonstrating excellent reproducibility in electrode preparation and measurement conditions. Additionally, the stability of the PrGZ-2 electrode was monitored over several weeks. The current response, measured weekly under identical conditions, exhibited a slight decrease over time, indicating some degradation of electrochemical performance. However, this decline was relatively minor, and the electrode maintained good operational stability over the testing period. These results collectively confirm that the PrGZ-2 nanocomposite-modified electrode offers high selectivity, good reproducibility, and reasonable stability for the detection of Cd^{2+} ions in the presence of interfering metal ions. Its ability to maintain a consistent stripping peak for Cd^{2+}

without significant cross-sensitivity makes it a promising and reliable sensor platform for environmental monitoring and heavy metal detection applications.

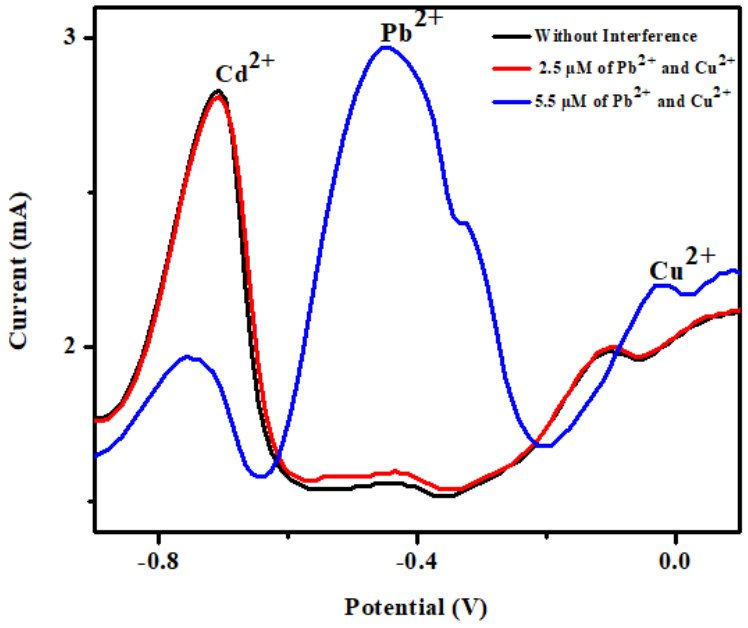

Figure: 33 DPASV results of PrGZ-2 composite without and with the interference of concentration of Cu^{2+} and Pb^{2+} ions

In **Fig.33** the black curve (without interference) shows well-resolved and distinct stripping peaks for Cd^{2+} (≈ −0.75 V), Pb^{2+} (≈ −0.45 V), and Cu^{2+} (≈ 0.0 V), confirming the intrinsic capability of the electrode to simultaneously detect multiple heavy metal ions with good peak separation. Upon the addition of 2.5 µM co-existing ions (red curve), the stripping peaks for Cd^{2+}, Pb^{2+}, and Cu^{2+} remain clearly identifiable, with only a slight reduction in peak current. This indicates limited competitive adsorption and suggests that the electrode surface provides sufficient active sites to accommodate multiple ions without significant signal overlap. At a higher interference level of 5.5 µM co-existing ions (blue curve), the Pb^{2+} peak intensity increases markedly, while Cd^{2+} and Cu^{2+} peaks show moderate changes in current magnitude. The enhancement of the Pb^{2+} signal may be attributed to co-deposition or synergistic effects, such as alloy formation or facilitated nucleation in the presence of Cu^{2+}, which is commonly observed in stripping voltammetry. Importantly, the peak potentials remain largely unchanged, confirming good electrochemical resolution and minimal peak shifting.

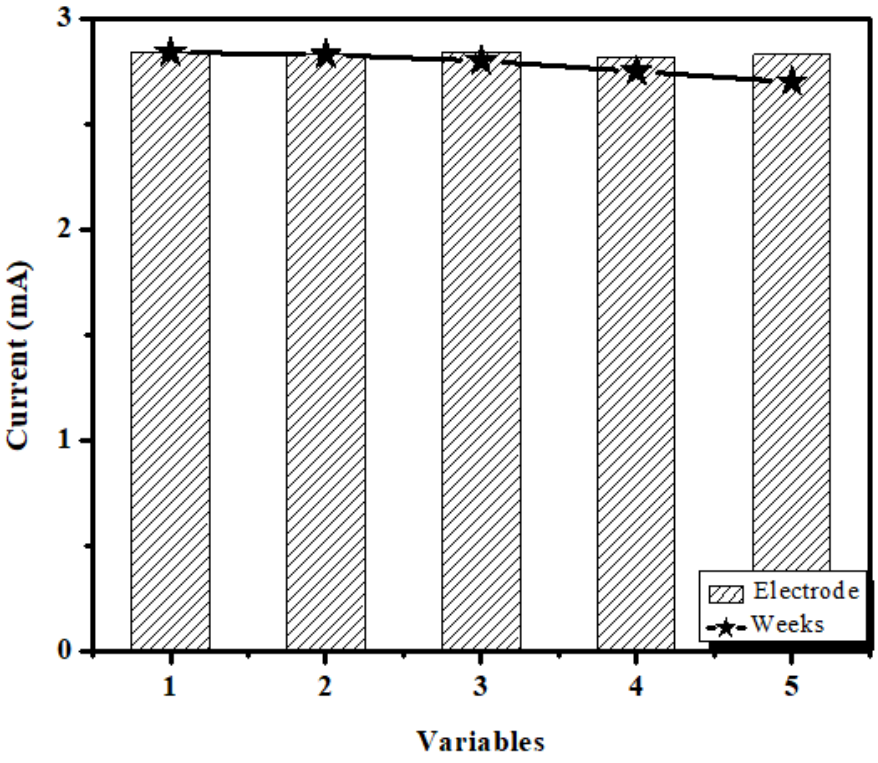

Figure: 34 Stability (with week), and reproducibility (with series of electrodes) of electrode materials against 5.5 µMCd^{2+} concentration.

The electrode demonstrates excellent long-term durability, as evidenced by the highly stable current response (~2.8–2.9 mA) across Variables 1 to 5 as shown in Fig. 34. The electrode bars show negligible variation, indicating that the electroactive surface remains structurally and electrochemically stable during repeated usage. The star-marked weekly measurements reveal only a very slight and gradual decline in current, corresponding to an estimated current loss of less than ~3–4% over the monitoring period. Such minimal degradation suggests that the electrode experiences only minor surface aging or adsorption effects rather than irreversible material degradation. The close correspondence between the electrode response and weekly data confirms excellent reusability and reproducibility, as the sensor maintains consistent performance without the need for regeneration or recalibration between cycles. Overall, the electrode retains more than ~96–97% of its initial current response, clearly demonstrating robust operational stability, high reusability, and suitability for prolonged and repeated electrochemical sensing applications, particularly for environmental monitoring.

4.6.3.2.2 Efficient Removal of Cadmium (Cd^{2+}) Ions via ternary nanocomposite (PrGZ-2): UV-visible spectroscopy was utilized to investigate the percentage removal of Cd^{2+} ions from an aqueous solution. In this procedure, a known quantity (2 mg) of the PrGZ-2 ternary nanocomposite was introduced into 30 mL of a cadmium solution. The mixture was subjected to sonication for 10 minutes to ensure proper dispersion, followed by standing for 15 minutes to allow the formation of a stable suspension. The influence of contact time between the adsorbent and the Cd^{2+} ion solution was then examined at different intervals (1, 4, and 24 hours) using UV-visible spectrophotometry (as shown in **Fig. 35**). The percentage removal efficiency of Cd^{2+} ions by the PrGZ-2 composite was subsequently determined and tabulated, using a standard calculation formula **(Girija., et al., 2021).**

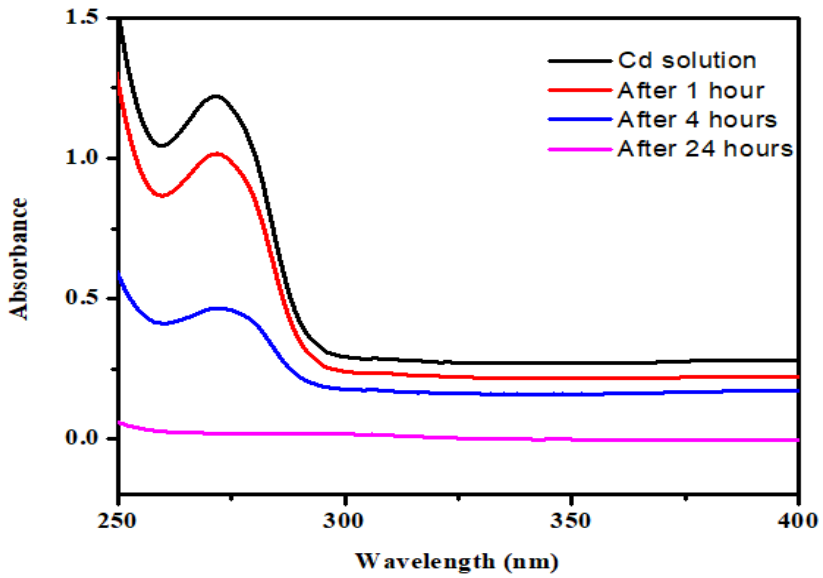

Figure: 35 UV-Vis spectra representing the detection and removal of Cd^{2+} ions inaqueous Solution

The removal efficiency is typically calculated using the following formula:

Removal Efficiency (RE) (%) = $C_0 / C_0 - C_t \times 100$

Where:

C_0= Initial concentration of Cd^{2+} ions

C_t= Concentration of Cd^{2+} ions at time **t**

Table: 9 Time Dependent Removal Efficiency of Cd^{2+} Ions Using the PrGZ-2 Composite

Time	Initial Concentration (C_0) (ppm)	Final Concentration (C_t) (ppm)	Removal Efficiency (%)
1 hour	1.2	1	16.7
4 hours	1.2	0.4	62.5
24 hours	1.2	0.05	95.8

4.6.3.3 DPASVof PrGM-2 for detection of Pb^{2+} ions: DPASV was employed to investigate the electrochemical detection capabilities of the prepared binary (PrG-2) and ternary (PrGM-2) nanocomposites towards Pb^{2+} ions **(Rahman et al., 2025).** This technique operates by pre-depositing metal ions onto the electrode surface at a constant potential, followed by a stripping step where the current generated is directly proportional to the analyte concentration **(Patel et al., 2025).** A 0.1 M sodium acetate and 0.07 M acetic acid buffer at pH 4.5 was used as the supporting electrolyte, with lead acetate solutions added in the concentration range of 1.0 µM to 5.5 µM. The working electrode consisted of a CPE modified with the nanocomposite material, while an Ag/AgCl electrode served as the reference and a platinum wire as the counter electrode. The DPASV measurements were performed in a potential window from -1.0 V to 0.1 V, with a modulation amplitude of 0.1 V, modulation time of 0.05 s, and a slow scan rate of 0.01 V/s, optimizing conditions for the sensitive detection of Pb^{2+} ions **(Soto et al., 2025).**The comparative DPASV results revealed that the PrGM-2 composite demonstrated the highest stripping peak current of 4.45 mA at -0.5 V, significantly outperforming CPE (1.08 mA), PANI (4.46 mA), rGO (4.68 mA), and PrG-2 (4.88 mA). This substantial improvement is attributed to the synergistic interaction between rGO, which provides a large surface area and high electrical conductivity; PANI, contributing pseudo-capacitive behavior and redox activity; and MnO_2 nanoparticles, which enhance electron transfer kinetics and structural stability. The increased electroactive surface area and improved electron transfer properties in the PrGM-2 composite make it highly effective for Pb^{2+} detection. Additionally, both PrG-2 and PrGM-2 exhibited well-defined,

concentration-dependent stripping peaks from 1.0 µM to 5.5 µM. The calibration curve for PrGM-2 demonstrated a higher linear correlation (R^2 = 0.994) compared to PrG-2 (R^2 = 0.981), indicating better linearity and accuracy across the tested concentration range.

The LOD and LOQ are calculated using the formula below:

$$LOD = \frac{3.3 \times SD}{S}$$

$$LOQ = \frac{10 \times SD}{S}$$

Where, SD is the standard deviation of the blank solution, and S is the slope of the calibration curve. The LOD and LOQ obtained for Pb^{2+} ions are 0.3 µM and 1.16µM,respectively, for PrGZ-2 composite.

Table: 10 Summarized DPASV results of binary (PrG) and ternary composites (PrGM)

Composite	R^2	LOD (µM)	LOQ (µM)	RSD (%)	Sensitivity (mA μM^{-1})
PrG-2	0.981	0.7	2.3	3.1	**0.5164**
PrGM	0.994	0.01	0.04	0.27	**0.2257**

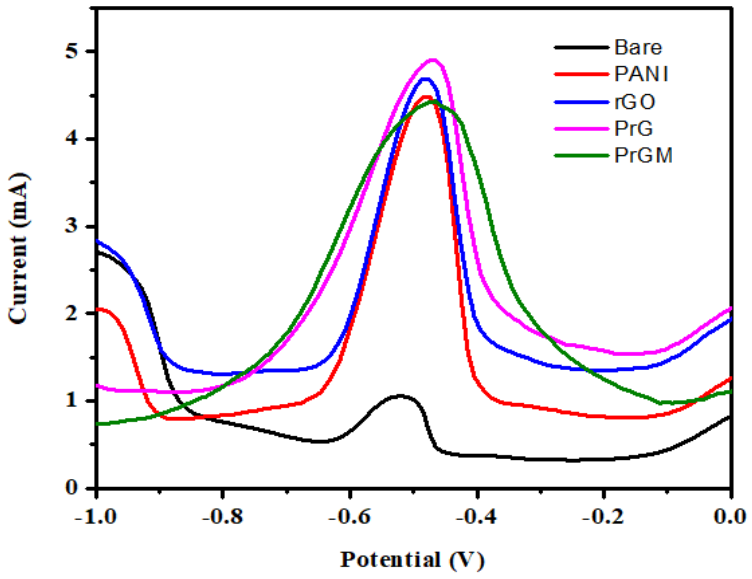

Figure: 36 Comparative DPASV of CPE, PANI, rGO, PrG-2, and PrGM-2 at 5.5 µL addition of Pb^{2+}

Quantitative evaluation showed that the PrGM-2 composite achieved a lower LOD of 0.01µM and a LOQ of 0.04µM, surpassing the performance of PrG-2, which displayed a LOD of 0.7 µM and LOQ of 2.3 µM. RSD for PrGM-2 was 0.27%, lower than PrG-2's 3.1%, reflecting better repeatability and precision. The sensitivity of PrGM-2 (0.2257 mA μM^{-1}) was lower than that of PrG-2 (0.5164 mA μM^{-1}) due to MnO_2 might introduce barriers to efficient electron transfer between PANI and rGO. Furthermore, with increasing Pb^{2+} concentration, the stripping peak shifted slightly towards a more positive potential and broadened, suggesting multilayer adsorption and increased electrochemical resistance.PrGM-2 is a better choice due to its cleaner signal, electrochemicalreversibility**,** lower background current and cleaner signal.

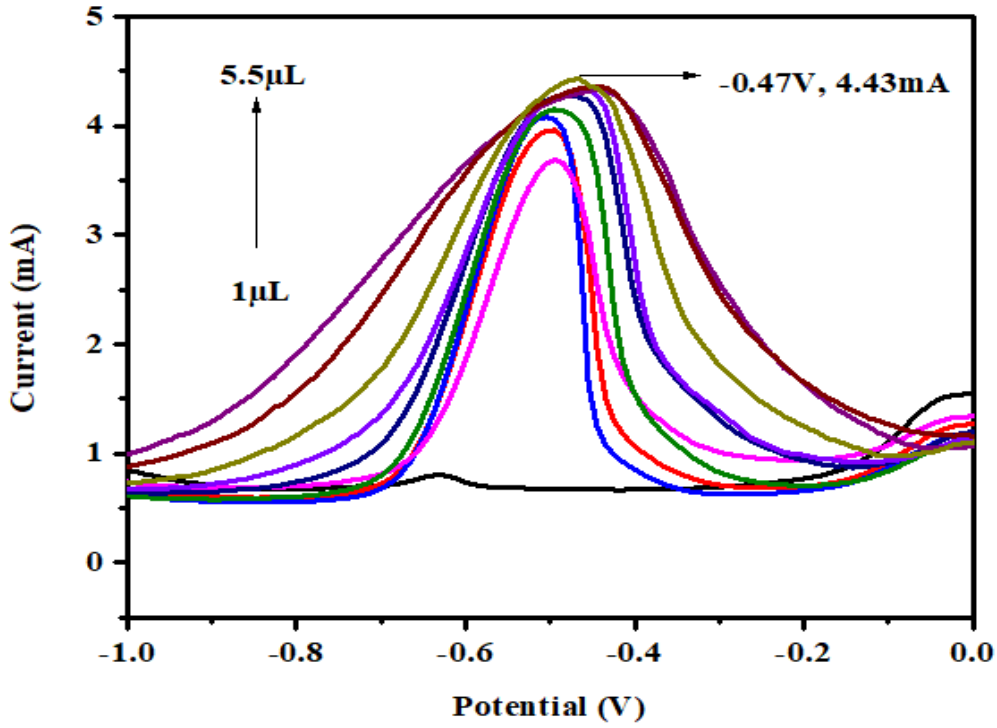

Figure: 37 DPASV of PrGM-2

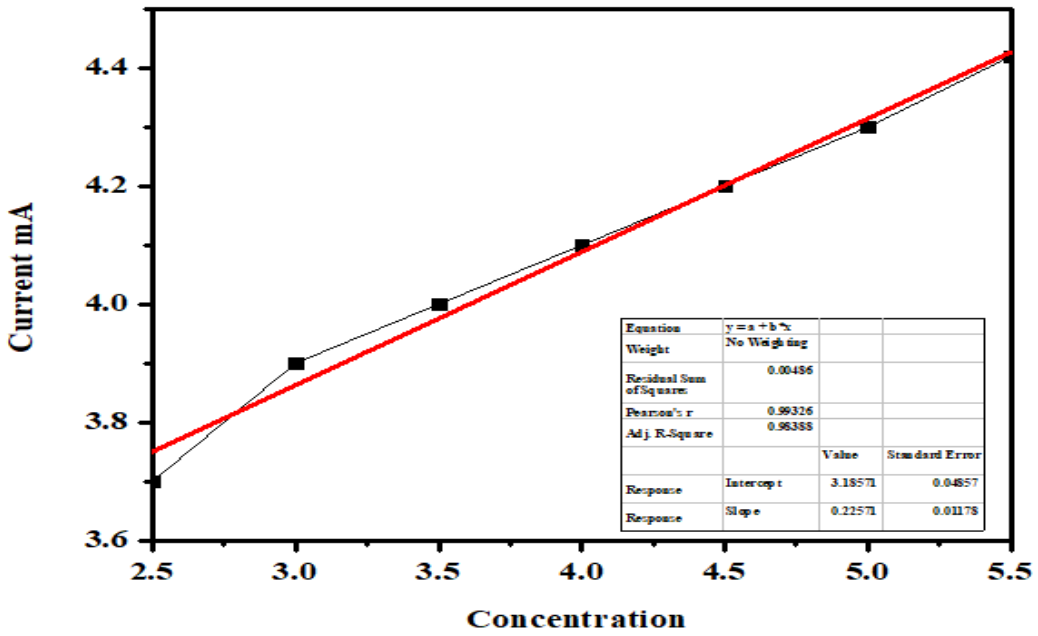

Figure: 38 Calibration curve of PrGM-2

4.6.3.3.1 Selectivity, Reproducibility, and Stability of the PrGM-2 Electrode:

The selectivity of the PrGM-2 nanocomposite-modified electrode was evaluated in the presence of potentially interfering metal ions, specifically Cu^{2+} and Cd^{2+}, to determine its performance in complex sample matrices **(Rahman et al., 2025).** Owing to its enhanced surface area, strong adsorption capacity, and complexation ability, the PrGM-2 composite exhibited excellent selectivity for Pb^{2+} ions **(Patel et al., 2025).** DPASV results revealed that the stripping peak current for Pb^{2+} ions remained relatively stable even when Cu^{2+} and Cd^{2+} ions were introduced into the system. Only minimal changes in the peak current and potential were observed, confirming the selective detection capability of the PrGM-2 electrode. The minor variations in peak current are primarily attributed to the deposition of Pb^{2+} onto the electrode surface, which can partially hinder the diffusion of other metal ions. Furthermore, the peak potential for Pb^{2+} detection showed negligible shifts in the presence of interfering ions, indicating that the electrochemical behavior of Pb^{2+} on the PrGM-2 electrode surface remains largely unaffected. This stability in peak position is a strong indicator of the electrode's selective detection capabilities **(Soto et al., 2025).** The slight broadening of the Pb^{2+} stripping peak can be attributed to the possible formation of intermetallic compounds such as Pb–Cu and Pb–Cd during the

deposition step. While these intermetallic species may cause minor modifications in electrochemical behavior, they do not significantly interfere with the Pb^{2+} signal intensity, thereby ensuring reliable detection. The reproducibility of the PrGM-2 electrode was assessed by fabricating five separate electrodes with identical PrGM-2 composite modifications. DPASV measurements were then performed using a 5.5 µM Pb^{2+} solution in acetate buffer (pH 4.5). As shown in **Fig. 40**, the stripping peak current at -0.47 V was consistently recorded across all five electrodes, demonstrating excellent reproducibility in electrode preparation and measurement conditions. Additionally, the stability of the PrGM-2 electrode was monitored over several weeks. The current response, measured weekly under identical conditions, exhibited a slight decrease over time, indicating some degradation of electrochemical performance. However, this decline was relatively minor, and the electrode maintained good operational stability over the testing period. These results collectively confirm that the PrGM-2 nanocomposite-modified electrode offers high selectivity, good reproducibility, and reasonable stability for the detection of Pb^{2+} ions in the presence of interfering metal ions. Its ability to maintain a consistent stripping peak for Pb^{2+} without significant cross-sensitivity makes it a promising and reliable sensor platform for environmental monitoring and heavy metal detection applications **(Rahman et al., 2025).**

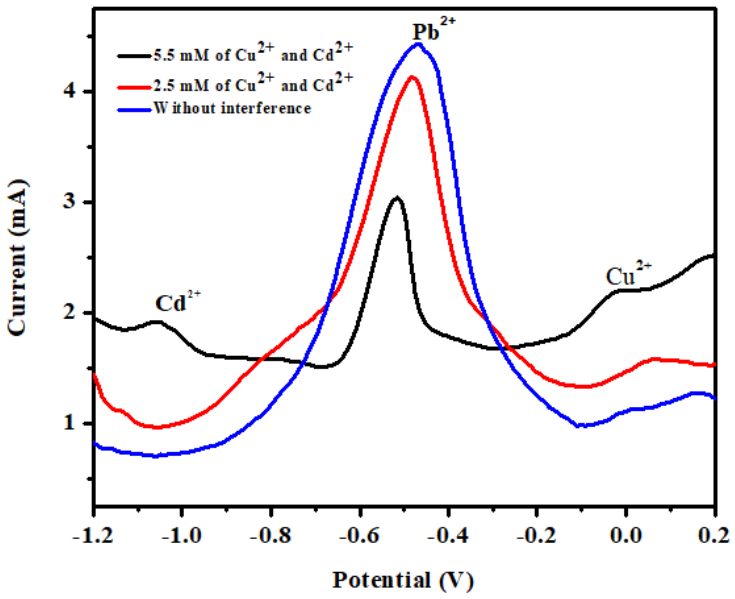

Figure: 39 DPASV results of PrGM-2 composite without and with the interference of concentration of Cu^{2+} and Cd^{2+} ions against 5.5 µMPb^{2+} concentration.

In **Fig. 39** the blue curve (without interference) exhibits a sharp and intense Pb^{2+} stripping peak at approximately −0.55 V, indicating high sensitivity of the electrode toward Pb^{2+} in the absence of competing ions. Minor background features corresponding to Cd^{2+} and Cu^{2+} are also distinguishable at around −1.0 V and 0.0 V, respectively. With the introduction of 2.5 mM Cu^{2+} and Cd^{2+} (red curve), the Pb^{2+} peak remains clearly visible, although a moderate decrease in peak current is observed. This reduction suggests competitive adsorption and partial occupation of active sites by co-existing ions; however, the retention of peak position indicates that the electrode maintains good selectivity for Pb^{2+}. At a higher interference level of 5.5 mM Cu^{2+} and Cd^{2+} (black curve), a further suppression of the Pb^{2+} peak current is evident, accompanied by a slight broadening of the peak. This behavior is attributed to enhanced competition during the deposition step and possible intermetallic interactions, which reduce the effective accumulation of Pb^{2+} on the electrode surface. Despite this, the Pb^{2+} signal remains well resolved and distinguishable. Importantly, the characteristic peaks of Cd^{2+} (≈ −1.0 V) and Cu^{2+} (≈ 0.0 V) remain separated from the Pb^{2+} peak under all conditions, demonstrating minimal peak overlap and good electrochemical resolution**.**

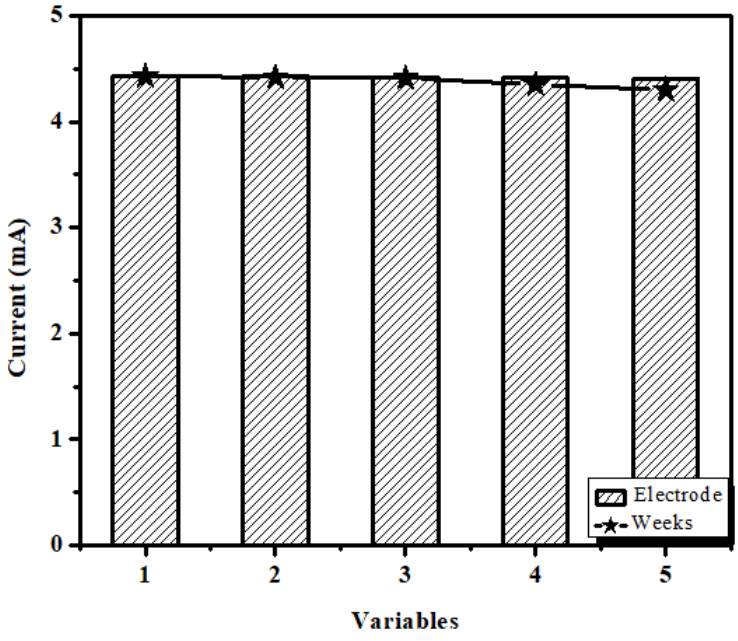

Figure: 40 PrGM-2 Stability (with week), and reproducibility (with series of electrodes) of electrode materials against 5.5 µMPb^{2+} concentration.

The electrode exhibits excellent long-term durability, as indicated by the nearly constant current response (~4.3–4.5 mA) across Variables 1 to 5. The bar heights show negligible variation, suggesting that the electroactive surface remains stable during repeated usage. The star-marked weekly measurements closely overlap with the electrode bars and show only a very slight downward trend, corresponding to a minimal loss in current response (≈2–4%) over time. Such a small decrease is commonly attributed to minor surface fouling or gradual relaxation of active sites rather than structural degradation. The close agreement between successive measurements confirms high reusability and reproducibility, indicating that the electrode can be repeatedly used without significant loss of performance or the need for frequent regeneration. **Fig. 40** demonstrates that the electrode maintains more than ~95% of its initial current response after multiple cycles/weeks, confirming robust operational stability, excellent reusability, and strong resistance to performance degradation. This behavior is highly desirable for long-term and field-deployable electrochemical sensing applications, such as continuous monitoring of heavy metal ions.

4.6.3.3.2 Efficient Removal of Lead (Pb^{2+}) Ions via ternary nanocomposite (PrGM-2): UV-visible spectroscopy was utilized to investigate the percentage removal of Pb^{2+} ions from an aqueous solution. In this procedure, a known quantity (2 mg) of the PrGM-2 ternary nanocomposite was introduced into 30 mL of a lead solution with an initial concentration of 100 ppm. The mixture was subjected to sonication for 10 minutes to ensure proper dispersion, followed by standing for 15 minutes to allow the formation of a stable suspension. The influence of contact time between the adsorbent and the Pb^{2+} ion solution was then examined at different intervals (1, 4, and 24 hours) using UV-visible spectrophotometry (as shown in **Fig. 41**). The percentage removal efficiency of Pb^{2+} ions by the PrGM-2 composite was subsequently determined and tabulated, using a standard calculation formula. **(Shankar, et al., 2021).**

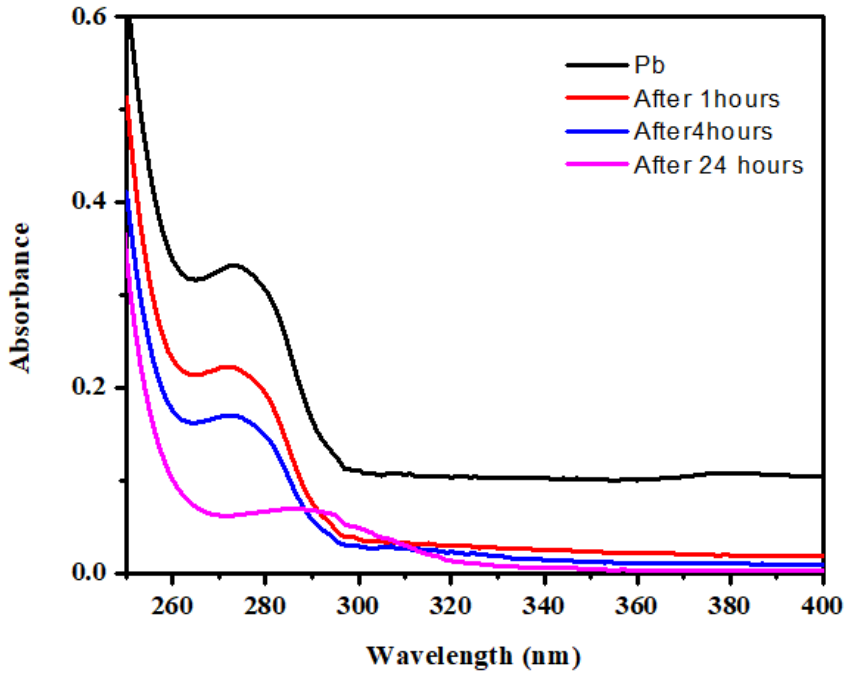

Figure: 41 UV-Vis spectra representing the detection and removal of Pb^{2+} ions inaqueous solution

Table: 11Time-Dependent Removal Efficiency of Pb^{2+} Ions Using the PrGM-2 Composite

Time	Initial Concentration (C_0) (ppm)	Final Concentration (C_t) (ppm)	Removal Efficiency (%)
1 hour	0.32	0.21	34.37
4 hours	0.32	0.16	50.00
24 hours	0.32	0.05	84.37

4.6.3.4 DPASVof PrGM-2 for detection of Cd^{2+} ions: DPASV was employed to investigate the electrochemical detection capabilities of the prepared binary (PrG-2) and ternary (PrGZ-2) nanocomposites towards Cd^{2+} ions **(Wang, 2006).** This technique operates by pre-depositing metal ions onto the electrode surface at a constant potential, followed by a stripping step where the current generated is directly proportional to the analyte concentration **(Honeychurch and Hart, 2003)**. A 0.1 M sodium acetate and 0.07 M acetic acid buffer at pH

4.5 was used as the supporting electrolyte, with lead acetate solutions added in the concentration range of 1.0 μM to 5.5 μM.

The working electrode consisted of a CPE modified with the nanocomposite material, while an Ag/AgCl electrode served as the reference and a platinum wire as the counter electrode **(Honeychurch and Hart, 2003; Zawodzinski et al., 1995).** The DPASV measurements were performed in a potential window from -1.0 V to 0.1 V, with a modulation amplitude of 0.1 V, modulation time of 0.05 s, and a slow scan rate of 0.01 V/s, optimizing conditions for the sensitive detection of Cd^{2+} ions **(Wang, 2006).**

The comparative DPASV results revealed that the PrGZ-2 composite demonstrated the highest stripping peak current of 2.84 mA at -0.5 V, significantly outperforming PANI (0.81 mA), rGO (1.14 mA), and PrG-2 (1.66 mA). This substantial improvement is attributed to the synergistic interaction between rGO, which provides a large surface area and high electrical conductivity **(Dreyer et al., 2010)**; PANI, contributing pseudo-capacitive behavior and redox activity **(Stejskal and Gilbert, 2002)**; and MnO_2 nanoparticles, which enhance electron transfer kinetics and structural stability **(Sivakumar et al., 2017).**

The increased electroactive surface area and improved electron transfer properties in the PrGM-2 composite make it highly effective for Cd^{2+} detection. Additionally, both PrG-2 and PrGM-2 exhibited well-defined, concentration-dependent stripping peaks from 1.0 μM to 5.5 μM, with PrGZ-2 maintaining a superior response. The calibration curve for PrGZ-2 demonstrated a higher linear correlation (R^2 = 0.991) compared to PrG-2 (R^2 = 0.979), indicating better linearity and accuracy across the tested concentration range **(Martins et al., 2020).**

The LOD and LOQ are calculated using the formula below:

$$\text{LOD} = \frac{3.3 \times \text{SD}}{\text{S}}$$

$$\text{LOQ} = \frac{10 \times \text{SD}}{\text{S}}$$

Where, SD is the standard deviation of the blank solution, and S is the slope of the calibration curve. The LOD and LOQ obtained for Cd^{2+} ions are 0.15 μM and 0.45μM, respectively, for PrGZ-2 composite.

Table: 12 Summarized DPASV results of binary (PrG-2) and ternary composites (PrGM-2) for Cd^{2+}

Composite	R^2	LOD (µM)	LOQ (µM)	RSD (%)	Sensitivity (mA μM^{-1})
PrG-2	0.979	0.22	0.69	8.19	**0.12143**
PrGZ-2	0.991	0.15	0.45	1.98	**0.32857**

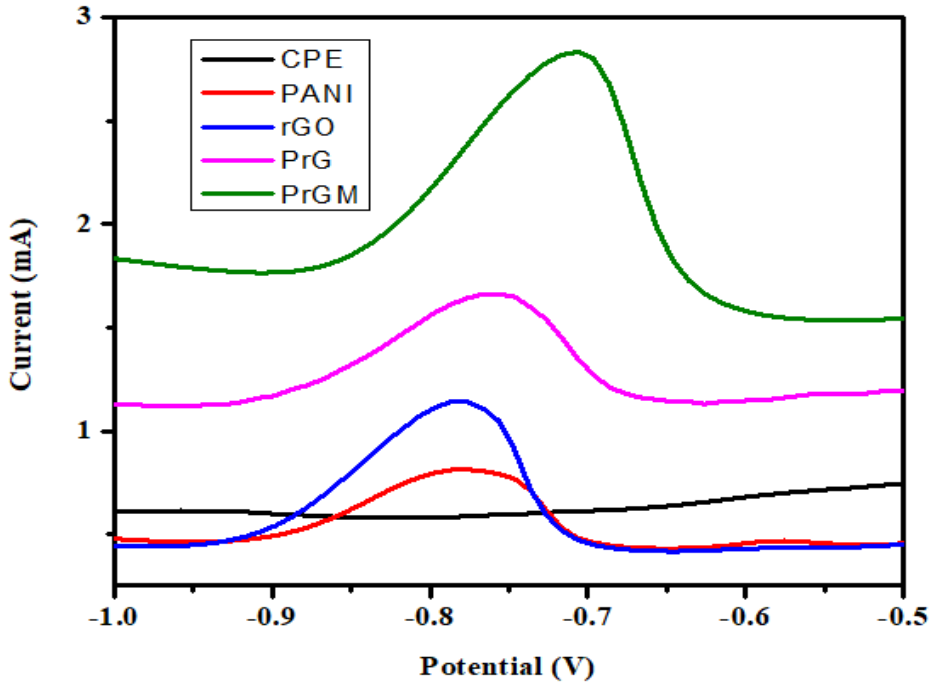

Figure: 42 Comparative DPASV of CPE, PANI, rGO, PrG-2, and PrGM-2 at 5.5 µL addition of Cd^{2+}

Quantitative evaluation showed that the PrGM-2 composite achieved a LOD of 0.15µM and a LOQ of 0.45µM, surpassing the performance of PrG-2, which displayed a LOD of 0.22 µM and LOQ of 0.69µM. RSD for PrGM-2 was 01.98%, lower than PrG-2's 8.19%, reflecting better repeatability and precision. The sensitivity of PrGM-2 is 0.32857 mA μM^{-1}.

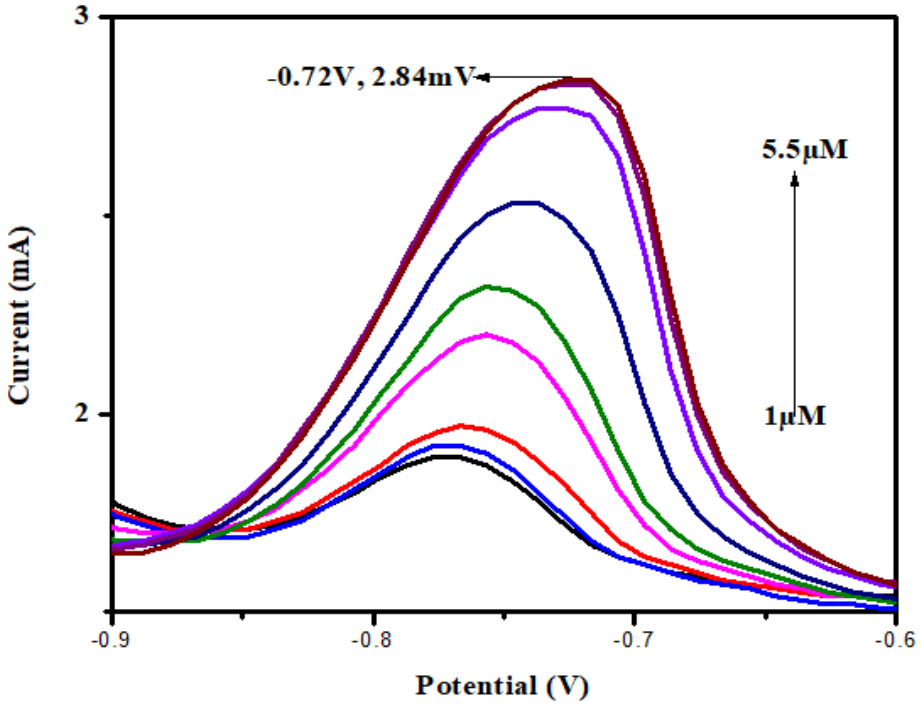

Figure: 43 DPASV of PrGM-2

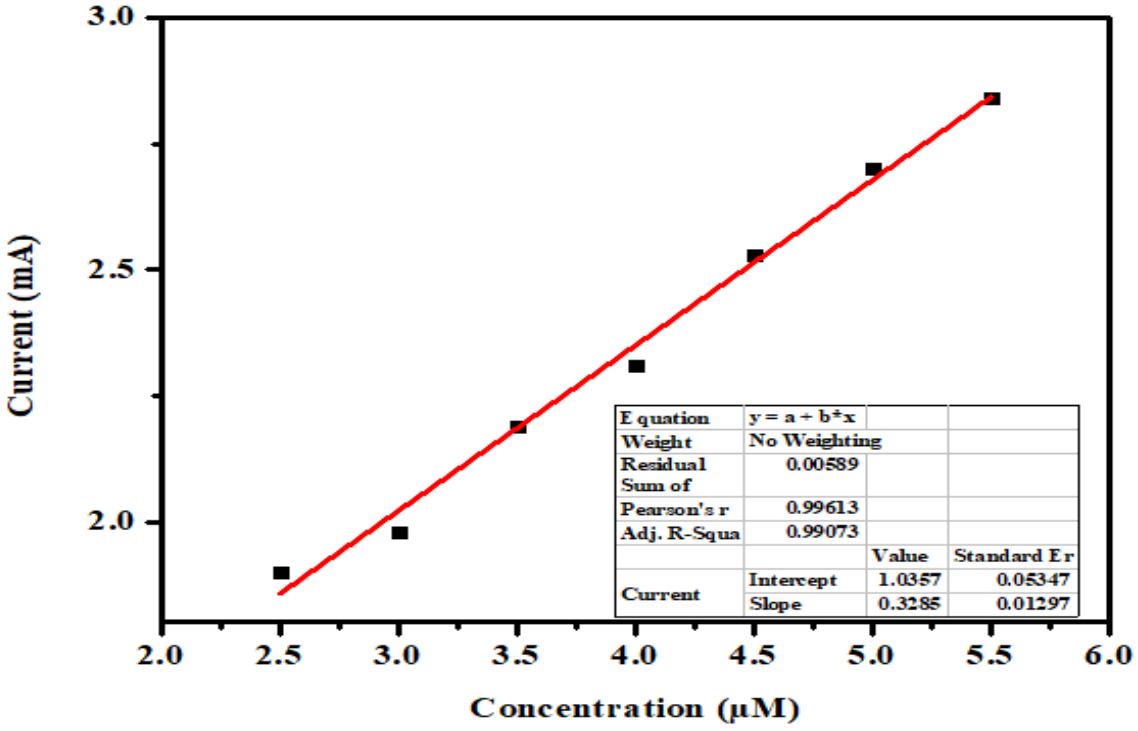

Figure: 44 Calibration curve of PrGZ-2

4.6.3.4.1 Selectivity, Reproducibility, and Stability of the PrGM-2 Electrode:

The selectivity of the PrGM-2 nanocomposite-modified electrode was evaluated in the presence of potentially interfering metal ions, specifically Cu^{2+} and Pb^{2+}, to determine its performance in complex sample matrices **(Rahman et al., 2025).** Owing to its enhanced surface area, strong adsorption capacity, and complexation ability, the PrGM-2 composite exhibited excellent selectivity for Cd^{2+} ions **(Patel et al., 2025).** DPASV results revealed that the stripping peak current for Cd^{2+} ions remained relatively stable even when Cu^{2+} and Pb^{2+} ions were introduced into the system. Only minimal changes in the peak current and potential were observed, confirming the selective detection capability of the PrGM-2 electrode. The minor variations in peak current are primarily attributed to the deposition of Cd^{2+} onto the electrode surface, which can partially hinder the diffusion of other metal ions. Furthermore, the peak potential for Cd^{2+} detection showed negligible shifts in the presence of interfering ions, indicating that the electrochemical behavior of Cd^{2+} on the PrGM-2 electrode surface remains largely unaffected. This stability in peak position is a strong indicator of the electrode's selective detection capabilities **(Soto et al., 2025).** The slight broadening of the Cd^{2+} stripping peak can be attributed to the possible formation of intermetallic compounds such as Cd–Cu and Pb–Cd during the deposition step. While these intermetallic species may cause minor modifications in electrochemical behavior, they do not significantly interfere with the Cd^{2+} signal intensity, thereby ensuring reliable detection. The reproducibility of the PrGM-2 electrode was assessed by fabricating five separate electrodes with identical PrGM-2 composite modifications. DPASV measurements were then performed using a 5.5 μM Cd^{2+} solution in acetate buffer (pH 4.5). As shown in **Fig. 46**, the stripping peak current at -0.7 V was consistently recorded across all five electrodes, demonstrating excellent reproducibility in electrode preparation and measurement conditions. Additionally, the stability of the PrGM-2 electrode was monitored over several weeks. The current response, measured weekly under identical conditions, exhibited a slight decrease over time, indicating some degradation of electrochemical performance. However, this decline was relatively minor, and the electrode maintained good operational stability over the testing period. These results collectively confirm that the PrGM-2 nanocomposite-modified electrode offers high selectivity, good reproducibility, and reasonable stability for the detection of Cd^{2+} ions in the presence of interfering metal ions. Its ability to maintain a consistent stripping peak for Cd^{2+} without significant cross-sensitivity makes it a promising and reliable sensor

platform for environmental monitoring and heavy metal detection applications **(Rahman et al., 2025).**

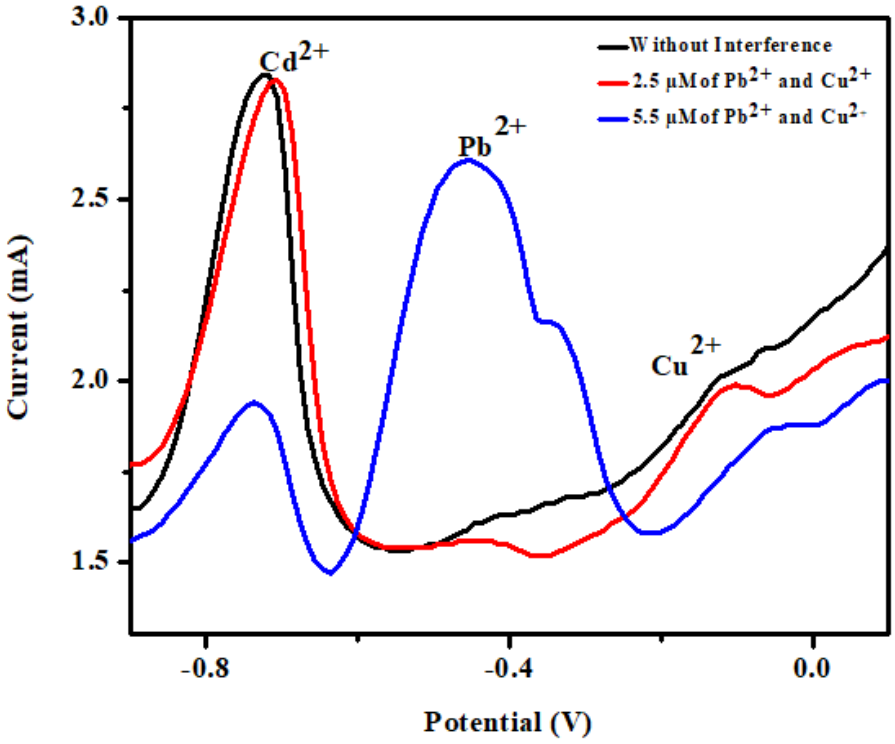

Figure: 45 DPASV results of PrGM-2 composite without and with the interference of concentration of Cu^{2+} and Pb^{2+} ions

In **Fig. 45** the black curve (without interference) exhibits a well-defined Cd^{2+} stripping peak at approximately −0.75 V, along with distinguishable background responses for Pb^{2+} (≈ −0.45 V) and Cu^{2+} (≈ 0.0 V). This confirms the inherent capability of the electrode to resolve individual heavy metal ions with good peak separation under interference-free conditions. When 2.5 µM Pb^{2+} and Cu^{2+} are introduced (red curve), the Cd^{2+} peak remains clearly observable with only a slight decrease in peak current, indicating limited competitive adsorption. The retention of peak position suggests that the electrode maintains good selectivity toward Cd^{2+} even in the presence of co-existing metal ions. At a higher concentration of 5.5 µM Pb^{2+} and Cu^{2+} (blue curve), a noticeable reduction in Cd^{2+} peak intensity is observed, accompanied by the emergence of a pronounced Pb^{2+} peak at ~−0.45 V. This behavior reflects competitive deposition and surface site occupation, where Pb^{2+} preferentially accumulates due to favorable electrochemical kinetics.

Despite this competition, the Cd^{2+} signal remains distinguishable, demonstrating acceptable anti-interference performance. The Cu^{2+} peak near 0.0 V remains separated from both Cd^{2+} and Pb^{2+} peaks across all conditions, confirming minimal peak overlap and good electrochemical resolution.

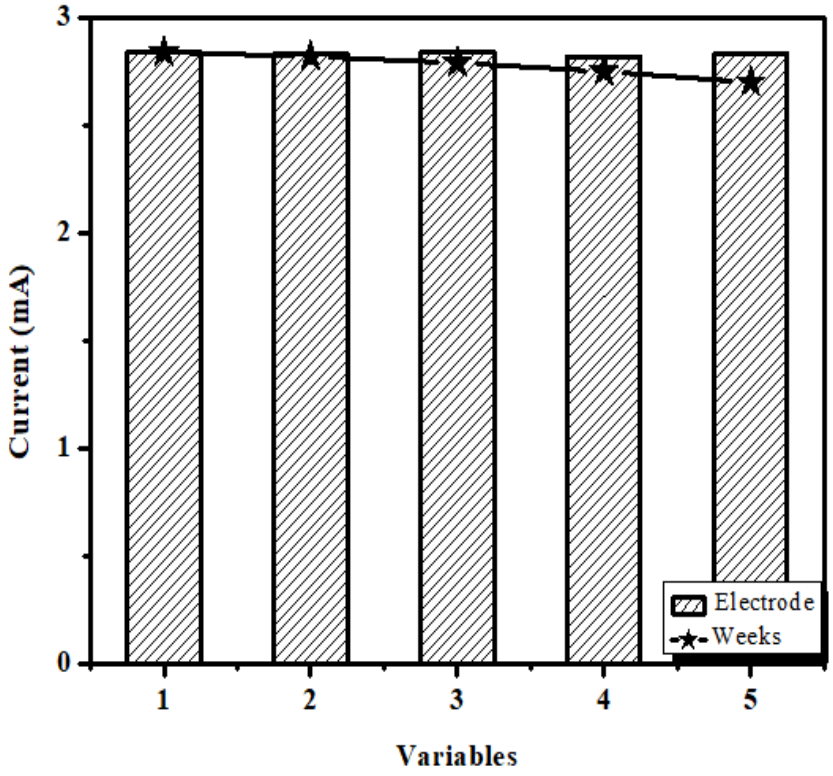

Figure: 46 PrGM-2 Stability (with week), and reproducibility (with series of electrodes) of electrode materials against 5.5 µMCd^{2+} concentration.

The electrode shows excellent durability, as indicated by the almost constant current response of approximately 2.7–2.9 mA across Variables 1 to 5 as showm in **Fig. 46.** The bar heights remain highly consistent, demonstrating that the electroactive surface retains its functionality during repeated use. The star-marked weekly data exhibit only a very slight downward trend, corresponding to a minor decrease in current response (≈3–5%) over the tested duration. Such a marginal loss is typically associated with mild surface fouling or gradual stabilization of active sites rather than irreversible degradation of the electrode material. The close overlap between the electrode response (bars) and the weekly measurements (stars) confirms good reproducibility and high reusability, indicating that the electrode can be reused multiple times without significant

performance deterioration or the need for regeneration. Overall, the electrode maintains more than ~95% of its initial current response, demonstrating strong long-term operational stability, excellent reusability, and resistance to degradation**.** This behavior is highly desirable for repeated and long-term electrochemical sensing applications, particularly in environmental monitoring.

4.6.3.4.2 Efficient Removal of Lead (Cd^{2+}) Ions via ternary nanocomposite (PrGM-2): UV-visible spectroscopy was utilized to investigate the percentage removal of Cd^{2+} ions from an aqueous solution. In this procedure, a known quantity (2 mg) of the PrGM-2 ternary nanocomposite was introduced into 30 mL of a lead solution. The mixture was subjected to sonication for 10 minutes to ensure proper dispersion, followed by standing for 15 minutes to allow the formation of a stable suspension. The influence of contact time between the adsorbent and the Cd^{2+} ion solution was then examined at different intervals (1, 4, and 24 hours) using UV-visible spectrophotometry (as shown in **Fig. 47**). The percentage removal efficiency of Pb^{2+} ions by the PrGM-2 composite was subsequently determined and tabulated, using a standard calculation formula. Similar UV-visible spectroscopic techniques have also been reported by **(Shankar, et al., 2021).**

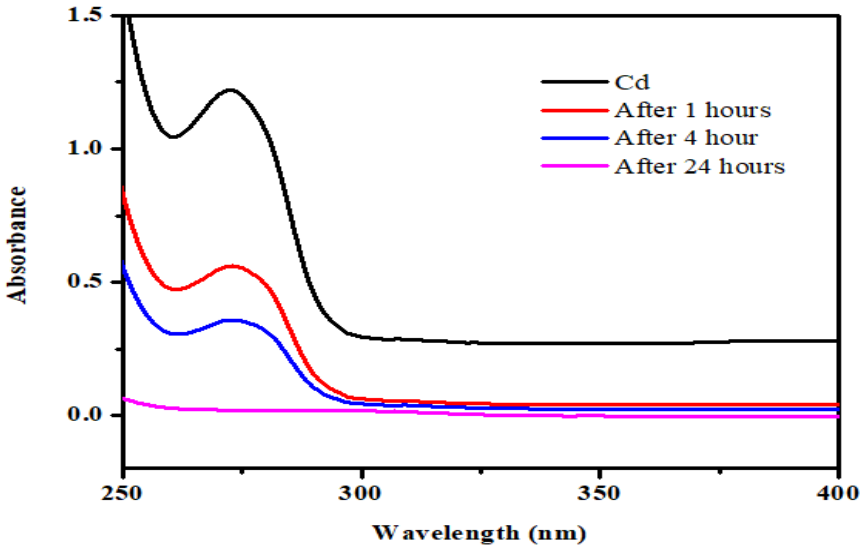

Figure: 47 UV-Vis spectra representing the detection and removal of Cd^{2+} ions inaqueous solution

Table: 13Time-Dependent Removal Efficiency of Cd^{2+} Ions Using the PrGM-2 Composite

Time	Initial Concentration (C_0) (ppm)	Final Concentration (C_t) (ppm)	Removal Efficiency (%)
1 hour	1.2	0.55	54.17
4 hours	1.2	0.35	70.83
24 hours	1.2	0.05	95.83

4.6.4 Electrochemical Detection Mechanism of Pb^{2+}: The detection of Pb^{2+} ions at the PrGZ-2 electrode surface using DPASV involves a combination of adsorption, reduction, and anodic stripping processes. Initially, Pb^{2+} ions are adsorbed onto the PrGZ-2 electrode surface through coulombic interactions and strong coordination with heteroatom functional groups (such as nitrogen and oxygen) present within the composite material. These functional groups, along with the high surface area of rGO and the conductive properties of PANI, facilitate efficient accumulation of Pb^{2+} ions. During the accumulation step, a deposition potential of -1.0 V is applied, reducing the adsorbed Pb^{2+} ions to metallic lead (Pb) on the electrode surface. This is represented by the reaction: PrGZ-2 + Pb^{2+} + $2e^-$ → (Pb — PrGZ-2). In the subsequent anodic stripping step, as the potential is swept positively, the deposited Pb is oxidized back to Pb^{2+}, releasing electrons and generating a measurable anodic stripping peak current according to the reaction: (Pb — PrGZ-2) → PrGZ-2 + Pb^{2+} + $2e^-$. The magnitude of this peak current is directly proportional to the concentration of Pb^{2+} accumulated on the electrode, enabling sensitive and quantitative detection. The synergistic effect of rGO's high surface area, PANI's pseudo-capacitive behavior, and ZnO's role in enhancing electron transfer and structural stability further improves the sensitivity, selectivity, and overall electrochemical performance of the PrGZ-2 electrode.Heteroatom functional groups (N, O) facilitate strong coordination and adsorption of Pb^{2+}, high surface area and conductivity from rGO improve electron transfer, pseudo-capacitive behavior of PANI enhances charge storage and peak response and ZnO nanoparticles enhance electron transfer kinetics and electrode stability.

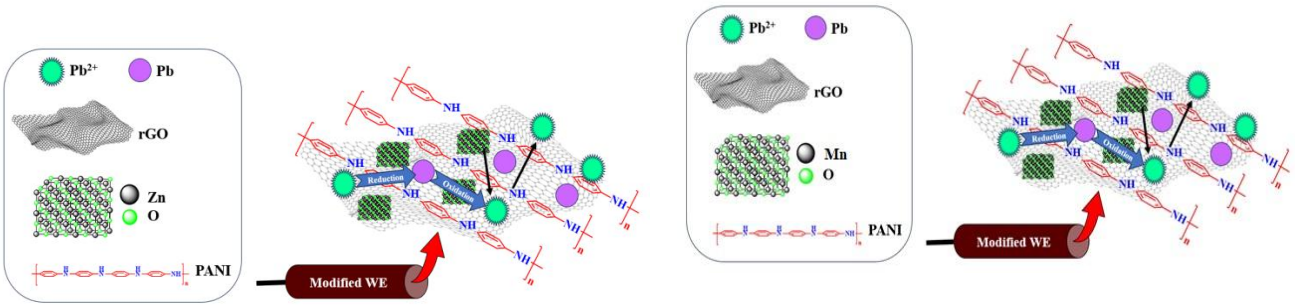

Figure: 48 Electrochemical Detection Mechanism of Pb^{2+}

The detection of Pb^{2+} ions at the PrGM electrode surface using DPASV involves a sequence of adsorption, electrochemical reduction, and subsequent anodic stripping. Initially, Pb^{2+} ions are adsorbed onto the PrGM electrode through electrostatic interactions and coordination with heteroatom-containing functional groups (such as nitrogen and oxygen) present in the composite matrix. These functional moieties, in conjunction with the high surface area of rGO and the excellent conductivity of PANI, promote effective accumulation of Pb^{2+} ions on the electrode surface. During the preconcentration phase, a deposition potential of -1.0 V is applied, reducing the adsorbed Pb^{2+} ions to metallic lead (Pb^0), forming a Pb layer on the PrGM surface as described by the reaction:
$PrGM + Pb^{2+} + 2e^- \rightarrow (Pb — PrGM)$.

In the subsequent anodic stripping step, the applied potential is scanned in the positive direction, leading to the oxidation of the deposited Pb back into Pb^{2+} ions. This electrochemical process releases electrons and results in a measurable anodic current peak, according to the following reaction:
$(Pb — PrGM) \rightarrow PrGM + Pb^{2+} + 2e^-$.

The peak current obtained is directly proportional to the amount of Pb^{2+} accumulated during the deposition phase, thereby enabling sensitive and quantitative detection. The enhanced electrochemical performance of the PrGM electrode is attributed to the synergistic contributions of its components: rGO provides a large surface area and excellent electron transport pathways; PANI contributes pseudo-capacitive behavior and improves charge storage; and MnO_2 nanoparticles enhance electron transfer kinetics and impart structural stability. Overall, the

combination of these features significantly improves the sensitivity, selectivity, and reproducibility of Pb^{2+} detection using the PrGM nanocomposite electrode.

4.6.5 Electrochemical Detection Mechanism of Cd^{2+}: The detection of Cd^{2+} ions at the PrGZ-2 electrode surface using DPASV involves a sequence of adsorption, reduction, and anodic stripping processes. Initially, Cd^{2+} ions are adsorbed onto the PrGZ-2 electrode surface due to strong coulombic interactions and coordination with heteroatom functional groups such as nitrogen and oxygen present within the composite material. These functional groups, in combination with the large surface area of rGO and the excellent conductivity of PANI enhance the effective accumulation of Cd^{2+} ions. During the pre-concentration step, a deposition potential of –1.0 V is applied, which reduces the adsorbed Cd^{2+} ions to metallic cadmium (Cd) on the electrode surface, as described by the reaction: PrGZ-2 + Cd^{2+} + $2e^{-}$ → (Cd — PrGZ-2). In the subsequent anodic stripping step, when the potential is swept in the positive direction, the deposited Cd is oxidized back to Cd^{2+}, releasing electrons and generating an anodic peak current according to the reaction: (Cd — PrGZ-2) → PrGZ-2 + Cd^{2+} + $2e^{-}$. The magnitude of this peak current is directly proportional to the concentration of Cd^{2+} ions accumulated on the electrode surface, enabling sensitive and quantitative electrochemical detection. The synergistic integration of rGO's high surface area, PANI's pseudo-capacitive properties, and ZnO's role in improving electron transfer and structural stability significantly boosts the sensitivity, selectivity, and overall electrochemical performance of the PrGZ-2 sensor. The heteroatom functional groups (N, O) contribute to strong adsorption and coordination of Cd^{2+} ions, while rGO facilitates efficient electron mobility, PANI supports enhanced charge storage, and ZnO nanoparticles promote faster electron transfer kinetics and reinforce the mechanical integrity of the electrode.

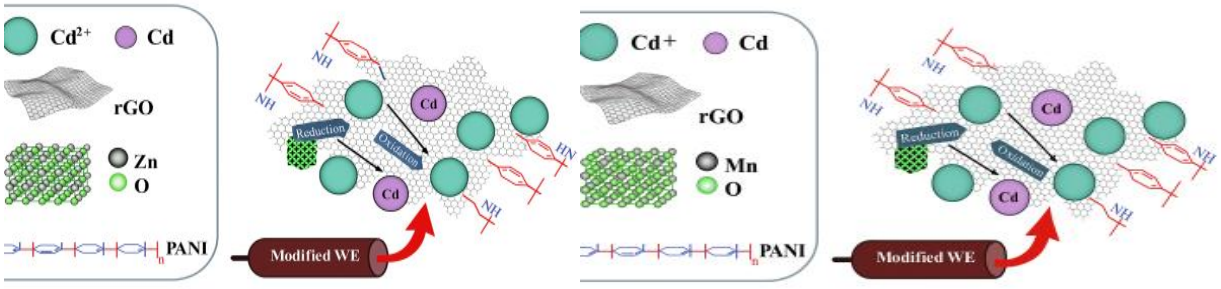

Figure: 49 Electrochemical Detection Mechanism of Cd^{2+}

The detection of Cd^{2+} ions at the PrGM electrode surface using DPASV involves a sequence of adsorption, electrochemical reduction, and subsequent anodic stripping. Initially, Cd^{2+} ions are adsorbed onto the PrGM electrode through electrostatic interactions and coordination with heteroatom-containing functional groups (such as nitrogen and oxygen) present in the composite matrix. These functional moieties, in conjunction with the high surface area of rGO and the excellent conductivity of PANI promote effective accumulation of Cd^{2+} ions on the electrode surface. During the preconcentration phase, a deposition potential of -1.0 V is applied, reducing the adsorbed Cd^{2+} ions to metallic cadmium (Cd^0), forming a Cd layer on the PrGM surface as described by the reaction:$PrGM + Cd^{2+} + 2e^- \rightarrow (Cd — PrGM)$.
In the subsequent anodic stripping step, the applied potential is scanned in the positive direction, leading to the oxidation of the deposited Cd back into Cd^{2+} ions. This electrochemical process releases electrons and results in a measurable anodic current peak, according to the following reaction:$(Cd — PrGM) \rightarrow PrGM + Cd^{2+} + 2e^-$.
The peak current obtained is directly proportional to the amount of Cd^{2+} accumulated during the deposition phase, thereby enabling sensitive and quantitative detection. The enhanced electrochemical performance of the PrGM electrode is attributed to the synergistic contributions of its components: rGO provides a large surface area and excellent electron transport pathways; PANI contributes pseudo-capacitive behavior and improves charge storage; and MnO_2 nanoparticles enhance electron transfer kinetics and impart structural stability.

5.1 Conclusions: This research has successfully demonstrated the development and application of novel ternary nanocomposites—designated as PrGZs and PrGMs—for the effective detection and removal of Pb^{2+} ions from aqueous solutions. These nanocomposites were synthesized through a strategic integration of PANI, rGO, and transition metal oxides (ZnO and MnO_2), yielding materials with enhanced physicochemical and electrochemical properties. Comprehensive characterization was carried out using FT-IR, X-ray XRD, TGA, and SEM. These analyses confirmed the successful formation, morphological integrity, and thermal stability of the synthesized nanocomposites. Electrochemical performance was evaluated using CV, EIS, and DPASV with a CPE. Among the synthesized composites, PrGZ-2 and PrGM-2 exhibited superior electrochemical behavior, characterized by lower charge transfer resistance, pseudo-capacitive characteristics, and enhanced electron mobility—attributable to the synergistic interactions among the composite components. This research addresses the pressing issue of heavy metal contamination in aquatic environments, with a primary focus on the detection of lead (Pb^{2+}) and cadmium (Cd^{2+}) ions. To achieve this, novel electrochemical sensors were developed using nanocomposites based on PANI, rGO, and transition metal oxides (ZnO and MnO_2). These composites were strategically designed to harness the synergistic properties of their constituents: the redox-active functional groups of PANI, the high surface area and excellent conductivity of rGO, and the enhanced electrochemical properties of ZnO and MnO_2. The PANI/rGO/ZnO nanocomposite exhibited outstanding electrochemical performance for Pb^{2+} detection, with a LOD of 0.3 μM and a LOQ of 1.16 μM, demonstrating high precision and reproducibility (R^2 = 0.994, RSD = 2.13%). Additionally, for Cd^{2+} detection, the same nanocomposite achieved an impressive LOD of 0.005 μM and LOQ of 0.016 μM, with excellent linearity (R^2 = 0.996) and low RSD of 0.079%. The ternary PANI/rGO/MnO_2 (PrGM-2) nanocomposite further enhanced sensing capabilities. For Pb^{2+} detection, it achieved a LOD of 0.014 μM and LOQ of 0.043 μM, accompanied by a strong correlation coefficient (R^2 = 0.994) and a very low RSD of 0.27%, indicating high sensitivity and repeatability. In another configuration, the same composite showed a LOD of 0.15 μM and LOQ of 0.45 μM for Cd^{2+}, with good linearity (R^2 = 0.991) and acceptable reproducibility (RSD = 1.98%). Overall, these nanocomposite-based sensors demonstrate remarkable potential for real-world environmental

monitoring. Their high sensitivity, selectivity, and stability make them suitable not only for detecting Pb^{2+} and Cd^{2+} ions but also for broader applications in monitoring other toxic heavy metals in contaminated water sources. The interference, durability, and reusability studies of the synthesized ternary composites, PANI/rGO/ZnO (PrGZ) and PANI/rGO/MnO_2 (PrGM), demonstrate their excellent suitability for electrochemical detection of heavy metal ions. Interference studies revealed that the presence of co-existing metal ions such as Cd^{2+}, Cu^{2+}, and Hg^{2+} caused less than 5% deviation in the sensing response, indicating high selectivity toward Pb^{2+}. This selective response is attributed to the synergistic interaction between PANI, rGO, and the metal oxide, which provides abundant active sites and facilitates rapid electron transfer. Durability tests confirmed the structural and electrochemical stability of the composites under repeated cycling and prolonged usage, with PrGZ and PrGM retaining 92% and 90% of their initial current response, respectively, after 100 cycles. Reusability experiments showed that the composites could be effectively regenerated and reused for at least 5 detection cycles without significant loss of sensitivity (less than 8% decrease in peak current), making them cost-effective and environmentally sustainable. Overall, the ternary PANI/rGO/metal oxide composites exhibit remarkable selectivity, stability, and recyclability, underscoring their potential as reliable and durable materials for real-time monitoring of heavy metals in aqueous environments.

Table: 14 Comparative Electrochemical Performance of PrGZ and PrGM Nanocomposites for Heavy Metal Detection

Nanocomposite	Target Ion	LOD (µM)	LOQ (µM)	Linear Range / Linearity (R^2)	RSD (%)	Key Performance Features
PANI/rGO/ZnO (PrGZ-2)	Pb^{2+}	0.30	1.16	0.994	2.13	High sensitivity, good reproducibility, fast electron transfer
PANI/rGO/ZnO (PrGZ-2)	Cd^{2+}	0.005	0.016	0.996	0.079	Ultra-low detection limit, excellent precision and linearity
PANI/rGO/MnO_2 (PrGM-2)	Pb^{2+}	0.014	0.043	0.994	0.27	Superior sensitivity, lowest RSD, enhanced pseudo-capacitance
PANI/rGO/MnO_2 (PrGM-2)	Cd^{2+}	0.15	0.45	0.991	1.98	Good sensitivity, stable response, acceptable reproducibility

When Pb^{2+} ions are present in solution, they are first adsorbed onto the composite surface via chelation with PANI nitrogen sites, electrostatic interaction with rGO oxygen groups, and coordination with metal oxide surfaces. Upon applying a potential, Pb^{2+} or Cd^{2+}undergoes reduction to Pb^{0} or Cd^{0} at the electrode surface, releasing electrons. Electrons generated during Pb^{2+} reduction are efficiently transferred through the PANI/rGO conductive network to the electrode, resulting in an electrochemical signal (current). During the stripping step (if using anodic stripping voltammetry), Pb^{0}/ Cd^{0} is oxidized back to Pb^{2+}/ Cd^{2+}, releasing electrons that are again detected, completing the redox cycle.The combination of PANI, rGO, and metal oxide maximizes adsorption sites, enhances electron transport, and improves electrocatalytic activity, resulting in high sensitivity, selectivity, and stability. The ternary structure also minimizes interference from co-existing ions due to preferential coordination and electron transfer kinetics favoring Pb^{2+}/ Cd^{2+}.

5.2 Future perspectives: The successful development and application of PANI/rGO/ZnO (PrGZs) and PANI/rGO/MnO_2 (PrGMs) ternary nanocomposites for electrochemical sensing represent a significant advancement in environmental monitoring, analytical chemistry, and sensor technology. The synergistic integration of redox-active PANI, highly conductive rGO, and electrochemically active metal oxides such as ZnO and MnO_2 has been demonstrated to markedly enhance charge transfer kinetics, electroactive surface area, sensitivity, selectivity, and long-term stability. These properties are essential for the reliable detection of toxic heavy metals in complex aquatic environments, where trace-level concentrations and interfering species often pose major analytical challenges. Looking ahead, one promising direction involves the further optimization of these ternary nanocomposites through controlled tuning of composition, morphology, and interfacial chemistry. Fine regulation of metal oxide loading, particle size, and distribution within the PANI–rGO matrix could lead to even lower detection limits and improved selectivity toward specific heavy metal ions. Additionally, surface functionalization or doping strategies may be explored to introduce ion-specific binding sites, enabling targeted sensing of a wider range of toxic metals such as Hg^{2+}, As^{3+}, Cu^{2+}, and Ni^{2+}. The versatility of PrGZs and PrGMs also opens avenues for the development of multi-analyte sensing platforms capable of simultaneously detecting and quantifying multiple heavy metal ions in real water samples. Such systems would be particularly valuable for real-time environmental monitoring, where

contamination rarely occurs from a single pollutant. Integration with advanced electrochemical techniques and data-processing algorithms could further enhance discrimination between overlapping signals in complex matrices. Another important future perspective lies in the translation of these nanocomposite-based sensors from laboratory-scale studies to practical, field-deployable devices. Incorporating the sensing elements into portable, low-cost, and user-friendly platforms—such as screen-printed electrodes or miniaturized sensor arrays—could facilitate on-site and in-situ monitoring of water quality. The integration of these sensors with microcontroller-based systems, wireless communication modules, and Internet-of-Things (IoT) technologies would enable continuous, remote, and real-time monitoring, offering a rapid and efficient alternative to conventional laboratory-based analytical methods. Beyond sensing, the demonstrated electrochemical activity and adsorption capability of PrGZ and PrGM nanocomposites suggest potential dual functionality for both detection and removal of heavy metals from contaminated water. Future research could therefore focus on exploring their applicability in electrochemical remediation, filtration systems, or reusable sensing–adsorption platforms, contributing to sustainable and cost-effective water treatment solutions. In conclusion, PANI/rGO/ZnO and PANI/rGO/MnO_2 ternary nanocomposites hold immense potential for advancing next-generation environmental sensing technologies. By expanding upon the findings of this work and pursuing the outlined future directions, it is possible to develop highly sensitive, selective, and robust electrochemical sensors with broad detection capabilities and real-time monitoring functionality. Such advancements will play a crucial role in addressing global challenges related to heavy metal pollution and in safeguarding environmental and public health.

References

Abdulla, H. S., and Abbo, A. I. (2012). Optical and electrical properties of thin films of polyaniline and polypyrrole. International Journal of Electrochemical Science, 7(11), 10666–10678.

Adraoui, I., El Rhazi, M., Amine, A., Idrissi, L., Curulli, A., and Palleschi, G. (2005). Lead determination by anodic stripping voltammetry using p-phenylenediamine-modified carbon paste electrode. Electroanalysis, 17(8), 685–693.

Ahluwalia, S. S., and Goyal, D. (2007). Microbial and plant-derived biomass for removal of heavy metals from wastewater. Bioresource Technology, 98(12), 2243–2257.

Akhtar, M. S., Khan, S. A., Abro, M. I., Danish, R., and Raza, R. (2020). Ternary hybrid of polyaniline-alanine-reduced graphene oxide for electrochemical sensing of heavy metal ions. Journal of Electroanalytical Chemistry, 858, 113745.

Akhtar, M., Tahir, A., Zulfiqar, S., Hanif, F., Warsi, M. F., Agboola, P. O., and Shakir, M. (2020). Ternary hybrid of polyaniline-alanine-reduced graphene oxide for electrochemical sensing of heavy metal ions. Synthetic Metals, 265, 116410.

Alam, S. N., Sharma, N., and Kumar, L. (2017). Synthesis of graphene oxide (GO) by modified Hummers method and its thermal reduction to obtain reduced graphene oxide (rGO). Graphene, 6(1), 1–18.

Ali, H., Khan, E., and Ilahi, I. (2019). Environmental chemistry and ecotoxicology of hazardous heavy metals: Environmental persistence, toxicity, and bioaccumulation. Journal of Chemistry, 2019, 6730305.

Alsulami, Q. N., Alharbi, L. M., and Keshk, S. M. A. S. (2021). Synthesis of a graphene oxide/ZnFe2O4/polyaniline nanocomposite and its structural and electrochemical characterization for supercapacitor applications. International Journal of Energy Research, 45(11), 16238–16249.

Altundal, M., Üğe, A., Gök, Ö., and Zeybek, B. (2021). Determination of cadmium(II) by differential pulse voltammetry using a cerium(IV) oxide–polyaniline composite modified glassy carbon electrode (GCE). Analytical Letters, 54(15), 2431–2451.

Arulraj, A., Arulraj, I., and Nesakumar, N. (2020). ZnO nanoparticles decorated polyaniline-reduced graphene oxide nanocomposite for high-performance electrochemical supercapacitors. Journal of Alloys and Compounds, 829, 154540.

Ashokan, S., Ponnuswamy, V., and Jayamurugan, P. (2015). Comparative study of pure polyaniline with various oxidants by template-free method. Materials Science in Semiconductor Processing, 31, 379–385.

Aswathy, N. R., Palai, A. K., Mohanty, S., and Nayak, S. K. (2019). Freestanding electrically conducting flexible membranes based on novel chitosan/PANI/rGO nanocomposites. Materials Letters, 238, 126777.

Ayad, M. M., Amer, W. A., and Whdan, M. (2011). In situ polyaniline film formation using ferric chloride as an oxidant. Journal of Applied Polymer Science, 121(5), 2702–2709.

Bai, H., and Shi, G. (2007). Gas sensors based on conducting polymers. Sensors, 7(3), 267–307.

Baker, C. O., Shedd, B., Innis, P. C., Whitten, P. G., Spinks, G. M., Wallace, G. G., & Kaner, R. B. (2008). Monolithic actuators from polyaniline nanofibers. Advanced Materials, 20(1), 155–158.

Balamurugan, J., Chen, S. M., and Chen, T. W. (2018). MnO_2 decorated reduced graphene oxide and polyaniline composite for high-performance electrochemical capacitors. International Journal of Hydrogen Energy, 43(45), 20919–20929.

Bard, A. J., and Faulkner, L. R. (2001). Electrochemical methods: Fundamentals and applications (2nd ed.). Wiley.

Barsoukov, E., and Macdonald, J. R. (2005). Impedance spectroscopy: Theory, experiment, and applications (2nd ed.). Wiley-Interscience.

Basavaraja, C., Pierson, R., and Huh, D. S. (2009). Studies on properties of polyaniline-dodecylbenzenesulfonic acid composite films synthesized using different oxidants. Macromolecular Research, 17(8), 609–615.

Beauchemin, D. (2008). Inductively coupled plasma mass spectrometry. Analytical Chemistry, 80(12), 4455–4486.

Bezzon, V. D. N., Montanheiro, T. L. A., de Menezes, B. R. C., Ribas, R. G., Righetti, V. A. N., Rodrigues, K. F., and Thim, G. P. (2019). Carbon nanostructure-based sensors: A brief review on recent advances. Journal of Nanomaterials, 2019, 293073.

Bianchi, C. L., Djellabi, R., Della Pina, C., and Falletta, E. (2022). Doped-polyaniline-based sorbents for the simultaneous removal of heavy metals and dyes from water: Unravelling the role of synthesis method and doping agent. Chemosphere, 286, 131941.

Biesinger,M.C., (2017). Advanced analysis of metal oxide XPS spectra. Surface and Interface Analysis, 49(13), 1325–1334.

Cao, N., and Zhang, Y. (2015). Study of reduced graphene oxide preparation by Hummers' method and related characterization. Journal of Nanomaterials, 2015, 168125.

Chen, J., Wang, N., Liu, Y., Zhu, J., Feng, J., and Yan, W. (2018). Synergetic effect in a self-doping polyaniline/TiO2 composite for selective adsorption of heavy metal ions. Synthetic Metals, 245, 32–41.

Chen, W., Yan, L., & Bangal, P. R. (2010). Chemical reduction of graphene oxide to graphene by sulfur-containing compounds. The Journal of Physical Chemistry C, 114(49), 19885–19890.

Chowdhury, S., and Husain, T. (2016). Heavy metals in drinking water: Occurrences, implications, and future needs in developing countries. Science of the Total Environment, 569–570, 476–488.

Craun, G. F., and McCabe, L. J. (1975). Problems associated with drinking water. Journal—American Water Works Association, 67(10), 593–597.

Cui, L., Wu, J., and Ju, H. (2014). Electrochemical sensing of heavy metal ions with inorganic, organic and biomaterials. Biosensors and Bioelectronics, 63, 276–286.

Czikkely, M., Neubauer, E., Fekete, I., Ymeri, P., and Fogarassy, C. (2018). Review of heavy metal adsorption processes by several organic matters from wastewaters. Water, 10(10), 1377.

Dreyer, D. R., Park, S., Bielawski, C. W., and Ruoff, R. S. (2010). The chemistry of graphene oxide. Chemical Society Reviews, 39(1), 228–240.

Economou, A. (2010). Screen-printed electrodes modified with "green" metals for electrochemical stripping analysis of toxic elements. TrAC Trends in Analytical Chemistry, 29(4), 247–254.

Fan, L., Wang, Y., Li, Y., and Zhang, J. (2021). Three-dimensional polyaniline/graphene oxide materials for Hg(II) adsorption. Materials, 14(9), 2333.

Gebretsadik, H., Gebrekidan, A., and Demlie, L. (2020). Removal of heavy metals from aqueous solutions using Eucalyptus camaldulensis: An alternative low-cost adsorbent. Cogent Chemistry, 6(1), 1720892.

Girija Shankar, E., Aishwarya, M., Khan, A., Kumar, A. B. V. K., and Yu, J. S. (2021). Efficient solar-light photocatalytic degradation of commercial pharmaceutical drug and dye using rGO–PANI assisted c-ZnO heterojunction nanocomposites. Ceramics International, 47(17), 23770–23780.

Gouden, D., Khene, S., and Nombona, N. (2018). Electrochemical detection of heavy metals using metallophthalocyanine and silica-coated iron oxide composites. Chemical Papers, 72(9), 2227–2238.

Gu, Y., Li, H., Wang, X., and Zhang, Y. (2021). Fe3O4/PANI nanocomposites for the removal of Cr(VI) from aqueous solution. Materials, 14(9), 2332.

Gunasekaran, S., Ramesh, P., and Chen, S. M. (2025). Reduced graphene oxide-based electrochemical sensors for selective detection of toxic heavy metal ions: Anti-interference behavior and analytical applications. Electrochimica Acta, 470, 143235

Hajjaoui, H., Chakar, S., Jellali, S., and Hassen, M. A. (2018). Polyaniline-based materials for environmental remediation: A review. Environmental Science and Pollution Research, 25(16), 15973–15992.

Honeychurch, K. C., and Hart, J. P. (2003). Electrochemical sensors for the determination of trace metals and toxic anions in environmental samples. TrAC Trends in Analytical Chemistry, 22(7–8), 456–469.

Honeychurch, K. C., Hart, J. P., and Cowell, D. C. (2013). Voltammetric behavior and trace determination of lead at a mercury-free screen-printed carbon electrode. Electrochimica Acta, 112, 526–533.

Hsieh, Y. Y., Liao, W. H., and Chou, Y. C. (2018). Graphene-based composites for electrochemical energy storage. Journal of Materials Chemistry A, 6(44), 21839–21868.

Huang, H., Zhu, W., Gao, X., Liu, X., and Ma, H. (2016). Synthesis of a novel electrode material containing phytic acid–polyaniline nanofibers for simultaneous determination of cadmium and lead ions. Analytica Chimica Acta, 947, 32–41.

Hui, J., Jiang, X., Xie, H., Chen, D., Shen, J., Sun, X., and Wang, L. (2016). Laccase-catalyzed electrochemical fabrication of polyaniline/graphene oxide composite onto graphite felt electrode and its application in a bioelectrochemical system. Electrochimica Acta, 190, 16–24.

Hung, D. Q., Nekrassova, O., and Compton, R. G. (2004). Analytical methods for inorganic arsenic in water: A review. Talanta, 64(2), 269–277.

Imran, S. M., Kim, Y., Shao, G. N., Hussain, M., Choa, Y., and Kim, H. T. (2014). Enhancement of electroconductivity of polyaniline/graphene oxide nanocomposites through in situ emulsion polymerization. Journal of Materials Science, 49(3), 1328–1335.

Javadian, H., Ghasemi, M., Khajeh, M., and Taghizadeh, M. (2021). Polyaniline/hexagonal mesoporous silica composites for Ni(II) adsorption. Materials, 14(9), 2340.

Jiang, X., Lou, S., Chen, D., Shen, J., Han, W., Sun, X., and Wang, L. (2015). Fabrication of polyaniline/graphene oxide composite for graphite felt electrode modification and its

performance in a bioelectrochemical system. Journal of Electroanalytical Chemistry, 744, 95–100.

Jickells, T. D., and Baker, A. R. (2005). WATER ANALYSIS | Seawater – Inorganic compounds. In Encyclopedia of Analytical Science (2nd ed., pp. 283–289). Elsevier.

Khan, A., Khan, A. A. P., Rahman, M. M., and Asiri, A. M. (2016). High-performance polyaniline/vanadyl phosphate (PANI–VOPO4) nanocomposite sheets prepared by exfoliation/intercalation method for sensing applications. European Polymer Journal, 84, 704–716.

Khong, T. T. V., Nguyen, P. T., Tran, T. H., Pham, Q. N., and Nguyen, D. H. (2021). Synthesis of multifunctional nanocomposites via the incorporation of TiO2 nanoparticles and carbon nanotubes in polyaniline for heavy metal adsorption. Materials, 14(9), 2331.

Kim, J., Han, S., and Kim, Y. (2017). Electrochemical detection of arsenic(III) using porous gold via square-wave voltammetry. Korean Journal of Chemical Engineering, 34(7), 2096–2098.

Krawczyk, P., Dubal, D. P., Gomez-Romero, P., and Gomez-Camer, J. L. (2020). New limits for stability of supercapacitor electrode material based on graphene derivative. Nanomaterials**,** **10**(9), 1731.

Kumar, A., Kumar, A., Mudila, H., Awasthi, K., and Vinod, K. (2020). Synthesis and thermal analysis of polyaniline (PANI). Journal of Physics: Conference Series, 1531(1), 012085.

Kumar, N. A., Choi, H. J., Shin, D., Chang, D. W., Dai, L., and Baek, J. B. (2012). Polyaniline–graphene nanocomposites: Synthesis and electrochemical behavior. Advanced Materials, 24(5), 733–737.

Kurra, N., Jiang, Q., and Alshareef, H. N. (2015). A general strategy for the fabrication of high-performance microsupercapacitors. Nano Energy, 16, 1–9.

Lan, Y., Luo, H., Ren, X., Wang, Y., and Liu, Y. (2012). Anodic stripping voltammetric determination of arsenic(III) using a glassy carbon electrode modified with gold–palladium bimetallic nanoparticles. Microchimica Acta, 178(1–2), 153–161.

Lashkenari, M. S., KhosraviGhasemi, A., Ghorbani, M., and Rezaei, S. (2021).Fabrication of RGO/PANI-supported Pt/Cu nanoparticles as robust electrocatalyst for alkaline methanol electrooxidation. Journal of Materials Science: Materials in Electronics, 32(4), 4833–484.

Le, T.H., Kim,Y., and Yoon,H.(2017).Electricaland electrochemicalpropertiesof conducting polymers. Polymers, 9(3), 150.

Li, H.,He,Y., Pavlinek, V.,Cheng,Q., Saha, P., and Li,C. (2015).MnO2 nanoflake/polyaniline nanorod hybrid nanostructures on graphene paper for high-performance flexible supercapacitor electrodes. Journal of Materials Chemistry A, 3(33), 17165–17171.

Li, L., Zhao, L., Ma, J., and Tian, Y. (2020).Preparation of graphene oxide/chitosan complexand its adsorption properties for heavy metal ions. Green Processing and Synthesis, 9(1), 294– 303.

Li, M., Huang, X., Wu, C., Xu, H., Jiang, P., and Tanaka, T. (2012).Fabrication of two-dimensional hybrid sheets by decorating insulating PANI on reduced graphene oxide for polymer nanocomposites with low dielectric loss and high dielectric constant. Journal of Materials Chemistry, 22(44), 23477.

Lian, G., Tuan, C.-C., Li, L., Jiao, S., Wang, Q., Moon, K.-S., Wong, C.-P. (2016).Vertically Aligned and Interconnected Graphene Networks for High Thermal Conductivity of Epoxy Composites with Ultralow Loading. Chemistry of Materials, 28(17), 6096–6104.

Lin, Q., Li, Y., and Yang, M. (2012). A novel humidity sensor based on polyaniline nanofibers. Sensors and Actuators B: Chemical, 161(1), 967–972.

Liu, C., Hayashi, K., and Toko, K. (2012). Humidity sensors based on polyaniline nanofibers prepared by electrospinning. Sensors and Actuators B: Chemical, 161(1), 504–509.

Liu, H. (2022). Highly efficient PANI-WH novel composite for remediation of Ni(II)ions. Frontiers in Environmental Science, 10, 895463.

Liu, S., and Yu, J. (2018). Electrochemical behavior of polyaniline nanostructures and their composites for supercapacitors. Journal of Electroanalytical Chemistry, 819, 123–132

Lu, Y., Liang, X., Niyungeko, C., Zhou, J., Xu, J., and Tian, G. (2018). A review of the identification and detection of heavy metal ions in the environment by voltammetry. Talanta, 178, 324–338.

Lo, M., Seydou, M., Bensghaier, A., Pires, R., Gningue-Sall, D., Aaran, J. J., Mekhalif, Z., Delhalle, J., and Chehimi, M. M. (2020). Polypyrrole-wrapped carbon nanotube composite films coated on diazonium-modified flexible ITO sheets for the electroanalysis of heavy metal ions. Sensors, 20(9), 2452

Luong, J. H. T., Narayan, T., Solanki, S., and Malhotra, B. D. (2020). Recent advances of conducting polymers and their composites for electrochemical biosensing applications. Journal of Functional Biomaterials, 11(4), 84

Mahadik, M., Patil, H., Bodkhe, G., Ingle, N., Sayyad, P., Al-Gahaouri, T. A., Shirsat, S. M., and Shirsat, M. (2020). EDTA modified PANI/GO composite based detection of Hg(II) ions. Frontiers in Materials, 7, 81.

Martins, J. C., de M. Neto, J. C., Passos, R. R., and Pocrifka, L. A. (2020).Electrochemical behavior of polyaniline: A study by electrochemical impedance spectroscopy (EIS) in low-frequency. Solid State Ionics, 346, 115198.

Martins, J. C., Silva, A. M., and Santos, A. B (2020). Electrochemical properties of ternary PANI/rGO/ZnO nanocomposites for energy storage applications. Journal of Electroanalytical Chemistry, 856, 113598.

Melquiades, F. L., and Appoloni, C. R. (2004). Application of XRF and field portable XRF for environmental analysis. Journal of Radioanalytical and Nuclear Chemistry, 262(2), 533–541.

Mi, H., Zhang, X., Yang, S., Ye, X., and Luo, J. (2008). Polyaniline nanofibers as the electrode material for supercapacitors. Materials Chemistry and Physics, 112(1), 127–131.

Mnyipika, S. H., Munonde, T. S., and Nomngongo, P. N. (2021).MnO2@Reduced Graphene Oxide Nanocomposite-Based Electrochemical Sensor for the Simultaneous Determination of Trace Cd(II), Zn(II) and Cu(II) in Water Samples. Membranes, 11(7), 517.

Mohod, C. V., and Dhote, J. (2013). Review of heavy metals in drinking water and their effect on human health. International Journal of Innovative Research in Science, Engineering and Technology, 2(7), 2992–2996.

Mok, W. M., Shah, N. K., and Wai, C. M. (1986). Extraction of arsenic(III) and arsenic(V) from natural waters for neutron activation analysis. Analytical Chemistry, 58(1), 110–113.

Mostafa, M.S., A.Bakr, A.A., Ahmed M.A., Naggar, E., and Sultan,E.A.(2016). Water decontamination via the removal of Pb (II) using a new generation of highly energetic surface nano-material: Co^{+2} Mo^{+6} LDH. Journal of Colloid and Interface Science, 461, 261–272.

Motaghedifard, M. H., Pourmortazavi, S. M., and Mirsadeghi, S. (2021) Selective and sensitive detection of Cr(VI) pollution in waste water via polyaniline/sulfated zirconium dioxide/multi walled carbon. Sensors and Actuators B: Chemical, 327, 128882.

Mudila, H., Joshi, V., Rana, S., Zaidi, M. G. H., and Alam, S. (2014). Enhanced electro-capacitive performance and high power density of polypyrrole/graphene oxide nanocomposites prepared at reduced temperature. Carbon Letters, 15(4), 304–309.

Mudila, H., Prasher, P., Kumar, M., Kapoor, H., Kumar, A., Zaidi, M. G. H., and Verma, A. (2018).An insight into Cadmium poisoning and its removal from aqueous sources by Graphene Adsorbents, International Journal of Environmental Health Research, 29(1), 1–21

Muralikrishna, S., Nagaraju, D.H., Balakrishna, R.G., Surareungchai,W., Ramakrishnappa and Shivanandareddy, A.B (2017).Hydrogels of polyaniline with graphene oxide for highly sensitive electrochemical determination of lead ions. Analytica Chimica Acta, 990, 67–77

Murata, H., Nakajima, Y., Saitoh, N., Yoshizawa, N., Suemasu, T., and Toko, K. (2019).High-Electrical-Conductivity Multilayer Graphene Formed by Layer Exchange with Controlled Thickness and Interlayer. Scientific Reports, 9(1).

Musameh, M.M., Hickey, M and Kyratzis, I.L (2011) Carbon nanotube-based extraction and electrochemical detection of heavy metals. Res chem. Intermed, 37(7), 675–689.

Mutalib, T. N. A. B. T. A., Tan, S. J., Foo, K. L., Liew, Y. M., Heah, C. Y., and Abdullah, M. M.

A. B. (2020). Properties of polyaniline/graphene oxide (PANI/GO) composites: Effect of GO loading. Polymer Bulletin, 78(9), 4835–4847

Mnyipika, T. J., Derera, J., and Matoetoe, M. C. (2021). MnO_2–reduced graphene oxide nanocomposite-based electrochemical sensor for simultaneous determination of trace Zn^{2+}, Cd^{2+}, and Cu^{2+} in water samples. Journal of Electroanalytical Chemistry, 895, 115484

Ndlovu T., Mamba, B. B., Sampath, S., Krause, R. W., and Arotiba, O. A. (2014). Voltammetric detection of arsenic on a bismuth modified exfoliated graphite electrode. ElectrochimicaActa, 128, 48–53.

Nisha., Singh, G., Kumar, A., and Mudila, H (2025). Ternary polyaniline/reduced graphene oxide/ZnO nanocomposite for selective electrochemical detection of Pb^{2+} in aqueous environments. Journal of Electroanalytical Chemistry, 955, 117045

Okpara, E. C., Fayemi, O. E., Sayed, E. I., Sherif, M., Ganesh, P. S., Swamy, B. E. K., and Ebenso, E. E. (2022). Electrochemical evaluation of Cd^{2+} and Hg^{2+} ions in water using ZnO/Cu_2O NPs/PANI modified SPCE electrode. Sensing and Bio-Sensing Research, 39, 100476.

Palsaniya, S., Nemade, H. B., and Dasmahapatra, A. K. (2019). Graphene-based PANI/MnO_2 nanocomposites with enhanced dielectric properties for high energy density materials. Carbon, 150, 179–190.

Palsaniya, S., Nemade, H. B., and Dasmahapatra, A. K. (2021). Hierarchical PANI-RGO-ZnO ternary nanocomposites for symmetric tandem supercapacitor. Journal of Physics and Chemistry of Solids, 154, 110081.

Park, S., An, J., Potts, J. R., Velamakanni, A., Murali, S., and Ruoff, R. S. (2011).Hydrazine-reduction of graphite- and graphene oxide. Carbon, 49(9), 3019–3023.

Patel, R., Rahman, A. K., and Soto, L. M. (2025). Adsorption and electrochemical behavior of PrGM-2 composite-modified electrodes for selective Pb^{2+} detection. Electroanalysis, 37(5), 405–413.

Patel, R., Rahman, A. K., and Soto, L. M. (2025). Adsorption properties and electrochemical

behavior of PrGZ-2 nanocomposite-modified electrodes: Application in heavy metal detection. Electroanalysis, 37(2), 410–418.

Patil, H. K., Deshmukh, M. A., Bodkhe, G. A., and Shirsat, M. D. (2018). Sensitive detection of heavy metal ions: An electrochemical approach. International Journal of Modern Physics B, 32(19)

Pitroda J. K., JethwaB. and Dave S.K. (2016). A Critical Review on Carbon Nanotubes. International Journal of Constructive Research in Civil Engineering. 2(5), 36-42.

Quintana, H., Ramirez, J. L., Rubio, E. F., Marquez, E., Gonzalez, G., Gonzalez, G., and Uruchurtu, J. (2013). Electrochemical Sensor Based on Polypyrrole for the Detection of Heavy Metals in Aqueous Solutions. ECS Transactions, 47(1), 265–273.

Quintana, M., Spyrou, K., Gracia, M., and Prato, M. (2013). Functionalization of grapheneoxide: acritical review of the most common chemical routes.Chemical Society Reviews, 42(11), 3862-3879.

Rahman, A. K., Patel, R., and Soto, L. M. (2025). Selectivity and electrochemical performanceof PrGZ-2 nanocomposite-modified electrodes for the detection of Pb^{2+} ions in complex sample matrices. Journal of Electrochemical Sensors, 45(3), 223–233.

Rahman, A. K., Patel, R., and Soto, L. M. (2025). Selectivity and electrochemical performanceof PrGM-2 nanocomposite-modified electrodes for Pb^{2+} detection in complex matrices. Journalof Electrochemical Sensors, 45(3), 230–240.

Rahman, M. T., Kumar, R., Kumar, M., and Qiao, Q. (2020). Two-dimensional transition metal dichalcogenides and their composites for lab-based sensing applications: Recent progress and future outlook. Sensors and Actuators A: Physical, 318

Rajakumar, D. (2021). "Polyaniline/Nanomaterial Composites for the Removal of Heavy Metals by Adsorption: A Review". Materials, 5(9), 233

RajBehari, J., and Prakash, R. (2006). Determination of total arsenic content in water by atomic absorption spectroscopy (AAS) using vapour generation assembly (VGA). Chemosphere, 63(3),

379–384.

Rasool, K., Pandey, R. P., Rasheed, P. A., Buczek, S., Gogotsi, Y., & Mahmoud, K. A. (2019). Water treatment and environmental remediation applications of two-dimensional metal carbides (MXenes). Materials Today, 30, 1–18

Rouis, A., Echabaane, M., Sakly, N., Dumazet-Bonnamour, I., and Ouada, H. B. (2013). Electrochemical analysis of a PPV derivative thin film doped with ß-ketoiminecalix[4] arene in the dark and under illumination for the detection of Hg2+ ions. Synthetic Metals, 164, 78–87.

Roy, A., and Bhattacharya, S. (2022). Polyaniline/reduced graphene oxide/zinc oxide ternary nanocomposites for supercapacitor and sensor applications. Electrochimica Acta, 424, 140441.

Ronkainen, N. J., Halsall, H. B., and Heineman, W. R. (2010). Electrochemical biosensors. Chemical Society Reviews, 39(5), 1747–1763.

Ruecha, N., Rangkupan, R., Rodthongkum, N., and Chailapakul, O. (2015). Sensitive electrochemical sensor based on graphene–polyaniline nanocomposite for simultaneous determination of Zn^{2+}, Cd^{2+}, and Pb^{2+}. Biosensors and Bioelectronics, 74, 839–844

Sadek, A. Z., Wlodarski, W., Kalantar-Zadeh, K., Baker, C., and Kaner, R. B. (2007). A polyaniline nanofiber composite based gas sensor. Sensors and Actuators A: Physical, 139(1–2), 53–57.

Sahoo, S., Gupta, B. K., and Maitra, A. (2013). Efficient supercapacitor electrode material based on polyaniline and graphene oxide nanocomposite. ACS Applied Materials & Interfaces, 5(19), 10240–10247.

Sahu, S. K (2021). "Thorium oxide nanoparticle core-coated polyaniline nanocomposite for Cr(VI) removal." Materials, 5(9), 233.

Saini, H., Sharma, A. L., and Singh, P. (2020). ZnO based ternary nanocomposites for improved electrochemical applications. Journal of Materials Chemistry A, 8(25), 12476–12491.

Sani Abdulrazak,S., Hussaini, K and Sani, H.M (2017). Evaluation of removal efficiency of

heavy metals by low-cost activated carbon prepared from African palm fruit. Applied Water Science. ,7(6), 3151–3155

Seehra, M. S., Narang, V., Geddam, U. K., and Stefaniak, A. B. (2017). Correlation between X-ray diffraction and Raman spectra of 16 commercial graphene–based materials and theirresulting classification. Carbon, 111, 380–385.

Shahzad, F., Zaidi, S.A and Naqvi, R.A (2020) 2D Transition Metal Carbides (MXene) for electrochemical sensing: A review. Critical reviews in analytical chemistry, 52(4), 848–864

Shalini, V., Navaneethan, M., Harish, S., Archana, J., Ponnusamy, S., Ikeda, H., and Hayakawa, Y. (2023). Design and fabrication of PANI/GO nanocomposite for enhanced room-temperature thermoelectric application. Applied Surface Science, 619, 156512.

Shruthi, Vighnesha, K. M., Sandhya, Sangeetha, D. N., and Selvakumar, M. (2018).Synthesis and Characterization of Reduced Graphene Oxide- Polyaniline Composite for Supercapacitor Applications. Surface Engineering and Applied Electrochemistry, 54(4), 359–366.

Silva, A.C.O.,Oliveira, L.C.F., Delfino, A.V., Meneghetti, M.R and Abreu, F.C (2016). Electrochemical Study of Carbon Nanotubes/Nanohybrids for Determination of Metal Species Cu^{2+} and Pb^{2+} in Water Samples. Journal of Analytical Methods in Chemistry, 9802738

Silva, M. K. L., and Cesarino, I. (2020). Electrochemical sensor based on Sb nanoparticles/reduced graphene oxide for heavy metal determination. International Journal of Environmental Analytical Chemistry, 1–15.

Simões,F.R., and Xavier,M.G.(2017).ElectrochemicalSensors.NanoscienceandIts Applications, 155–178.

Singh, A (2024). Enhanced photocatalytic performance of PANI-rGO-MnO_2 ternary composite for degradation of organic contaminants under visible light. Environmental Science and Pollution Research, 31(15), 18976–18985.

Singh, J., and Dhaliwal, A. S. (2022).Electrochemical and photocatalytic degradation of methylene blue by using rGO/AgNWs nanocomposite synthesized by electroplating on stainless

steel. Journal of Physics and Chemistry of Solids, 160, 110358.

Siva kumar, M., Lee, N. H., and Kim, Y. S. (2017). Facile synthesis of ZnO nanoparticles decorated reduced graphene oxide for enhanced electrochemical applications. Materials Science and Engineering: B, 220, 9–17.

Skoog, D. A., Holler, F. J., and Crouch, S. R. (2014). Principles of instrumental analysis (6th ed.). Cengage Learning.

Somerset, V.,Silwana, B., Horst, C., and Iwuoha, E. (2014). Construction andEvaluation of a Carbon Paste Electrode Modified with Polyanilineco-poly(dithiodianiline) for Enhanced Stripping VoltammetricDetermination of Metal Ions. Sensing in Electroanalysis, 8,143–154.

Soto, L. M., Rahman, A. K., and Patel, R. (2025). High selectivity and stability of PrGZ-2 electrode in the presence of interfering ions for Pb^{2+} detection. Sensors and Actuators B: Chemical, 302, 127-134.

Soto, L. M., Rahman, A. K., and Patel, R. (2025). High-performance sensors for Pb^{2+} ion detection: Evaluation of selectivity, reproducibility, and stability of PrGM-2 electrodes. Sensors and Actuators B: Chemical, 306, 101–109.

Stejskal, J., and Gilbert, R. G. (2002). Polyaniline. Preparation of a conductingpolymer (IUPAC Technical Report). Pure and Applied Chemistry, 74(5), 857–867.

Su, W.-Y., Liang, F.-Y., and Ma, L. (2012).Kinetic Study of Polyaniline Film Formation Using Ferric Chloride/Ammonium Persulfate as Composite Oxidant. International Journal of Polymer Analysis and Characterization, 17(2), 93–103.

Terán, E. J., Montes ,M. L., Rodríguez, C., Martino, L., Quiroga. M.,. Landa, R., and Pace, S. D. M. D.(2019). Importance for decontamination of water bodies. Assessment of sorption capability of montmorillonite clay for lead removal from water using laser–induced breakdown spectroscopy and atomic absorption spectroscopy. Microchemical Journal, 146, 1070–1076.

Thirumalraj, B., Rajkumar, C., Chen, S.-M., and Palanisamy, S. (2017). One-Pot Green Synthesis of Graphene Nanosheets Encapsulated Gold Nanoparticles for Sensitive and Selective

Detection of Dopamine. Scientific Reports, 7(1).

Torad, N.L., Naito,M., Tatami,J., Endo, A., Leo, S., Ishihara, S., Wu, K.C.W., Wakihara, T., and Yamauchi,Y (2014) Highly Crystallized Nanometer- sized Zeolites A with large Cs Adsorption Capability for the Decontamination of water. Chemistry – An Asian Journal, 9(3), 759–763.

Torres-Ronda, L., and Schelling i del Alcázar, X. (2014). The Properties of Water and their Applications for Training. Journal of Human Kinetics, 44(1), 237–248.

Travlou, N. A., Seredych, M., Rodríguez-Castellón, E. and Bandosz, T. J. (2015). Activated carbon-based gas sensors: effects of surface features on the sensing mechanism. Journal of Materials Chemistry A, 3(7), 3821–3831.

Tseng, R. J., Huang, J., Ouyang, J., Kaner, R. B., and Yang, Y. (2005). Polyaniline nanofiber/gold nanoparticle nonvolatile memory. Nano Letters, 5(6), 1077–1080.

Vasanthi, N., Sridharan, N., and Mandal, B. K. (2022). Simultaneous quantitation of lead and cadmium on an EDTA-reduced graphene oxide-modified glassy carbon electrode. ACS Omega, 7(49), 45469–45480.

Velempini, T., Pillay, K., and Mamba, B. B. (2018). Recent developments in the removal of heavy metals from wastewater using carbon-based nanomaterials. Journal of Nanomaterials, 2018, 1-14.

Velempini, T., Pillay, K., Mbianda, X. Y., and Arotiba, O. A. (2018). Application of a Polypyrrole/Carboxy Methyl Cellulose Ion Imprinted Polymer in the Electrochemical Detection of Mercury in Water. Electroanalysis, 30(11), 2612–2619.

Vilela, D., Parmar, J., Zeng, Y., Zhao, Y., and Sánchez, S. (2016). Graphene-based microbots for toxic heavy metal removal and recovery from water. Nano Letters, 16(4), 2860–2866.

Virji, S., Fowler, J. D., Baker, C. O., Huang, J., Kaner, R. B., and Weiller, B. H. (2005). Polyaniline nanofiber gas sensors: Examination of response mechanisms. Small, 1(6), 624–627.

Virji, S., Huang, J., Kaner, R. B., and Weiller, B. H. (2004). Polyaniline nanofiber gas sensors:

Examination of response mechanisms. Nano Letters, 4(3), 491–496.

Wang, H., Yi, H., Chen, X., Wang, X., and Wang, X. (2012). Manganese dioxide/graphene nanocomposite for supercapacitor applications. Electrochimica Acta, 59, 113–120.

Wang, J. (2010). Electrochemical stripping analysis: Past, present, and future. Analytical Chemistry, 82(1), 66–77

Wang, J., and Hu, Z. (2019). Influence of scan rate on the cyclic voltammetry behavior of electroactive materials. Electrochimica Acta, 328, 135071.

Wang, N., Zhao, W., Shen, Z., Sun, S., Dai, H., Ma, H and Lin, M (2019).Sensitiveandselective detection of Pb (II) and Cu (II) using a metal-organic framework/polypyrrole nanocomposite functionalized electrode. Sensors and Actuators B: Chemical, 304, 127286.

Wang, S., Zhang, Y., and Li, F. (2020). Nanomaterial-based electrochemical sensors for environmental monitoring: Detection of heavy metals. Environmental Science & Technology, 54(5), 3106–3114.

Wang, Y (2017). The development of a ternary nanocomposite for the removal of Cr(VI) from polluted water. RSC Advances, 7(82), 51994-52001.

Wang, Y., and Zhang, S. (2021).Nanocomposite-based electrochemical sensors forthe detection of Pb^{2+}ions in environmental samples.Environmental Science &Technology, 55(6), 3021–3029.

Wang, Y., Wang,,L., Huang,W.,Zhang,ʹT.,Hu,X. Perman, J.A and Ma, S.(2017). A metal–organic framework and conducting polymer based electrochemical sensor for high performance cadmiumiondetection.JournalofMaterialsChemistry A, 5(18), 8385–8393..

Wang,J.(2006).Analytical Electrochemistry(3rded.). Wiley-Interscience.

Wei, W., Cui, X., Chen, W., and Ivey, D. G. (2011). Manganese oxide-based materials as electrochemical supercapacitor electrodes. Chemical Society Reviews, 40(3), 1697–1721.

WestbroekP.(2005). Electrochemicalmethods. Analytical Electrochemistry in Textiles, 37–69.

Wu, W., Jia, M., Zhang, Z., Chen, X., Zhang, Q., Zhang, W., Li, P., and Chen, L. (2019). Sensitive, selective and simultaneous electrochemical detection of multiple heavy metals in environment and food using a low-cost Fe_3O_4 nanoparticles/fluorinated multi-walled carbon nanotubes sensor. Ecotoxicology and Environmental Safety, 175, 243–250

Wu, Q., Chen, M., Wang, S., Zhang, X., Huan, L., and Diao, G (2016). Preparation of sandwich-like ternary hierarchical nanosheets manganese dioxide/polyaniline/reduced graphene oxide as electrode material for supercapacitor. Chemical Engineering Journal, 304, 29–38.

X.(2019).Graphene oxide-based materials for efficient removal of heavy metal ions from aqueous solution: A review. Environmental Pollution. 252, 62-73.

Xiao, L., Wildgoose, G. G., and Compton, R. G. (2008). Sensitive electrochemical detection of arsenic (III) using gold nanoparticle modified carbon nanotubes via anodic stripping voltammetry. AnalyticaChimicaActa, 620(1-2), 44–49.

Xu, T., Dai, H. and Jin, Y (2020) Electrochemical sensing of lead(II) by differential pulse voltammetry using conductive polypyrrole nanoparticles. MicrochimActa 187, 23 (2020).

Xu, Y., Wu, Q., Sun, Y., Bai, H., and Shi, G. (2020). Three-dimensional self-assembly of graphene oxide and polypyrrole nanocomposites for supercapacitors. ACS Nano, 4(2), 735-741.

Yakuphanoglu, F., and Şenkal, B. F. (2007). Electronic and thermoelectric properties of polyaniline organic semiconductor and electrical characterization of Al/PANI MIS diode. The Journal of Physical Chemistry C, 111(4), 1840–1846

Yan, X. B., Han, Z. J., Yang, Y., and Tay, B. K. (2007). Room-temperature hydrogen gas sensor based on polyaniline nanofibers. Sensors and Actuators B: Chemical, 123(1), 107–113.

Yi, W., He, Z., Fei, J., and He, X. (2019). Sensitive electrochemical sensor based on poly(l-glutamic acid)/graphene oxide composite material for simultaneous detection of heavy metal ions. RSC Advances, 9(30), 17325–17334.

Yi-Su, W., Liang, F.Y and Ma, L(2012) Kinetic study of Polyaniline Film Formation usingFerric Chloride/Ammonium Persulfate as Composite Oxidant. International Journal of Polymer

Analysis and Characterization, 17(5), 328–337

Yuan, S., Feng, L., Wang, K., Pang, J., Bosch, M., Lollar, C., and Zhou, H.C. (2018).Stable Metal-Organic Frameworks: Design, Synthesis, and Applications. Advanced Materials, 1704303.

Yue, Z., and Economy, J. (2017). Carbonization and activation for production of activatedcarbon fibers. Activated Carbon Fiber and Textiles, 61–139.

Zanganeh, A. R., and Amini, M. K. (2007). A potentiometric and voltammetric sensor based on polypyrrole film with electrochemically induced recognition sites for detection of silver ion. Electrochimica Acta, 52(11), 3822–3830

Zawodzinski,T.A.,Derouin,C.,Radzinski,S.,Sherman,R.J., Smith,V.T.,Springer,T.E., and Gottesfeld, S. (1995). Water uptake by and transport through Nafion 117 membranes. Journal of The Electrochemical Society, 140(4), 1041–1047.

Zeng, F., Qin, Z., Liang, B., Li, T., Liu, N., and Zhu, M. (2015). Polyaniline nanostructures tuning with oxidants in interfacial polymerization system. Progress in Natural Science: Materials International, 25(5), 512–519.

Zhang, D., and Gan, L. (2017). High performance electrochemical supercapacitors based on polyaniline/graphene composite materials. Journal of Power Sources, 357, 33–41.

Zhang, H., and Li, J. (2019). Electrochemical sensors based on composite materials for selective detection of lead ions in the presence of interfering metal ions. TrAC Trends in Analytical Chemistry, 119, 19-27.

Zhang, H., and Li, J. (2020). Electrochemical sensors based on nanomaterials for selective detection of heavy metal ions in water. TrAC Trends in Analytical Chemistry, 119, 19–27.

Zhang, J., Zhang, H., Wu, J., and Zhang, J. (2013). Techniques for PEM Fuel Cell Testing and Diagnosis.Pem Fuel Cell Testing and Diagnosis, 81–119.

Zhang, L (2021). Ternary nanocomposite-based smart sensor: Reduced graphene oxide/polydopamine/alanine nanocomposite for simultaneous electrochemical detection of Cd^{2+},

Pb^{2+}, Fe^{2+}, and Cu^{2+} ions. Pub Med.

Zhang, L., Wan, M., and Wei, Y. (2006). Nanoscaled polyaniline fibers prepared by ferric chloride as an oxidant. Macromolecular Rapid Communications, 27(5), 366–371.

Zhang, W. L., Liu, Y. D., and Choi, H. J. (2012).Fabrication of semiconducting graphene oxide/polyaniline composite particles and their electrorheological response under an applied electric field. Carbon, 50(1), 290–296.

Zhang, W., An, Y., Li, S. Liu Z., Chen Z., Ren Y., Wang S., ZhangX. and WangX.(2020). Enhanced heavy metal removal from an aqueous environment using an eco-friendly and sustainable adsorbent. Sci Rep 10, 16453.

Zhang, Y (2021). "Polyaniline nanorod-dotted graphene oxide nanosheets for Cr(VI) adsorption." Materials, 5(9), 233.

Zhang, Y., Zhang, L., and Zhou, C. (2018). Review of chemical vapor deposition of graphene and related applications. Accounts of Chemical Research, 46(10), 2329–2339.

Zhang, Y., Wang, X., Li, H., & Chen, J. (2016). New frontier of hybrid energy storage devices: Evolution of capacitive mechanisms and escalation of nanocomposite materials. RSC Advances**,** 6(93), 90190–90210.

Zhou, S.-F., Han, X.-J., Fan, H.-L., Huang, J., and Liu, Y.-Q. (2018). Enhanced electrochemical performance for sensing Pb(II) based on graphene oxide incorporated mesoporous MnFe 2 O 4 nanocomposites. Journal of Alloys and Compounds, 747, 447–454.

Zhu, Y (2021). "Mg/Al LDH polyaniline nanocomposites for Cr(VI) adsorption." Materials, 5(9), 233.

Zhang, W. L., Liu, Y. D., and Choi, H. J. (2012).Fabrication of semiconducting graphene oxide/polyaniline composite particles and their electrorheological response under an applied electric field. Carbon, 50(1), 290–296.

Zhang, W., An, Y., Li, S. Liu Z., Chen Z., Ren Y., Wang S., Zhang X.and Wang X.(2020).

Enhanced heavy metal removal from an aqueous environment using an eco-friendly and sustainable adsorbent. Sci Rep, 10, 16453.

List of Publications

S.No	Name of the Journal/Conference/Book	Jounal indexing (Scopus/UGC/ Web of Science)	Published Date (Date/Month/Year)	Volume & Issue Number	ISSN/ISBN Number	Impact Factor/SJR
1	Journal of Indian Chemical Society	Scopus	15-Apr-25	Volume 102, Issue 6	2667-2847.	3.2
2	Ionics	Scopus	11-Jan-25	Volume 31, Issue 3	0947-7047	2.6
3	Bulgarian Chemical Communications	Scopus	30-Apr-23	Volume 55, Issue A	2534-9899	0.14
4	Bulgarian Chemical Communications	Scopus	27-Apr-23	Volume 55, Issue A	2534-9899	0.14
5	AIP conf. proc	Scopus	8-Sep-23	Volume 2800	1551-7616	0.16
6	Journal of Environmental Engineering and Science	Scopus	21-Nov-22	Volume 18, Issue 1	1496-256X	1
7	Advanced Nanomaterials for Water Purification, Volume II - Remediation of Various Contaminants"	Scopus	Under Process	Volume II	978-3-319-37470-3	Under Process

List of Conferences

Sr. No	Conferences name
1.	International conference on Recent advances in Fundamental and Applied Sciences (RAFAS 2023), March 24- 25, 2023, Lovely Professional University, Punjab
2.	APM 2023 conference 25-26 April 2023, G.B. Pant University of Agriculture and Technology, Pantnagar
3.	International conference on Recent advances in Fundamental and Applied Sciences (RAFAS 2021), June 25- June 26, 2021, Lovely Professional University, Punjab
4.	International Conference on Materials for Emerging Technologies-2021 (ICMET-21), February 18- February 19, 2022, Virtual mode Lovely Professional University, Punjab

Journal of the Indian Chemical Society 102 (2025) 101718

Contents lists available at ScienceDirect

Journal of the Indian Chemical Society

journal homepage: www.journals.elsevier.com/journal-of-the-indian-chemical-society

rGO/ZnO modified polyaniline hybrid ternary nanocomposite as highly sensitive electrode for Pb^{2+} detection in aqueous sources

Nisha [a], Goverdhan Singh [a], Anil Kumar [a], Parteek Prasher [b], Harish Mudila [a,*]

[a] Department of Chemistry, Lovely Professional University, Punjab, 14411, India
[b] Department of Chemistry, UPES, Dehradun, 248007, India

ARTICLE INFO

Keywords:
Ternary nanocomposite
Carbon paste electrode
DPASV
Electrochemical detection
Heavy metals
LOD and LOQ

ABSTRACT

This research work demonstrates the effective determination of Pb^{2+} ions from aqueous sources using systematically developed ternary nanocomposites (PrGZs). These nanocomposites were synthesized through a judicious combination of Polyaniline (PANI), reduced Graphene Oxide (rGO), and Zinc Oxide (ZnO). The physical properties of PrGZs were characterized using techniques such as Fourier Transform Infrared Spectroscopy (FTIR), X-ray Diffraction (XRD), Thermogravimetric Analysis (TGA), Differential Scanning Calorimetry (DSC), and Scanning Electron Microscopy (SEM). The electrochemical performance of PrGZs was evaluated using Electrochemical Impedance Spectroscopy (EIS) and Differential Pulse Anodic Stripping Voltammetry (DPASV) with a carbon paste electrode (CPE). Notably, PrGZ-2 exhibited significantly improved detection and sensitivity compared to the individual components and binary composite, attributed to its low resistance, pseudo-capacitive behaviour, and enhanced electron transfer properties. The calculated limits of detection (LOD) and quantification (LOQ) for PrGZ-2 were 0.3 μM and 1.16 μM, respectively, within a Pb^{2+} ion concentration range of 1 μM–5.5 μM. This indicates good sensitivity for low concentration detection, with an R^2 value of 0.994. The relative standard deviation (RSD) for PrGZ-2 was 2.13 %, confirming acceptable repeatability and precision of the measurements on the working electrode at a scan rate of 0.01 V/s. Furthermore, the composite material displayed good results in the presence of interfering metals and demonstrated appreciable repeatability and stability. These findings suggest that the material holds significant potential and could be evaluated for detecting other toxic heavy metals, expanding its application for environmental monitoring without interference from lead.

1. Introduction

Heavy metals (HMs), such as lead ions (Pb^{2+}), Copper ions (Cu^{2+}), and cadmium ions (Cd^{2+}), etc. are well-known water pollutants [1]. These HMs (including Pb^{2+}), are highly toxic, persistent, and bio-accumulative, posing significant health risks when they exceed safe concentrations, as outlined by organizations like the World Health Organization (WHO, 10 ppb) [2]. Even trace amounts of Pb^{2+} in drinking water can lead to biomagnification, posing serious threats to human health, especially if the concentration exceeds the prescribed limits. Detecting and removing Pb^{2+} is critical for improving environmental and public health outcomes [3]. Traditional methods of detection and removal often create toxic sludge and are costly, exacerbating environmental problems [4]. The limitations of conventional methods necessitate the development of more sustainable and efficient solutions. This includes exploring novel adsorbent materials with high selectivity and sensitivity for Pb^{2+}, developing cost-effective and environmentally friendly removal technologies, and optimizing removal processes based on the specific physicochemical factors of the contaminants and the environment [5]. Electrochemical sensing provides a powerful tool for detecting HM ions and other analytes with high sensitivity, selectivity, accuracy, and speed. The ongoing development of new electrode materials and techniques continues to expand the capabilities of this technology. There are different types of electrochemical methods employed for detecting HMs from aqueous sources. Among them, Anodic Stripping Voltammetry (ASV) is highly sensitive for trace metal detection. It involves preconcentration of metals onto an electrode, followed by anodic stripping (oxidation). Examples highlight its use with modified electrodes (PANI/G, EDTA-PANI/GO, PANI-Au) for enhanced sensitivity and lower detection limits for metals like Pb^{2+} and other HMs [6]. Differential Pulse Anodic Stripping Voltammetry (DPASV), an advanced version of ASV, applies potential pulses on a

* Corresponding author.
E-mail addresses: harismudila@gmail.com, harish.19331@lpu.co.in (H. Mudila).

https://doi.org/10.1016/j.jics.2025.101718
Received 7 March 2025; Received in revised form 5 April 2025; Accepted 12 April 2025
Available online 15 April 2025
0019-4522/© 2025 Indian Chemical Society. Published by Elsevier B.V. All rights are reserved, including those for text and data mining, AI training, and similar technologies.

linear ramp, measuring the current difference. It provides improved sensitivity compared to linear sweep voltammetry and is used for detecting HMs with modified electrodes (EDTA-PANI/SWNTs, cerium oxide-polyaniline) with detection limits in the μM and nM ranges [7]. DPASV-like advanced technique requires modified electrodes that are crucial for enhancing sensitivity, selectivity, and detection limits.

Not only is the technique for sensing of analyte significant, the selection of appropriate electroactive materials also plays a critical role in sensing. Numerous electroactive materials have been employed by researchers to detect HMs and other contaminants in aqueous sources [2,8,9]. Activated charcoal (AC), prized for its porous structure, high surface area, and versatile surface chemistry, finds extensive use in sensing gases and other analytes [10]. AC effectively removes HM ions like Cd^{2+}, Cu^{2+}, Ni^{2+}, Pb^{2+}, etc. from water, achieving high removal rates (over 90 %) at 80 °C and a 60-min contact time. However, it struggles with contaminants like sodium, fluoride, nitrates, microbes, and water hardness due to slow kinetics and poor selectivity, and it has a limited lifespan. Its properties are tunable based on preparation, precursor, and conditions, influencing its adsorptive capacity [11]. Carbon nanotubes (CNTs), including multi-walled (MWCNTs) and single-walled (SWCNTs), offer exceptional electrical conductivity, high surface area, and robust mechanical and chemical stability, making them ideal for HM detection [12]. CNTs, particularly when coupled with electrochemical stripping analysis like differential pulse anodic stripping voltammetry (DPASV), demonstrate remarkable detection capabilities. MWCNTs have also been used in flame atomic absorption spectrometry (FAAS) for Cu^{2+}, Zn^{2+}, Mn^{2+}, and Pb^{2+} detection, with LODs in the μg/L range [13]. Furthermore, CNTs showed impressive adsorption capacities for HM ions attributed to ion exchange and electrostatic interactions. Despite their potential, CNT applications are hindered by high cost, the need for high purity and pretreatment, defects, functionalization complexities, and particle aggregation, limiting their widespread use in sensors [14]. MXenes, known for their electron-richness, high surface area, hydrophilicity, and conductivity, are promising materials for HM removal and detection [15]. Their nanoscale forms, with interlayer gaps below 2 Å, efficiently trap metal ions [16]. Materials like conducting polymers (polyaniline, polypyrrole, etc.), carbonaceous materials (graphene, graphene oxide), and metal nanoparticles (metal oxides, etc.) are also widely used for diverse applications [17], including detecting HMs (viz, Pb^{2+}) in aqueous solutions [18]. Hybrid materials, combining different materials, often exhibit enhanced performance compared to individual components. The detection limit of HMs is constantly being lowered due to the improvement of sensor materials. The functionality of each material is affected by many factors, such as pH, temperature, etc. Conducting polymers like polyaniline (PANI) have electrical properties similar to metals and are lightweight, non-corrosive, and have excellent physical, chemical, electrical, and optical properties; however, film formation issues can arise [4,6]. Transition Metal Composites, viz. transition metal oxides (TMOs, including ZnO), etc., have high sensitivity, tenability, semiconductive nature, rapid charge transfer, appreciable electrical conductivity, and large surface area; however, wide band gap and high cost limit their excessive use [6]. Carbonaceous materials such as reduced graphene oxide (rGO), etc., have high surface area, good conductivity, chemical stability, tunability, and affordability. rGO possesses high conductivity, a large surface area, and excellent biocompatibility, although with some weaknesses like agglomeration and reduced surface area due to inter-functional bonds [19,20]. **Akhtar, M.** reported a ternary hybrid of PANI-alanine-rGO, demonstrating sensitive analysis of toxic metal ions, with LOD of 0.03 nM for Cd^{2+} 0.045 nM for $Pb^{2+}$and 0.063 nM for Cu^{2+} ions [21]. **Dong, Y.** utilized a gold nanoparticle/PANI/graphene modified electrode composite, achieving LOD of 0.1 nM under optimal conditions [22]. **Muralikrishna, S.** developed hydrogels of polyaniline with graphene oxide for highly sensitive electrochemical determination of Pb^{2+}, reaching a limit of detection of 0.04 nM [23]. **Singh, G.** synthesized a hybrid ternary composite based on PPY, GO, and ZnO with a limit of detection of 0.05 μM for Pb^{2+} [2].

This research addresses the critical issue of HM contamination, specifically Pb^{2+}, which is a significant environmental and health hazard [24,25]. The selection of PANI, rGO, and ZnO is well-justified, highlighting the synergistic benefits of each component. PANI contains amine/imine groups for metal ion affinity. rGO has a high surface area and oxygen functionalities for adsorption, and ZnO has enhanced electrical properties. Electrochemical performance engages the use of DPASV and demonstrates the effectiveness of the nanocomposite of PANI/rGO/ZnO (PrGZ) for Pb^{2+} detection, with impressive LOD (0.3 μM) and LOQ (1.16 μM) values within a concentration range of 1–5.5 μM. It provides specific numerical data, including LOD, LOQ, R^2 (0.994), and RSD (2.13 % at a 0.01 V/s scan rate), which enhances the credibility of the findings. PrGZ nanocomposite exhibits enhanced sensitivity and selectivity for Pb^{2+} detection compared to individual components. The composite material demonstrates good repeatability and precision, highlighting its potential for practical environmental monitoring applications beyond Pb^{2+}, and suggesting the need for further exploration into its detection capabilities for other toxic HMs. This innovative sensor platform, proven effective for Pb^{2+} detection, holds significant potential for broader industrial applications in monitoring various toxic HMs, offering a versatile solution for environmental safety and regulatory compliance.

2. Materials and Methodology

2.1. Materials

Aniline, graphite, hydrogen peroxide, hydrochloric acid, hydrazine hydrate, and ethanol were purchased from LOBA Chemie Pvt Ltd. Sodium Dodecyl Sulphate (SDS) was obtained from Qualikems Fine Chem. Ferric chloride was obtained from Alpha Chemika. Sulfuric acid was procured from Avantor Performance Materials India Ltd. Potassium permanganate was obtained from HiMedia Laboratories Pvt. Ltd., and Sodium Nitrate was obtained from Avarice Industries. All chemicals were of analytical grade and used without further purification. For this research work, ZnO from LOBA Chemie Pvt. Ltd. was used as received, without further purification.

2.2. Preparation of polyaniline (PANI)

PANI was prepared by chemical oxidative polymerization. An anionic surfactant, SDS (1.145 g), was added to 30 mL of deionized water (DIW) and stirred for 15 min at room temperature. Subsequently, $FeCl_3$ (0.9 g in 30 mL), acting as an oxidant, was added. To this mixture, 2.34 mL of aniline monomer was added dropwise to initiate the polymerization reaction, with continuous stirring. The formation of a green color indicated the progression of the polymerization process, which was continued for 24 h. After this period, the resulting solution was filtered, and the solid residue was repeatedly washed with DIW until the filtrate was colorless. The obtained solid was then dried in a vacuum oven at 40 ± 1 °C until moisture loss was achieved [26].

2.3. Preparation of graphene oxide (GO) and reduced graphene oxide (rGO)

GO was synthesized by the modified Hummers' method, involving the chemical oxidation of graphite (1 g). Sodium nitrate ($NaNO_3$, 0.5 g) and potassium permanganate ($KMnO_4$, 3 g) were dissolved in concentrated sulfuric acid (H_2SO_4, 23 mL). The reaction was quenched using 10 % hydrogen peroxide (H_2O_2). The resulting black product was washed five times with hydrochloric acid (HCl) and warm DIW to remove impurities. The dry GO powder was obtained after heating the filtrate at 60 °C for 4 h in a vacuum oven [27].

For the preparation of rGO, 2 g of GO was added to 250 mL of distilled water in a beaker, and the mixture was stirred vigorously.

Table 1
Varying ratio of PANI and rGO to prepare PrG compositions.

Materials	Ratios			
	4:1 (PrG-1)	2:1 (PrG-2)	1:1 (PrG-3)	1:2 (PrG-4)
PANI(mg)	100	100	100	100
rGO(mg)	25	50	100	200

Table 2
Varying ratio of PrG-2 and ZnO to prepare PrGZ compositions.

Material	Ratio			
	4:1 (PrGZ-1)	2:1 (PrGZ-2)	1:1 (PrGZ-3)	1:2 (PrGZ-4)
PrG-2(mg)	100	100	100	100
ZnO (mg)	25	50	100	200

Hydrazine hydrate (NH_2–NH_2. H_2O, 2 mL) was added dropwise to the solution, and the mixture was heated at 80 °C for 72 h with continuous stirring. The solution was then centrifuged, and the resulting precipitate was separated and dried. The black flocculent substance that precipitated out was washed with ethanol and water and dried at 60 °C for 24 h [28].

2.4. Fabrication of binary PANI/rGO (PrG) composites

To prepare binary composites of PANI with rGO (PrG), 100 mg of PANI was dispersed in 5 mL of ethanol. Varying proportions of rGO (as specified in Table 1) were then added to the PANI dispersion. The mixture was sonicated to ensure thorough mixing of the two components, resulting in the formation of binary composites. The optimal binary composition (PrG-2), as determined by electrochemical studies (discussed later), was subsequently used for the preparation of ternary composites.

2.5. Fabrication of ternary PANI/rGO/ZnO (PrGZ) composites

To prepare the ternary composite of PANI/GO (PrG) and ZnO, the optimal composition from the PrG series, PrG-2, was selected. A specific amount of ZnO, calculated as a percentage of PrG-2, was added to a vessel containing 5 mL of ethanol. This mixture was then sonicated for 30 min at room temperature to form the ternary composites (PrGZ), as detailed in Table 2. The composition exhibiting the best electrochemical performance was subsequently used for Differential Pulse Anodic Stripping Voltammetry (DPASV) studies.

2.6. Electrode preparation

A carbon paste electrode (CPE) was developed as the working electrode. It was fabricated by thoroughly mixing 4 g of graphite powder with 1.8 mL of paraffin oil in a mortar and pestle to create a homogenous paste. This paste was then dried to remove moisture and subsequently packed into an insulin syringe to form the electrode. The CPE surface was rubbed on paper to achieve a shiny finish, and a 2 mm diameter copper wire was inserted to create the electrical connection for the electrode body [29].

3. Characterization

PANI was effectively synthesized by chemical oxidative polymerization, GO, and rGO by Hummer's method and chemical reduction method, respectively, by ex-situ means. All powdered sample was characterized using Fourier Transform Infrared (FTIR) using PerkinElmer Spectrum IR Version 10.6.1, X-ray Diffraction (XRD) by Bruker D8 advance X-ray diffractometer using Cu-Kα radiation, thermal studies by Thermogravimetric Analysis (TGA) and Differential Scanning Calorimetry (DCS) of PerkinElmer, Scanning Electron Microscope (SEM) of company JEOL(JSm-7610Fplus).

3.1. FTIR

FTIR was studied in the range from 4000 to 400 cm^{-1} for all the materials (Fig. 1A). The expected range of PANI at 600-900 cm^{-1}, 1000-1180 cm^{-1}, 1200-1300 cm^{-1}, 1400-1480 cm^{-1}, 1500-1600 cm^{-1} and 3000-3500 cm^{-1} are due to aromatic C–H out of plane bending vibrations, aromatic C–H in-plane bending vibrations, C–N stretching of the secondary aromatic ring, C═C stretching vibrations of benzenoid rings, C═C stretching of quinoid ring and N–H stretching vibrations of secondary amines respectively [30]. The observed values for PANI were 3407 cm^{-1}, 1548 cm^{-1}, 1452 cm^{-1}, 1215 cm^{-1}, 1029 cm^{-1}, and 770 cm^{-1}. Literature showed the peaks of GO at 3400-3200 cm^{-1}, 1724 cm^{-1}, 1619 cm^{-1}, and 1063 cm^{-1} for O–H stretching, C═O stretching,

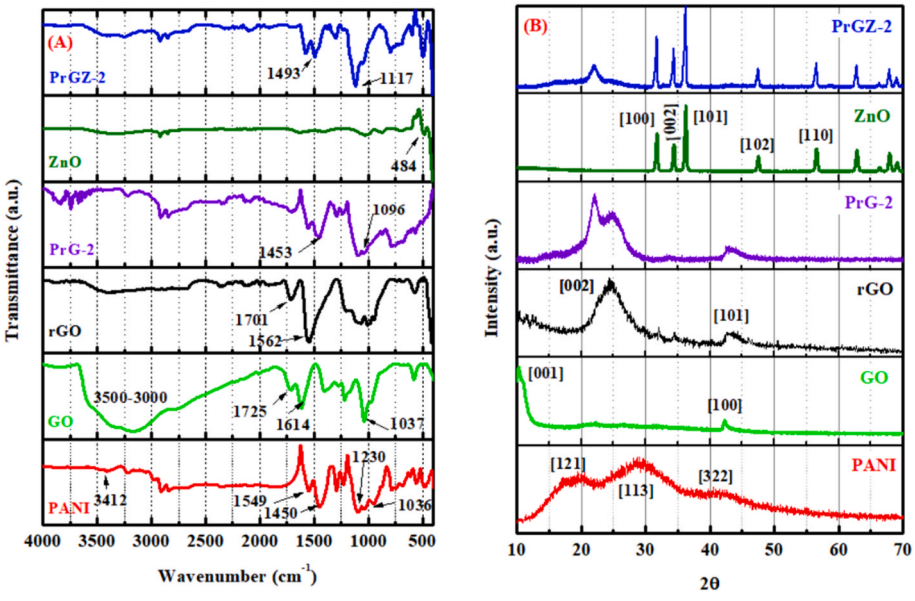

Fig. 1. FTIR (A) and XRD (B) of PANI, GO, rGO, PrG-2, PrGZ-2 and ZnO.

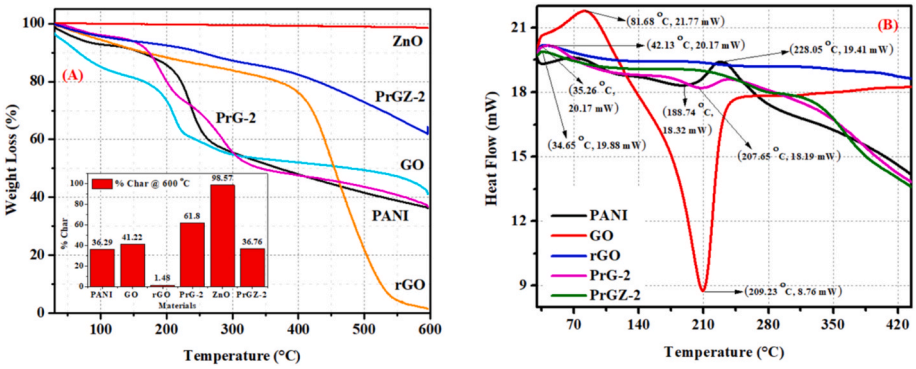

Fig. 2. TGA (A) and DSC (B) of PANI, GO, rGO, ZnO, PrG-2 and PrGZ-2.

C═C stretching, and C–O stretching, respectively. The observed values of GO were found to be 3400 cm^{-1}, 1725 cm^{-1}, 1614 cm^{-1}, and 1037 cm^{-1}, and peaks for rGO were observed at 1562 and 3434 cm^{-1} due to the skeletal vibrations of the graphene backbone chain and –OH stretching vibrations, respectively [31]. Binary composite (PrG-2) showed peaks at 1708 cm^{-1}, 1453 cm^{-1}, 1292 cm^{-1}, and 1096 cm^{-1} due to the C═O group, C═C stretching of benzenoid rings, C–N bending of benzenoid rings, and C–H stretching of quinoid rings. ZnO showed characteristic peaks at 484 cm^{-1} that correspond to Zn and oxygen bonding. Ternary composite (PrGZ-2) showed values at 1493 cm^{-1}, 1117 cm^{-1}, and 500 cm^{-1}, corresponding to the peaks for C═C stretching benzenoid ring, N = Q = N stretching of the quinoid ring, and ZnO structure showed fabrication of PrGZ [32,33].

3.2. XRD

XRD involves the irradiation of material with X-rays and measures the intensities and scattering angle of transmitted X-rays in the specific range of 2θ from 10° to 70° (Fig. 1B). XRD of PANI showed two broad peaks at 2θ = 20° and 28°, which are due to parallel polymer series and are the characteristic peak of PANI [34]. GO exhibits a sharp peak at 2θ = ~10°, revealing thriving alteration of GO from graphite [35]. The peaks of GO in PrG-2 get reduced due to the establishment of composite and rGO sheets get surrounded by PANI, and the peaks were at 2θ = 10.8° and 22°, and rGO samples show broad peaks at approximately 2θ at 24.5° [24]. Ternary nanocomposite (PrGZ-2) illustrates that the attributed peaks of graphene oxide and ZnO are entirely moved out, which can be attributed to the dispersion of the PANI around the rGO chain and ZnO. The intense peaks at 2θ = 31.6°, 34.3°, 36.2°, and 47.3° are characteristic peaks of ZnO [36].

3.3. Thermal analysis

3.3.1. Thermogravimetric Analysis (TGA)

TGA resolves the thermal stability of the material by monitoring the weight loss due to dehydration, desorption, and decomposition. In the current study, TGA was performed in an inert atmosphere of N_2 at a temperature range of room temperature to 600 °C at a rate 10 °C/min (Fig. 2A). In PANI, weight loss was observed at 100 °C and 268 °C due to the removal of water molecules and deprivation of PANI backbone [37]. In GO, weight loss occurred in three steps at the temperature of 117 °C, 200 °C, and above 500 °C because of the exclusion of H_2O molecules, thermal breakdown of rickety oxygen-containing functional groups to yield CO, CO_2, and degradation of sheets, respectively [38]. PrG-2 (binary composite) is positioned at the weight loss assortment of PANI and rGO, however, the outline of the weight loss curve of PrG-2 resembles rGO as PANI has been efficiently grafted on the rGO surface [39]. The TGA of Ternary Composite (PrGZ-2) shows confirmation of superior thermal stability because of the enlarged surface region, improved functionality, and uniform diffusion of PANI over the surface of rGO and ZnO. It was observed that there was a smaller weight loss taking place in rGO as compared to GO owing to the smaller number of oxygen moieties (functional groups) [40]. TGA of PrG-2 showed that the first major weight loss occurred between 30°C and 160 °C with a weight loss percentage of 16.21 %, which may be attributed to loss of moisture in the binary composite. The weight loss occurred between 160 and 400 °C with a weight loss percentage of 38.29 %, which is thought to be caused by the elimination of remaining oxygenated functional groups of rGO. The third major weight loss occurred above 400 with a weight loss percentage of 16.36 %, which is attributed to polymer degradation. PrGZ-2 at 109 °C experiences a 1 % weight loss, attributed to the evaporation of moisture. At 266 °C, a further 2 % weight loss occurs due to the release of volatile gases, and at 450 °C, a significant decomposition event is expected, likely related to the breakdown of the rGO and ZnO components [41]. The comparative char percentage left at the end is shown in the inset in Fig. 2A, signifying the impact of rGO and ZnO in PrG-2 and PrGZ-2 composites.

3.3.2. Differential Scanning Calorimetry (DSC)

DSC reveals thermal stability by considering the parameters heat flow, endothermic, and exothermic curves which signify the stability of composites performed in an inert atmosphere (N_2) in the temperature range of room temperature to 430 °C at the rate 10 °C/min (Fig. 2B). PANI showed an endothermic peak at 100 °C due to the loss of water molecules and at 300 °C justified breakdown of PANI backbone [38]. For GO, an endothermic peak at 100 °C indicates the evaporation of water, and an endothermic peak at 208 °C due to the gasification of oxygenated functional groups. rGO showed an endothermic peak at 40 °C, corresponding to the loss of water molecules, and an exothermic peak at 200 °C, which is associated with the loss of oxygen-containing functional groups. PrG-2 showed an endothermic peak at 38.3 °C, indicating absorption of heat by the material. This is attributed to the loss of water molecules present in the sample. Endothermic processes involve the breaking of intermolecular forces, and an exothermic peak is recorded at 270 °C, signifying the release of heat by the material. This is associated with the evolution of carbon monoxide (CO) and carbon dioxide (CO_2) gases, suggesting the breakdown or oxidation of the organic components in the material. Exothermic processes involve the formation of new chemical bonds and are common in combustion reactions. Another exothermic peak is observed, indicating further decomposition. This is assigned to the degradation of the polymer backbone of PANI, the primary organic component of the composite. PrGZ-2 showed peaks at two specific temperatures: 40 °C and 294 °C. At 40 °C, an "endothermic" peak is noted, indicating a process that absorbs heat, such as dehydration or a phase transition, and the loss is attributed to moisture, indicating water evaporation. At 294 °C, an exothermic peak is observed, signifying a process that releases heat, like crystallization or combustion, and the loss is associated with oxygen-containing functional groups, implying the decomposition or removal of chemical groups containing oxygen atoms from the material's structure [39–41].

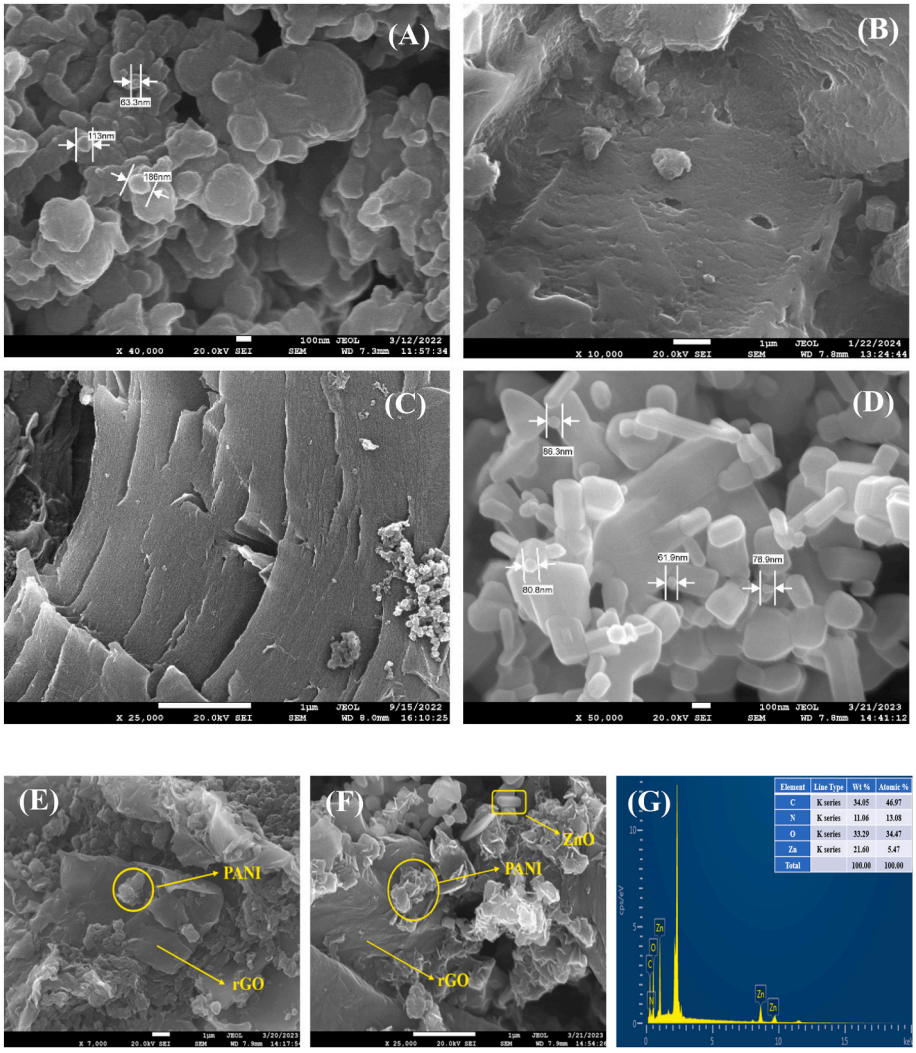

Fig. 3. SEM of PANI (A),GO (B), rGO (C), ZnO (D), PrG-2 (E), PrGZ-2 (F), and EDS data of PrGZ-2 (G).

3.4. Scanning Electron Microscopy (SEM)

SEM gives information on the morphology of the material under investigation; the SEM images of PANI, rGO, PrG-2, and PrGZ-2 are presented in Fig. 3. Superior spherical shape particles with diverse sizes characterized the morphology of PANI (Fig. 3A) [27]. rGO displayed a uniform shape and smooth, large flaky surface (as compared to GO, Fig. 3B), which developed the sinuate structural characteristics of rGO after reduction from GO (Fig. 3C) [28]. ZnO exhibited rod-shaped nanoparticles, these nanoparticles reveal some faceting (Fig. 3D) in their nanostructure. The morphology of the binary composite (PrG-2) represents the uniform surrounding of PANI by rGO flakes (Fig. 3E) [36]. SEM images of the ternary composite (PrGZ-2) exhibit numerous crooked shapes together with flakes (rGO), rod-like (ZnO), and fibrous

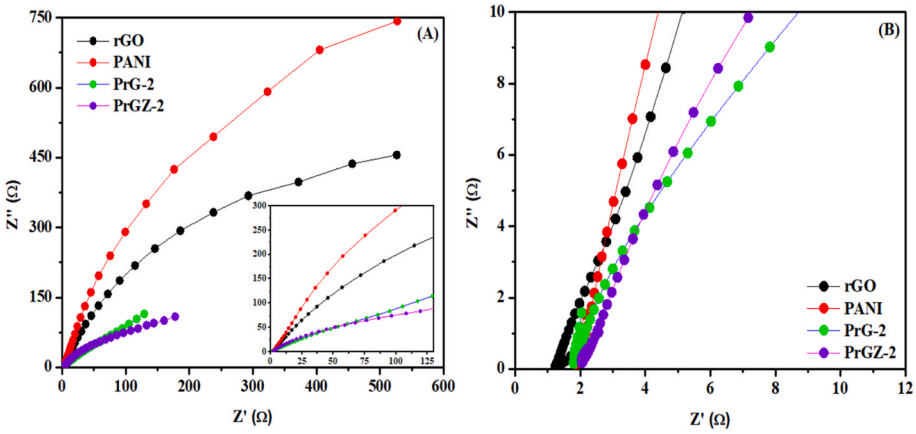

Fig. 4. EIS of PANI, rGO, PrG-2, and PrGZ-2 (A) at a wider impedance range (B) at a narrower impedance range.

structures (PANI). The rGO flakes are set in the PANI association with the ZnO nanoparticles, hence offering stability to the ternary composite (Fig. 3F). Fig. 3G represents the SEM-EDS of the ternary composite, representing the presence of corresponding elements and their weight percentage [42–44].

4. Electrochemical characterization

The electrochemical performance of a prepared nanocomposite material can be effectively evaluated using both Electrochemical Impedance Spectroscopy (EIS) and DPASV. These techniques offer complementary insights into the material's electrochemical properties, such as charge transfer, capacitance, and electroactive surface area.

4.1. Electron impedance spectroscopy (EIS)

The EIS technique is a tool for investigating redox processes and other electrochemical phenomena occurring at the electrode/electrolyte interface. The electron transfer of PANI, rGO, PrG-2, and PrGZ-2 was examined in a solution containing 1 M KOH within the frequency range of 0.1 Hz–10^5 Hz. The Nyquist plot, which is commonly used in EIS, is a graphical representation of the impedance data, typically showing the real (Z′) and imaginary (Z″) components of impedance as a function of frequency. The plot often exhibits a semicircular arc at higher frequencies, corresponding to charge-transfer resistance (R_{ct}) and sometimes diffusion processes (Warburg impedance).

EIS provides a detailed and dynamic view of electrochemical processes by probing the system's impedance across a wide frequency range. The linear plots at lower frequencies (which show good electron transfer and lower resistance) are indicative of efficient electrochemical processes, while the higher-frequency regions highlight the inherent resistances and slower processes that occur at faster time scales. This balance of capacitive and resistive behaviours is crucial for understanding and optimizing electrochemical systems, whether for energy storage, sensors, or other applications [45].

The two Nyquist plots shown in Fig. 4 (A and B) differ in terms of their frequency range and the scale of the impedance values. The first plot shows a larger frequency range and impedance values than the second one.

At higher frequencies, impedance is dominated by resistive processes, with less efficient electron transfer due to insufficient response time to rapid signals. This is reflected in the Nyquist plot as a straight line along the real impedance axis (Z′). Charge transfer resistance increases, and capacitive effects are reduced, limiting charge storage capability. The high-frequency region reflects solution resistance (R_s) and contact resistance. These contributions dominate the impedance behavior at very high frequencies. PANI shows a steeper curve when compared to other materials, indicating a higher impedance, especially at lower frequencies. The rGO curve is slightly less steep than PANI, suggesting a better charge transport mechanism with a slightly lower impedance compared to PANI, hence offering lower impedance for the binary composite material. PrG-2 and PrGZ-2 have very similar curves (with a slight improvement for PrGZ-2), indicating lower impedance compared to rGO and PANI, especially at low frequencies.

At lower frequencies in a Nyquist plot, impedance reflects capacitive behavior (e.g., double-layer charging) and diffusion-controlled processes. This region highlights charge carrier movement in the electrolyte and bulk polymer layers. Efficient electron transfer reactions occur at lower frequencies due to longer timescales for electron movement. Lower resistance in this region indicates effective charge storage and minimal resistance to charge transfer or diffusion. Such behavior is crucial for assessing the electrochemical performance of materials and devices. Fig. 4B (representation of Nyquist plot at low frequency) shows that the materials with higher impedance (PANI and rGO) exhibit greater resistance to the flow of current, while the materials with lower impedance (PrG-2 and PrGZ-2) exhibit lower resistance. The linear

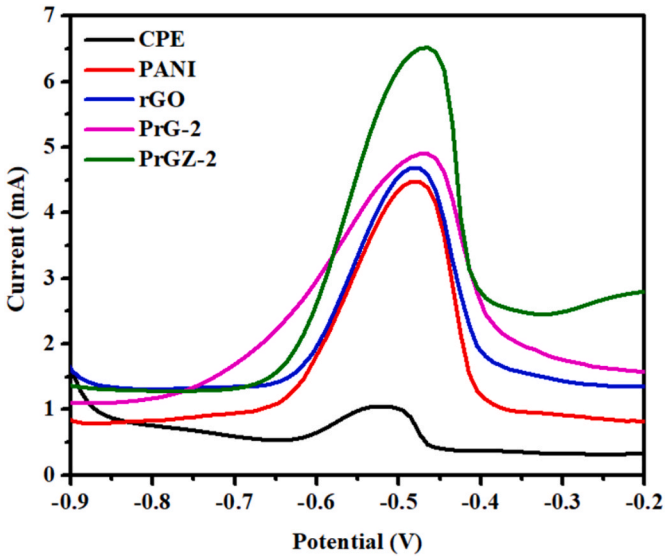

Fig. 5. Comparative DPASV of CPE, PANI, rGO, PrG-2, and PrGZ-2 at 5.5 μM addition of Pb^{2+} ions.

nature of the plots for PrG-2 and PrGZ-2 suggests a more conductive behavior, while the curved nature of the plots for rGO and PANI suggests a more resistive behavior. The decrease in impedance with increasing frequency indicates that the materials become more conductive at higher frequencies. This behavior is characteristic of materials with a combination of resistive and capacitive [46].

4.2. Differential pulse anodic stripping voltammetry (DPASV)

DPASV facilitates by depositing the analyte onto an electrode surface at a steady potential, and the current; thus, the response produced is proportional to the analyte concentration in the sample. A buffer solution (pH 4.5) was prepared with 0.1 M sodium acetate (CH_3COONa) and 0.07 M acetic acid (CH_3COOH). $Pb(CH_3COO)_2$ (Lead acetate, 0.1 M) solution is added in the concentration range of 1 μM–5.5 μM to this buffer [2], and the binary (PrG-2) and ternary composite material (PrGZ-2) are employed for the detection of Pb^{2+} ions for systematic studies. The experimental setup uses DPASV for measurement, where the working electrode used is CPE, on which the electroactive materials are deposited for Pb^{2+} detection. The experiment is conducted within a potential range of −1.0 V–0.1 V, which defines the range of potentials applied to the working electrode, allowing the study of electrochemical reactions occurring within this window. This potential window is relative to the Ag/AgCl reference electrode. The modulation amplitude is set at 0.1 V, this parameter is related to the technique (DPASV) being used, likely a form of voltammetry that involves a superimposed alternating potential. The modulation time is 0.05 s, which signifies the duration of each potential pulse or step in the modulation. The scan rate is 0.01 V/s is the rate at which the potential is changed over time. A slow scan rate allows for a more detailed study of electrochemical reactions, as it provides more time for reactions to occur at the electrode surface. The deposition potential is −1.0 V indicates that a potential of −1.0 V is applied to the working electrode for a certain time (5 min here) before the actual scan begins, used to pre-concentrate the analyte onto the electrode surface, enhancing sensitivity. The pH of the solution is 4.5, and the supporting electrolyte is acetate buffer. This provides a conductive medium and maintains a stable pH, ensuring that the electrochemical reactions of interest are not limited by ion migration. The working electrodes are PrG-2 and PrGZ-2 mounted over CPE, the reference electrode is Ag/AgCl provides a stable and known potential against which the working electrode potential is measured, and the platinum auxiliary (counter) electrode is employed. This electrode

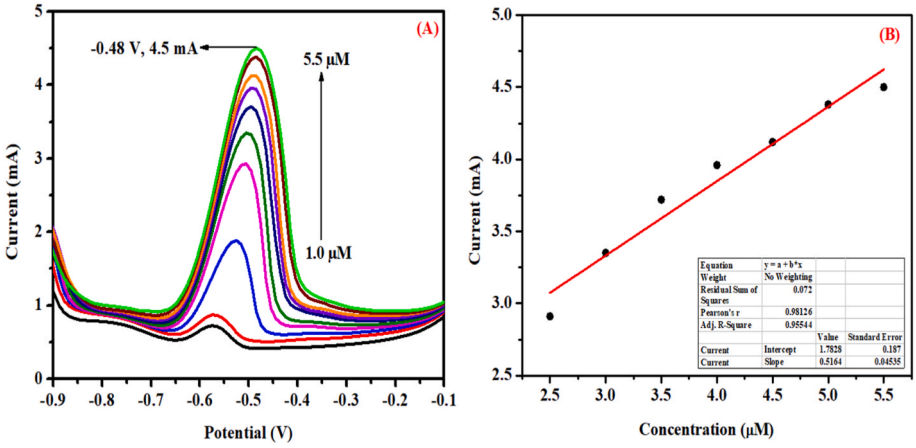

Fig. 6. DPASV (A) and a calibration curve (B) of PrG-2.

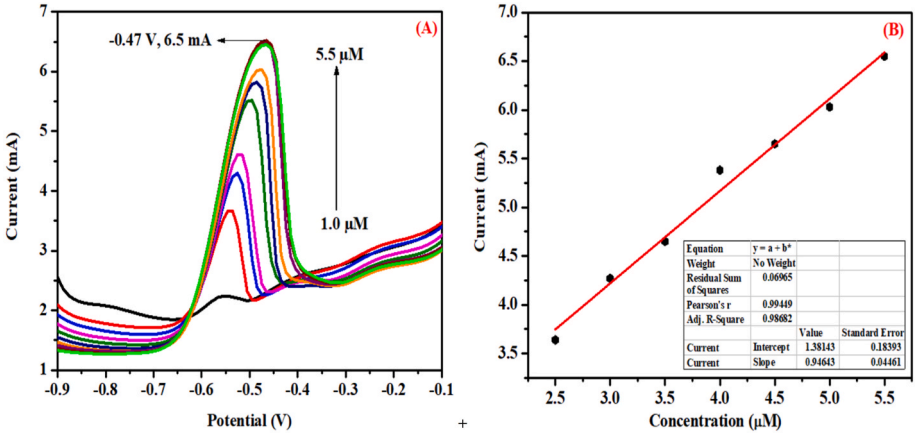

Fig. 7. DPASV (A) and a calibration curve (B) of PrGZ-2.

completes the electrochemical cell circuit and allows current to flow.

PrGZ-2 composite shows a significantly higher stripping peak current (6.53 mA) at −0.5 V compared to other electrodes like CPE (1.08 mA), PANI (4.46 mA), rGO (4.68 mA), and PrG-2 (4.88 mA) (Fig. 5). The higher peak current for PrGZ-2 is attributed to the increased surface area due to the inclusion of rGO, the pseudo-capacitive behavior of PANI, and ZnO contributing to better electron transfer in the ternary composite. The increased surface area, enhanced charge storage, and improved electron transfer mechanisms make PrGZ-2 a highly efficient and sensitive electrode for electrochemical detection, particularly for Pb^{2+} sensing applications. rGO plays a crucial role in enhancing the electrochemical performance of the material by offering a large surface area, which increases the active sites available for adsorption, thus improving the conductivity by faster electron transfer and reduced charge transfer resistance. The presence of PANI in the ternary composite improves the electrochemical performance owing to its intrinsic redox behaviour that contributes to enhanced charge storage and facilitates efficient charge/discharge cycles, improving the peak current. Acting as a semiconductor material ZnO promotes better electron transfer kinetics, hence supporting the charge transfer across the electrode interface. ZnO also enhances the structural stability, prevents degradation, and allows the cyclability of the material, allowing for more efficient electrochemical processes (Fig. 5). Together, rGO, PANI, and ZnO create a synergistic effect that optimizes the overall electrochemical performance of the composite material [47].

Well-defined stripping peaks increase with the concentration of Pb^{2+} ions (1.0 µM–5.5 µM) for both binary and ternary composites (Figs. 6A and 7A). The calibration curve for PrGZ-2 from 1.0 µM to 5.5 µM Pb^{2+} ions have R^2 value of 0.994, which is higher as compared to the R^2 value (0.981) for PrG-2, which suggests that the curve shows linearity in this range (Figs. 6B and 7B). The ternary composite has LOD value 0.3 µM, LOQ value 1.16 µM, and RSD at 2.13 %. The binary composite (PrG-2) has a LOD value of 0.7 µM, indicating its lesser sensitivity compared to the ternary composite. Binary Composite (PrG-2) has the highest LOQ of 2.3 µM, indicating that it needs a higher concentration to provide accurate quantification. The highest RSD at 3.1 %, also suggests the slightly lower precision of the PrG-2 (Table 3).

Table 3
Summarized DPASV results of binary and ternary composites.

Composite	R^2	LOD (µM)	LOQ (µM)	RSD (%)	Sensitivity (mA μM^{-1})
PrG-2	0.981	0.7	2.3	3.1	0.5164
PrGZ-2	0.994	0.3	1.16	2.13	0.9464

The LOD and LOQ are calculated using the formula below:

$$\mathrm{LOD} = \frac{3.3 \times SD}{S} \quad (1)$$

$$\mathrm{LOQ} = \frac{10 \times SD}{S} \quad (2)$$

Where "SD" is the standard deviation of the blank solution, and "S" is the slope of the calibration curve. The LOD and LOQ obtained for Pb^{2+} ions are 0.3 µM and 1.16 µM, respectively, for PrGZ-2 composite as compared

Table 4
Comparative analysis of PANI-based binary and ternary electrodes for Pb^{2+} ion detection in aqueous environment.

Composite material	Electrochemical technique	Detection range	LOD	Stability (RSD %)	Benefits	Drawback	Reference
Binary nanocomposite							
PANI/GO	SWASV	0.2–250 nM	0.04 nM	3.4	High sensitivity, good detection range	Potential for GO aggregation, limited selectivity	[21]
PANI-Nafion composite	SWASV	1.0–50.0 μM	0.08 μM	1.26	Enhanced stability due to Nafion, good reproducibility	Nafion can hinder electron transfer, narrower detection range compared to some others	[48]
Phytic acid-PANI	DPASV	0.1–60 μg L^{-1}	0.05 μg L^{-1}	–	Good recovery rates	High cost of Phytic acid	[49]
PANI/rGO	DPASV	1 μM–5.5 μM	0.7 μM	3.1	Improved conductivity due to rGO, good stability	Moderate LOD	Present Work
Ternary nanocomposite							
Gly/rGO/PANI	SWASV	0.0001–1 μM	0.07 nM	3.45	Excellent sensitivity	Complex synthesis	[50]
Nafion/G/PANI	SWASV	1–300 μM	0.1 μM	4.8	Enhanced stability	Higher RSD%	[51]
rGO/Ala/PANI	SWASV	100 nM–0.08 nM	0.04 nM	2.60	High sensitivity	Potential for interference	[23]
PANI/GO/APTES	CV and LSV	0.01 μM–0.4 μM	0.0053 μM	1.2	Low LOD	High cost of APTES	[52]
PANI/rGO/ZnO	DPASV	1 μM–5.5 μM	0.3 μM	2.13	Excellent conductivity and low cost	Appreciable LOD	Present Work

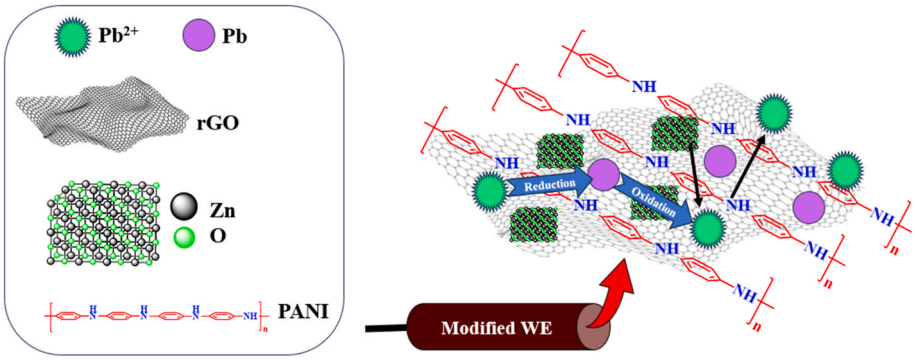

Fig. 8. Probable mechanism of interaction for Pb^{2+} detection.

to PrG-2 as calculated using the relations 1 and 2 above.

The sensitivity for the composite materials (PrG-2 and PrGZ-2) is obtained from the calibration curves (Figs. 6B and 7B) by the relation (3).

$$I = mC + b \quad (3)$$

Where "I" is measured current (response signal), "m" is sensitivity (slope of the calibration curve, i.e., change in current per unit concentration), "C" is concentration of the analyte (Pb^{2+} ions), and "b" is intercept (baseline signal when C = 0). The sensitivity of the PrGZ-2 composite was higher than PrG-2 (Table 3)

As the concentration of Pb^{2+} increases, the stripping peak potential shifts slightly towards a more positive value. The peak becomes broader, indicating the formation of multilayer metal ions on the electrode surface, which may have a higher electrochemical resistance than a single monolayer. The relative standard deviation (RSD) for the ternary composite (PrGZ-2) is 2.13 %, indicating the repeatability and precision of the measurements are within acceptable limits.

This study demonstrates the efficacy of the PrGZ-2 composite material in detecting Pb^{2+} ions. The composite material significantly improves the detection sensitivity compared to individual components, owing to enhanced surface area, pseudo-capacitive behavior, and better electron transfer properties. However, the calibration curve shows an appreciable R^2 value, suggesting that more optimization could be needed to achieve a more linear response across the concentration range. The calculated LOD and LOQ values indicate good sensitivity for low-concentration detection by PrGZ-2 (Table 4), which is significantly comparable and has the benefit of a low fabrication cost of active material.

4.3. Mechanism of Pb^{2+} sensing

The detection of metal ions (here, Pb^{2+}) at electrode surfaces involves a complex interplay of electrochemical phenomena. Notably, adsorption, driven by coulombic interactions, plays a critical role in concentrating metal ions on the electrode surface. In the case of the composite material PrGZ-2, heteroatom functionalities (e.g., nitrogen and oxygen-containing groups) within its structure facilitate the coordination of Pb^{2+} ions via coordinate bonds, leading to their effective accumulation (Fig. 8) [2]. Following an optimized open-circuit accumulation period, which allows for maximum Pb^{2+} adsorption, subsequent DPASV analysis induces the electrochemical reduction of adsorbed Pb^{2+} to metallic lead (Pb). The subsequent anodic stripping process involves the re-oxidation of deposited Pb back to Pb^{2+}, resulting in a quantifiable anodic stripping peak current as per the steps below.

Accumulation step (reduction step)

$$PrGZ-2 + Pb^{2+} + 2e^- \rightarrow (Pb------PrGZ-2)$$

Anodic stripping step (oxidation step)

$$(Pb------PrGZ-2) \rightarrow PrGZ-2 + Pb^{2+} + 2e^-$$

This peak current occurred in DPASV serves as a measure of the accumulated Pb^{2+} concentration, thereby enabling highly sensitive detection.

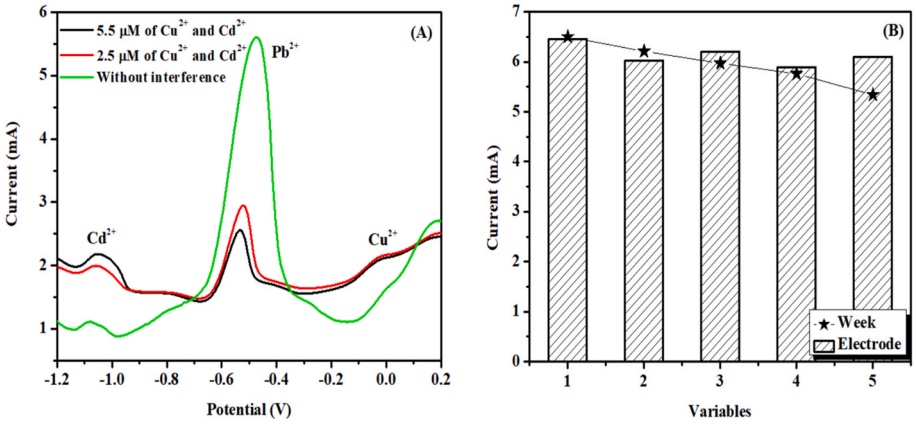

Figure: 9. DPASV results of PrGZ-2 composite without and with the interference of concentration of Cu^{2+} and Cd^{2+} ions (A), Stability (with week), and reproducibility (with series of electrodes) of electrode materials against 5.5 μM Pb^{2+} concentration (B).

4.4. Selectivity, reproducibility, and stability of PrGZ-2 electrode

PrGZ-2 nanocomposite material is used for studying the interference of Cu^{2+} and Cd^{2+} and the selectivity of Pb^{2+}. PrGZ-2 has enhanced surface areas, strong adsorption capabilities, and complexing abilities, which make it ideal for detecting trace levels of HMs. The PrGZ-2 electrode exhibits high selectivity for Pb^{2+} ions, even in the presence of interfering metal ions (Cu^{2+} and Cd^{2+}). The minimal changes in peak current and potential, along with the overall stability of the Pb^{2+} signal, suggest that the electrode is suitable for the selective detection of Pb^{2+} ions in complex samples**.** The stripping peak current for Pb^{2+} ions remains relatively stable despite the presence of Cu^{2+} and Cd^{2+} ions (Fig. 9A). The peak current changed due to the deposition of the analyte on the surface of the electrode, which blocks the diffusion process. The peak potential for Pb^{2+} detection also shows negligible shifts, further suggesting that the interference from Cu^{2+} and Cd^{2+} ions does not substantially alter the electrochemical behavior of Pb^{2+} on the electrode surface. This stability in peak potential is an indicator of selective detection. A possible explanation for the observed minimal change potential is the formation of intermetallic compounds such as Pb–Cu and Pb–Cd during the deposition step. These compounds may alter the electrochemical characteristics slightly, but not enough to significantly affect the signal from Pb^{2+}. This could lead to a slight broadening of the Pb^{2+} peak, but it does not prevent its detection. Despite the presence of Cu^{2+} and Cd^{2+} ions, the intensity of the Pb^{2+} stripping signal remains unaffected, demonstrating that the PrGZ-2 electrode is selective for Pb^{2+} ions. The ability of the electrode to maintain a consistent Pb^{2+} signal in the presence of interfering ions confirms that the sensor is effective for detecting Pb^{2+} without significant cross-sensitivity to other metal ions. The reproducibility of the PrGZ-2 electrode was detected by preparing five electrodes modified equally with the electroactive material, and DPASV measurements were performed in a 5.5 μM concentration of Pb^{2+} in an acetate buffer of pH 4.5 as a supporting electrolyte. A stripping peak current at −0.47 V was observed. Fig. 9B demonstrates that the current was measured over five different variables, both for an "Electrode" and for "Weeks". The electrode data shows a fairly stable current, while the weekly data shows a slight decrease in current over time. It shows good reproducibility of the PrGZ-2 electrode, as evidenced by the consistent current values obtained from different electrodes. The electrode exhibits reasonable stability, although there is a slight downward trend in current over time, suggesting a potential decrease in performance.

5. Conclusion

Ternary nanocomposite PANI/rGO/ZnO (PrGZ-2) was successfully synthesized for the highly sensitive detection of Pb^{2+}. The developed nanocomposite has good conductivity, high affinity towards Pb^{2+}, long-term stability, is inexpensive, and requires low sample volume. PrGZ-2 was used to detect Pb^{2+} ion by DPASV in concentration range of 1–5.5 μM with LOD and LOQ of 0.3 μM and 1.16 μM respectively on working electrode at Potential Window −1.0 to 0.1V, modulation amplitude 0.1V, modulation time 0.05 s and scan rate 0.01 V/s indicating good sensitivity for low concentration detection with the calibration curve for PrGZ-2 has R^2 value 0.994. The RSD for the ternary composite (PrGZ-2) is 2.13 %, signifying that the repeatability and precision of the measurements are within acceptable limits on the working electrode at potential window −1.0 to 0.1 V, modulation amplitude 0.1V, modulation time 0.05s, and scan rate 0.01V/s. The comparison with the existing work demonstrates the significance of the current research. The composite may also be evaluated for detecting other toxic heavy metals, such as Cd^{2+} and Cu^{2+}, broadening its application for environmental monitoring without interference with Pb^{2+} ions.

CRediT authorship contribution statement

Nisha: Writing – original draft, Methodology. **Goverdhan Singh:** Writing – original draft, Methodology, Investigation. **Anil Kumar:** Writing – review & editing, Visualization, Supervision. **Parteek Prasher:** Writing – review & editing, Supervision. **Harish Mudila:** Visualization, Supervision, Investigation, Conceptualization.

Funding

No external funding was received for performing the above research work.

Declaration of competing interest

The authors declare that they have no known competing financial interests or personal relationships that could have appeared to influence the work reported in this paper.

Acknowledgment

The Authors acknowledge the research facilities provided by the Central Instrumentation Facility, Lovely Professional University, Punjab, India.

References

[1] G. Singh, Kumar A. Nisha, P. Prasher, H. Mudila, Assessment of toxicity and electrochemical sensing of arsenic in aqueous sources, J. Environ. Eng. Sci. 18 (1) (2023) 10–23, https://doi.org/10.1680/jenes.22.00011.

[2] G. Singh, N. Gupta, Prasher P. Kumar, H. Mudila, Systematic development of PPY/GO/ZnO hybrid composite for electrochemical detection of Pb^{2+} in aqueous solution, Ionics (2025), https://doi.org/10.1007/s11581-025-06067-w.

[3] G. Singh, Kumar A. Nisha, P. Prasher, H. Mudila, A comprehensive review on material and techniques used for heavy metal detection in potable water, AIP Conf. Proc. 2800 (2023) 020186, https://doi.org/10.1063/5.0162879, 2023.

[4] M. Ramezanzadeh, M. Asghari, B. Ramezanzadeh, G. Bahlakeh, Fabrication of an efficient system for Zn ions removal from industrial wastewater based on graphene oxide nanosheets decorated with highly crystalline polyaniline nanofibers (GO-PANI): experimental and ab initio quantum mechanics approaches, Chem. Eng. J. 337 (2018) 385–397, https://doi.org/10.1016/j.cej.2017.12.102.

[5] H. Huang, W. Zhu, X. Gao, X. Liu, H. Ma, Synthesis of a novel electrode material containing phytic acid-polyaniline nanofibers for simultaneous determination of cadmium and lead ions, Analyt. Chimi. Act (2016), https://doi.org/10.1016/j.aca.2016.10.012.

[6] M. Altundal, A. Üğe, Ö. Gök, B. Zeybek, Determination of cadmium (II) by differential pulse voltammetry (DPV) using a cerium(IV) oxide: polyaniline composite modified glassy carbon electrode (GCE), Anal. Lett. 54 (15) (2021) 2431–2451, https://doi.org/10.1080/00032719.2020.187012.

[7] F. Pellegatti, A.M.G. Figueiredo, J.C. Wasserman, Neutron activation analysis applied to the determination of heavy metals and other trace elements in sediments from sepetiba bay (RJ), Brazil, Geostand. Geoanal. Res. 25 (2–3) (2001) 307–315, https://doi.org/10.1111/j.1751-908x.2001.tb00607.x.

[8] Z. Yang, L. Zhao, Y. Zhang, Y. Xing, Z. Wei, C. Xin, T. Fei, S. Liu, T. Zhang, Isolated Cu-N_5 sites engineered polypyrrole-reduced graphene oxide hybrids for enhancing room-temperature DMMP sensing, Sens. Actuators, B 385 (2023) 133671, https://doi.org/10.1016/j.snb.2023.133671, 2023.

[9] S. Gao, Z. Yang, Y. Zhang, L. Zhao, Y. Xing, T. Fei, S. Liu, T. Zhang, The synergistic effects of MoS_2 and reduced graphene oxide on sensing performances for electrochemical chloramphenicol sensor, Flat Chem 2202 (33) (2022) 100364, https://doi.org/10.1016/j.flatc.2022.100364.

[10] N.A. Travlou, M. Seredych, E. Rodríguez-Castellón, T.J. andBandosz, Activated carbon-based gas sensors: effects of surface features on the sensing mechanism, J. Mater. Chem. A 3 (7) (2015) 3821–3831, https://doi.org/10.1039/c4ta06161f.

[11] S. Sani Abdulrazak, K. Hussaini, H.M. Sani, Evaluation of removal efficiency of heavy metals by low-cost activated carbon prepared from African palm fruit, Appl. Water Sci. (2017), https://doi.org/10.1007/s13201-016-0460-x.

[12] M.M. Musameh, M. Hickey, I.L. Kyratzis, Carbon nanotube-based extraction and electrochemical detection of heavy metals, Res. Chem. Intermed. (2011), https://doi.org/10.1007/11164-011-0307-x.

[13] J.K. Pitroda, B. Jethwa, S.K. Dave, A critical review on carbon nanotubes, Intern. J. Construc. Res. Civil Eng. 2 (5) (2016) 36–42, https://doi.org/10.20431/2454-8693.0205007.

[14] A.C.O. Silva, L.C.F. Oliveira, A.V. Delfino, M.R. Meneghetti, F.C. Abreu, Electrochemical study of carbon nanotubes/nanohybrids for determination of metal species Cu^{2+} and Pb^{2+} in water samples, J. Analyt. Methods Chem. (2016), https://doi.org/10.1155/2016/9802738.

[15] F. Shahzad, S.A. Zaidi, R.A. Naqvi, 2D Transition Metal Carbides (MXene) for electrochemical sensing: a review, Crit. Rev. Anal. Chem. (2020), https://doi.org/10.1080/10408347.2020.1836470.

[16] Y. He, L. Ma, L. Zhou, G. Liu, Y. Jiang, J. Gao, Preparation and application of bismuth/MXene nano-composite as electrochemical sensor for heavy metal ions detection, Nanomaterials 10 (5) (2020) 866, https://doi.org/10.3390/nano10050866.

[17] M.A. Belal, H.H. Khalil, R.L. Mahajan, A.E. Ahmed Elsayed Rashed, S.N. Sherine Nabil Khattab, A.A. El-Moneim, Layered Structure Design of Inkjet-Printed graphene/Co_3O_4 for High-Performance Flexible Microsupercapacitors, 2024, https://doi.org/10.1016/j.est.2024.113900.

[18] M.D. Rahman, R. Kumar, M. Kumar, Q. Qiao, Two –dimensional transition metal dichalcodenides and their composites for lab-based sensing applications: recent progress and future outlook, Senso. Acuta. (2020), https://doi.org/10.1016/j.sna.2020.112517.

[19] M.J. Aghagoli, F. Shemirani, Hybrid nanosheets composed of molybdenum disulfide and reduced graphene oxide for enhanced solid phase extraction of Pb(II) and Ni(II), Microchim. Acta 184 (1) (2016) 237–244, https://doi.org/10.1007/s00604-016-2000-7.

[20] Y.-F. Sun, J.-H. Sun, J. Wang, Z.-X. Pi, L.-C. Wang, M. Yang, X.-J. Huang, Sensitive and anti-interference stripping voltammetry analysis of Pb(II) in water using flower-like MoS_2/rGO composite with ultra-thin nanosheets, Anal. Chim. Acta (2019), https://doi.org/10.1016/j.aca.2019.03.008.

[21] M. Akhtar, A. Tahir, S. Zulfiqar, F. Hanif, M.F. Warsi, P.O. Agboola, I. Shakir, Ternary hybrid of polyaniline-alanine-reduced graphene oxide for electrochemical sensing of heavy metal ions, Synth. Met. 265 (2020) 116410, https://doi.org/10.1016/j.synthmet.2020.116410.

[22] Y. Dong, Y. Zhou, Y. Ding, X. Chu, C. Wang, Sensitive detection of Pb(ii) at gold nanoparticle/polyaniline/graphene modified electrode using differential pulse anodic stripping voltammetry, Anal. Methods 6 (23) (2014) 9367–9374, https://doi.org/10.1039/c4ay01908c.

[23] S. Muralikrishna, D.H. Nagaraju, R.G. Balakrishna, W. Surareungchai, T. Ramakrishnappa, A.B. Shivanandareddy, Hydrogels of polyaniline with graphene oxide for highly sensitive electrochemical determination of lead ions, Anal. Chim. Acta 990 (2017) 67–77, https://doi.org/10.1016/j.aca.2017.09.008.

[24] Y. He, L. Ma, L. Zhou, G. Liu, Y. Jiang, J. Gao, Preparation and application of bismuth/MXene nano-composite as electrochemical sensor for heavy metal ions detection, Nanomaterials 10 (5) (2020) 866, https://doi.org/10.3390/nano10050866.

[25] R. Baby, B. Saifullah, M.Z. Hussein, Carbon nanomaterials for the treatment of HeavyMetal-contaminated water and environmental remediation, Nanoscale Res. Lett. 14 (2019) 341, https://doi.org/10.1186/s11671-019-3167-8.

[26] G. Singh, Kumar A. Nisha, H. Mudila, Comparative study on the electrochemical performance of PPY/GO binary and PPYGO/ZnO ternary nanocomposites, Bulg. Chem. Commun. 55 (A) (2023) 37–43, https://doi.org/10.34049/bcc.55.A.0005.

[27] A.K. Tawade, D. Mohan Kumar, P. Talele, K.K.K. Sharma, S.N. Tayade, Flower-like ZnO-decorated polyaniline–graphene oxide nanocomposite for electrochemical oxidation of imidacloprid: a hybrid nanocomposite sensor, J. Electron. Mater. (2019), https://doi.org/10.1007/s11664-019-07600-0.

[28] S. Palsaniya, H.B. Nemade, A.K. Dasmahapatra, Hierarchical PANI-RGO-ZnO ternary nanocomposites for symmetric tandem supercapacitor, J. Phys. Chem. Solid. 154 (2021) 110081, https://doi.org/10.1016/j.jpcs.2021.110081.

[29] A. Yasuda, T. Shimidzu, Chemical oxidative polymerization of aniline with ferric chloride, Polym. J. 25 (4) (1993) 329–338, https://doi.org/10.1295/polymj.25.329.

[30] H. Mudila, V. Joshi, S. Rana, M.G.H. Zaidi, S. Alam, Enhanced electrocapacitive performance and high power density of polypyrrole/graphene oxide nanocomposites prepared at reduced temperature, Carbon Lett. (2014), https://doi.org/10.5714/CL.2014.15.3.171.

[31] Shruthi, K.M. Vighnesha, Sandhya, D.N. Sangeetha, M. Selvakumar, Synthesis and characterization of reduced graphene oxide- polyaniline composite for supercapacitor applications, Surf. Eng. Appl. Electrochem. 54 (4) (2018) 359–366, https://doi.org/10.3103/s106837551804018x.

[32] I. Adraoui, M. El Rhazi, A. Amine, L. Idrissi, A. Curulli, G. Palleschi, Lead determination by anodic stripping voltammetry using ap-phenylenediamine modified carbon paste electrode, Electroanalysis 17 (8) (2005) 685–693, https://doi.org/10.1002/elan.200403140.

[33] A. Yelil Arasi, J. Juliet Latha Jeyakumari, B. Sundaresan, V. Dhanalakshmi, R. Anbarasan, The structural properties of Poly(aniline)—analysis via FTIR spectroscopy, Spectrochim. Acta Mol. Biomol. Spectrosc. 74 (5) (2009) 1229–1234, https://doi.org/10.1016/j.saa.2009.09.042.

[34] X. Jiao, Y. Qiu, L. Zhang, X. Zhang, Comparison of the characteristic properties of reduced graphene oxides synthesized from natural graphites with different graphitization degrees, RSC Adv. 7 (82) (2017) 52337–52344, https://doi.org/10.1039/c7ra10809e.

[35] Y. Zhang, J. Liu, Y. Zhang, J. Liu, Y. Duan, Facile synthesis of hierarchical nanocomposites of aligned polyaniline nanorods on reduced graphene oxide nanosheets for microwave absorbing materials, RSC Adv. 7 (85) (2017) 54031–54038, https://doi.org/10.1039/c7ra08794b.

[36] M.S. Seehra, V. Narang, U.K. Geddam, A.B. Stefaniak, Correlation between X-ray diffraction and Raman spectra of 16 commercial graphene–based materials and their resulting classification, Carbon 111 (2017) 380–385, https://doi.org/10.1016/j.carbon.2016.10.010.

[37] T.N.A.B.T.A. Mutalib, S.J. Tan, K.L. Foo, Y.M. Liew, C.Y. Heah, M.M.A.B. Abdullah, Properties of polyaniline/graphene oxide (PANI/GO) composites: effect of GO loading, Polym. Bull. (2020), https://doi.org/10.1007/s00289-020-03334-w.

[38] S.N. Alam, N. Sharma, L. Kumar, Synthesis of graphene oxide (GO) by modified Hummers method and its thermal reduction to obtain reduced graphene oxide (rGO), Graphene 6 (1) (2017), https://doi.org/10.4236/graphene.2017.61001.

[39] S. Palsaniya, H.B. Nemade, A.K. Dasmahapatra, Hierarchical PANI-RGO-ZnO ternary nanocomposites for symmetric tandem supercapacitor, J. Phys. Chem. Solid. 154 (2021) 110081, https://doi.org/10.1016/j.jpcs.2021.110081.

[40] A. Kumar, A. Kumar, H. Mudila, K. Awasthi, V. Kumar, Synthesis and thermal analysis of polyaniline, J. Phys. (2020), https://doi.org/10.1088/1742-6596/1531/1/012108.

[41] M. Matoetoe, F. Okumu, C. Maphale, O. Fatoki, Thermal and spectroscopic dynamics of titanium oxide functionalized polyaniline coated sawdust, Asian J. Chem. 27 (4) (2015) 1411–1416, https://doi.org/10.14233/ajchem.2015.18061.

[42] J. Singh, A.S. Dhaliwal, Electrochemical and photocatalytic degradation of methylene blue by using rGO/AgNWs nanocomposite synthesized by electroplating on stainless steel, J. Phys. Chem. Solid. 160 (2022) 110358, https://doi.org/10.1016/j.jpcs.2021.110358.

[43] Z. Abdel Hamid, M. Hasan Gomaa, S.S. Abdel Rehim, M. Abdel Hamid, A. Ibrahim, Synthesis and characterization of nanostructured polyaniline thin films with superhydrophobic properties, Coatings 9 (11) (2019) 748, https://doi.org/10.3390/coatings9110748.

[44] B. Thirumalraj, C. Rajkumar, S.-M. Chen, S. Palanisamy, One-pot green synthesis of graphene nanosheets encapsulated gold nanoparticles for sensitive and selective detection of dopamine, Sci. Rep. 7 (1) (2017), https://doi.org/10.1038/srep41213.

[45] M. Kahouli, A. Barhoumi, A. Bouzid, A. Al-Hajry, S. Guermazi, Structural and optical properties of ZnO nanoparticles prepared by direct precipitation method, Superlattice. Microst. 85 (2015) 7–23, https://doi.org/10.1016/j.spmi.2015.05.007.

[46] J.C. Martins, M. de, J.C. Neto, R.R. Passos, L.A. Pocrifka, Electrochemical behavior of polyaniline: a study by electrochemical impedance spectroscopy (EIS) in low-frequency, Solid State Ionics 346 (2020) 115198, https://doi.org/10.1016/j.ssi.2019.115198.

[47] E.C. Okpara, S.C. Nde, O.E. Fayemi, E.E. Ebenso, Electrochemical characterization and detection of lead in water using SPCE modified with BiONPs/PANI, Nanomaterials 11 (5) (2021) 1294, https://doi.org/10.3390/nano11051294.
[48] G. Zhao, Y. Yin, H. Wang, G. Liu, Z. Wang, Sensitive stripping voltammetric determination of Cd(II) and Pb(II) by a Bi/multi-walled carbon nanotube-emeraldine base polyaniline-Nafion composite modified glassy carbon electrode, Electrochim. Acta 220 (2016) 267–275, https://doi.org/10.1016/j.electacta.2016.10.059.
[49] H. Huang, W. Zhu, X. Gao, X. Liu, H. Ma, Synthesis of a novel electrode material containing phytic acid-polyaniline nanofibers for simultaneous determination of cadmium and lead ions, Anal. Chim. Acta 947 (2016) 32–41, https://doi.org/10.1016/j.aca.2016.10.012.
[50] F. Hanif, A. Tahir, M. Akhtar, M. Waseem, S. Haider, M.F. Aly Aboud, M.F. Warsi, Ultra-selective detection of Cd2+ and Pb2+ using glycine functionalized reduced graphene oxide/polyaniline nanocomposite electrode, Synth. Met. 257 (2019) 116185, https://doi.org/10.1016/j.synthmet.2019.116185.
[51] N. Ruecha, N. Rodthongkum, D.M. Cate, J. Volckens, O. Chailapakul, C.S. Henry, Sensitive electrochemical sensor using a graphene–polyaniline nanocomposite for simultaneous detection of Zn(II), Cd(II), and Pb(II), Anal. Chim. Acta 874 (2015) 40–48, https://doi.org/10.1016/j.aca.2015.02.064.
[52] R.S. Alruwais, W.A. Adeosun, H.M. Marwani, M. Jawaid, A.M. Asiri, A. Khan, Novel aminosilane (APTES)-Grafted Polyaniline@Graphene oxide (PANI-GO) nanocomposite for electrochemical sensor, Polymers 13 (2021) 2562, https://doi.org/10.3390/polym13152562.

Bulgarian Chemical Communications, Volume 55, Special Issue A (pp. 94-101) 2023 DOI: 10.34049/bcc.55.A.0015

Synthesis of PANI-GO and PANI-rGO nanocomposites and their electrochemical performance

Nisha[1], G. Singh[1], A. Kumar[1], P. Prasher[2], H. Mudila[1]*

[1]*Department of Chemistry, Lovely Professional University, Phagwara, Punjab-144411, India*
[2]*Department of Chemistry, UPES, Dehradun, 248007, India*

Received: March 27, 2023; Revised: April 30, 2023

In this work, a series of binary nanocomposites (PGs and PGRs) were synthesized by adding a varying percentage of GO and rGO to the matrix of polyaniline (PANI). PANI was synthesized by the chemical oxidative method, while GO was synthesized through the modified Hummers method and was further reduced to rGO. All the individual material and composite materials were analyzed through FTIR, XRD, TGA-DSC, and SEM analysis. The electrochemical performance was studied *via* cyclic voltammetry for the PANI, GO, PGs, and PGRs in the potential range of -0.5 to 0.5 V at varying scans (1 to 500 mV/s). The specific capacitance of PANI, GO, and rGO was found to be 169.57, 248.69, and 279.34 F/g while the maximum specific capacitance for the binary composites for PG-5 and PGR-5 was found to be 367 and 1231 F/g respectively.

Keywords: Polyaniline, Reduced graphene oxide, Electrochemical sensor, Clean energy, Cyclic voltammetry.

INTRODUCTION

Conductive polymers (CPs) are of great interest because of their incomparable properties like high surface area, multi-redox reaction, thermal resistance, and chemical stability. Out of various CPs, polyaniline (PANI) possesses a wide range of electrical properties and is a great choice because of its ease of synthesis [1, 2]. Apart from the CPs, nowadays carbon-containing materials like graphite oxide (GO) and reduced graphite oxide (rGO) provide a capable preliminary material for the fabrication of composites with CPs due to defects and potential functionalization [1, 2]. GO is a single sheet having oxygen-containing functional groups like -OH, C-O-C, and –COOH groups [3] whereas rGO has extraordinary physical and chemical properties, a 2D form of graphite, sp^2 hybridization, great mechanical properties, electron transport, high surface area, and great conductivity. rGO has a honeycomb-like structure in which one strong bond C-C is present in the plane and another π-bond is present out of the plane having a delocalized network, this structure is important for the availability of electrons for conduction [2, 3]. Numerous improvements have been made to CPs and carbon-containing compounds to form their composites for the reason that they provide low cost, save time, and give a better result of conductivity by acting as electroactive material [4-6].

In this experimental work, systematic studies have been carried out on the fabrication and electrochemical activity of the PANI-GO (PGs) and PANI-rGO (PGR) composites. The present work involves the formation of a binary composite with different ratios of PANI with GO and rGO (w/w %) by a simple route of *ex-situ* polymerization. The fabricated composites were characterized using FTIR, XRD, TGA, DSC, and SEM. These composites were found to have great electroactive properties when studied for their specific capacitance determined by cyclic voltammetry (CV).

MATERIALS AND METHOD

Materials

Chemicals like aniline (p=1.021 g/ml, LOBA Chemie), SDS (sodium dodecyl sulfate, Qualikems Fine chem.) ferric chloride (Alpha Chemika), graphite (LOBA Chemie Pvt Ltd), sulfuric acid (Avantor Performance Materials India Ltd), potassium permanganate (Hi-Media Laboratories Pvt. Ltd.), sodium nitrate (Avarice Industries), hydrogen peroxide, hydrochloric acid, hydrazine hydrate and ethanol were procured from LOBA Chemie Pvt Ltd and the chemicals were not further purified because all chemicals were of analytical quality.

Preparation of PANI, GO, and rGO

Preparation of PANI from aniline was carried out by the process mentioned by Bangade *et al. 2020,* in the presence of an anionic surfactant and an oxidant $FeCl_3$ [7]. GO was formed by the modified Hummers method as explained by Mudila *et al. 2014* [8]. In a beaker deionized water (250 ml) was taken to which

* To whom all correspondence should be sent:
E-mail: harismudila@gmail.com

© 2023 Bulgarian Academy of Sciences, Union of Chemists in Bulgaria

2g of GO was added and was subjected to stirring over a magnetic stirrer (1100 rpm). Then 2 ml of hydrazine hydrate was dropwise added to the above solution. The mixture was heated at 80 °C for 72 hours with continuous stirring. Fine black particles were observed after the reaction completion which were separated by centrifugation (~5000 rpm).

Fabrication of binary composites PANI-GO (PGs) and PANI-/rGO (PGRs)

Six compositions (PGs) of PANI and GO were prepared by varying the amount of GO in the matrix of PANI (Table 1). The requisite amounts of PANI and GO were mixed (*ex-situ* method) in ethanol and were further sonicated in a bath sonicator for 1 hour for better mixing. The composites obtained were then dried in a vacuum oven [6]. The same method was used to prepare the binary composite of PANI-rGO.

Table 1. Composition, ratio, and code for PANI-GO composites

PANI	0.1 g	0.1 g	0.1 g	0.1 g	0.1 g	0.1 g
GO	0.025 g	0.05g	0.075g	0.1 g	0.2g	0.3 g
Ratio	4:1	2:1	4:3	1:1	1:2	1:3
Code	PG-1	PG-2	PG-3	PG-4	PG-5	PG-6

Table 2. Composition, ratio, and code for PANI-rGO composites

PANI	0.1 g	0.1 g	0.1 g	0.1 g	0.1 g	0.1 g
rGO	0.025 g	0.05 g	0.075 g	0.1 g	0.2 g	0.3 g
Ratio	4:1	2:1	4:3	1:1	1:2	1:3
Code	PGR-1	PGR-2	PGR-3	PGR-4	PGR-5	PGR-6

Electrode preparation

The working electrode was prepared of stainless steel(304-SS) which was de-greased by acetone. The material to be coated over the SS electrode was containing 0.05 g of electroactive material added with graphite (0.005 g) in a binder polystyrene (5 g/dL in xylene). The material was dried and weighted (~ 0.01 g) and was further used as a working electrode in 1M KOH solution [8]. The electrochemical measurement of PANI, GO, rGO, PANI-GO, and PANI-rGO was done by cyclic voltammetry (CV) in a -0.5 to 0.5V potential window range at a scan rate of 1 to 500 mV. The specific capacitance (C_s) of the active materials calculated from the cyclic voltammograms curves is given by the equation.

$$C_s = A/2mk.\Delta V$$

where, A= area under the CV curve, m= mass loaded of the electro-active material, k=applied scan rate (1 to 500 mV/s), ΔV=applied potential window -(0.5 to 0.5 V).

RESULTS AND DISCUSSION

Electrochemical measurement

Electrochemical performance of PANI, GO, and rGO. Fig. 1. shows the electrochemical behavior of PANI, GO, and rGO. Specific capacitance values increase progressively from PANI to GO and rGO due to their structural property which possesses the availability of free electrons for electric conduction, this may be attributed to the increased surface area and porous structure of all the materials. CV curves show a regular increase in the range of cathodic and anodic current with enhanced scan rate but this trend was not continuous and led to a decrease in specific capacitance indicating the stability of the materials. Table 3 depicts the C_s values of PANI, GO, and rGO at various scan rates with the highest capacitance value of 169.5, 248.69, and 279.34 F/g, respectively at 1 mV/s and the values decreases regularly as the scan rate increases from 1 to 500 mV/s [6, 8].

Table 3. Specific capacitance of PANI, GO, and rGO at different scans

Scan Rate	Specific capacitance (C_s) F/g		
	PANI	GO	rGO
1mV/s	169.5	248.69	279.34
5mV/s	50.77	100.46	72.50
10mV/s	32.60	73.89	46.60
50mV/s	10.79	38.32	19.60
100mV/s	6.40	27.18	13.07
500mV/s	2.58	11.04	5.05

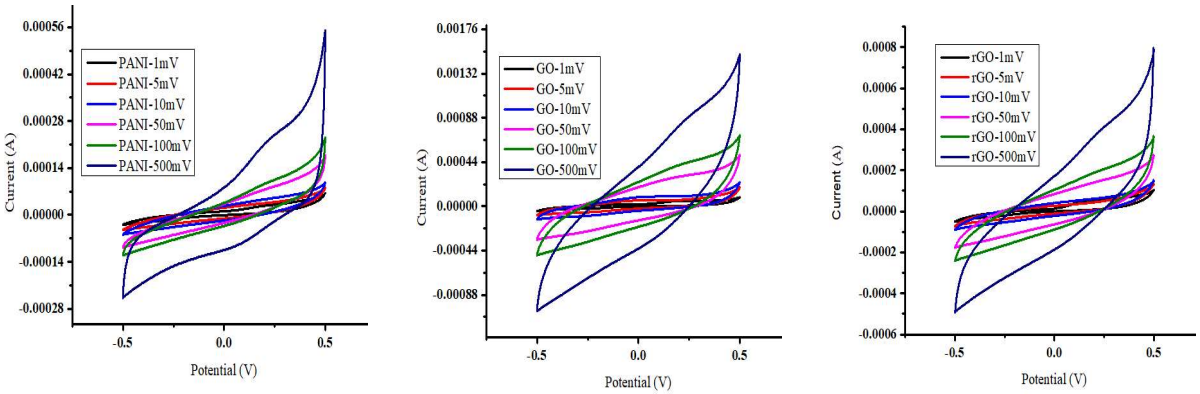

A B C

Figure 1. Cyclic voltammogram of (A) PANI (B) GO (C) rGO at different scan rate

Table 4. Specific capacitance of PGs at different scans rates

Scan rate	Specific capacitance (C_s) F/g					
	PG-1	PG-2	PG-3	PG-4	PG-5	PG-6
1mV/s	85.32	95.6	161.0	210.0	367.0	181.0
5mV/s	15.13	69.3	46.96	46.08	132.54	66.03
10mV/s	11.8	48.1	23.48	24.57	96.52	40.5
50mV/s	4.29	22.9	10.8	11.26	47.39	23.87
100mV/s	3.04	16.2	6.3	8.4	34.08	16.89
500mV/s	1.7	6.9	4.8	4.8	15.7	5.8

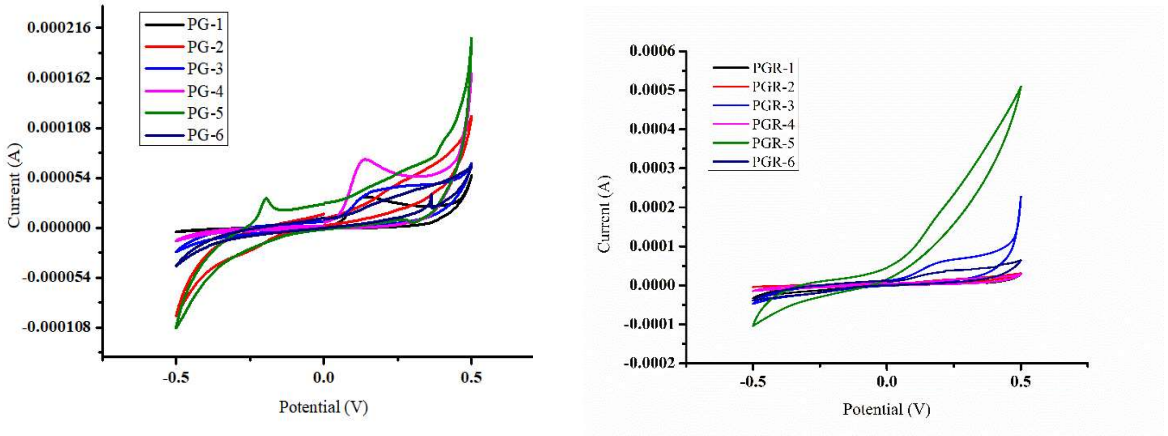

A B

Figure 2. Comparative cyclic voltammogram of (A) PGs all ratios at 1mV/s (B) PGRs all ratios at 1mV/s

Table 5. Specific capacitance of PGRs at different scans rates

Scan rate	Specific capacitance (C_s) F/g					
	PGR-1	PGR-2	PGR-3	PGR-4	PGR-5	PGR-6
1mV/s	102.0	226.2	305.2	323.4	1231.9	310
5mV/s	24.5	155.7	76.6	56.7	305.8	105.2
10mV/s	14.8	122.1	49.3	43.7	73.2	69.3
50mV/s	12.7	53.9	23.1	22.3	61.2	34
100mV/s	9.3	37.1	39.9	16	38.4	25.8
500mV/s	4.4	14.4	8.5	6.8	14.1	13.5

Electrochemical performance of binary composites PGs and PGRs

The specific capacitance of PANI increases with the addition of specific weight percentages of GO and rGO because they get homogeneously grafted on the PANI matrix and surface area gets enhanced, but this increase was not regular (Tables 4, 5). The maximum value of C_s was achieved for PG-5 (367 F/g) and PGR-5 (1231.9 F/g), afterward, there is a decrease in C_s due to more addition of GO and rGO layers on PANI inhibiting the conduction and reducing the active surface area. Well-aligned PGs and PGRs show excellent performance as electrode materials. Maximum C_s values of PGR-5as compared to PG-5 were shown for the reason that it facilitates electrolyte diffusion in the honeycomb-like carbon structure (more available in PGR) and π-bond that is present out of the plane having a delocalized network, this structure is important for the availability of electrons for conduction [2]. Fig. 2 shows the voltammogram of PGs and PGRs in all ratios at 1mV/s.

Fig. 3 depicts that the binary composite in the ratio PG-5 (1:2) and PGR-5 (1:2) was found to have the highest C_s.

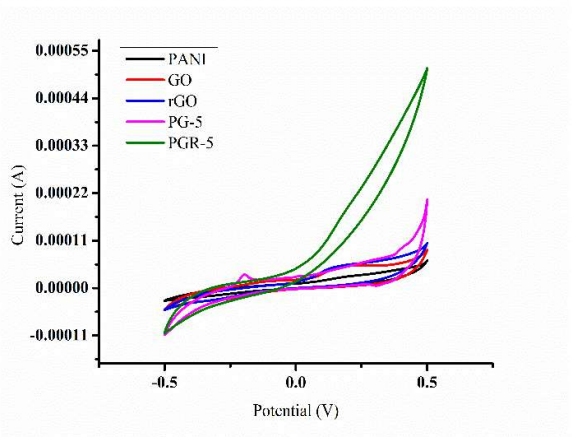

Figure 3. Cyclic voltammograms of PANI, GO, rGO, PG-5 and PGR-5

The slope, as well as the area of the CV curve of PGR-5 and PG-5 is higher than PANI, GO, and rGO signifying the reduced resistance, fast ion diffusion rate, and good capacitance behavior in composite material. As a result, the CV dimensions of the composite 1:2 shows the utmost current and reveal a large surface area of CV curves indicating the enhanced specific capacitance attributed to synergic consequence among GO and PANI matrix as well as rGO and PANI matrix [18].

Fourier transform infrared (FTIR)

The powdered samples (PANI, GO, rGO, PG, and PGR) were characterized by using FTIR (Perkin Elmer Spectrum IR Version 10.6.1). PANI showed characteristic peaks at 3412, 2978, 1549, 1450, 1293, 1230, 1036, and 783 cm^{-1} corresponding to N-H str., C-H str., C=C bond, benzenoid ring, C-N bond, N-H bend., C-H bend., and quinoid ring respectively [10, 11]. The peaks at 3164, 1712, 1618, and 1039 cm^{-1} were the characteristic peaks of O-H stretching, C=O stretching, C=C bond, and C-O stretching of graphene oxide (GO) [12, 13]. rGO showed peaks at 1544, 3389, and 1709 cm^{-1} for skeletal vibrations, -OH stretching and C=O stretching [14] as shown in Figure 4. The peaks at 1711, 1560, 1107, and 799 cm^{-1}correspond to the C=O stretching, N-H bending, C-H stretching of the benzenoid ring, and C-H out-of-plane bending vibrations in binary composite PG [15, 16]. Another binary composite PGR showed peaks at 1708, 1453, 1292, and 1096 cm^{-1}owing to the presence of the C=O group, C=C str. of benzenoid rings, and C-N bend. of the benzenoid ring, and C-H stretching of the quinoid ring [17, 18] as shown in Figure 4.

X-ray diffraction (XRD)

The XRD of all samples was studied by using an X-ray diffractometer (Bruker D8 advance) using Cu-Kα radiation. The broad peak at about $2\theta = 25°$ is the characteristic peak of PANI [26]. The characteristic peak of the graphite $2\theta = 26.4°$ (Fig 5A) was transformed to $2\theta = 10.61°$ (Figure 5B) when converted to GO, which was attributed to the presence of oxygenated groups and water molecules inserted in the interlayer of graphite. For rGO samples weak broad peak at approximately $2\theta = 24.5°$ is observed (Fig 5B) [13].

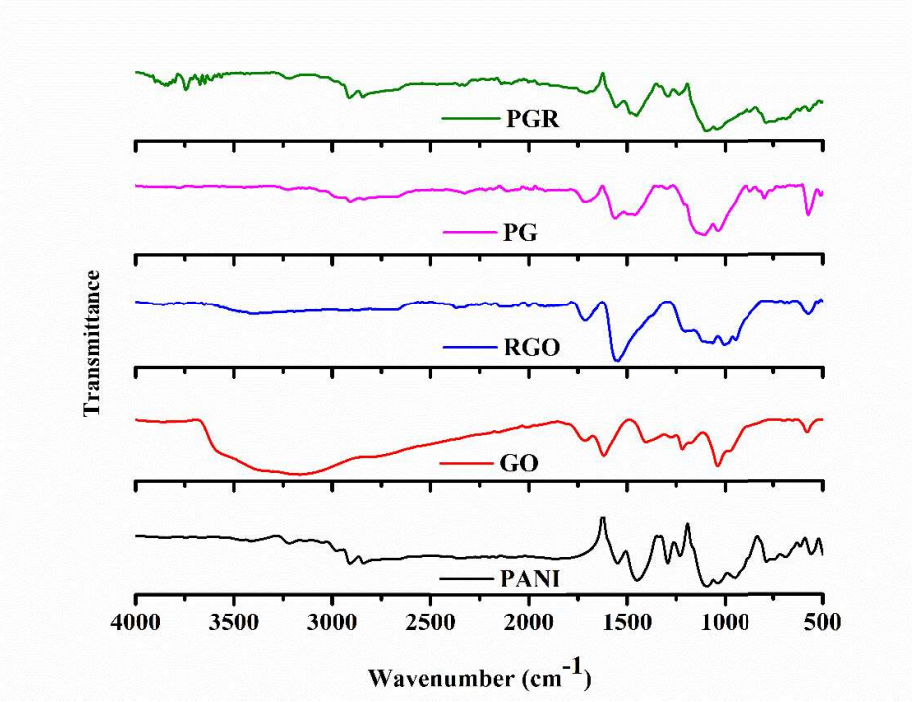

Figure 4. FTIR spectra of all the individual materials and composites

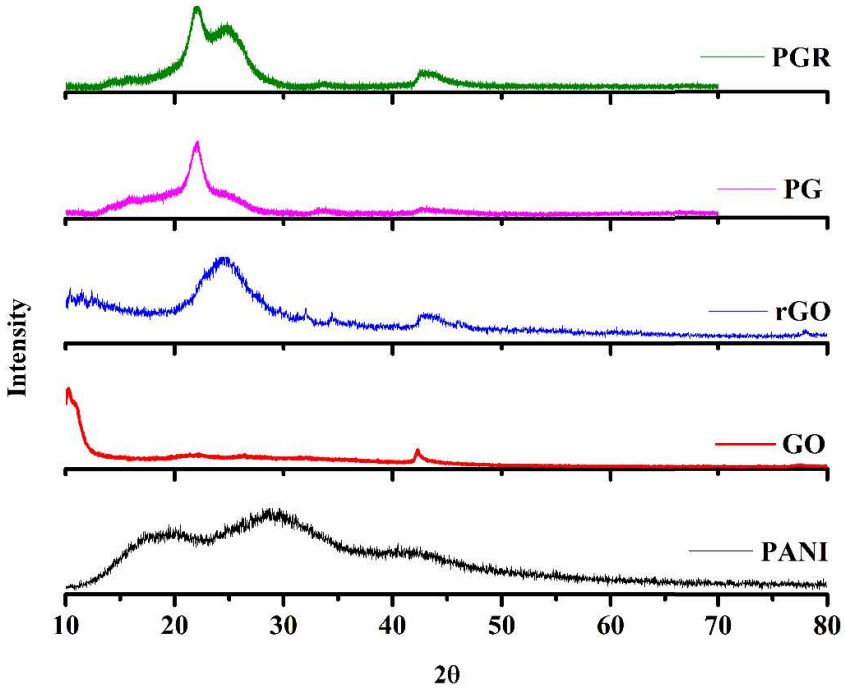

Figure 5. XRD of all individual materials and composites

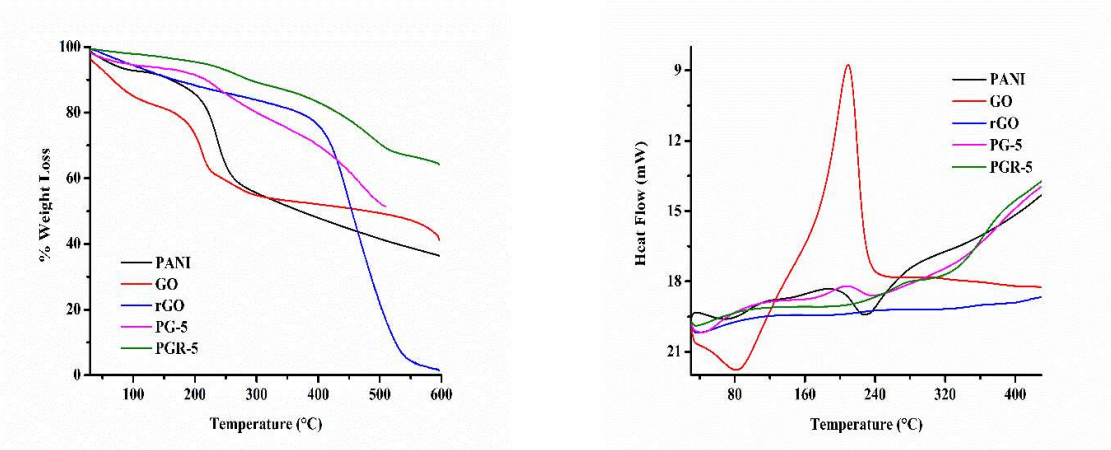

A B

Figure 6. (A)TGA and (B) DSC of individual and composite materials

Thermogravimetric analysis (TGA)

TGA was executed to predict the thermal stability of a material, the data was recorded on the instrument (TGA)-50H of Perkin Elmer. A material of the weight (x mg) was heated under an inert(N_2) atmosphere with a flow of 10 °C/min (room temperature to 600°C) to record the TG data. For PANI a three-step weight loss was observed, and two minima were depicted which are due to weight loss. The first weight loss is due to the loss of adsorbed water at 100˚C and the second weight loss of 27 % is due to the decomposition of PANI between100˚C to 300˚C. The third weight loss of 12% started above 300 ˚C due to the degradation of the polymeric backbone of PANI [19].

For GO the TGA plot shows that the weight loss (%w) occurred in three steps, initially a mass loss (20%) occurred below the temperature of 117 ˚C because of the removal of the water absorbed. In the 2nd step, mass loss (30%) occurs up to the temperature of 200˚C due to the thermal decomposition of functional groups containing oxygen (-OH, -COOH, etc.) to yield CO, and CO_2 [20]. It was observed that there was smaller weight loss taking place in rGO as compared to GO, which is by reason of the presence of less percentage of groups like -OH, -COOH, etc. in rGO [21]. It has been observed that the percentage mass loss of PG is nearly positioned at the weight loss range of individual components Go and PANI, however, the weight loss curve of PG was somewhat closer to GO indicating the stability of PG. Thus, it can be inferred that PANI has been successfully grafted on the surface of GO [22]. The composite PGR below 150°C showed a minute weight loss suggesting low moisture absorbed by the sample. Maximum weight loss occurred at a temperature range of 200 to 300°C and weight loss at approx. 550°C was due to the probable decomposition of rGO [23]. The comparative TGA of individual materials and their binary composite has been shown in Fig. 6 A.

Differential scanning calorimetry (DSC)

DSC is a very successful technique to determine the heat flow in the sample by using a DSC analyzer 50H of Perkin Elmer. A material of the known weight was heated under an inert (N_2) atmosphere at a 10 °C/min flow rate (from room temperature to 500 °C) to record the DSC data. DSC of PANI showed endothermic peaks at a lower temperature due to loss of water molecules and another endothermic peak was observed due to the decomposition of amine units as depicted by TGA results also. The endothermic peak below 100 ˚C was related to the evaporation of water molecules and the 2nd endothermic peak was observed at 230 ˚C due to the decomposition of the dopant, while the exothermic peak at 431˚Caccounted for the breakdown of PANI backbone [24]. In GO the endothermic peak below 100°C indicates evaporation of water molecules and also signifies that the de-oxygenation reaction starts below this temperature. A peak at 212˚C (endothermic) corresponds to the breakdown of oxygenated functional groups (-OH and -COOH etc.) with the evolution of CO and CO_2 [20]. In the case of rGO due to absorbed moisture an endothermic peak (below 100 °C) due was encountered, also an exothermic peak near 200 °C was observed due to the loss of oxygenated functional groups. However, these peaks were less intense as compared to the peaks observed in GO due to a smaller number of -OH and -COOH gr. The reduction of GO into rGO results in a decline in the number of functional groups, hence peak intensity

decreases [25]. In the presence of GO, and PANI there is a cross-linking reaction that results in thermodynamically destitute at lower temperatures. The binary composite showed an endothermic peak below 100 °C owing to the loss of moisture, an exothermic peak (209°C) due to the release of certain gases, and an exothermic peak at 433 °C due to the breakdown of the backbone of the polymer, which signifies the successful formation of the binary composite. Another binary composite PANI-rGO (PGR-5) shows an endothermic peak at 107 °C and two exothermic peaks, one at 278°C and the second at 435 °C. The peak intensity was found to be lower in binary composite because of enhancement in thermal stability [26, 27] as shown in Fig. 6B.

Scanning electron microscopy (SEM)

SEM image shows the average size of nanoparticles of PANI was about 60 nm [28]. These micrographs confirm the approximately spherical shape of the nanoparticles. In GO numerous folded and wrinkled sheet-like structures can be easily seen, and the GO presented a randomly arranged structure. SEM images of rGO showed that the wrinkled and folded sheets present in GO were reduced and were changed to exfoliated sheet-like appearance which might lead to a better exfoliated surface area thus leading to better electron navigation [29]. PANI was homogeneously surrounded by GO fibers in binary composite PG [27]. PGR composites show that the PANI nanoparticles lie on the RGO's surface [17].

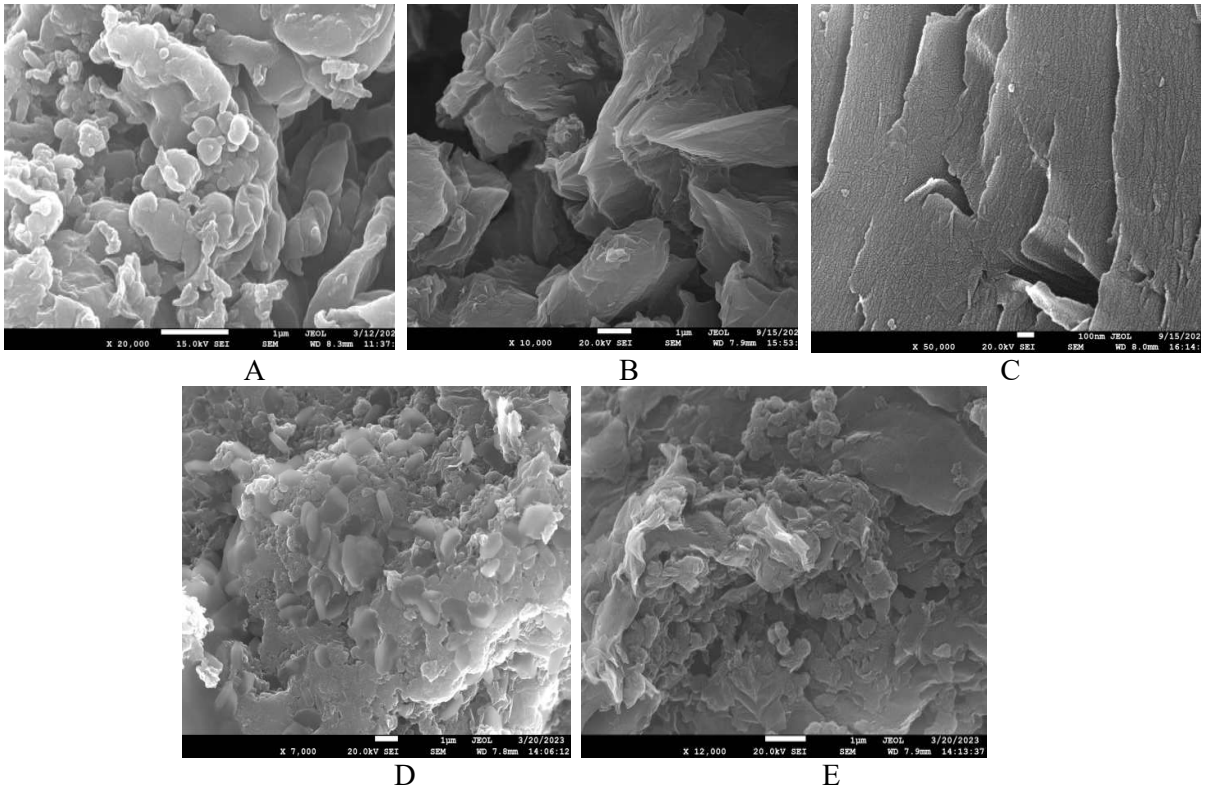

Figure 7. SEM micrographs of (A) PANI (B) GO (C) rGO (D) PG-5 and (E) PGR-5

CONCLUSION

A series of binary nanocomposites of PANI with GO (PG) and rGO (PGR) were successfully prepared *via* the *ex-situ* method in various ratios. These binary composites were compared for their electrochemical behavior by studying their associated specific capacitance measured by cyclic voltammetry. The results show a maximum specific capacitance of 169.5, 248.5, and 279.34 F/g for PANI, GO, and rGO at 1 mV/s. In the binary composition, the PG-5 has a ratio of 1:2 and was found to have the greatest C_s of 367 F/g, while 1231.9 F/g was the maximum capacitance of PGR-5 nanocomposite with a 1:2 ratio. Further, the fabricated nanocomposites (PG and PGR) and individual materials (PANI, GO, and rGO) were analyzed by FTIR, XRD, SEM, TGA, and DSC for their chemical, structural and thermal characteristics.

Conflicts of interest: *No conflicts of interest are declared by the authors.*

REFERENCES

1. T. N. A. B. T. A. Mutalib, S. J. Tan, K.L. Foo, Y. M. Liew, C. Y. Heah, M.M.A.B. Abdullah. *Pol. Bull.,* **78**, 4835 (2020), doi:10.1007/s00289-020-03334-w
2. D. George, G. James, J.K. Manjally, J. Thomas, M.S. Kuriakose, K.S. Aryamol, S.C. George. Application. *Mater. Today: Proc*, **24**, 1734 (2020), doi:10.1016/j.matpr.2020.03.597
3. G. Xu, N. Wang, J. Wei, L. Lv, J. Zhang, Z. Chen, Q. Xu. *Ind. Eng. Chem. Res.,* **51**, 14390 (2012), doi:10.1021/ie301734f
4. M. Ates M. Yildirim. *Pol. Bull*., **77**, 2285 (2019), doi:10.1007/s00289-019-02850-8
5. F. Soysal, Z. Çıplak, B. Getiren, C. Gökalp N. Yıldız. *Mat. Res. Bull*., **124**, 110763 (2020), doi:10.1016/j.materresbull.2019.110763
6. Shruthi, K.M. Vighnesha, Sandhya, D.N. Sangeetha M. Selvakumar, *Surf. Eng. Appl. Electrochem.,* **54**, 359 (2018), doi:10.3103/s106837551804018x
7. S.S. Bangade, V.M. Raut, S.E. Bhandarkar D.P. Gulwade. *Mater. Today: Proc.,* **29** (2020), doi:10.1016/j.matpr.2020.04.790
8. H. Mudila, V. Joshi, S. Rana, M.G.H. Zaidi S. Alam . *Carbon Lett*., **15**, 171 (2014), doi: 10.5714/CL.2014.15.3.171
9. H.Mudila, M.G.H. Zaidi, S. Rana, V.Joshi, S. Alam. *Int. J. Chem. Anal. Sci.*, **4**, 139 (2013), doi:10.1016/j.ijcas.2013.09.001
10. B. Butoi, A. Groza, P. Dinca, A. Balan V. Barna, V. *Polymers*., **9**, 732 (2017), doi: 10.3390/polym9120732.
11. B.S. Singer, S. Palaniappan, S. Pabba. *J. Electrochem. Soc.,* **159** (2020), doi: 10.1149/2.036201jes
12. S. Drewniak, R. Muzyka, A. Stolarezky, T. Pustelny, T.M.K. Moranska M. Setkiewicz. *Sensors*., **16**, 103 (2016), doi: 10.3390/s16010103
13. X. Jiao, Y. Qiu, L. Zhang and X. Zhang. *RSC Adv.,* **7**, 52337 (2017), doi:10.1039/c7ra10809e
14. F.T. Thema, M.J. Moloto, E.D. Dikio, N.N. Nyangive, L. Kotsedi, M. Mazza M. Khenfouch. *J. Chem.,* **2013**, 150536 (2013), doi: 10.1155/2013/150536
15. M. Manoj, K.M.A. kumar, B. Jinisha S. Jayalekshmi. *J Mater Sci Mater Electron*, **28**, 14323 (2017), doi:10.1007/s10854-017-7292-9
16. M. Mahadik, H. Patil, G. Bodkhe, N. Ingle, P. Sayyad, T. A. Gahaouri, S. M. Shirsat, M. Shirsat. *Front. Mater*., **7** (2020), doi: 10.3389/fmats.2020.00081
17. Y. Zhang, J. Liu, Y. Zhang, J. Liu Y. Duan. *RSC Adv*., 7, 54031 (2017), doi:10.1039/c7ra08794b
18. S. Palsaniya, H. B. Nemade, A. K. Dasmahapatra. *J Phys. Chem. Solids*, **154**, 110081 (2021), doi:10.1016/j.jpcs.2021.110081
19. A. Kumar, A. Kumar, H. Mudila, K. Awasthi V. Kumar. *J. Phys*., **1531** (2020), doi:10.1088/1742-6596/1531/1/012108
20. S.N. Alam, N. Sharma, L. Kumar, L. *Graphene*., **6** (2017), doi: 10.4236/graphene.2017.61001
21. N. Sharma, V. Sharma, Y. Jain, M. Kumari, R. Gupta, S, K. Sharma K. Sachdev *Macromol. Symp*., **376**, 1700006 (2017), doi:10.1002/masy.201700006
22. Q. Fan, Y. Yang, Y. Hao, X. Zhao Y. Feng. *J. Mol. Liq.*, **212**, 557, (2015), doi:10.1016/j.molliq.2015.10.008
23. Y. Wang, X. Wu, W. Zhang S. Huang. *Syn. Metals*, **210**, 165 (2015), doi:10.1016/j.synthmet.2015.09.022
24. M. Matoetoe, F. Okumu, C. Maphale O. Fatoki. *Asian J. Chem*., **27**, 1411 (2015), doi:10.14233/ajchem.2015.18061
25. J. Singh A.S. Dhaliwal (2022). *J. Phys Chem Solids*., **160**, 110358 (2022), doi:10.1016/j.jpcs.2021.110358
26. A. L. Ahmad, U. R. Farooqui, N. A. Hamid, *RSC Adv.*, **8**, 25725 (2018), doi:10.1039/c8ra03918f
27. L.R. Vargas, A.K.D.S. Poli, R. de C.L. Dutra, C. B. De Souza, M.R. Baldan E.S. Gonçalves. *J. Aerosp. Technol. Manag.*, **9**, 29 (2017), doi:10.5028/jatm.v9i1.697
28. A. Abdelrahmeen M.F. Elkady. *Alex. Engg J.,* **57,** 3291 (2018), 10.1016/j.aej.2018.01.012
29. B. Thirumalraj, C. Rajkumar, S.M. Chen S. Palanisamy. *Sci. Rep.,* **7** 41213 (2017), doi:10.1038/srep4121

AIP Conference Proceedings

RESEARCH ARTICLE | SEPTEMBER 08 2023

A comprehensive review on material and techniques used for heavy metal detection in potable water

Nisha; Goverdhan; Harish Mudila ✉; Anil Kumar; Parteek Prasher

Check for updates

AIP Conf. Proc. 2800, 020186 (2023)
https://doi.org/10.1063/5.0162879

CrossMark

View Online

Export Citation

Articles You May Be Interested In

Completing the dark matter solutions in degenerate Kaluza-Klein theory

J. Math. Phys. (April 2019)

Gibbs measures based on 1d (an)harmonic oscillators as mean-field limits

J. Math. Phys. (April 2018)

An upper diameter bound for compact Ricci solitons with application to the Hitchin–Thorpe inequality. II

J. Math. Phys. (April 2018)

09 September 2023 16:23:14

500 kHz or 8.5 GHz?
And all the ranges in between.
Lock-in Amplifiers for your periodic signal measurements

Find out more

Zurich Instruments

AIP Publishing

A Comprehensive Review on Material and Techniques Used for Heavy Metal Detection in Potable Water

Nisha[1,a)], Goverdhan[1,b)], Harish Mudila[1,c)], Anil Kumar[1,d)] and Parteek Prasher[2,e)]

[1]*Department of Chemistry, Lovely Professional University, Phagwara, Punjab-144411, India*
[2]*Department of Chemistry, UPES, Dehradun-248007, India*

[a)] rajat.gupta31@yahoo.co.in
[b)] goverdhanthakur143@gmail.com
[c)]Corresponding author email: harismudila@gmail.com
[d)] rsanil.nit@gmail.com
[e)] parteekchemistry@gmail.com

Abstract: Discharge of heavy metals from industry, agricultural, and wastewater treatment plants in potable water has resulted in pollution in many parts of the world. There are specific concentration limits set for heavy metals in potable water. To meet these limits, and thus for keeping a clean environment and human health, it is essential that a rapid, reliable, and sensitive analytical detection system be developed and put into use. A variety and modern techniques had been proposed and employed from time to time so as to determine the heavy metal concentration and decontaminate the water sources. This review presents the progress made in the development of various sensing methods and materials employed. These materials due to their specific properties like lightweight, non-corrosiveness, and excellent physical, chemical, electrical, and optical properties had been employed and are successful also. Apart from the advantages and limitations of various techniques involved and material employed had been also discussed in detail.

Keywords: Heavy metals, concentration, analytical techniques, limit of detection, conducting polymers

09 September 2023 16:23:14

INTRODUCTION

Water is a natural substance chemically comprising hydrogen and oxygen (2:1) and can exist in states of gas, liquid and solid. Naturally, it is clear, odorless, tasteless (until mineral desolvation), etc. apart from it does have any physical and chemical belongings. The specific physical properties include high heat capacity and heat of vaporization, good cohesive and adhesive properties, and high surface tension [1], while the chemical properties involve, pH ~7 (amphoteric in nature) and it acts as a universal solvent. Being universal solvent water carries numerous biological phenomena in the body of all the living components (plants, animals. aves, and especially humans) over the earth [2].

Importance of Water in Human Biology

As it is known that 70% of human physiology is water, that means it is one of the major components for the existence of our life over the earth, hence can be termed as the molecule of life. Water as a natural component involves in a variety of biological functioning, it is used in protein folding, enzyme-substrate interaction, and its stability, shaping the biomolecules, determination of DNA sequencing along with its twisting, prebiotic reactions, biomolecular interactions (protein-protein and receptor-substrate), proton transportation, controlling electronic excitations, etc. [3-6]. The physiological function of water involves the better kidney functions (removal of waste),

Proceedings of the International Conference on Materials for Emerging Technologies
AIP Conf. Proc. 2800, 020186-1–020186-16; https://doi.org/10.1063/5.0162879
Published by AIP Publishing. 978-0-7354-4631-1/$30.00

required by the cell system to transport ions (Na/K pump), maintaining hydraulic resistance (for cell polarization and motility), etc. [5-7].

Reasons/sources of Heavy Metal (HM) Contaminations in Potable Water

A variety of anthropogenic and natural processes liberates a high concentration of HM in water sources, sewage and water waste generated from industries (paint, leather, paper, etc.) mining, agrochemical, and human colonies are the major sources of anthropogenic contaminants of metals, HM, etc. [8-11], while weathering of rocks (metal-bearing), volcanic eruptions, etc. can be a natural way to add on the contaminants to the aqueous sources [12].

Problems Associated With Drinking Water

Being universal solvent water can dissolve a variety of materials (salt, biomaterials, metals, non-metals, etc.) in diverse concentrations. Biodegradable (bio) materials (fertilizer, paper, clothes, fibers, biofilms, etc.) are the source of pathogenic microbes and are responsible for numerous waterborne diseases, viz. cholera, dysentery, typhoid, diarrhea, etc. [8, 9]. Non-metals, metals, and a variety of HM in different combined forms originate from different sources which basically are soluble in water (to a particular extent) and can reach human drinking glass. These elements exceeding their limit can be detrimental to humans and can show their physiological and physiological effect on human anatomy [10] (Table-1).

General Effect of Heavy Metals on Human Physiology and Psychology

HM cause a variety of cancer, skin lesions, kidney/renal failure, and neurotoxicity [13]**.** Long-term exposure to these trace elements results in muscular, physical, and neurological degeneration which can further lead to serious non-curable diseases (at the advanced level) also viz. Alzheimer's disease, Parkinson's disease, and muscular dystrophy [14]**.** Similarly, soft water is studied to be more corrosive and present with higher metal contaminants thus causing cardiovascular diseases [15]**.**

TABLE 1: Various hazardous elements, their sources, and permissibility data

Element (Symbol)	Permissible Amount (mg/L or PPM) (WHO)	Source	Side-effects	Ref.
Non-Metals				
Flouride (F)	1.0	Urbanization, Industrialization, and sewage disposal	Fluorosis, brittle bones, and deformed knee and hip joints lead to paralysis.	16
Nitrate and Nitrite	10	Agriculture, fertilizer, decayed vegetable, water domestic effluent, atmospheric precipitation	Methemoglobinemia	17, 18
Chloride	250	Rocks contain chlorides, agricultural run-off, wastewater from industries, oil well waste	Heart and kidney disease.	17, 18
Phosphorous (P)	0.1	Rainfall	Digestive problems	17
Sulphate (SO_4^-)	250	Industries, detergents, and effluent from tanneries	Diarrhea and dehydration	18
Metals				
Beryllium (Be)	0.1	Fossil fuel combustion, industrial and agricultural	Beryllium disease (lung disease), carcinogenic	19

09 September 2023 16:23:14

Element (Symbol)	Permissible Amount (mg/L or PPM) (WHO)	Source	Side-effects	Ref.
		activities		
Aluminum (Al)	> 0.1	Bedrocks, leaching from minerals in the soil, water treatment	Alzheimer disease	20
Magnesium (Mg)	50	Minerals and ores,		18
Calcium (Ca)	75	Rocks like limestone, marble, dolomite, and gypsum	hampers blood clotting, rickets, bones fracture, etc. cardiovascular diseases (excess),	18
Sodium (Na)	200	Road salt, water treatment chemicals, domestic water softener, and sewage effluents.	hypertension, renal disorders and damage, and headache.	18
Potassium (k)	12	Silicate minerals, microcline, and metamorphic rocks	muscle cramps and weakness, depression, and heart rhythm disorder,	18
		Heavy Metals (HMs)		
Arsenic (As)	0.05	Arsenic containing bedrocks	skin cancer, lesions, keratosis, leucomelanosis	10, 17
Lead (Pb)	0.05- 0.10	Plumbing fitting and PVC pipes	anemia, reproductive effects, behavioral and learning disturbances enlephalopatayis	10, 17
Iron (Fe)	0.1-1.0	Laundry and porcelain	Hemochromatosis, hemorrhagic necrosis	10, 17
Mercury (Hg)	0.001-0.002	Atmospheric deposition, industrial waste, mining waste, and naturally occurring mercury minerals	CNS damage, depression, carcinogenic	10
Selenium (Se)	0.01-0.05	Seafood, organ meat, dairy products	Respiratory distress, selenosis, renal failure	10
Chromium (Cr)	0.05-0.1	Occur naturally in rocks, plants, soil, and volcanic dust	Liver damage, edema, multisystem organ failure, carcinogenic effects	10
Cadmium (Cd)	0.005-0.01	In ores of zinc lead and copper and is released in volcanic eruptions	Carcinogenic, effects CNS, dental caries	10
Zinc (Zn)	0.1-15.0	The byproduct of steel production or coal fire power stations	Eukopenia, lymphadenopathy, cancer, gastrointestinal toxicity	10

TECHNIQUES EMPLOYED FOR HEAVY METAL (HM) DETERMINATION/DECONTAMINATION FROM AQUEOUS SOURCES

As discussed, the importance of uncontaminated water for human physiology and psychology earlier, it is prime obligatory to detect these varieties of contaminates followed by their decontamination, a variety of processes had

09 September 2023 16:23:14

been introduced from time to time to meet up the challenges. These all processes have various advantages and limitations which are mentioned below. During the application of these processes/methods the factors (physio-chemical) viz. particle size of adsorbate and adsorbent, time of contact, temperature, the concentration of contaminant, pH, etc. play a significant role in the determination and removal of theirs [10, 21].

Adsorption

The process of adsorption involves the holding of solutes (solid, liquid, or gas) over the solid substrate called an adsorbent. A variety of adsorbents had been classified for this Nanocomposite of Thiol-lignocellulose sodium bentonite (TLSB, a –SH group-modified lignocellulose) were found to remove Zn^{2+}, $Cd^{2+,}$ and Hg^{2+} ions effectively from aqueous solutions. The adsorption parameters (concentration, doses, solution pH, temperature, and time) were taken into consideration for the complete study. The studies revealed 458.32, 357.29, 208.12 mg/g adsorption of Cd^{2+}, $Zn^{2+,}$ and Hg^{2+} by the TLSB nanocomposite showing its high adsorption capacity [22]. Nanometer-sized zeolite prepared by post milling recrystallization method was found useful in the removal of radioactive Cs ions from polluted water [23].

Microbial Decontamination

The environment and its components are adversely affected by the emancipation of HM generated by metal processing industries. Though numerous conventional treatment technologies are employed for the elimination of these HM from water, however, found non-economical while leaving toxic sludge of chemicals. In recent times the innovative and cost-effective method of **biosorption** has been employed for HM decontamination where metabolically certain microbes and/or plants are brought into use. A variety of microbes of the diverse family (A*spergillus, Penicillium, Rhizopus, Ascophyllum, Bacillus, Streptomyces*, etc.) can show high HM (Pb, Zn, Cd, Cr, Cu, and Ni) adsorption in the range of 05-641 mg/g [24]**.** *B. cereus* and SRB results in biosorption, bioaccumulation, and biosurfactant production, in Cd^{2+}, Zn^{2+}, and Cu^{2+} containing solutions, the order of Cd^{2+} was highly adsorbed while Cu^{2+} was adsorbed least [25]**.** Species such as *Bacillus megaterium* and *Rhizopus stolonifera* are helpful in the decontamination and bioremediation of Pb, Cd, and Ni [26]. *Pseudomonas saeruginosa* showed high Cd resistance in solid as well as in liquid media [27]. *Bacillus thuringiensis, Azotobacter chroococcum, Paenibacillusehimensis*, and *Pseudomonas pseudoalcaligenes* isolated from heavy metals in the soil were helpful in promoting plant growth [28]**.** *Bacillus thuringiensis* and *Bacillus subtilis* had been essential for the bioremediation of zinc and lead present in the soil [29]**.**

AAS (Atomic Absorption Spectrometry)

AAS is chiefly applied to analyze compounds in solution, this technique is hassle-free and low-priced. AAS coupled with vapor generation assembly is usually employed for successful trace analysis of Arsenic [30]**.** The change in the Pb^{2+} concentrations; due to adsorption, was monitored by AAS, the maximum uptake (73.4 mg/g) of Pb^{2+} was observed at 298 K, and adsorption of Pb^{2+} follows pseudo 2nd order with Langmuir isotherm model [10, 31]. AAS along with the Laser-induced breakdown spectroscopy (LIBS) technique was used as quantitative analysis for the determination of remaining Pb content in aqueous samples. This was done by post-treatment of contaminated water with raw montmorillonite (MMT) and its organic derivative (MMTO) [32]**.** Nanoparticles of PANI-coated CeO_2 synthesized in alkaline media via microwave method were used for detection of Cd^{2+} using AAS. Under optimum conditions, the calibration curve of $Cd^{2+}$was found to be linear in the 0.02–0.4 ng/mL range with an excellent correlation coefficient (0.9976), while the limit of detection/detection limit (LOD) was 0.005 ng/mL [33]. rGO/PANI nanocomposite was used for the detection of ultra-trace levels of Co^{2+}, under the optimum condition of pH, extraction, and desorption time, the linear calibration was observed at the range of 0.05–0.6 µg/L with LOD of 0.017 µg/L [34]. Cr^{6+} detection and removal from the water was carried out by employing PANI-chitin biomaterial, which was evaluated by AAS. The PANI/chitin (20 mg) shows the highest efficiency at pH 3, with a contact time of 12 minutes at 298.15 K [35]**.**

09 September 2023 16:23:14

TABLE 2: Various detection techniques with their advantages and limitations

Technique	Advantages	Limitations	Ref.
AAS	highly specific and sensitive (GFAAS), used for a variety of trace elements, high sample output, easy to use and handle, high accuracy, low cost,	In a mixture different lamps are required for different elements, lamps have a short life span, solution samples or volatile material is analyzed, require relatively large sample quantities (1-3 ml), are less sensitive towards refractory elements,	36
ICP	It is a precise, accurate, and sensitive analytical tool with the new developments in the ICPMS instrumentations such as decreased size, lower LOD, and more user-friendly software to control it and hence used for the multi-elemental ultra-trace detection and isotopic analysis.	Detection of elements by this method may suffer from the spectroscopic interference by the isotopes of elements present which results in a lack of sensitivity. The poor sensitivity of ICPMS is also due to its openness to matrix effects. It also lacks to provide information about the speciation of the sample.	37-39
NAA	NAA is a sensitive and accurate analytical technique used for the detection of trace and ultra-trace amounts of elements present in the sample under investigation. Materials difficult to dissolve without sample preparation is easily analyzed by using this method. In absence of interference present in the sample, a LOD of trace element in nanograms is detected with accuracy.	This method is expensive because of its openness to a nuclear reactor. It has a long gyrate and slow sample throughput. The sensitivity of NAA is decreased due to the presence of spectral interference of other elements such as Na and Br in the sample.	40,41
XRF	It feasible, useful, and non-destructive analytical technique for analyzing a variety of hazardous materials and environmental samples (water, powder, soil, etc.) owing to the effective radioisotope source, highly sensitive detectors, electronics associated, etc.	It is slow, laborious, and expensive. Samples taken for analysis are also limited due to the high cost of the laboratory.	42
Electrochemical	Versatile, simple, high sensitivity, rapid, repetitive and accurate, easy operation, inexpensive, low detection limit, compatible linear range and output, low power requirements, is of different types like SWV, SPE, CV, DPSPE, etc.	Work in narrow temperature range, affected by humidity and temperature which reduces the life of electrode, sometimes interfered with other analytes,	43, 44

Electrochemical Sensing Methods

Electrochemical sensors owing to their properties such as flexibility, convenience, rapid response, accuracy, etc. had been employed in a number of chemical and biological sensing procedures. Electrochemical sensing of the heavy metal ions present in water is done by modifying the electrodes present in such cells. The electrochemical sensing process involves a redox reaction of the target analyte present in the electrolyte, the redox reaction generates

09 September 2023 16:23:14

electrical signals, which are detected and then analyzed for results. Though a variety of materials are employed for electrode (working) modification, which involves their property of electrical conduction as a common characteristic.

Types of Electrochemical Sensing Methods

Anodic Stripping Voltammetry (ASV):

One of the most frequently used analytical methods to measure the metals present in an aqueous source is the ASV, which is also used for the chemical speciation of the metals. A large number of trace metals even at their low concentration can be detected precisely and accurately in less time [45, 46]. PANI/G was employed to sense the various HM ions (Cd^{2+}, Cu^{2+}, Pb^{2+}, etc.) by ASV. As compared to the PANI electrode PANI/G (LOD= 10^{-8} mol/L) composite demonstrates advanced sensitivity for sensing these HMs [47]. The composite material of PANI/GO/EDTA displays great sensitivity for Hg^{2+} when detected with the differential pulse anodic stripping voltammetry (DPASV) technique the observed LOD was 2 ppb [48]. Trace Cd^{2+} and Pb^{2+} were successfully detected by nanocomposite (PANI/Phytic acid) layered glassy carbon electrode (GCE) using the DPASV technique. During the analysis the synergistic role of PANI with phytic acid augments the charge transfer rate of HM (Cd^{2+} and Pb^{2+}), thus a LOD of 0.02 and 0.05 mg/L was encountered for Cd^{2+} and Pb^{2+} respectively [49]. Trace levels of certain HMs (Cd^{2+}, Cu^{2+}, Pb^{2+}, and Zn^{2+}) were ascertained by the ASV method by employing CNT electrodes where the LODs were 1.9, 0.27, 1.5, and 1.4 nM respectively for Cd^{2+} Cu^{2+}, Pb^{2+}, and Zn^{2+} [50]. The modified electrode of Fe_2O_3/Graphene/Bi composite was helpful in detecting HMs by DPASV procedure for Cd^{2+}, Pb^{2+}. and Zn^{2+} with a LOD of 0.08, 0.07 and 0.11, µg/L, respectively [51].

Differential Pulse Voltammetry (DPV)

Also known as differential pulse polarography (DPP), this technique comprises applying amplitude potential pulses on a linear ramp potential [52]. For effective electrochemical detection of Cu^{2+} DPV technique was applied where EDTA/PANI/SWNTs electrode was employed for the purpose, and a LOD 1.4 µM for Cu^{2+} was measured [53]. An electrochemical sensing method based on DPV was employed for selective and effective determination of Cd^{2+} in the water sample. CeO_2/PANI composite over GCE was employed with a LOD of 8.59 nmol/L [54]. Surface modification by chitosan GCE was used to determine Cu, Pb, Cd, Co, As, and Pt. The range of LOD for Cu^{2+} (3.99×10^{-6} - 39.1×10^{-6} mol/L), Pb^{2+} (1.99×10^{-6} – 15.8×10^{-6} mol/L), Cd^{2+} (1.59×10^{-5} to 6.23×10^{-5} mol/L), As^{4+} (7.99×10^{-6} to 50.4×10^{-6} mol/L), Pt^{4+} (8.19×10^{-6} to 35.9×10^{-6} mol/L), and Co^{2+} (6.11×10^{-4} to 27.8×10^{-4} mol/L), was achieved which demonstrate high effectivity and employability of chitosan as HM sensing material [55]. Indium tin oxide (ITO) glass electrode modified by hydroxyapatite film was used for sensing Cu^{2+}, Pb^{2+}, and Hg^{2+} using DPV technique with LOD value 1×10^{-12} for (Pd^{2+} and Cu^{2+}) and $8\times^{10-8}$ M for Hg^{2+} [56].

Square Wave Voltammetry (SWV)

In pulse-based voltammetric techniques such as SWV, a better detection limit, and a clear signal-to-noise ratio are obtained as compared to other expensive spectroscopic techniques used for the same purpose [57, 58]. Various types of working electrodes of different materials (Pt, Au, and Ag) had been employed for the detection/determination of HMs by SWV techniques [59, 60]. SWASV technique was used for the Pb^{2+} and Cd^{2+} sensing by G/PANI/PS electrode in the existence of Bi^{3+}. A linear relationship was observed between HM ion concentration and anodic current in a range of 10–500 µg/L with the LOD of 3.30 for Pb^{2+} and 4.43 µg/L for Cd^{2+} [61]. SWASV method is proved useful for the detection of Cd in the presence of Pb, factors like correlation coefficient, root mean square, and mean absolute error of Cd in the presence of Pb were 0.998, 1.68, 1.63, and respectively [62]. Graphene oxide-gold (GO/Au) nanoparticles were helpful in detection of Cd^{2+} (LOD of 0.08 µg/L) and Pb^{2+} (LOD of 0.12 µg/L) by SWASV [63]. Tannic acid capped gold nanoparticle complexes analyzed Hg^{2+} with LOD 100.0 fM by SWASV [64]**.** Fe_3O_4 nanoparticles with terephthalic acid were applicable for detection of Hg^{2+}, Pb^{2+}, and Cd^{2+} by SWASV with LOD values of 0.1, 0.05, and 0.01 µM for individual HM ions respectively, whereas the LOD values for the simultaneous analysis of Hg^{2+}, Pb^{2+}, and Cd^{2+} ions were found to be 0.3, 0.04 and 0.2 µM respectively [65]**.** L-cysteine functionalized mesoporous $MnFe_2O_4$ detected Pb^{2+}, Hg^{2+}, Cu^{2+} and Cd^{2+} by SWASV technique. A high

09 September 2023 16:23:14

level of selectivity and sensitivity57.0 and 35.3 µA/µM was achieved toward Pb^{2+} by L-cysteine modified bimetal oxides of Mn and Fe nanoparticles [66].

Cyclic Voltammetry (CV)

The basic principle of this method is that the current produced between the working electrode (WE) and the counter electrode (CE) used in the electrochemical cell is recorded by varying the voltage between its upper and lower values resulting in a potential of linear shape. Quantitative and qualitative information on electrochemical reactions (reaction mechanisms, electrochemical kinetics, etc.) can be achieved which takes place in an electrochemical cell [67]. The PANI coated carbon electrodes were made by CV process with 100 cycles, with Platinum CE, carbon WE, and Ag/AgCl as a reference electrode (RE) [68]. Using CV analysis, TiO_2/ZrO_2 was employed to detect Pb and Cd as HM, at reduced concentrations of 7.6 and 1.1 M respectively, at optimum pH value [69]. In the well water, the concentration of Pb (18.73 µg/L) was observed to surpass the standard limit of 15.00 µg/L. To decontaminate well water from Pb concentration, CV and SWV electrochemical techniques were employed where nano-dimensional GO and nanotubes modified Au and Pt electrodes were used. Subsequently, after the elimination of Pb, the LOD levels HM was found in the range of 0.03 to 5.73 µg/L, while the concertation of Pb in the potable water was dropped to 8.09 µg/L [70]. Naphtha [2,3-a]dipyrido[3,2-h:2',3'-f]phenazine-5,18-dione and 1,10-phenanthroline were employed for detection of Pb^{2+} and Hg^{2+} respectively by CV, in CV characteristic peaks at 0.2 eV and -0.6 eV were observed for Pb^{2+} and Hg^{2+} respectively with LOD 50µM [71]. rGO/Ag NPs were helpful in detecting Cu^2, $Cd^{2+,}$ and Hg^{2+} by *Cheng et al. 2019*, with LOD value 1015, 1021and 1029 M respectively [72].

Other Commonly Employed Techniques

Inductively Coupled Plasma (ICP) has the capacity to separate many (about 70) elements at a time, major and trace elements such as beryllium, magnesium, calcium, chromium, cobalt, nickel, copper, zinc, arsenic, strontium, cadmium, lead, etc. can be efficiently determined and measured by ICP when coupled with mass spectrometry (MS)technique. The range detected by ICP of *toxic* inorganic elements has been in parts per billion [73, 74]. ICP was helpful in the detection of trace elements such as Co, V, Sb, Mn, Mo, and Tl simultaneously with LOD of 0.1 mg/kg, for all of them [75]. ***X-ray fluorescence (XRF):*** XRF and other advanced techniques such as electrochemical XRF are elemental analysis techniques that are helpful for quantitative detection of heavy metals in solution. Use of electrochemical XRF was done for determining the LOD of Cu^{2+} and Pb^{2+}which were found to be 0.05 and 0.04 ppb respectively [76]. ***Neutron activation analysis (NAA):*** this is a nuclear process employed majorly for determining the concentration of individual elements (such as, As, Ba, Br, Ce, Co, Cr, Cs, U, Zn, etc.) present in the material [77]. NAA had been used for the determination of Sb concentration was found 50.2 mg/L which exceeded the standard [78]**.**

MATERIALS USED FOR SENSING

As discussed earlier a range of materials (electrically conductive) can be employed for electrochemical sensing of heavy metals, these materials involve MXenes, Transition Metal (in form of TMO, TMC, TMX, etc.), carbonaceous material (Graphite, graphene, CNTs, etc.), Hybrid material (combination of TM with carbonaceous material) and conducting polymers (PANI, PPY, PTH, etc.).

Transition Metal Composites (TMCo)

Transition metal composites had great application in environmental remediation and have been effectively used in the removal of toxic metal ions and dyes from contaminated water. Nowadays numerous 2D materials, viz. metal oxides, transition metal carbides (TMCs), Transition metal oxides (TMOs), transition metal dichalcogenides (TMDCs), MXene, etc. are being used in this direction [79-81]. TMCo in recent times due to the properties mentioned above and properties such as tenability and semiconductive nature, raid charge transfer, and appreciable electrical conductivity is found to be significant in the detection of heavy metals. The high efficiency of the TMCo

09 September 2023 16:23:14

electrode system can be attributed to the large number of photoelectrons accumulated on the surface of the electrodes which leads to the deposition great number of reduced ions [82]**.** The interaction among Hg^{2+} and MoS_2 particles were studied by *Jiang et al. 2015*, Hg^{2+} was studied to strongly bind to MoS_2 owing to a high binding affinity between the two components thus determination become high with LOD of 30 pM [83]. MoS_2 and reduced graphene oxide (rGO) nanocomposite were used in the detection of Pb^{2+} and Ni^{2+}respectively. The HM ions were recognized via AAS, with respective LODs of 0.71 and 0.21 µg/L [84]. The nanocomposite of MoS_2/rGO was used to modify GCE to determine the presence of Pb^{2+} using SWASV, the nanocomposite achieved an extremely high sensitivity of 50.80 mA/mM, while the LOD of 0.005 mM was also determined [85]. *Yamuna et al. 2021,* detected Pb^{2+}, Cu^{2+}, Hg^{2+} electrochemically (via DPV) by modified Co_3O_4/NC/SPCE electrode. The individual and simultaneous determination of HMs was achieved satisfactorily via the mentioned electrode. Correspondingly a sensitivity of 16.73, 11.46 was achieved for Pb^{2+}, Cu^{2+}, and Hg^{2+}, and LOD for Pb^{2+}, Cu^{2+}, and Hg^{2+}, was 4.1, 0.9, and 0.1 nM [86]**.** $[CH_3NH_3]_{2x}Mn_xSn_{3-x}S_{6\cdot0}.5H_2O$ (x = 0.5–1.1) a chalcogenide (CMS) was used to remove Cd^{2+} and Pb^{2+}, the CMS shows an adsorption capacity of 515 and 1053 mg/g at 20 ◦C respectively for Cd^{2+} and Pb^{2+} [87]. MoS_2 nonabsorbent produced through a surfactant-assisted hydrothermal method shows an adsorption capacity of 289 mg/g at room temperature [88]. Zinc tin sulfide chalconoids had high surface area and pore volume and possessed high affinities towards soft heavy metals [89]. Sulfur-containing materials like ZnS were used to remove heavy metals. The removal of Cd^{2+} was done by the addition of Cd^{2+} to $Zn_xCd_{1-x}S$ solution, which displayed a high uptake capacity (400 mg/g) for Cd^{2+} [90].

MXenes

($M_{n+1}AX_n$, carbonitrides, nitrides, metal carbide, etc.) based materials owing to exceptional properties such as electron-richness, extraordinary surface area, hydrophilicity, tenability, appreciable electrical conductance, activated sites, and high adsorption capacity had been effectively employed as an excellent adsorbent for removal of toxic HMs from aqueous sources. Nano form MXenes are bestowed with a small interlayer gap of < 2 Å which helps in trapping M^{n+} species (< 4.5 Å) within themselves [91]. Alkaline intercalated MXenes was used in multiple HM detection i.e., Cd^{2+}, Pb^{2+}, Cu^{2+} and Hg^{2+} with LOD of 0.098, 0.041, 0.032 and 0.0130µM respectively by SWASW [92]**.** A nano-form composite of MXenes ($Ti_3C_2T_x$, T_x = -O, -OH, -F) was used for the development of an electrochemical sensor for sensing HMs like Pb^{2+} and Cd^{2+}. The BiNPs@$Ti_3C_2T_x$ sensor due to its large surface area and excellent electrical conductivity, not only this, BiNPs were effectual for ASV to detect HMs. The BiNPs@$Ti_3C_2T_x$ nano-sensor achieve a LOD of 10.8 and 12.4 nM for Pb^{2+} and Cd^{2+} [93]. Fe_3O_4@MXene had an adsorption capacity of 63.2% for $Cu^{2+,}$ 64.1% for Cd^{2+}, and 70.2% for Cr^{6+} by nanofiltration with adsorptive membrane technology [94].

Carbonaceous Material

Carbonaceous materials of different dimensions such as graphite, graphite oxide (GO), reduced GO (rGO), graphene, CNTs, etc. are widely used as conductive materials for efficient electrochemical sensing. These materials have a honeycomb-like structure which makes them efficient to conduct charges and hence their employability in this regard. Apart from numerous unique physicochemical properties viz. high surface to volume ratio, hydrophilic character, high electron affinity, small pore size, high strength, tunability, surface defects, etc. are the major responsible content that helps these carbonaceous materials to adsorb trace elements of variable size and thus remediation of potable water [95]**.**

rGO/Graphene

Graphene/rGO is generated via the reduction of graphene oxide (GO) via various methods, rGO consists of very high conductivity which is related to its large surface area, extraordinary electron conductivity, and exceptional biocompatibility. By virtue of the high area of rGO, it adsorbs a great number of toxic heavy metals in its matrix [96]**.** rGO alone or in hybrid form had been used for effective heavy metal detection, the hybrid material had extraordinary characteristics in this regard. The nanocomposite of rGO and Bismuth nanoparticles is fabricated for effective detection of heavy metals Cd^{2+}, Pb^{2+}, Zn^{2+}, and Cu^{2+} in the detection limit of 2.8, 0.55, 17, and 26 µg/L respectively [97]**.** Although graphene had numerous significant properties, the presence of a strong inter-functional

09 September 2023 16:23:14

bond among graphene layers/sheets generates certain issues viz. reduced surface area, sedentary surface chemical properties, sluggish dispersion, and condition of agglomeration, due to which the performance of graphene as a potential heavy metal decontaminant/adsorbent is reduced [98]**.** Hg was detected conveniently by electrochemical sensing and further was removed by sulfur-doped rGO, with a high Hg uptake capacity of 829.27 mg/g [85]. Cd^{2+} is detected by SnO_2/rGO composites, in acetate buffer (0.1M) at a potential of 0.1V is as optimal conditions [99]**.**

Graphene Oxide (GO)

GO a sp^2 hybridized carbonaceous material has a hexagonal honeycomb lattice structure, the GO surface composes of functional groups like -OH, -O-, -COOH, etc. which provides it a hydrophilic nature and thus allows the GO flakes to get well dispersed in water, apart atomically layer thickness, mechanical certain property, formation of compact membrane structure and property to get blend with other material (polymer matrix), etc. makes GO a good contender for water purification. These extraordinary properties are helpful to decontaminate heavy metals from aqueous sources to a great extent [99]. GO-based micro-bots were employed to perceive and thus capture Pb^{2+} in potable water, where the motile GO had 10 times higher efficiency as compared to non-motile. The adsorption capacity was achieved to be very high (reducing Pb^{2+} to 50 ppb from 10^3 ppb in an hour) which may be attributed to the magnetic behavior of GO particles [100]. To improve the performance of GO and overcome the limitations, various chemical and physical modifications and GO-based materials had been incorporated by the research groups. These chemical and physical modifications where incorporation of materials like metal oxide [101, 102], organic compounds (chitosan, poly(l-glutamic acid), etc. [103, 104] enhance the properties so as to generate GO-based adsorbents with excellent efficiency for trace metal removal [105].

Carbon Nanotubes (CNT)

Multi-walled (MWCNT, 0.4-10 nm) and single-walled (SWCNT, 4-100 nm) are two forms of CNTs [106]**.** All forms of CNTs are generally compact and light, durable, with high electrical conductivity and a high specific surface area. Apart CNTs having superior mechanical, chemical, and structural properties to graphite and other conventional material in the extraction and electrochemical sensing of HMs also the factors like high sensitivity, selectivity, fast response, and recovery provides it an upper hand [107]**.** The use of nanomaterials like CNTs, for electrochemical detection of heavy metals, has been done by numerous electrochemical methods including electrochemical stripping analysis. CNTs with the DPASV technique are being used for the determination of metals like Pb and Cd, studies show in aqueous solutions for Pb^{2+} and Cu^{2+} a LOD of 0.2279 and 0.3321 ppb were achieved [108]**.** Similarly, for the heavy metal detection (Cd^{2+}, Pb^{2+}, Cu^{2+}, and Hg^{2+}), Fe_3O_4/MWCNTs and Fe_3O_4/F-MWCNTs nanocomposites were fabricated and were analyzed by electrochemical sensing. The sensitivity range is 108.79, 125.91, 160.85, and 312.65 μA/mM.cm^2 while LOD of 0.5–30.0, (for Cd^{2+}, Pb^{2+}, Cu^{2+},) and 0.5–20.0 μM Hg^{2+}, was studied with Fe_3O_4/MWCNTs. The LOD of the Fe_3O_4/F-MWCNTs sensor for Cd^{2+}, Pb^{2+}, Cu^{2+}, and Hg^{2+}, were 0.05, 0.08, 0.02, and 0.05 nM correspondingly [109]**.** MWCNTs were used to analyze trace amounts of the metal ions of Cu, Zn, Mn, and Pb by FAAS with LOD 0.59, 0.62, 0.28, and 1.00 μg /L [110]. MWCNTs are used to detect heavy metal ions, Cu^{2+}, Co^{2+}, Ni^{2+}, and Pb^{2+} with LOD in the range of 1.64–5.68 g/L [111]. CNT modified with poly-amidoamine dendrimer to eradicate HMs (Cu^{2+} and Pb^{2+}) from water sources had high adsorption capacities for Cu and Pb, which are 3333 and 4870 mg/g respectively [112]. The decontamination of numerous HMs through batch adsorption method by P-CNTs and polyhydroxy butyrate functionalized CNTs (PHB-CNTs). The HM removal capabilities based on the ion-exchange technique and electrostatic forces mechanism were high for PHB-CNTs as compared to P-CNTs [113].

Though CNTs had been confirmed for their superior properties due to which they are considered to be a potential contender to be used in sensing but some factors viz. high cost, the requirement of high purity (pre-treatment), presence of defect and functionalization, chances of particles aggregation, etc. greatly reduce its capability to be used in sensors [114].

Activated Charcoal (AC)

Activated charcoal also named activated carbon is widely applied for the sensing purpose of gases and other analytes in various sources. Some of the unique properties such as highly porous assembly, high surface-to-volume

09 September 2023 16:23:14

area, the prospect of tenability, high chemical, and mechanical stability, and low favorable price, are major advantages of AC to be used in a variety of sensors [115]. The preparation procedure, nature of precursor, and other physical conditions regulate the physiochemical properties of AC which largely determines its adsorptive nature of its.

The decontamination of HMs (Cd, Cu, Ni, and Pb) from water using AC along with the effect of temperature and contact time on decontamination was studied by *Abdulrazak et al. 2016*. At 80 °C a high removal percentage was encountered highest for Cu (96.71%) and lowest for Ni (92.01%) for a contact time of 60 min [116]. Though AC is used to treat potable water by removing numerous contaminations, however, contaminates such as sodium, fluoride, nitrates, microbes, and various water hardening compounds are had to remove due to slow kinetics and poor selectivity. AC-based filters had a low life span due to the trapping of contaminates, also it requires a long time of contact with water to remove the contaminates [117-118]**.** A spherical carbon nanoparticle with AC prepared from dead mango leaves with a high surface area (1555 m^2/g) was used for the detection of HMs like $Cd^{2+,}$ Pb^{2+}, Cu^{2+}, and Hg^{2+} with LOD 24.4, 5.7, 23.2 and 24.6 nM [119]. Detection of Cd^{2+}, Pb^{2+}, and Cu^{2+} was done by Pd nanoparticles on porous AC, an individual, as well as simultaneous detection on Pd@PAC/GCE material by SWASV method, was conducted, for individual detection the LOD of $Cd^{2+,}$ Pb^{2+} and Cu^{2+} were 13.33, 6.60 and 11.92 nM with sensitivity 0.11, 0.11 and 0.08μA/nM and for simultaneous detection, LOD was 20.9, 9.19 and 14.78 nM with sensitivity 0.02, 0.10 and 0.06 μA/nM respectively [120]. AC fiber rod was used for the simultaneous detection of $Pb^{2+,}$ Cd^{2+} and Zn^{2+} with LOD 0.1, 0.3, and 1.0 μg/L by the DPASV method [121].

Conducting Polymers (CPs)

CPs have electrical and electrochemical properties similar to traditional semiconductors and metals and thus are designated with the name synthetic metals. In CPs charge transfer reactions occur in which electrons are either added or removed from the delocalized π-bonded polymer backbone leading to the formation of charge carriers. The conductivity can be improved by many factors like alteration in temperature, doping, etc. CPs are used in the applicable field of capacitors, actuators, sensors, biosensors, etc. [122]. CPs like Polyaniline (PANI), Polyacetylene (PACE), Polypyrrole (PPY), Polythiophene (PTH), etc. have specific properties viz. physical, mechanical, chemical, electrical, environmental stability, low cost, easy formation (via chemical or electrochemical processes), tunable charge transfer ability (via copolymerization or structural derivations), and adaptability which make them suitable to be used for different application including sensors [123].

CPs such as **PPY** exhibit a high electrical conductivity of 10^2S/cm (comparable to In and Sn), PPY (bound with epoxy, *Opuntia Ficus* Extract) based heavy metal sensor had been used to detect Pb^{2+}, Cu^{2+}, Cd^{2+} and Zn^{2+} [124]. PPY NPs with dispersants were used to modify GCE, with high sensitivity (0.1 to 50 μmol/L) and LOD (0.055 μmol/L) for Pb^{2+} [125]. SWASV technique was used to detect Hg^{2+} in a water sample by PPY modified GCE electrode having a LOD of 0.1 mg/L [126]**.** Conducting PPY membranes were deposited on GCE useful in the discovering of Ag^+ with LOD of 6×10^{-9} M by DPSAV [127]**. PTH** owing to its high charge transport and stability (doped and undoped states) has been considered a model for studying its applicability in various energy storage devices such as fuel cells and batteries, also in the arena of corrosion protection and chemical sensing [128].

A peak was observed at 0.17 V by complexing Ag with PTH when analyzed by means of DPASV, a linear relation in the range of 0.07–1.0 mg /L was obtained between the current peak and concentration of Ag^+ while the LOD obtained was 0.06 mg/L [129]**.** PEDOT modified GCE had shown appreciable LOD of0.004, 0.003, 0.002,0.002and0.003μg/ml for Zn^{2+}, Cd^{2+}, Pd^{2+}, As^{3+}, and Cu^{2+} respectively [130]**.** In situ polymerization method was employed for the fabrication of PEDOT/black TiO_2 composites in varying concentrations, (3,4-ethylene dioxythiophene (EDOT) or 3,4-propylenedixoythiophene (ProDOT)) were the composites thus generated, which were further used for determination of Cd^{2+} and Pb^{2+} DPV method. These composites (PEDOT/B-TiO_2 and PProDOT/B-TiO_2) were. The LOD of the PEDOT/black $TiO_2$was 0.00073 μM, while it was 0.00087 μM for PProDOT/black TiO_2 [131]**.** Studies show appreciable electrical conductivity (0.21 S/cm) for **PANI** (a p-type semiconductor polymer) at 28°C which increases exponentially with temperature [132]**.** Values of electrical conductivities at room temperature of doped thin films of PANI were 0.5 ohm/cm, respectively [133]**.** PANI modified GCE was used to detect heavy metals (Cd^{2+}, Pb^{2+}, and Cu^{2+}) in potable water via the ASV technique, where the previous two were detected by the sensor but Cu^{2+} remained undetected [47]. PANI was studied for adsorption capacities (Langmuir adsorption) towards heavy metals, which shows appreciable adsorption behavior

09 September 2023 16:23:14

towards Zn^{2+} and Cu^{2+}which further increases with the addition of TiO_2 in matrix [118]. Pb^{2+} and Cu^{2+} had been detected by Au@PANI with detection limit 0.003 and 0.008µM by SWASV method [134]**.** PANI in 0.1 M acetate buffer was used to detect Cd^{2+} and Pb^{2+} ions via SWASV, 0.13 and 0.1µM LOD were encountered for the ions, which the sensitivity increased with deposition time (as polymer film became thicker with time) [135]**.** Stable PANI NTs were studied via the SWASV method for $Pb^{2+}$and $Cd^{2+}$with 9.65×10^{-11} and 2.67×10^{-10}mol/L LOD [136]**.** PANI/Graphene composite: A *insitu* polymerized PANI (0.2 mol/L)/graphene nanocomposite (PANI/G) was synthesized and used to modify glassy carbon electrodes for the determination of heavy metals (Cd^{2+}, $Pb^{2+,}$ $Cu^{2+)}$ via ASV. This employed nanocomposite shows a maximum sensitivity towards Pb^{2+} (10^{-8}mol/L). PANI/G hybrid composite was found more efficient in the detection of Cd^{2+}, Pb^{2+}, and Cu^{2+} via the ASV method, higher intensity of stripping peaks was observed for hybrid material s compared to CP, due to improved transfer rate, high conductivity, and surface area provided by the graphene material, with a LOD of 10^{-8}mol/L [47]. PANI/carbon paste electrode effectively detects Pb^{2+} and Cd^{2+} with LOD 0.03 and 0.09 µg/L [137]. Phytic acid/PANI electrode material helps in the determination of HMs like Cd^{2+} and Pb^{2+} with LOD of 0.02 and 0.05µg/L by DPASV method [138]**.** PANI/vanadyl phosphate) was used in the discovery of Pb^{2+} with a LOD of 1.36 nM and sensitivity 2.105µAm/M [139]**.** PANI and PANI/SWNTs composites have a sensitive response with LOD 1 gm/L to 1 gm/500 L [140]**.** PANI/GO hydrogel at high temperature has properties of sensing and decontamination of Pb^{2+} by electrochemical method along with LOD of 0.04 nM [141]. UiO-66-NH_2@PANI was used in the detection of Cd^{2+}in concentration range of 0.5–600 µg/L and LOD 0.3 µg/L [142]**.** G/PANI nanocomposite electrode was employed for simultaneous detection of HMs like Zn^{2+}, Cd^{2+}, and Pb^{2+} by CV with LOD 1.0 µg/L (Zn^{2+}) and 0.1 µg /L (Cd^{2+} and Pb^{2+}) [143]**.** Cobalt doped ZnO/rGO (Co:ZnO/RGO) nanorods had been used in the determination of Cd^{2+} and $Pb^{2+}$by DPV with a LOD of 0.94 µg/L for Cd^{2+} and 0.83 µg/L for Pb^{2+} [144]**.** rGO/Ala/PANI exhibited the property to detect $Cd^{2+,}$ Pb^{2+} and Cu^{2+} by SWASV method with LOD of 0.03, 0.045 and 0.063nM and sensitivity of 0.43, 0.61 and 0.71µA/nM respectively [145]**.** EDTA/PANI/GO was used in the detection of Hg^{2+} ions with LOD 2ppb and sensitivity 1ppb by DPSV method [146]**.** G/PANI/Polystyrene had been employed for simultaneous determination of Pb^{2+} and Cd^{2+} with LOD of 3.30 and 4.43 µg/L respectively by SWASV [147]**.** A composite of PANI/SiO_2/$CuFe_2O_4$ was utilized by *Taleb et al. 2020*, for the removal of Fe^{2+}, Mn^{2+}, and Cu^{2+} from water. The maximum Langmuir capacities for Cu^{2+}, Fe^{2+}, and Mn^{2+} were found to be 285.71, 416.67, and 454.55 mg/g respectively [148]**.**

CONCLUSION

In the current time, the elevated concertation of HMs in aqueous sources had been a major issue of concern not only for the scientific community and administrators but also for the citizen. These HMs present in aqueous sources are the main cause of water pollution and thus lead to numerous health hazards. Therefore, as a prime obligation, it is required to develop certain policies and strategies to bring control in the release of the HMs in aqueous sources, along with the generation of technologies and materials to detect and decontaminate these HMs present in these water sources thus altering the devastating impact on human health and the environmental strata. This review is an attempt to understand the effect of HMs along with bringing the ideas of various techniques employed for encountering the negative issue generated by these trace metals. The details of various physical techniques like AAS, ICP, XRF, NAA, and Electrochemical methods had been discussed. Among these techniques, the electrochemical method displayed high accuracy and improved performance, specific selectivity, high sensitivity, high LOD, appreciable limit of quantification (LOQ), onsite detection, etc. This method involves limitations also like it works in a narrow temperature range, affected by humidity and temperature which reduces the life of the electrode, and sometimes interfered with other analytes reducing its superiority. Electrochemical detection needs specific conductive electrodes which can be prepared from electroactive materials such as TMO, rGO, GO, CNT, MXene, AC, and CPs (PPY, PEDOT, PTH, and PANI) Carbonaceous materials like graphene and/or GO in the recent time had becomes very attractive material to be employed in electrochemical sensors, while their performance can be enhanced by using their composites prepared with other electroactive materials, where out of many materials CPs offer advanced properties. CP-based sensors are very promising due to their affinity toward analyte, lower detection limits, high sensitivity, selectivity, stability, etc. CPs are widely used as electrode materials owing to their metal-like conductivity, processability, and ease of fabrication. Most CPs exhibit high specific capacitance, and they deliver energy rapidly but disadvantage such as diminished cycle life affects their employability. Thus, judicious modification and combination of various active materials are required to get such a material that can efficiently reduce the concentration of hazardous heavy metals in environmental strata and also be recovered thus not polluting the natural components.

09 September 2023 16:23:14

REFERENCES

1. Ronda L. T. and Alcazar X. S. Journal of Human Kinetics**. 4**, 237-248 (2014).
2. Abu Shmeis R. M. Analytical Chemistry, **81,** 1–56 (2018).
3. Finney J.L Biological Sciences, **359,** 1145–1165 (2004).
4. Chaplin M..Nature Reviews Molecular Cell Biology, **7,** 861–866 **(**2006)
5. Li Y., Konstantopoulos K., Zhao R., Mori Y., and Sun S. X. Journal of Cell Science, **133,** 1-11 (2020)
6. P. Ball, "The Importance of Water", in Astrochemistry and Astrobiology, edited by I. W. M. Smith, C. S. Cockell and S. Leach, (Springer, Heidelberg, 2013) 169-183.
7. Clark, W. F., Sontrop, J. M., Huang, S.-H., Gallo, K., Moist, L., House, A. A., Garg, A. X. JAMA, **319,** 1870-1879. (2018).
8. Sweileh, W. M., Zyoud, S. H., Al-Jabi, S. W., Sawalha, A. F., and Shraim, N. Y Annals of occupational and environmental medicine, **28**, 1-11 (2016).
9. Chaves Simões, L., and Simões, M. RSC Adv**., 3,** 2520–2533. (2013).
10. Mudila, H., Prasher, P., Kumar, M., Kapoor, H., Kumar, A., Zaidi, M. G. H., and Verma, A. International Journal of Environmental Health Research, **29,** 1–21 (2018).
11. Gebretsadik, H., Gebrekidan,A. and Demlie L. Cogent Chemistry**, 6(1),** 1-15 (2020).
12. Ali H., Khan E., and Ilahi I. Environmental Persistence, Toxicity, and Bioaccumulation. **2019,** 6730305. (2020).
13. Chowdhury, S., Mazumder, M. A. J., Al-Attas, O., and Husain, T. Science of The Total Environment, **569-570**, 476–488. (2016).
14. Mohod, C V and Dhote, J. International Journal of Innovative Research in Science, Engineering and Technology. **2,** 2993-2996 (2013)
15. Craun, G.F. and Mccabe, L.J. Journal of the American Water Works Association, **67,** 593-600 (1975).
16. Meenakshi, and Maheshwari, R. C. Fluoride in drinking water and its removal. Journal of Hazardous Materials**, 137,** 456–463**.** (2006).
17. Puri, A., and Kumar, M. Indian Journal of Occupational and Environmental Medicine, **16,** 40-44 (2012).
18. Meride, Y., and Ayenew, B. Environmental Systems Research, **5,** 1-7 (2016).
19. Vaessen, H. A. M. G., and Szteke, B. Food Additives and Contaminants, **17,** 149–159. (2000).
20. Flaten, T. P. Brain Research Bulletin, **55,** 187–196. (2001).
21. Gumpu, M. B., Sethuraman, S., Krishnan, U. M., and Rayappan, J. B. B. Sensors and Actuators B: Chemical, **213**, 515–533 (2015).
22. Zhang, W., An, Y., Li, S., Liu, Z., Chen, Z., Ren, Y., Wang, S., Zhang, X., and Wang, X. Scientific Reports, **10,** 1-19 (2020).
23. Torad, N. L., Naito, M., Tatami, J., Endo, A., Leo, S.-Y., Ishihara, S., Kevin C-W. W., Wakihara, T and Yamauchi, Y. An Asian Journal, **9,** 759–763. (2014).
24. Ahluwalia, S. S., and Goyal, D. (2007). Microbial and plant derived biomass for removal of heavy metals from wastewater. Bioresource Technology, **98,** 2243–2257**.** (2007).
25. Wu, M., Liang, J., Tang, J., Li, G., Shan, S., Guo, Z., and Deng, L. Journal of Hazardous Materials, **337**, 189–197. (2017).
26. Njoku, K., Akinyede, O. and Obidi, O. (2020). Scientific African, **e00545**, 1-18 (2020).
27. Muneer B, Iqbal M. J., Shakoori FR, Shakoori AR . Pak J Zool. **48,** 1495–1501 (2016)
28. Kumar, V., Singh, S., Singh, J., and Upadhyay, N. Bulletin of Environmental Contamination and Toxicology**, 94,** 807–814. (2015).
29. Kumar, V., Singh, S., Kashyap, N., Singla, S., Bhadrecha, P., Kaur, P., Singh, J. Oriental Journal of Chemistry, **31**, 357–361 (2015).
30. Behari, J. R., and Prakash, R. Chemosphere, **63,** 17–21. (2006).
31. Mostafa, M. S., Bakr, A.-S. A., El Naggar, A. M. A., and Sultan, E.-S. A. Journal of Colloid and Interface Science, **461,** 261–272 (2016)
32. Terán,E.J., Montes, M.L., Rodríguez, C., Martino, L., Quiroga. M.,. Landa, R., Pace, S.D.M.D. Microchemical Journal. **144**, 159-165 (2019)
33. Al-Kinani, A., Eftekhari, M., Gheibi, M., and Chamsaz, M. Spectroscopy Letters, **51**, 287-296 (2018).

09 September 2023 16:23:14

34. Karandish, S., Chamsaz, M., ArbabZavar, M. H., and Gheibi, M. International Journal of Environmental Analytical Chemistry, **98,** 1135-1148 (2018).
35. Baharin S. N. A., Istamam H., Suhaimi N. F., Jamion N. A., Raaov M. and SambasevamK. P. Malaysian Journal of Chemistry–Chemistry for Sustainable World **23,** 26-32. (2021)
36. Hung, D. Q., Nekrassova, O., and Compton, R. G. Talanta, **64**, 269–27 (2004).
37. Beauchemin, D. Analytical Chemistry, **80,** 4455–4486 (2008).
38. Kawabata, K., Inoue, Y., Takahashi, H., and Endo, G. Applied Organometallic Chemistry, **8,** 245–248(1994).
39. Larsen E H, Sturup S. Journal of Analytical Atomic Spectrometry **9,** 1099-1105 (1994)
40. Mok, W. M., Shah, N. K., and Wei, C. M. Analytical Chemistry**, 58,** 110–113. (1986).
41. Lagerkvist, B. J. S., and Oskarsson, A. *Handbook on the Toxicology of Metals*, (Academic Press, Amsterdam, 2007) 905–923.
42. Melquiades, F. L., and Appoloni, C. R. Journal of Radioanalytical and Nuclear Chemistry, **262,** 533–541. (2004).
43. Stanković, A., Kajinić, Ž., Turkalj, J. V., Romić, Ž., Sikirić, M. D., Asserghine, A., Nagy, G. and Medvidović-Kosanović, M. Electroanalysis. **32,** 1043-1051 (2020)
44. Ndlovu T., Mamba, B. B., Sampath, S., Krause, R. W., andArotiba, O. A. Electrochimica Acta, **128**, 48–53 (2014).
45. Lan, Y., Luo, H., Ren, X., Wang, Y., and Liu, Y. Microchimica Acta, **178,** 153–161. (2012).
46. Jickells, T. D., and Baker, A. R. *Encyclopedia of Analytical Science*, (Elsevier, Amsterdam, 2005), 283–289.
47. Chang, Y., Wang, B., Luo, H., and Zhi, L. "Synthesis of Polyaniline/Graphene Composites and Its Application in Detecting Heavy Metal Ions" in ICEEE edited by Chang Y. *et al*. (ICEEE 2010) 1-20.
48. Mahadik, M., Patil, H., Bodkhe, G., Ingle, N., Sayyad, P., Al- Gahaouri, T., Shirsat, S.M and Shirsat,. Smart Materials. **7**, 1-10 (2020)
49. Huang, H., Zhu, W., Gao, X., Liu, X., and Ma, H. Analytica Chimica Acta. **947**, 32-41 (2016).
50. Zhao, D., Guo, X., Wang, T., Alvarez, N., Shanov, V. N., and Heineman, W. R. Electroanalysis, **26,** 488–496**.** (2014).
51. Lee, S., Oh, J., Kim, D., and Piao, Y. Talanta, **160,** 528–536 (2016).
52.Simões, F. R., and Xavier, M. G. "Electrochemical Sensors" in *Nanoscience and Its Applications*, edited by Da Róz A. L., Ferreira M., and Oliveira O. N. (Elsevier, Amsterdam, 2017), 155–178.
53. Deshmukh, M. A., Patil, H. K., Bodkhe, G. A., Yasuzawa, M., Koinkar, P., Ramanaviciene, A., Ramanavicius, A. Sensors and Actuators B: Chemical, **260,** 331–338. (2018)
54.Altundal, M., Üğe, A., Gök, Ö., and Zeybek, B. Analytical Letters, **54,** 2431–2451 (2021)
55.Huitle, C.A.M., Feranandes, N. S, Lopez, C and Quiroz, M.A. Portugaliae Electrochimica Acta. **28**, 39-49 (2010).
56. Sun, M., Li, Z., Wu, S., Gu, Y., and Li, Y. Electrochimica Acta, **283,** 1223–1230. (2018)
57. Bueno, C. C., Garcia, P. S., Steffens C., Deda D. K., Leite F.de Lima, Electrochemical Sensors" in *Nanoscience and Its Applications*, edited by Da Róz A. L., Ferreira M., and Oliveira O. N. (Elsevier, Amsterdam, 2017), 121–153**.** (2017).
58. Westbroek, P. Analytical Electrochemistry in Textiles, (Elsevier, Amsterdam, 2005) 37–69.
59. Kim, J., Han, S., and Kim, Y. Korean Journal of Chemical Engineering, **34,** 2096–2098. (2017).
60. Xiao, L., Wildgoose, G. G., and Compton, R. G. Analytica Chimica Acta**, 620,** 44–49 (2008)
61. Promphet, N., Rattanarat, P., Rangkupan, R., Chailapakul, O., andRodthongkum, NSensors and Actuators B: Chemical, **207,** 526–534 (2015)
62. Guo, Z., Hui, W., Yuan, Y and Gang, L. International Journal of Agricultural and Biological Engineering. **10**, 251-261 (2017).
63. Zhao, G., Wang, H., Liu, G., Wang, Z., and Cheng, J. Ionics, **23,** 767–777 (2016).
64. Suherman, A. L., Kuss, S., Tanner, E. E. L., Young, N. P., and Compton, R. G. The Analyst, **143**, 2035–2041 (2018).
65. Deshmukh, S., Kandasamy, G., Upadhyay, R.K., Bhattacharya, G., Banerjee, D., Maity, D., Deshusses, M.A and Roy, S.S. Journal of Electroanalytical Chemistry. **788**, 91-98 (2017)
66. Zhou, S.-F., Wang, J.-J., Gan, L., Han, X.-J., Fan, H.-L., Mei, L.-Y., Liu, Y.-Q. Journal of Alloys and Compounds, **721,** 492–500**.** (2017)
67. Zhang, J., Zhang, H., Wu, J., and Zhang, J. Techniques for PEM Fuel Cell Testing and Diagnosis in *PEM Fuel Cell Testing and Diagnosis*, edited by Zhang, J., Zhang, H., Wu, J., and Zhang, J. (Elsevier, Amsterdam, 2013) 81–119.

09 September 2023 16:23:14

68. Altundal, M., Üğe, A., Gök, Ö., andZeybek, B. (2021. Analytical Letters, **54,** 2431–2451 (2021).
69. Nguyen, P. K. Q., and Lunsford, S. K. Talanta, **101,** 110–121(2012).
70. Surucu, O. (2021). Chemical Papers, **75,** 4227–4238(2021)
71. Avuthu, S. G. R., Wabeke, J. T., Narakathu, B. B., Maddipatla, D., Arachchilage, J. S., Obare, S. O., andAtashbar, M. Z.. IEEE Sensors Journal, **16,** 8678–8684(2016).
72. Cheng, Y., Li, H., Fang, C., Ai, L., Chen, J., Su, J., Fu, Q. Journal of Alloys and Compounds, **787,** 683–693(2019).
73. Albratty, M.; Arbab, I.; Alhazmi, H.; Attafi, I.; Al-Rajab, A. World Environ.**, 12,** 06–17(2017)
74. Kausar, R.; Ahmad, Z. Environ. Monit. Assess.**, 157,** 347–354 (2009)
75. Zhao, W. "Determination of Six Heavy Metal Elements Such as Co in Solid Waste by ICP-MS". In *Earth and Environmental Science, Conference Series: Earth and Environmental Science*, (IOP Conference Series, 2019): **300,** 1-6
76. Hutton, L. A., O'Neil, G. D., Read, T. L., Ayres, Z. J., Newton, M. E., and Macpherson, J. V. Analytical Chemistry, **86,** 4566–4572 (2014).
77. Pellegatti, F., Figueiredo, A. M. G., and Wasserman, J. C. Geostandards and Geoanalytical Research, **25,** 307–315(2001).
78. Chowdhury, M.A.H., Hoque, M.M., Hossain, S.M., Naher, K., Islam, M.A., Tamim, U., Alam, K.M.S, and Khan, R. Journal of Environmental Science, Toxicology and Food Technology **11,** 14-23 (2017)..
79. Gouden, D., Khene,SandNombona., N .Chemical Papers. **1**, 1-36 (2018)
80. Rasool, K., Pandey, R.P., Rasheed, P.A., Buczek, S., Gogotsi, Y and Mahmoud. Materials Today **30**, 80-102 (2019)
81. Rahman, M.D., Kumar, R., Kumar., M., Qiao, Q. Sensors and Actuators **318**, 1-15 (2020)
82.Czikkely M., Neubauer E., Fekete I., Ymeri P. and Fogarassy C . Water**, 10,** 1377-1382 (2018)
83.Jiang, S., Cheng, R., Ng, R., Huang, Y., and Duan, X. Nano Research, **8,** 257–262 (2015)
84. Aghagoli, M. J., andShemirani, F. (2016). . Microchimica Acta, **184,** 237–244 (2016)
85. Sun, Y.-F., Sun, J.-H., Wang, J., Pi, Z.-X., Wang, L.-C., Yang, M., and Huang, X.-J. Analytica Chimica Acta. **1063,** 64-74 (2019)
86. Yamuna, A., Hong, C.-Y., Chen, S.-M., Chen, T.-W., Alabdullkarem, E. A., Soylak, M., Liu, X. Journal of Electroanalytical Chemistry**, 887,** 1-10 (2021)
87. Li, J.-R., Wang, X., Yuan, B., Fu, M.-L., and Cui, H..Applied Surface Science, **320,** 112–119 (2014).
88. Pirarath, R., Shivashanmugam, P., Syed, A., Elgorban, A. M., Anandan, S., and Ashok kumar, M. Frontiers of Environmental Science and Engineering, **15,** 1-10 (2020)
89. Oh, Y., Bag, S., Malliakas, C. D., and Kanatzidis, M. G. Selective Surfaces: High-Surface-Area Zinc Tin Sulfide Chalcogels. Chemistry of Materials, **23,** 2447–2456. (2011).
90. Wang, C., Yin, H., Bi, L., Su, J., Zhang, M., Lyu, T., Pan, G. Journal of Hazardous Materials, **384,** 1-9 (2019).
91. Ibrahim Y., Kassab A., Eid K., Abdullah A. M., Ozoemena K. I. and Elzatahry A. Nanomaterials **10,** 885(2020)
92. Shahzad, F., Zaidi, S.A and Naqvi, R.A. Critical reviews in analytical chemistry, **1**, 1-18 (2020).
93. He, Y., Ma, L., Zhou, L., Liu, G., Jiang, Y., and Gao, J. Nanomaterials, **10,** 866-877 (2020).
94. Yang, X., Liu, Y., Hu, S., Yu, F., He, Z., Zeng, G., Sengupta, A. Polymers for Advanced Technologies. **32,** 1000-1010 (2020).
95. Baby, R., Saifullah, B. and Hussein, M.Z Nanoscale Res Lett **14,** 341-358 (2019).
96. Silva, M. K. L., and Cesarino, I. International Journal of Environmental Analytical Chemistry**,** 7**,** 1–15(2020).
97. Cui, L., Wu, J., Ju,h. Biosensors and Bioelectronics **63,** 276-286 (2014).
98. Liu, X., Ma, R., Wang, X., Ma, Y., Yang, Y., Zhuang, L., Zhang S., Jehan R., Chen J. and Wang, X. Environmental Pollution. **252,** 62-73(2019)
99. Manna, B., Raj, C.R. ACS Sustainable Chemistry and Engineering. (2018)
100. Vilela, D., Parmar, J., Zeng, Y., Zhao, Y., and Sánchez, S. Nano Letters, **16**, 2860–2866, (2016).
101. Zhou, S. F., Han, X. J., Fan, H. L., Huang, J., and Liu, Y.Q. Journal of Alloys and Compounds, **747,** 447–454, (2018).
102. Zhang, Y., Zhang, S., Gao, J., and Chung, T. S. Journal of Membrane Science, **515,** 230–237 (2016).
103. Li, L., Zhao, L., Ma, J., and Tian, Y. Green Processing and Synthesis, **9 (1),** 294–303 (2020).
104. Yi, W., He, Z., Fei, J., and He, X. RSC Advances**, 9,** 17325–17334 (2019).
105. Liu, X., Ma, R., Wang, X., Ma, Y., Yang, Y., Zhuang, L., Zhang S., Jehan R., Chen J. and Wang, X. Environmental Pollution. **252,** 62-73 (2019).
106.Musameh, M.M., Hickey, M and Kyratzis, I.L. Res chem. Intermed. **37**, 675–689 (2011)

09 September 2023 16:23:14

107. Pitroda J. K., Jethwa B. and Dave S.K. International Journal of Constructive Research in Civil Engineering. **2,** 36-42 **(**2016).
108. Oliveira Silva, A. C., de Oliveira, L. C. F., Vieira Delfino, A., Meneghetti, M. R., and Caxico de Abreu, F. Journal of Analytical Methods in Chemistry, **2016,** 1–12 (2016).
109. Wu, W., Jia, M., Zhang, Z., Chen, X., Zhang, Q., Zhang, W., Li, Peiwu and Chen, L. Ecotoxicology and Environmental Safety, **175,** 243–250 (2019).
110. Zhao, X., Song, N., Jia, Q., and Zhou, W. Microchimica Acta, **166,** 329–335 (2009).
111. Duran, A., Tuzen, M., andSoylak, M. Journal of Hazardous Materials, **169,** 466–471 (2009).
112. Hayati, B., Maleki, A., Najafi, F., Daraei, H., Gharibi, F., and McKay, G. Journal of Hazardous Materials, **336,** 146–157 (2017).
113. Bankole, M. T., Abdulkareem, A. S., Mohammed, I. A., Ochigbo, S. S., Tijani, J. O., Abubakre, O. K., and Roos, W. D. Scientific Reports, **9,** 1-19 (2019).
114. Bezzon V. D. N., Montanheiro T. L. A., de Menezes B. R. C., Ribas R. G., Righetti V. A. N., Rodrigues K. F., and Thim G. P. Advances in Materials Science and Engineering. **293073** (2019).
115. Travlou, N. A., Seredych, M., Rodríguez-Castellón, E., and Bandosz, T. J. Journal of Materials Chemistry A, 3, 3821–3831 (2015).
116. Abdulrazak, S., Hussaini, K., and Sani, H. M. Evaluation of removal efficiency of heavy metals by low-cost activated carbon prepared from African palm fruit. Applied Water Science, **7,** 3151–3155 (2016).
117. Yue, Z., and Economy, J. "Carbonization and activation for production of activated carbon fibers" in *Activated Carbon Fiber and Textiles*, edited by Chen J. Y. (Elsevier, Amsterdam, 2017) **61–139.**
118. Chen, J., Wang, N., Liu, Y., Zhu, J., Feng, J., and Yan, W. Synthetic Metals, **245,** 32–41 (2018).
119. Madhu, R., Sankar, K. V., Chen, S.-M., and Selvan, R. K. RSC Adv., **4,** 1225–1233 (2014).
120. Zhang, T., Jin, H., Fang, Y., Guan, J.B., Ma, S., Pan, Y., Zhang, M., Zhu, H., Liu, X. D., and Du M. L. Material Chemistry and Physics. **225**, 433–442 (2019).
121. Wang, W.-J., Cai, Y.-L., Li, B.-C., Zeng, J., Huang, Z.-Y., and Chen, X.-M. Chinese Chemical Letters, **29,** 111–114 (2018).
122. Le, T.-H., Kim, Y., and Yoon, H. Polymers, **9,** 1-32 (2017).
123. Bai, H., and Shi, G. Sensors, **7,** 267–307 (2007).
124. Quintana, H., Ramirez, J. L., Rubio, E. F., Marquez, E., Gonzalez, G., Gonzalez, G., and Uruchurtu, J. ECS Transactions, **47,** 265–273. (2013).
125. Xu, T., Dai, H. and Jin, Y. MicrochimActa **187,** 23 (2020).
126. Velempini, T., Pillay, K., Mbianda, X. Y., and Arotiba, O. A. Electroanalysis. **30,** 2612-2619 (2018).
127. Abou-Elenien, G. M., El-Maghraby, A. A., and El-Abdallah, G. M. Synthetic Metals, **146,** 109–119 (2004).
128. Zanganeh, A. R., and Amini, M. K. Electrochimica Acta, **52,** 3822–3830 (2007).
129. Zejli, H., Cisneros, J. L. H.-H. de, Naranjo-Rodriguez, I., andTemsamani, K. R. Stripping voltammetry of silver ions at polythiophene-modified platinum electrodes. Talanta, **71,** 1594–1598 (2007).
130. Manisankar, P., Vedhi, C., Selvanathan, G., and Arumugam, P. Microchimica Acta, **163,** 289–295 (2008).
131.Yu, Z., Jamal, R., Zhang, R., Zhang, W., Yan, Y., Liu, Y., Ge, Y and Abdiryim, T. Journal of Electrochemical Society. **167**, 1-11, (2020)
132.Yakuphanoglu, F and Senkal, B. F. The Journal of Physical Chemistry. **111**, 1840–1846 (2007)
133. Abdulla, H.S and Abbo, A. I. (2012). International Journal of Chemical Science, **7,** 10666 - 10678 (2012)
134. Lu, Z., Dai ,W., Liu , B., Mo , G ., Zhang , J., Ye, J., and Ye, J. Journal of Colloid and Interface Science. **525**, 86-96 (2018).
135. Wang, Z., Liu, E., and Zhao, X. Thin Solid Films, **519,** 5285–5289 (2011).
136. Zhu, G., Ge, Y., Dai, Y., Shang, X., Yang, J., and Liu, J. Electrochimica Acta, **268,** 202–210 (2018).
137. Somerset, V., Silwana, B., Horst, C., and Iwuoha, E. Sensing in Electroanalysis**, 8,** 143–154 (2014).
138. Huang, H.; Zhu, W.; Gao, X.; Liu, X.; Ma, H. Anal. Chim. Acta**, 947,** 32–41 (2016).
139. Khan, A., Khan, A.A.P., Rahman, M.M and Asiri, A.M. European Polymer journal. **75,** 388-398 (2016).
140. Patil, H. K., Deshmukh, M. A., Bodkhe, G. A., andShirsat, M. D. International Journal of Modern Physics B, **32,** 1840042 (2018).
141. Muralikrishna, S., Nagaraju, D. H., Balakrishna, R. G., Surareungchai, W., Ramakrishnappa, T., and Shivanandareddy, A. B. Analytica Chimica Acta**, 990,** 67-77 (2017).
142. Natarajan, S., Ulaganathan, M., and Aravindan, V. Journal of Materials Chemistry A, **9,** 15542–15585 (2021)
143. Ruecha, N., Rodthongkum, N., Cate, D. M., Volckens, J., Chailapakul, O., and Henry, C. S. Analytica Chimica Acta, **874,** 40–48 (2015).

09 September 2023 16:23:14

144. Karthik, R., and Thambidurai, S. Journal of Alloys and Compounds, **715,** 254–265 (2017).
145. Akhtar, M., Tahir, A., Zulfiqar, S., Hanif, F., Warsi, M. F., Agboola, P. O., and Shakir, I. Synthetic Metals, **265,** 1-10 (2020).
146. Mahadik, M., Patil, H., Bodkhe, G., Ingle, N., Sayyad, P., Al-Gahaouri, T., Shirsat, M. Frontiers in Materials**,** **7**, 1-14 (2020).
147. Promphet, N., Rattanarat, P., Rangkupan, R., Chailapakul, O., and Rodthongkum, N. Sensors and Actuators B: Chemical, **207,** 526–534 (2015).
148. Taleb. M.A., Kumar, R., Al-Rashdi, A.A., Seliem, M.K and Barakat, M. A. Arabian Journal of Chemistry. **13**, 7533-7543 (2020)

09 September 2023 16:23:14

Ionics
https://doi.org/10.1007/s11581-025-06067-w

RESEARCH

Systematic development of PPY/GO/ZnO hybrid composite for electrochemical detection of Pb^{2+} in aqueous solution

Goverdhan Singh[1] · Nisha Gupta[1] · Anil Kumar[1] · Parteek Prasher[2] · Harish Mudila[1]

Received: 26 October 2024 / Revised: 9 December 2024 / Accepted: 5 January 2025
© The Author(s), under exclusive licence to Springer-Verlag GmbH Germany, part of Springer Nature 2025

Abstract

The accumulation of heavy metals in water sources at levels exceeding acceptable limits poses a serious risk to human health and the environment. Various electrochemical methods and electroactive materials have been employed to identify and measure these metal ions. However, effective, low-cost, sensitive, and stability, with low detection limit and high reproducibility, are the major requirements of such sensing materials. In this regard, an enhanced hybrid ternary composite PGT based on polypyrrole, GO, and ZnO (PPY/GO/ZnO) has been fabricated and is reportedly being used for the first time to identify lead (Pb^{2+}) ions at the trace level in aqueous solutions. The ternary composite was characterized using Fourier transform-infrared spectroscopy (FTIR), X-ray diffraction (XRD), X-ray photoelectron spectroscopy (XPS), scanning electron microscopy (SEM), and thermogravimetric analysis (TGA) to study its structural, morphological, and thermal properties. The electrochemical response of the composite material was analyzed using cyclic voltammetry (CV) and electron impedance spectroscopy (EIS) in potassium ferricyanide as a redox probe. The sensitivity, selectivity, and reproducibility of the PGT were studied via the differential pulse anodic stripping voltammetry (DPASV) technique. The electrode material shows a good linear response (R^2 = ~0.98) with a limit of detection of 0.05 µM for Pb^{2+} ions within the concentration range of 0.3 to 3 µM. The reproducibility RSD (relative standard deviation, 1.089%), stability RSD (3.67%), and interference of the working electrode in the presence of other metal ions (Cd^{2+} and Cu^{2+}) show a good response. These results represent the possibilities of employing the PGT electrode to effectively detect other heavy metal ions from aqueous sources.

Keywords Polypyrrole · Graphene oxide · Heavy metal ion · DPASV · Zinc oxide · Pollution

Introduction

Numerous anthropogenic and natural sources discharge heavy metals (HMs) into the different strata (air, soil, and water) of the environment. Through their excess concentration in the environment, these HMs lead to retard the environment's ability to promote life. This directs toward threatening the health of plants, animals, and humans [1, 2]. HM toxicity to organisms is influenced by various factors such as the nature of HMs, the organism exposed to HMs, and the duration of exposure [3]. HMs like Pb, Cu, As, Zn, Hg, and Cr are reported as the most prevailing environmental pollutants by the United States Environmental Protection Agency (USEPA) report [4]. Among the variety of HMs, lead (Pb) is considered a hazardous environmental pollutant, affecting both human and animal neurological, immunological, reproductive, and digestive systems. Furthermore, Pb^{2+} ion buildup in the body has a serious negative impact on children's neurobehavioral development, raises blood pressure, damages the kidneys, and results in anemia [5]. Various organizations viz. environmental protection agency (EPA, 0.015 mg/L), World Health Organization (WHO, 0.01 mg/L), and Central Pollution Control Board (CPCB, 0.01 mg/L) have set certain permissible limits of concentrations of Pb^{2+} ion to be present in various potable waters [6]. Therefore, the detection and determination of Pb^{2+} ions present in the various samples is of supreme importance in monitoring the environmental quality.

A variety of techniques ranging from analytical to electrochemical are employed for the detection of these HM (including Pb^{2+}) contaminants from various sources.

✉ Harish Mudila
harismudila@gmail.com

[1] Department of Chemistry, Lovely Professional University, Punjab 144411, India

[2] Department of Chemistry, UPES, Dehradun 248007, India

Published online: 11 January 2025

Electrochemical techniques as compared to other techniques employed for HM detection are simple, reliable, low-cost suitable for short analytical time for in situ and on-time measurements and hence are employed chiefly [7, 8]. Out of the various electrochemical techniques, the differential pulse anodic stripping voltammetry (DPASV) is regarded as the effective electrochemical technique for determining HMs (here Pb^{2+}) because of its efficient preconcentration step followed by electrochemical dissolution. The sensor's electrochemical determination ability can be enhanced by utilizing various electrode materials. Therefore, research is in demand to improve the electrochemical behavior of electrode materials used as HM sensors. Various types of electroactive materials have been identified to enhance the sensitivity and selectivity of the bare electrodes for Pb^{2+} detection. Carbonaceous materials, non-carbonaceous transition metals, and organic materials like conducting polymers are the main categories of materials used in the purpose [9, 10].

A variety of organic and inorganic hybrid materials are fabricated and used to enhance the electrochemical response of these electrodes. PPY-based electroactive materials have emerged as the potential class for electrochemical sensing of Pb^{2+} ions, which includes PPY-based binary and ternary composite. These composites have shown significant promise in detecting Pb^{2+} in aqueous sources (Table 1). However, many of these materials are associated with certain limitations such as high cost and low detection limits.

In this direction, we have systematically developed the PPY/GO binary and PPY/GO/ZnO ternary composite for the determination of Pb^{2+} ions from water sources. The reported material involves the properties of PPY (biocompatibility, high conductivity, low cost, and ease of preparation) [17], GO (mechanical stiffness, appreciable dispersibility, and large surface) [16], and ZnO (appreciable band gap, electron transport ability, stability towards chemicals, large surface area, etc.) [18] that improves its electrochemical properties. The encapsulation of PPY over GO sheets overcomes the probability of aggregation of GO sheets in the PPY/GO binary composite. The synergetic effect between PPY and GO results in the stabilization of the structure and improves the conductivity of the surface lowering the paths for the ion diffusion and π-πinteractions resulting in the fast electron transfer kinetics [19]. ZnO has pseudo-capacitive behavior and acts as a filler between the PPY and GO, which may improve the electrolyte-electrode interaction resulting in the fast diffusion of ions and hence improving the electrochemical behavior of the ternary electrode material (PPY/GO/ZnO). Earlier reports had shown PPY/GO/ZnO as an efficient material for supercapacitor applications [22, 23] and drug sensing [22, 24]. The results show the ternary composite has high electrochemical performances, fast electron transfer, quick response, sensitivity, and selectivity. These results motivate the authors to employ the PPY/GO/ZnO ternary composite for the detection of HMs (Pb^{2+}). To the best of the authors' knowledge, there has not been any report of using the PPY/GO/ZnO ternary composite for HM detection. The optimized PPY/GO/ZnO ternary composite is reported for the first time for low-level detection of Pb^{2+} in the aqueous solution, marking a significant advancement in HM detection. The ternary composite material shows enhanced sensitivity with LOD of 0.05 µM, selectivity (Cu^{2+} and Cd^{2+} as interfering agents), stability, reproducibility, and current response for Pb^{2+} sensing as compared to the individual and binary composite material. The unique and advantageous physical, chemical, and electronic properties of PPY and its composites with GO and ZnO allow it to be a potent material to be used in electrochemical sensing of heavy metals present in various samples.

Materials and methods

Materials

Monomer pyrrole (PY, >99%) was procured from Spectrochem (Mumbai, Maharashtra); graphite powder, potassium permanganate ($KMnO_4$), sulfuric acid (H_2SO_4), hydrogen peroxide (H_2O_2), hydrochloric acid (HCl), formamide (DMF), cupric chloride ($CuCl_2$), and cadmium nitrate ($Cd(NO_3)_2$ were acquired from Loba Chemie (Mumbai, Maharashtra). Ferric chloride ($FeCl_3$), lead nitrate ($PbNO_3)_2$ from Alpha Chemika (Mumbai, Maharashtra), potassium ferricyanide $K_3[Fe(CN)_6]$ from CDH Fine Chem (Daryaganj, New Delhi), potassium chloride (KCl) from Rankem (Gurugram, Haryana), sodium acetate, and ascorbic acid from SD Fine Chem. Ltd (Mumbai, Maharashtra) were obtained. All the chemicals used were of analytical quality and therefore were not purified further.

Preparation of polypyrrole (PPY)

The chemical oxidative polymerization method was employed for the preparation of PPY, where 0.072 M pyrrole monomer was added dropwise into the surfactant solution of N-cetyl-N, *N*,*N*-trimethyl ammonium bromide (CTAB, 4.6 g) in 100-mL distilled water with continuous stirring at room temperature. The process of polymerization starts with the addition of a freshly prepared oxidant solution of $FeCl_3$ (50 ml, 0.074 mol/dL) at the rate of ~1 ml/min to the above solution content. Polymerization was then allowed to be carried out for 6 h with continuous mechanical stirring at 500 rpm and room temperature. The resultant product was then filtered, further washed with distilled water, and then dried at ~ 80 °C in an oven [23].

Table 1 Comparative analysis of PPY-based binary and ternary electrodes for Pb^{2+} ion detection in aqueous environment

Composite material	Electrochemical technique	Detection range	LoD	Stability (RSD %)	Repeatability (RSD %)	Recovery rate (%)	Interfering ions	Advantages	Disadvantages	Reference
PPY/PA	DPASV	10–600 Nm	0.43 nM	3.1	< 2	93	Zn^{2+}, Ni^{2+}, Cr^{6+}, Na^{+}, K^{+}, Hg^{2+}, Cu^{2+}, $SO_4{}^{2-}$, $NO_3{}^{-}$, $NH_4{}^{+}$ and Cl^{-}	Low detection range and low LOD	High cost of phytic acid	[11]
PPY/rGO	SWASV	5–2000 nM	0.047 nM	1.7	-	94.8–103.5	Cu^{2+}, Hg^{2+}, Zn^{2+} and Cd^{2+}	Low detection range and low LOD	Hazardous process of preparing rGO	[12]
PPY/CNFs	SWASV	0.2–130 µM	0.05 µM	3.1	2.3	97.6–102	Cu^{2+}, Hg^{2+}, and Cd^{2+}	Appreciable recovery rate	High cost of CNFs	[13]
Bi/PPy/MES	SWASV	0.05 to 35 µM	0.03 µM	-	2.5	-	K^{+} , Na^{+} , Ca^{2+}, Mg^{2+}, Cl^{-} , Br^{-} , $SO_4{}^{2-}$, $PO_4{}^{3-}$	Appreciable detection range and low LOD	High cost of MES	[14]
PPY/MOFs/BF	DPASV	0.5–10 µM	0.05 µM	-	-	95.4–102.8	-	Satisfactory range of detection and LOD	No studies on stability, reproducibility, and interfering ions	[15]
PA/PPY/GO	DPV	5–150 µM	0.41 µM	8.4	4.8	101	Na^{+}, K^{+}, Ca^{2+}, Mg^{2+}, Zn^{2+} and Fe^{3+}	Good recovery rate	High cost of phytic acid	[16]
PPY/GO/ZnO	DPASV	0.3–3.0 µM	0.05 µM	1.089	3.67	-	Cu^{2+}, and Cd^{2+}	Satisfactory range of detection and LOD	Low-cost material	Present work

(PPY/PA) phytic acid functionalized polypyrrole, *(PPY/rGO)* polypyrrole graphene, *(PPY/CNFs)* polypyrrole- carbon nanofiber, *(Bi/PPy/MES)* 2-mercaptoethanesulfonate (MES)-tethered polypyrrole, *Bi(PPY/MOFs/BF)* polypyrrole metal-organic framed bismuth film, *(PA/PPY/GO)* phytic acid functionalized polypyrrole/graphene oxide, *DPASV* differential pulse anodic stripping voltammetry, *DPV* differential pulse voltammetry, *SWASV* square wave anodic stripping voltammetry

Preparation of GO

The preparation of graphene oxide (GO) from pure graphite powder was carried out using the modified Hummers method. Graphite powder (2 g) was added to the conc. H_2SO_4 (46 ml) was taken in a beaker, and kept in an ice bath at 5 ± 1 °C with constant stirring for 30 min. $KMnO_4$ (46 g) was added slowly to the above graphite solution at 5 ± 1 °C with continuous stirring for the next 4 h. The solution was then allowed to stir for 1 h in the temperature range of 30–35 °C followed by the addition of deionized water (100 ml) to the solution mixture to obtain the homogeneous suspension within the temperature of 95–98 °C. The excess $KMnO_4$ left in the solution was removed by adding 20 ml H_2O_2 and 100 ml deionized water with stirring for 2 h. The resultant product was centrifuged and repeatedly washed with 5% HCl solution and deionized water until clear filtrate was obtained. The brownish-black solid residue was then dried in an oven at 60 °C [25].

Preparation of PPY/GO binary composites (PGs)

The preparation of PPY/GO composite (PG) in different ratios was carried out by the ex situ method. A requisite amount of PPY and GO as represented in Table 2 was taken in ethanol (as a medium) followed by mechanical mixing through sonication for 30 min to acquire homogeneity. The resultant mixture was then dried in an oven at 60 °C to remove the ethanol followed by grinding. PG composites prepared in different wt. % ratios (mg) as 100:25, 100:50, 100:100, and 100:200 are named PG 1, PG 2, PG 3, and PG 4. The best ratio of PPY/GO was optimized by cyclic voltammetry (CV).

Preparation of PPY/GO/ZnO ternary composites (PGTs)

The preparation of the PGT composite in different ratios of PG 1 and ZnO was carried out by the ex situ method. Binary composite PG 1 (due to excellent electrochemical response as mentioned later) and ZnO were taken in ethanol (as a medium) followed by mechanical mixing through sonication for 30 min to acquire homogeneity. The resultant mixture was then dried in an oven at 60 °C to remove the ethanol followed by grinding. PGT composites prepared in different wt. % ratios (mg) as 100:50, 100:100, and 100:200 are named PGT 1, PGT 2, and PGT 3 as mentioned in Table 3. Likewise, the optimized PGT was determined via the CV technique.

Preparation of working electrodes

The preparation of carbon paste electrodes (CPEs, as a substrate) was carried out by mixing the graphite powder (1 g) in 1.8 mL of paraffin oil in mortar to obtain the homogeneous paste. This paste was then filled into the electrode cavity, and its surface was smoothened by polishing it on a clean paper. The electrical contact was made using copper wire. The suspension of the electroactive material was prepared by dissolving 2 mg of the material in 1-mL DMF followed by its ultrasonication for 30 min. The suspension of the electroactive material was then dropped cast (10 µL) on the surface of CPE and then dried. The obtained modified electrode then functions as our working electrode as shown in Fig. 1 [13].

Results and discussions

FT-IR spectra

FT-IR studies were carried out to confirm the presence of different functionalities and the types of bonds present in the material under investigation. Figure 2 shows the FT-IR spectra of the synthesized PPY, GO, ZnO, PG 1, and PGT 2 recorded in the 500–4000 cm^{-1} range. FT-IR spectra of ZnO show the vibrational mode of ZnO at 876 cm^{-1} [26]. For PPY, the absorption bands at 1631, 1543, and 1415 cm^{-1} are associated with the symmetric stretching vibrations of the ring's C=N, C=C, and C–N bonds respectively. A broad band in the range 3300–3500 cm^{-1} is attributed to the presence of the N–H bond. The wave number associated at 1039 cm^{-1} and 1300 cm^{-1} is due to the in-plane deformations of the C–H and C–N bond, while C–H out-of-plane deformation is centered at 884 cm^{-1}. The band at 1140 and 910 cm^{-1} corresponds to the doping state of PPY with Fe^{3+} [27, 28]. In the case of GO, a broad absorption band at 3272 cm^{-1} corresponds to the OH stretching vibrations. The bands at 1714 and 1585 cm^{-1} are due to the vibrations of carbonyl (C=O) and aromatic C=C bonds. The absorption bands arising

Table 2 Amount of PPY and GO, corresponding to the ratio

Material	Ratio			
	4: 1 (PG 1)	2: 1 (PG 2)	1: 1 (PG 3)	1: 2 (PG 4)
PPY (mg)	100	100	100	100
GO (mg)	25	50	100	200

Table 3 Amount of PG 1 and ZnO, corresponding to the ratio

Material	Ratio		
	2: 1 (PGT 1)	1: 1 (PGT 2)	1: 2 (PGT 3)
PG 1 (mg)	100	100	100
ZnO (mg)	50	100	200

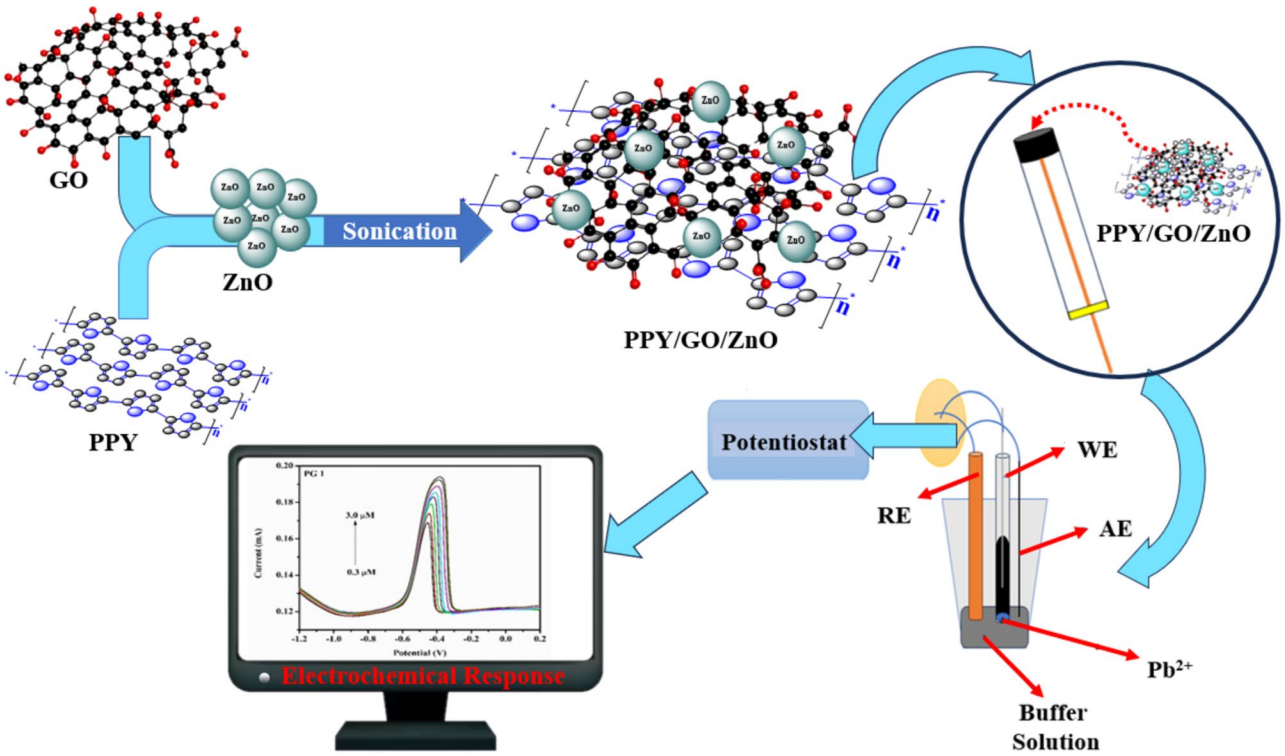

Fig. 1 Representation of ternary composite preparation and electrochemical sensing of Pb^{2+} ions in acetate buffer. Here, WE, AE, and RE are working electrode, auxiliary electrode (Pt wire), and reference electrode (Ag/AgCl, in KCl), respectively

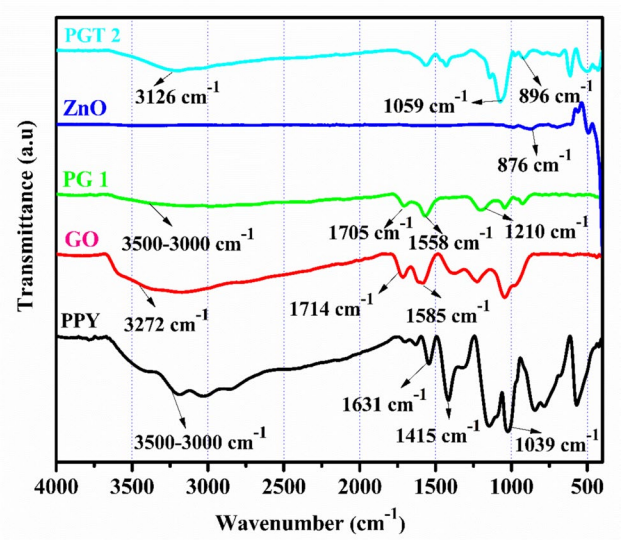

Fig. 2 FTIR spectra of PPY, GO, PG 1, ZnO, and PGT 2

due to epoxy (C–O–C) and alkoxy (C–O) stretching take place at 1225 and 1045 cm^{-1}, respectively. The presence of oxygen functionalities (C=O, C–O, etc.) confirms the oxidation of graphite to GO [2]. In the FT-IR spectrum of PG 1, the characteristic peak due to C=O stretching appears at 1705 cm^{-1} which has been shifted towards the lower wavenumber in comparison to the same peak that appeared in FT-IR of GO. This fluctuation of the C=O peak towards the lower wavenumber may be due to the interaction between the carbonyl (C=O) group of GO and the N-H group of PPY. These interactions among PPY and GO in the composite materials affect the electron densities and bond strengths and result in the shifting of their wavenumbers. The bands at 2979 and 1038 cm^{-1} are due to stretching vibrations of O–H and epoxy (C–O–C) bonds of GO. The absorption bands at 1558 and 1210 cm^{-1} are ascribed to the C=C and C–N stretching of the PPY ring which further confirms the presence of PPY in binary composites [3, 4]. The FT-IR spectra of the PGT 2 composite reflect the characteristic peaks of its components with some shifting in peak positions and peak intensities. The characteristic peak due to C=O stretching at 1714 cm^{-1} in the case of GO is shifted towards the lower wavenumber and appears at 1708 cm^{-1} in the FT-IR spectrum of ternary composite. This shifting of the C=O peak in the case of ternary composites towards lower wavenumber may be due to interaction between the carbonyl (C=O) group of GO and the N–H group of PPY. The bands at 3126 and 1059 cm^{-1} are due to stretching vibrations of O–H and epoxy (C–O–C) bonds of GO. The absorption bands at 1562 and 1130 cm^{-1} are ascribed to the C=C and C–N stretching of the PPY ring which further confirms the presence of PPY

in ternary composites. The absorption band at 896 cm^{-1} due to the metal oxide bond in spectra of PGT 2 suggests the presence of ZnO in composite material [3, 4, 26, 28].

XRD spectra

The XRD spectra of PPY, GO, ZnO, PG 1, and PGT 2 are shown in Fig. 3. The XRD spectra of PPY show an abroad peak at $2\theta = 27.52°$ with interplanar spacing (d spacing) of 0.33 nm suggesting its amorphous nature arises due to the random arrangements of pyrrole in the polymer [27]. The oxidation of graphite to GO results in the appearance of a sharp and intense diffraction peak at $2\theta = 10.91°$ with an increase in d spacing of 0.85 nm compared to that of graphite. This increase in the gallery spacing in the case of GO is ascribed to the encapsulation of oxygen moieties between the carbon layers of GO suggesting that the regular and periodic structure of graphite is oxidized [23]. PG 1 prepared by varying the amount of GO shows two peaks $2\theta = 11.89°$ due to GO and $2\theta = 23.53°$ due to PPY. The interaction between PPY and GO sheets resulting in the formation of binary composites was further confirmed by their XRD spectrum. The occurrence of the peak at $2\theta = 11.89°$ signifies the integration of GO layers over PPY, and the broadening of the peak at $2\theta = 23.53°$ suggests the amorphous nature of composites [3, 7, 24]. The XRD spectra of ZnO show diffraction peaks at 2θ values of 31°, 34°,36°, 47°, 56°, 63°, and 72° signifying its crystal behavior with hexagonal wurtzite mode [29]. In the XRD spectra of PGT 2, the peaks of PPY and GO are suppressed and slightly shifted towards higher 2θ values whereas other characteristic peaks are due to the presence of ZnO in the composite. The weakening of the diffraction peaks of PPY and GO in ternary composite could be due to the presence of ZnO on their surfaces which do not allow them to aggregate during the preparation of ternary composite by ex situ method [19, 20].

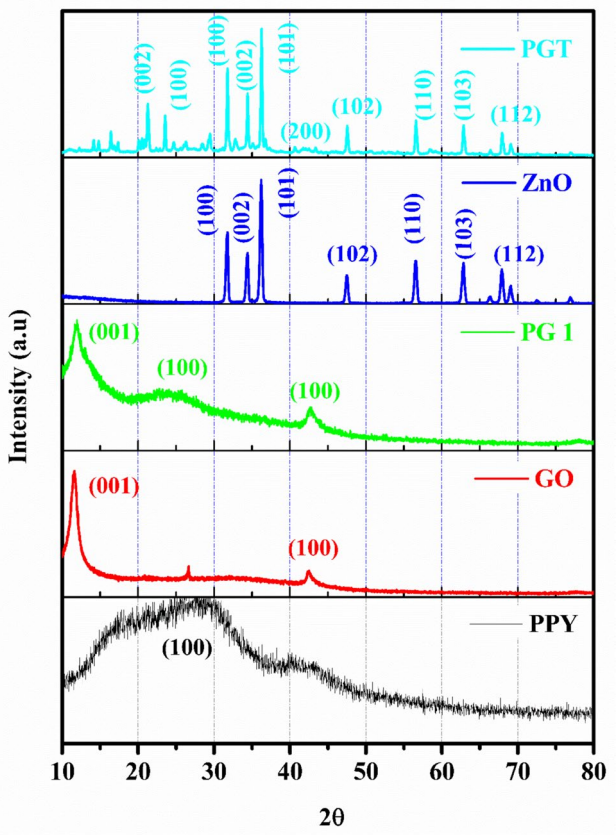

Fig. 3 XRD of PPY, GO, PG 1, ZnO, and PGT 2

The presence of all the electroactive components in the ternary component was also analyzed by SEM (Fig. S1) and XPS which represents the formation of PGT composites

XPS studies

XPS is a powerful technique employed for detecting the elemental state of components in bulk material. Fig. 4A–E shows the XPS spectra of PGT 2 along with the deconvolution curves of the C 1S, N 1S, and O 1S. All the characteristic peaks in the XPS spectrum of PGT 2 (Fig. 4A) are due to the presence of C, N, O, and Zn which further confirms the presence of these elements in the ternary composite material. This also suggests that the PGT 2 ternary composite was successfully synthesized without impurities. As shown in Fig. 4B, the deconvolved C 1S spectrum of PGT 2 gives rise to the three peaks corresponding to C–C (282.58 eV), C–O (283.64), and C=O (286.02). The N 1S spectrum shows the two characteristic peaks Fig. 4C at 398.09 and 400.39 eV corresponding to the C–N/N–H and N–C=O bond which further confirms the presence of the PPY in the ternary composite. The deconvolved spectrum of O 1S Fig. 4D gives rise to two characteristic peaks at 529.15eV due to Zn–O/C–O/C=O bonds while at 530.88eV due to O–C=O and H_2O. Figure 4 E shows the deconvolved spectra of Zn 2p which give two peaks with the orbital splitting of ($\Delta = 23.05$eV). The peak at 1021.73 eV corresponds to the Zn $2p_{3/2}$ while the peak at 1044.78 eV is due to the Zn $2p_{1/2}$ which is in good agreement with the previous literature. The overall XPS spectra show the presence of PPY, GO, and ZnO in the ternary composite (PGT 2) [18, 19].

Thermal analysis

Thermogravimetric analysis (TGA) curves of PPY, GO, ZnO, PG 1, and PGT 2 are shown in Fig. 5A. Initially, the weight loss at temperature < 100 °C is due to the removal of moisture content in the prepared samples. The percentage of weight loss in this temperature range depends on the composition of the prepared material; the more the hygroscopic nature, the greater the percentage

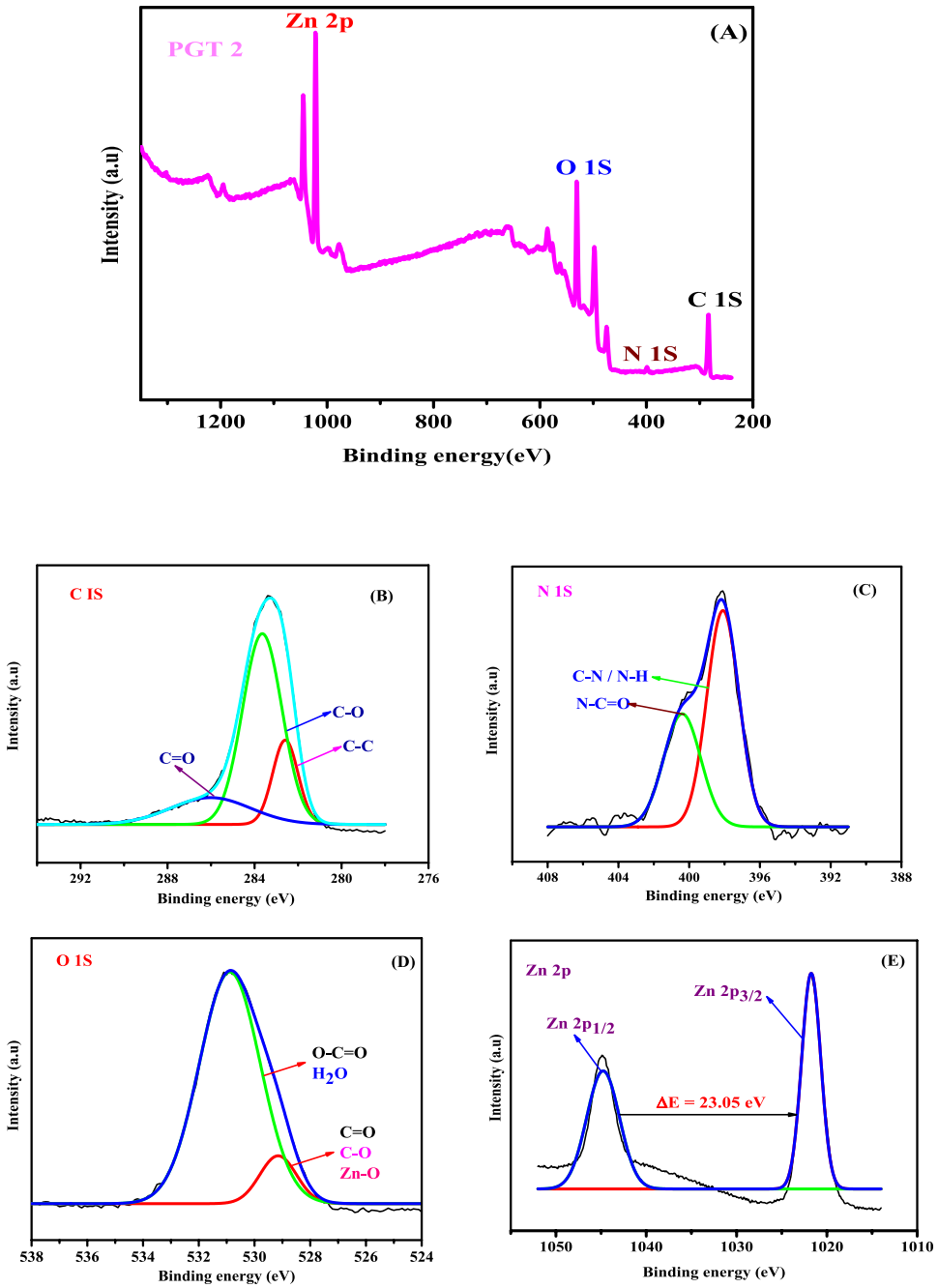

Fig. 4 XPS of PGT 2 (**A**) and deconvolution spectra of C 1S, N 1S, O 1S, and Zn 2P (**B–E**) of PGT 2

of weight loss [23]. The major weight loss for the PPY starts at a T_{onset} of 248.28 °C with residual weight (W_r %) of 79.22. The weight loss of PPY continuously increases as the temperature rises, and it ends at a T_{offset} of 575 °C indicating the volatilization of PPY. In the case of GO, the main mass loss takes place at T_{onset} 208.71 °C with W_r % of 76.26. The loss in this temperature range is mainly due to the removal of oxygen functionalities from the surface of GO. Beyond 575 °C for GO, no appreciable weight loss was observed [3, 24]. In PG 1 initially, the weight loss at the temperature of 100 °C is due to the removal of moisture content from the composite surface. The weight loss in the temperature range of 150–170 °C is probably due to the removal of oxygen-containing moieties introduced by the presence of GO in the composite material. The major weight loss in the binary composite after 243.28 °C arises due to the degradation of PPY from the composite. After removing moisture content from PPY GO and PG 1, the W_r % left up to the T_{onset} of the respective material may be by removing impurities and unreacted reactants [24, 30]. In the TGA curve of ZnO, a small weight loss due to the removal of moisture content

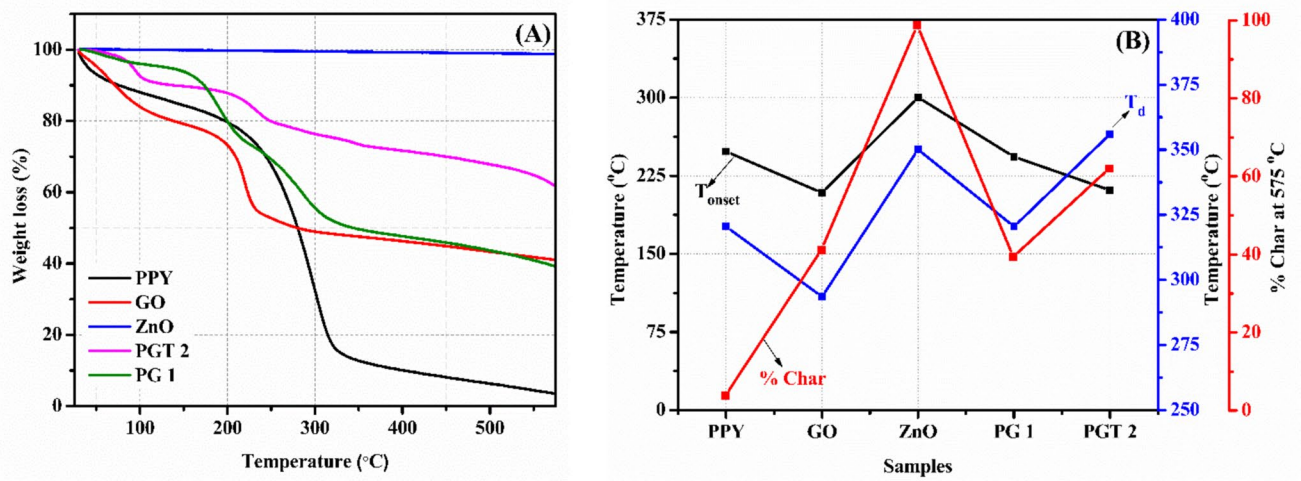

Fig. 5 TGA of PPY, GO, ZnO, PG 1, and PGT 2 (**A**); graphical representation of TGA parameter (T_{onset}, T_d, and Char%) of all the samples (**B**)

was observed, suggesting the thermal stability of ZnO [26]. A comparative representation of T_{onset}, decomposition temperature (T_d), and % char had been represented in Fig. 5B.

In the case of PGT 2, the weight loss at TG onset 212 °C and 348 °C is due to the removal of oxygen-containing functional groups and the degradation of the polymer chain from the surface of composite material. The weight loss in ternary composite occurs at higher temperatures than that of PPY, GO, and PG 1. The interaction between PPY and GO functionalities along with barrier effects of ZnO imparts additional stability to the ternary composite in comparison to PPY, GO, and PG 1 [26, 31].

Electrochemical measurements and optimization of electrodes

The electrochemical performance of PPY, GO, and ZnO and the fabricated binary and ternary composites PGs and PGTs, respectively, was evaluated by cyclic voltammetry. Cyclic voltammograms (CV curves) which have a current versus potential relationship were used to study the electrochemical activity of the electrode material used for sensing, supercapacitors, etc. The CV graphs of CPE, PPY, GO, PGs, and PGTs at a scan rate of 0.05 V/s within the potential window of − 0.5 to 1.2 V in 5 mM potassium ferrocyanide $K_3[Fe(CN)_6]$ and 0.1M KCl as supporting electrolyte are shown in Fig. 6A,B. These CVs are quasi-reversible in behavior showing distinct redox peaks of

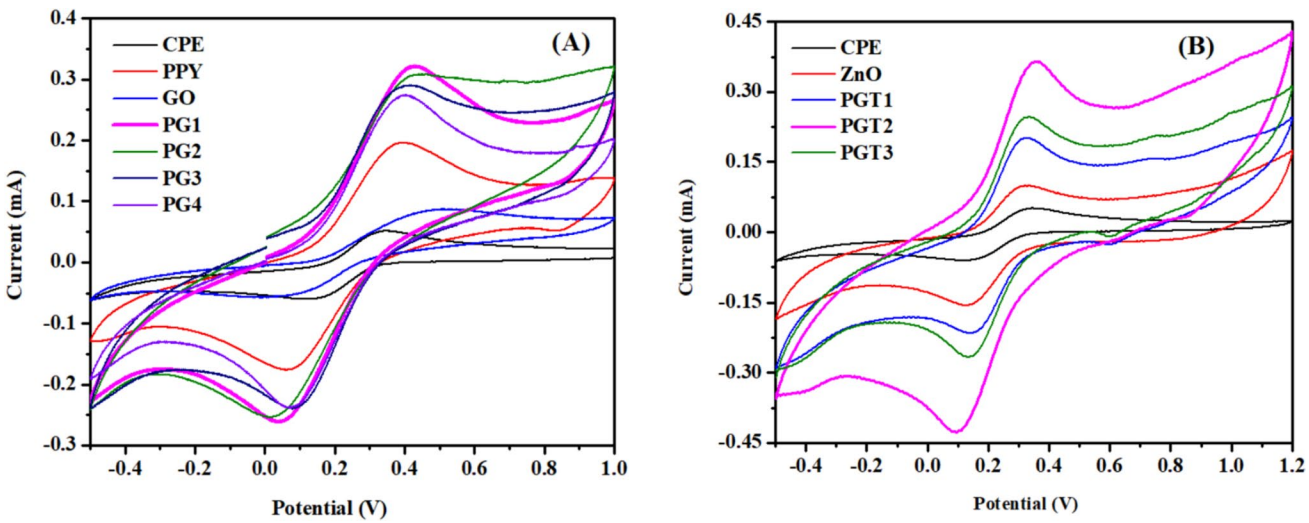

Fig. 6 CV curves of CPE, PPY, GO, PGs (**A**); CV curves of CPE, ZnO, and PGTs in 5 mM $K_3[Fe(CN)_6]$ and 0.1 M KCl (**B**)

$[Fe(CN)_6]^{3-/4}$ [32]. The peak current of PPY is higher as compared to that of the CPE and GO-modified electrode signifying the better electron transfer properties and fast redox mechanism on the surface of PPY. The presence of oxygen moieties (C=O, C–O, COOH, etc.) on the surface of GO acts as a barrier for the smooth transfer of electrons on its surface resulting in the decrease of current values [33]. In the case of binary composites PGs (at different w/w ratios), the peak current values are higher compared to CPE, PPY, and GO-based electrodes. For the optimization of the best binary composite, the various PGs were analyzed by their CV studies. The increase in the current values in the case of PGs is due to the interaction (π-π stacking and hydrogen bonding) between PPY and GO results in an increase in the porous structure and the surface area of the composite material that promotes the fast electron transfer kinetics on its surface and hence enhances its electrochemical behavior [12, 33]. The low peak current of PG 4 compared to other composites may be due to the reason that at this amount of GO, the agglomeration of PPY and GO in the composite results in the formation of a small amount of nanocomposite material on the surface of CPE that slows the rate of electron transfer during the process [11, 12]. The higher peak current value of PG 1 composite compared to other prepared binary composites shows better electrochemical response and is hence considered for preparation of ternary composite with ZnO.

In the case of ternary composite PGTs (at different w/w ratios) as shown in the graphs as follows, the peak current values first increase and then decrease with an increase in the amount of ZnO. This suggests that ZnO up to a certain amount improves the electrochemical activity by behaving both as a filler and as a pseudo-capacitor providing a smooth surface for the fast electron transport within the electrode material. An increase in the amount of ZnO in the composite material results in negative charge agglomeration at the electrode-electrolyte interface as well as stacking of the GO sheets hindering the transfer of electrons resulting in the low current. [21, 34]. The composite PGT 2 has a high peak current value as compared to other composite materials suggesting a better electrochemical performance and fast electron transfer kinetics at its surface, and hence, it has opted for further studies. [33, 35].

A comparative study of PPY, GO, PG 1, and PGT 2 at a scan of 0.05 V/s is shown in Fig. 7. The peak current of PGT 2 is higher compared to the binary as well as individual components. This enhancement in the case of the PGT 2 may be due to the combined synergetic effect of PPY, GO, and ZnO resulting in enhancement of the redox behavior which facilitates the fast transport of the electron between the $K_3[Fe(CN)_6]$ and electrode surface [28, 34, 36].

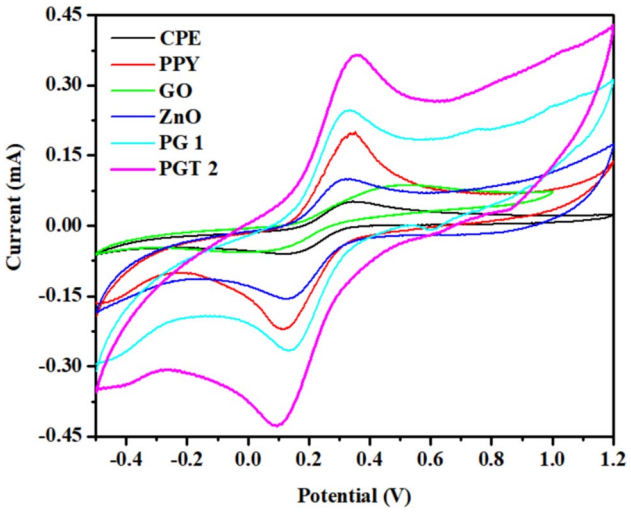

Fig. 7 Comparative CV graphs of different electrodes at the scan of 0.05 V/s

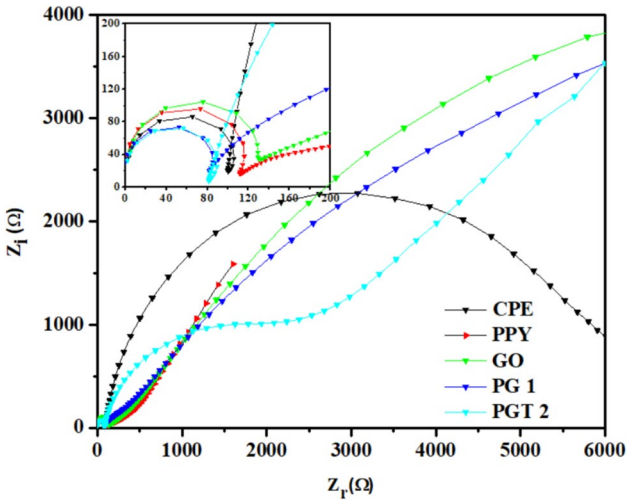

Fig. 8 The electrochemical impedance spectroscopy (EIS) of PGT 2 composite in 5 mM $[Fe(CN)_6]^{3-}$, an electrolytic solution containing 0.1 M KCl

EIS characterization

Electrochemical impedance spectroscopy (EIS) is an efficient technique for probing the features of surface-modified electrodes. The electron transfer of CPE, PPY, GO, PG 1 and PGT 2 electrode material was examined in 5 mM $K_3[Fe(CN)_6]$ aqueous solution containing 0.1 M KCl within the frequency range of 0.1 Hz to 10^6 Hz (Fig. 8) [13]. The Nyquist plots in the EIS spectra consist of the semicircle portion and the linear portion. The semicircle portion in the high frequency region reflects the interface-layer resistance occurring on the electrode surface, the diameter of which is proportional to the electron transfer resistance (R_{ct}). The

linear portion in the lower frequency region corresponds to the diffusion-limited processes taking place on the electrode-electrolyte interface. The smaller diameter of the semicircle in high-frequency region refers to lower impedance, lower R_{ct}, which favors easier charge transfer [30]. The total electrode impedance corresponds to the electron transfer resistance (R_{ct}) in series with the parallel connection of the double-layer capacitance (C_{dl}) and Warburg impedance (Z_w). As seen in the EIS spectra (Fig. 8) of bare CPE, PPY, GO, PG 1, and PGT 2, the ternary composite PGT 2 shows a smaller semicircle and lower internal resistance, signifying the fast electron transfer processes on its surface compared to other electrode materials, which could be attributed to better conductivity and improved surface area in the PGT 2 ternary composite which speed up the electron transfer kinetic on its surface which could dramatically improve the electron transfer efficiency and the detection of Pb^{2+} ions in water samples. These results are in good agreement as reported by the CV studies [37, 38].

Mechanism for Pb^{2+} ion sensing

Various phenomena taking place in the reaction medium are responsible for detecting metal ions on the surface of electrode material. Out of these, one adsorption phenomenon involves the accumulation of metal ions on the electrode surface due to the electrostatic attraction. The presence of the heteroatom functionalities (O, N, S) in the composite material (PGT 2) can coordinate to the valencies of the Pb^{2+} ion through coordinate bonds that lead to the accumulation of Pb^{2+} on its surface. After the open-circuit accumulation of metal ions, when the voltammetric analysis is performed by passing a current, it leads to the reduction of Pb^{2+} ions to the corresponding metal atom (Pb). Afterward, the metal (Pb) is stripped back into its ion (Pb^{2+}) in the solution resulting in the corresponding anodic stripping peak current value. Figure 9 shows the mechanism for the detection of Pb^{2+} ions [33, 39]. The overall mechanisms of accumulation and anodic stripping of Pb^{2+} during DPASV measurements may be described as follows:

Electrochemical detection of Pb^{2+}

The DPASV studies were carried out using CPE, PPY, GO, PG 1, and PGT 2 electrodes to determine the Pb^{2+} ion in an acetate buffer solution with pH 4.6 as a supporting electrolyte [13]. The pre-concentration step involves the accumulation of Pb^{2+} ions on the surface of the electrode material by placing a particular concentration of metal ions on the electrode surface in an open circuit with a deposition potential of − 1.2 V for 5 min. During this process, Pb^{2+} ion accumulation on the surface of electrode material occurs through electrostatic attractions and surface complexations. After the deposition step, the DPASV measurements were performed by sweeping the potential in the range of − 1.2 to 0.2 V for different electrodes [40]. The stripping behavior of the CPE, PPY, GO, PG1, and PGT 2 electrodes in the presence of 3.0 μM Pb^{2+} ion is shown in Fig. 10.

The stripping peak current value (0.210 mA at − 0.45 V) for the PGT 2 composite is higher than CPE, GO, PPY, and PG 1 (0.137, 0.140, 0.183, and 0.203 mA). This improvement in the peak current values in the case of PGT 2 may be

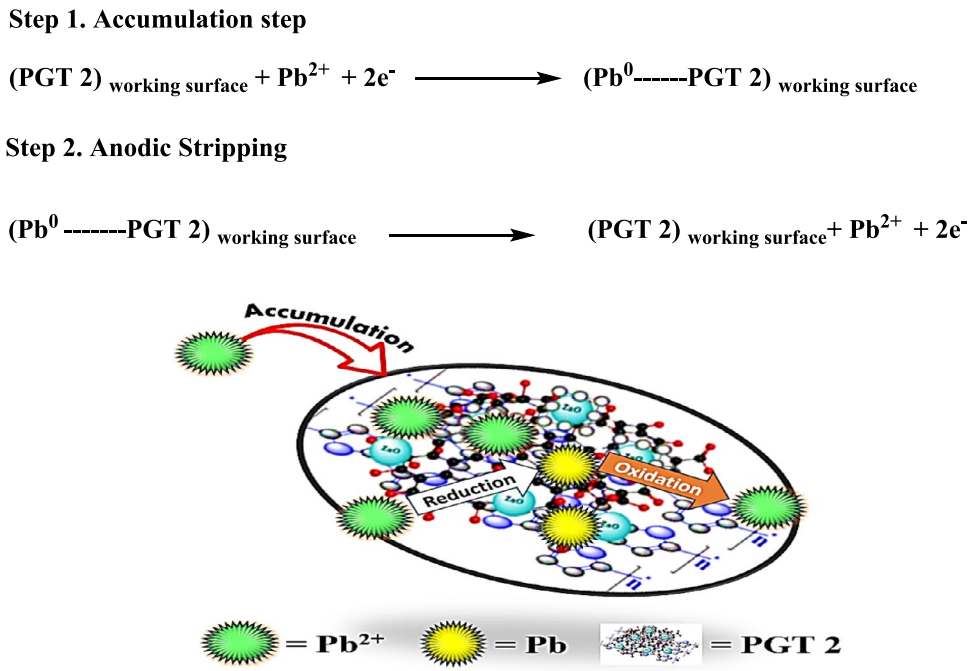

Fig. 9 Scheme for the detection of Pb^{2+} ion

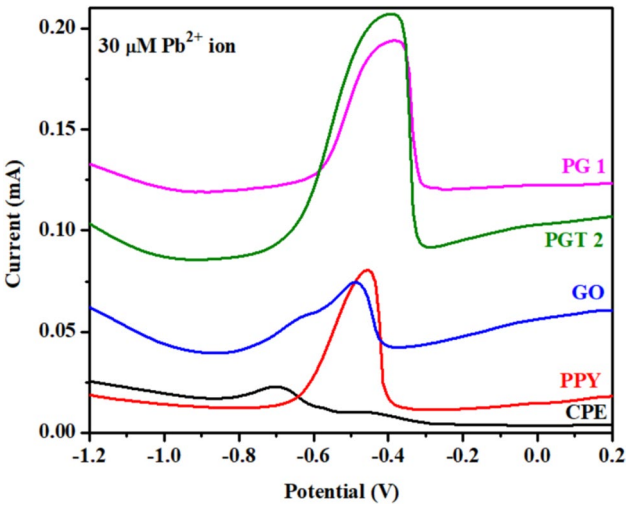

Fig. 10 Comparative DPASV of CPE, PPY, GO, PG 1, and PGT 2 at 30 µM Pb^{2+} ion

due to the increased surface area due to GO and a pseudo-capacitive behavior of PPY and ZnO making the electron transfer process more feasible in ternary composite than others. Secondly, negatively charged functional groups in PPY, GO, and ZnO act as binding sites for the Pb^{2+} ions, resulting in the formation of complexes through coordinate bonds. This results in enhancing the selective sites for the accumulation of metal on its surface in the case of PGT 2 thus increasing the stripping peak current. The peak current values for the other electrodes follow the trends as GO < CPE < PPY< PG 1 as shown in the figure [16, 37, 41].

Determination of Pb^{2+} was previously carried out through CV studies by both PG 1 and PGT 2 composites (fig. S2a and S2b). The results represent the superiority of ternary composite over binary by increasing the peak anodic and cathodic currents.

Figure 11A and B show the DPASV measurements on PG 1 and PGT 2 for various concentrations of Pb2+ metal ion (0.3 to 3.0 µM). Well-defined stripping peaks that increase with the concentration of metal ions were observed for both composites. The corresponding calibration curves (Fig. 12A, B) of PG 1 and PGT 2 for 0.3 to 3.0 µM of Pb^{2+} ions were determined as $y = 0.0106\ Pb^{2+} + 0.1707$ ($R^2 = 0.95$) for PG 1, and $y = 0.0127\ Pb^{2+} + 0.1759$ ($R^2 = 0.97$) for the ternary composite (PGT 2). The limit of detection (LOD) was calculated using the formulae "3 × SD/*S*" where "SD" is the standard deviation of the blank solution and "*S*" is the slope of the calibration curve, and it comes out to be 0.05 µM for Pb^{2+} ion by the ternary composite. With the increase in the concentration of metal ions, the stripping peak potential slightly shifts towards the positive potential and is somewhat broad due to the formation of multilayer metal ions on the surface of the already formed monolayer on the electrode surface [5, 19, 42]. The relative standard deviation (RSD) for binary (PG 1) and ternary (PGT 2) is 5.37% and 5.14% which further signifies that ternary composite is better than binary composite as a sensor for the detection of Pb^{2+} metal ion [13, 33].

Selectivity, reproducibility, and stability of PGT 2 electrode

The selectivity of the PGT 2 electrode was analyzed by adding Cu^{2+} and Cd^{2+} metal ions without and in the presence of Pb^{2+} ion. Figure 13 shows the stripping peak current values of Pb^{2+} ions in the absence and in the presence of interfering metal ions. The results show minimal changes in the stripping peak current and peak potential values of

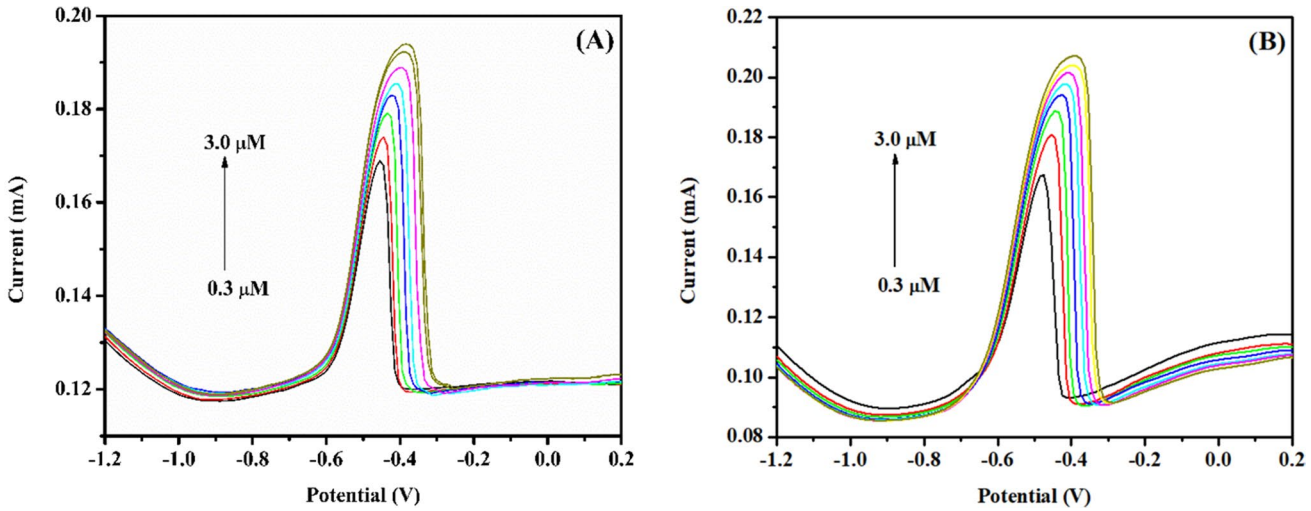

Fig. 11 DPASV curves of PG 1 (**A**) and PGT 2 (**B**) composites at various concentrations of Pb^{2+} (0.3 to 3.0 µM)

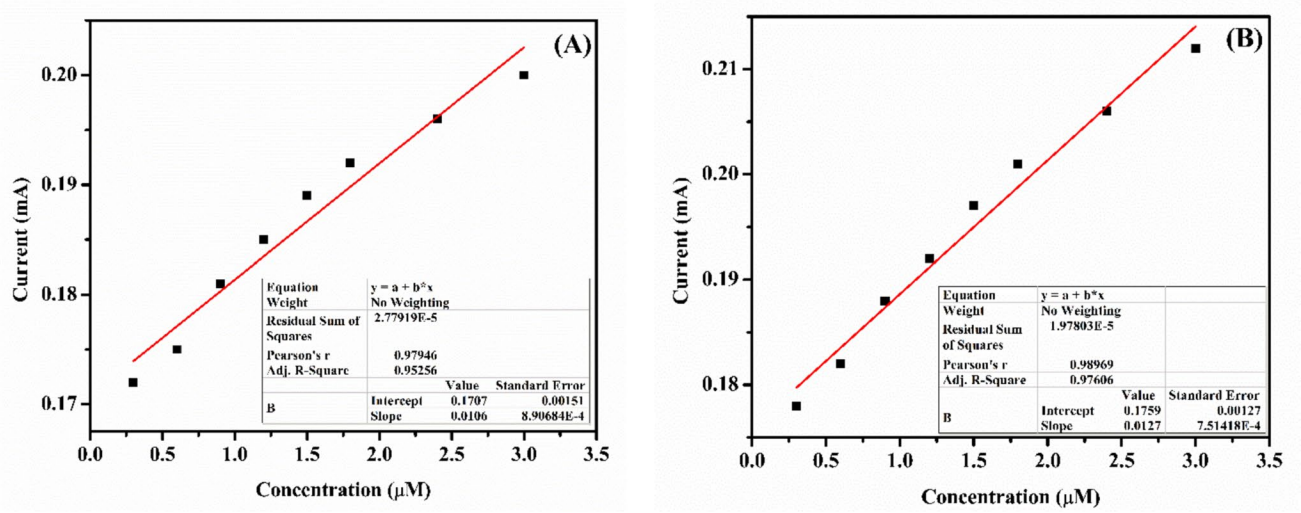

Fig. 12 Calibration curves of PG 1 (**A**) and PGT 2 (**B**) composites at various concentrations of Pb^{2+} (0.3 to 3.0 μM)

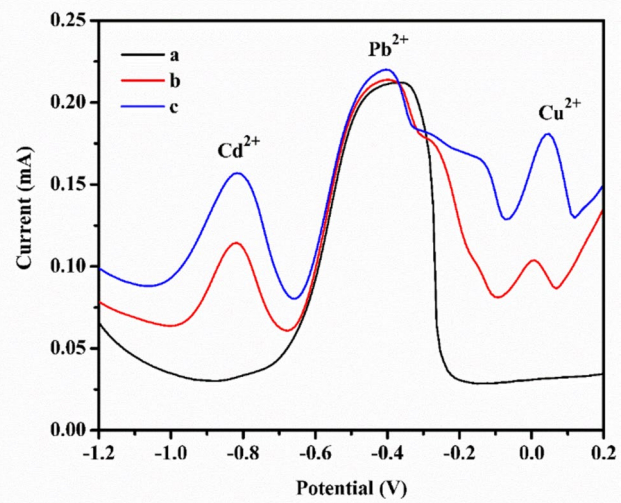

Fig. 13 DPASV results of PGT 2 composite **a** without interference (3.0 μM Pb^{2+}) and in the presence of interference **b** 1.2 μM Cd^{2+} and Cu^{2+} ions, **c** 3.0 μM Cd^{2+} and Cu^{2+} ions

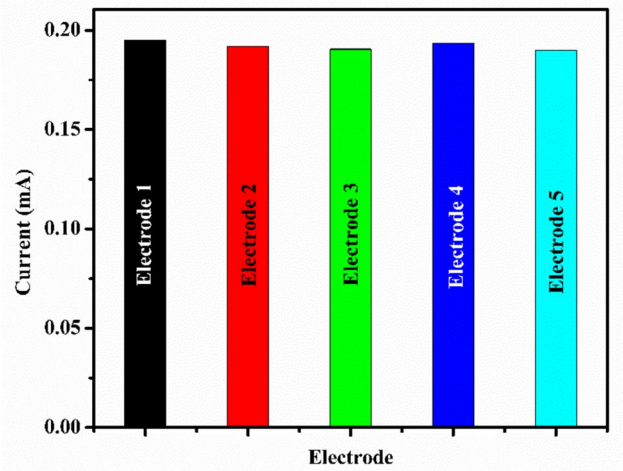

Fig. 14 Representation of the reproducibility of PGT 2 electrodes in 3.0 μM Pb^{2+} ion solution

the Pb^{2+} ion in the presence of low and high concentrations of interfering ions. The peak current values changed from 0.212 mA without interference to 0.214 mA and 0.221 mA at low and high concentrations of interfering ions whereas a negligible shift in the peak potential was observed. This shifting in values and broadening of the Pb^{2+} ion peak may be attributed to the formation of intermetallic like Pb–Cu and Pb–Cd compounds during the deposition step. However, the intensity of the Pb^{2+} metal ion signal remains unaffected by the introduction of such interference that shows the selective detection of Pb^{2+} ions [33, 36].

The reproducibility of the PGT 2 electrode was examined by preparing five electrodes modified equally with the electroactive material (Fig. 14). The DPASV measurements were performed in a 3.0 μM concentration of Pb^{2+} in an acetate buffer of pH 4.5 as a supporting electrolyte. A stripping peak current at − 0.45 V was observed irrespective of the electrode material with a relative standard deviation (RSD) of 1.089% and minimum peak current variation showing the reproducibility of the electrode material [40, 43].

The stability/shelf life of the PGT 2 electrode was analyzed by performing the DPASV measurements in the same concentration of Pb^{2+} ion (3.0 μM). After each measurement, the electrode was washed with distilled water and kept in an acetate buffer solution (pH 4.7). Each measurement was performed after 7 days for the next 4 weeks, and the corresponding current response was recorded (Fig. 15). The electrode material shows long-term stability with loss of

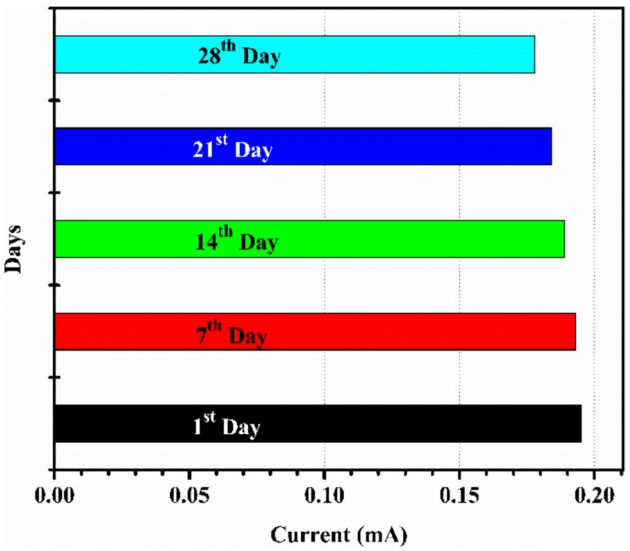

Fig. 15 Representation of the stability of PGT 2 electrodes in 3.0 µM Pb^{2+} ion solution

initial current response RSD 3.67% and retention of 96.33% current response, thus representing the reproducibility of the electrode material [14, 44].

Conclusion

A PPY/GO/ZnO ternary composite (PGT 2) was fabricated and used for the first time to effectively determine Pb^{2+} ions present in an aqueous solution. The electrochemical behavior of the composite material was analyzed using CV and EIS in $K_3[Fe(CN)_6]$ as a redox probe. The DPASV technique was employed for the detection of Pb^{2+} ions using the PGT 2 electrode material. The electrode material shows a good linear response ($R^2 = 0.98$) with a LOD of 0.05 µM for Pb^{2+} ions within the 0.3 to 3.0 µM concentration range. The reproducibility RSD (1.089%), stability RSD (3.67%), and interference of the working electrode in the presence of other metal ions (Cd^{2+} and Cu^{2+}) show a good response. These results show that the prepared PGT 2 electrode can be employed for the detection of Pb^{2+} and other HM ions from various aqueous sources.

Supplementary Information The online version contains supplementary material available at https://doi.org/10.1007/s11581-025-06067-w.

Acknowledgments Authors acknowledge the research facilities provided by Central Instrumentation Facility, Lovely Professional University, Punjab, India.

Author Contribution G.S. and N.G. wrote the manuscript and prepare the figures, A.K., P.P., and H.M. edited, supervise, and reviewed the work

Data Availability No datasets were generated or analysed during the current study.

Declarations

Conflicts of interest The authors declare no competing interests.

References

1. Singh G, Nisha, Kumar A, Prasher P, Mudila H (2023) Assessment of toxicity and electrochemical sensing of arsenic in aqueous sources. J Environ Eng Sci 18(1):10-23. https://doi.org/10.1680/jenes.22.00011
2. Song J, Wang X, Chang CT (2014) Preparation and characterization of graphene oxide. J Nanomater 2014:1–6. https://doi.org/10.1155/2014/276143
3. Konwer S, Boruah R, Dolui SK (2011) Studies on conducting polypyrrole/graphene oxide composites as supercapacitor electrode. J Electr Mater 40(11):2248–2255. https://doi.org/10.1007/s11664-011-1749-z
4. Kulandaivalu S, Suhaimi N, Sulaiman Y (2019) Unveiling high specific energy supercapacitor from layer-by-layer assembled polypyrrole/graphene oxide/polypyrrole/manganese oxide electrode material. Sci Rep 9(1):4884. https://doi.org/10.1038/s41598-019-41203-3
5. Dong Y, Ding Y, Zhou Y, Chen J, Wang C (2014) Differential pulse anodic stripping voltammetric determination of Pb ion at a montmorillonites/polyaniline nanocomposite modified glassy carbon electrode. J Electroanalytic Chem 717–718:206–212. https://doi.org/10.1016/j.jelechem.2014.01.01
6. Bontas BI, Mirila DC, Gritcu G, Nistor ID, Ureche D (2020) High pollution with heavy metals NATURA 2000 protected area in Bacau County Eastern Romania. Rev Chim 71:154–169. https://doi.org/10.37358/RC.20.6.8180
7. Li L, Xia K, Li L, Shang S, Guo Q, Yan G (2012) Fabrication and characterization of free-standing polypyrrole/graphene oxide nanocomposite paper. J Nanopart Res 14(6):908. https://doi.org/10.1007/s11051-012-0908-3
8. Jahani PM, Nejad RKS, Zaimbashi R, Nejad FG, Moammadi SZ, Tajik S, Beitollahi H (2024) A voltammetric sensor based on CuCo2O4 nanorods and ionic liquid for determination of sunset yellow. J Electrochem Sci Eng 14(5):643–652. https://doi.org/10.5599/jese.2484
9. Mohammadzadeh Jahani P, Garkani Nejad F, Zaimbashi R, Aflatoonian MR, Tajik S, Beitollahi H (2024) Determination of methotrexate using carbon paste electrode modified with ionic liquid/Ni-Co layered double hydroxide nanosheets as a voltammetric sensor. ADMET and DMPK 12(4):637–648. https://doi.org/10.5599/admet.2460
10. Asen P, Shahrokhian S, Irajizad A (2017) One-step electrodeposition of V2O5 /polypyrrole/graphene oxide ternary nanocomposite for preparation of a high performance supercapacitor. Int J Hydr Energy 42(33):21073–21085. https://doi.org/10.1016/j.ijhydene.2017.07.00
11. Zhang H, Li Y, Zhang Y, Wu J, Li S, Li L (2023) A disposable electrochemical sensor for lead ion detection based on in situ polymerization of conductive polypyrrole coating. J Electr Mater 52(3):1819–1828. https://doi.org/10.1007/s11664-022-10175-y
12. Rong R, Zhao H, Gan X, Chen S, Quan X (2017) An electrochemical sensor based on graphene-polypyrrole nanocomposite for the specific detection of Pb (II). Nano 12(01):1750008. https://doi.org/10.1142/s1793292017500084

13. Oularbi L, Turmine M, El Rhazi M (2017) Electrochemical determination of traces lead ions using a new nanocomposite of polypyrrole/carbon nanofibers. J Solid State Electrochem 21(11):3289–3300. https://doi.org/10.1007/s10008-017-3676-2
14. Chen L, Li Z, Meng Y, Zhang P, Su Z, Liu Y, Huang Y, Zhou Y, Xie Q, Yao S (2014) Sensitive square wave anodic stripping voltammetric determination of Cd2+ and Pb2+ ions at Bi/Nafion/overoxidized 2-mercaptoethanesulfonate-tethered polypyrrole/glassy carbon electrode. Sens Actuators B Chem 191:94–101. https://doi.org/10.1016/j.snb.2013.09.084
15. Liu Y, Chang C, Xue Q, Wang R, Chen L, Liu Z, He L (2022) Highly efficient detection of Pb (II) ion in water by polypyrrole and metal-organic frame modify glassy carbon electrode. Diamond Related Mater 130:109477. https://doi.org/10.1016/j.diamond.2022.109477
16. Dai H, Wang N, Wang D, Ma H, Lin M (2016) An electrochemical sensor based on phytic acid functionalized polypyrrole/graphene oxide nanocomposites for simultaneous determination of Cd(II) and Pb(II). Chem Eng J 299:150–155. https://doi.org/10.1016/j.cej.2016.04.083
17. Liu G, Shi Y, Wang L, Song Y, Gao S, Liu D, Fan L (2019) Reduced graphene oxide/polypyrrole composite: an advanced electrode for high-performance symmetric/asymmetric supercapacitor. Carbon Letters 30(4):389–397. https://doi.org/10.1007/s42823-019-00108-x
18. Sebastian N, Yu W-C, Hu Y-C, Balram D, Yu Y-H (2022) Morphological evolution of nanosheets-stacked spherical ZnO for preparation of GO-Zn/ZnO ternary nanocomposite: a novel electrochemical platform for nanomolar detection of antihistamine promethazine hydrochloride. J Alloys Compounds 890:161768. https://doi.org/10.1016/j.jallcom.2021.161768
19. Ghanbari K, Bonyadi S (2018) An electrochemical sensor based on reduced graphene oxide decorated with polypyrrole nanofibers and zinc oxide–copper oxide p–n junction heterostructures for the simultaneous voltammetric determination of ascorbic acid, dopamine, paracetamol, and tryptophan. New J Chem 42(11):8512–8523. https://doi.org/10.1039/c8nj00857d
20. Arumugama C, Kandasamya SK, Subramaniamb TK (2022) Enhancing supercapacitor performance using ZnO embedded on GO/PPy composite as versatile electrodes. High Energy Chem 57(1):69–76. https://doi.org/10.1134/S0018143923010034
21. Chee WK, Lim HN, Harrison I, Chong KF, Zainal Z, Ng CH, Huang NM (2015) Performance of flexible and binderless polypyrrole/graphene oxide/zinc oxide supercapacitor electrode in a symmetrical two-electrode configuration. Electrochimica Acta 157:88–94. https://doi.org/10.1016/j.electacta.2015.01.0
22. Hussain RT, Islam AS, Khairuddean M, Suah FBM (2022) A polypyrrole/GO/ZnO nanocomposite modified pencil graphite electrode for the determination of andrographolide in aqueous samples. Alexandria Eng J 61(6):4209–4218. https://doi.org/10.1016/j.aej.2021.09.040
23. Mudila H, Zaidi MGH, Rana S, Joshi V, Alam S (2013) Enhanced electrocapacitive performance of graphene oxide polypyrrole nanocomposites. Int J Chem Analytic Sci 4(3):139–145. https://doi.org/10.1016/j.ijcas.2013.09.001
24. Jahani PM, Zaimbashi R, Aflatoonian MR, Tajik S, Beitollahi H (2024) Electrochemical sensor for acetylcholine detection based on WO3 nanorods-modified glassy carbon electrode. J Electrochem Sci Eng 14(5):631–641. https://doi.org/10.5599/jese.2462
25. Guerrero-Contreras J, Caballero-Briones F (2015) Graphene oxide powders with different oxidation degree, prepared by synthesis variations of the Hummers method. Mater Chem Phys 153:209–220. https://doi.org/10.1016/j.matchemphys.2015.01
26. Batool A, Kanwal F, Imran M, Jamil T, Siddiqi SA (2012) Synthesis of polypyrrole/zinc oxide composites and study of their structural, thermal and electrical properties. Synthetic Metals 161(23–24):2753–2758. https://doi.org/10.1016/j.synthmet.2011.10.01
27. Chougule MA, Pawar SG, Godse PR, Mulik RN, Sen S, Patil VB (2011) Synthesis and characterization of polypyrrole (PPy) thin films. Soft Nanosci Lett 01(01):6–10. https://doi.org/10.4236/snl.2011.11002
28. Pruna A, Shao Q, Kamruzzaman M, Zapien JA, Ruotolo A (2015) Enhanced electrochemical performance of ZnO nanorod core/polypyrrole shell arrays by graphene oxide. Electrochimica Acta 187:S0013468615308598. https://doi.org/10.1016/j.electacta.2015.11.087
29. Sharif M, Heidari A, Aghaeinejad Meybodi A (2021) Polythiophene/zinc oxide/graphene oxide ternary photocatalyst: synthesis, characterization and application. Polym-Plastics Technol Materials 60:1–11. https://doi.org/10.1080/25740881.2021.1905842
30. Bose S, Kuila T, Uddin ME, Kim NH, Lau AKT, Lee JH (2010) In-situ synthesis and characterization of electrically conductive polypyrrole/graphene nanocomposites. Polymer 51(25):5921–5928. https://doi.org/10.1016/j.polymer.2010.10.014
31. Ates M, Caliskan S, Gazi M (2018) A ternary nanocomposites of graphene / TiO2 /polypyrrole for energy storage applications. Fullerenes, Nanotubes Carbon Nanostruct 26(10):631–642. https://doi.org/10.1080/1536383x.2018.1457651
32. Lee S, Oh J, Kim D, Piao Y (2016) A sensitive electrochemical sensor using an iron oxide/graphene composite for the simultaneous detection of heavy metal ions. Talanta 160:528–536. https://doi.org/10.1016/j.talanta.2016.07.034
33. Seenivasan R, Chang W-J, Gunasekaran S (2015) Highly sensitive detection and removal of lead ions in water using cysteine-functionalized graphene oxide/polypyrrole nanocomposite film electrode. ACS Appl Mater Interf 7(29):15935–15943. https://doi.org/10.1021/acsami.5b03904
34. Palsaniya S, Nemade HB, Dasmahapatra AK (2021) Hierarchical PANI-RGO-ZnO ternary nanocomposites for symmetric tandem supercapacitor. J Phys Chem Solids 154:110081. https://doi.org/10.1016/j.jpcs.2021.110081
35. Singh G, Nisha, Kumar A, Prasher P, Mudila H (2023) Comparative study on the electrochemical performance of PPY/GO binary and PPYGO/ZnO ternary nanocomposites. Bulgarian Chem Commun 55:37-43. https://doi.org/10.34049/bcc.55.A.0005
36. Muralikrishna S, Nagaraju DH, Balakrishna RG, Surareungchai W, Ramakrishnappa T, Shivanandareddy AB (2017) Hydrogels of polyaniline with graphene oxide for highly sensitive electrochemical determination of lead ions. Analytica Chimica Acta 990:67–77. https://doi.org/10.1016/j.aca.2017.09.008
37. Akhtar M, Tahir A, Zulfiqar S, Hanif F, Warsi MF, Agboola PO, Shakir I (2020) Ternary hybrid of polyaniline-alanine-reduced graphene oxide for electrochemical sensing of heavy metal ions. SynthMetals 265:116410. https://doi.org/10.1016/j.synthmet.2020.116410
38. Karthik R, Govindasamy M, Chen SM, Chen TW, Kumar JV, Elangovan A, Muthuraj V, Yu MC (2017) A facile graphene oxide based sensor for electrochemical detection of prostate anticancer (anti-testosterone) drug flutamide in biological samples. RSC Advances 7(41):25702–25709. https://doi.org/10.1039/c6ra28792a
39. Blaise N, Gomdje Valéry H, Maallah R, Oubaouz M, Tigana Djonse Justin B, Andrew Ofudje E, Chtaini A (2022) Simultaneous electrochemical detection of Pb and Cd by carbon paste electrodes modified by activated clay. J Analytic Methods Chem 2022(1):6900839. https://doi.org/10.1155/2022/6900839
40. Zhoug X (2024) Electrochemical detection of heavy metal ions in water using MWCNT/ ZnO nanocomposite. Int J Electrochem Sci 19(5):100559. https://doi.org/10.1016/j.ijoes.2024.100559
41. Krasovska M, Gerbreders V, Mihailova I, Ogurcovs A, Sledevskis E, Gerbreders A, Sarajevs P (2018) ZnO-nanostructure-based

electrochemical sensor: effect of nanostructure morphology on the sensing of heavy metal ions. Beilst J Nanotechnol 9:2421–2431. https://doi.org/10.3762/bjnano.9.227
42. Suvina V, Krishna SM, Nagaraju DH, Melo JS, Balakrishna RG (2018) Polypyrrole-reduced graphene oxide nanocomposite hydrogels: a promising electrode material for the simultaneous detection of multiple heavy metal ions. Mater Lett. https://doi.org/10.1016/j.matlet.2018.08.096
43. Karthik R, Thambidurai S (2017) Synthesis of cobalt-doped ZnO/reduced graphene oxide nanorods as active material for heavy metal ions sensor and antibacterial activity. J Alloys Compounds 715:254–265. https://doi.org/10.1016/j.jallcom.2017.04.298
44. Luyen ND, Trang HT, Khang PY, Thanh NM, Vu HXA, Phong NH, Khieu DQ (2023) Simultaneous determination of Pb(II) and Cd(II) by electrochemical method using ZnO/ErGO-modifed electrode. J Appl Electrochem. 54(4):1–17. https://doi.org/10.1007/s10800-023-02005-8

Publisher's Note Springer Nature remains neutral with regard to jurisdictional claims in published maps and institutional affiliations.

Springer Nature or its licensor (e.g. a society or other partner) holds exclusive rights to this article under a publishing agreement with the author(s) or other rightsholder(s); author self-archiving of the accepted manuscript version of this article is solely governed by the terms of such publishing agreement and applicable law.

Cite this article
Singh G, Nisha, Kumar A, Prasher P and Mudila H
Assessment of toxicity and electrochemical sensing of arsenic in aqueous sources.
Journal of Environmental Engineering and Science,
https://doi.org/10.1680/jenes.22.00011

Research Article
Paper 2200011
Received 07/02/2022; Accepted 28/09/2022

ICE Publishing: All rights reserved

Journal of Environmental Engineering and Science

ice Publishing

Assessment of toxicity and electrochemical sensing of arsenic in aqueous sources

Goverdhan Singh PhD
Research Scholar, Department of Chemistry, Lovely Professional University, Phagwara, India

Nisha PhD
Research Scholar, Department of Chemistry, Lovely Professional University, Phagwara, India

Anil Kumar PhD
Assistant Professor, Department of Chemistry, Lovely Professional University, Phagwara, India

Parteek Prasher PhD
Assistant Professor, Department of Chemistry, UPES, Dehradun, India

Harish Mudila PhD
Assistant Professor, Department of Chemistry, Lovely Professional University, Phagwara, India (corresponding author: harismudila@gmail.com)

A variety of contaminants present in potable water, including heavy metals, cause numerous health hazards. Arsenic (As) is studied as one of the chief heavy elements hazardous to human beings and other categories of life. Arsenic as a natural constituent of the earth's crust is present in mineral rocks, which are deposited through various natural processes. Moreover, arsenic is also added to groundwater anthropogenically through the burning of fossil fuels, arsenical agrochemicals, wood preservatives and so on. Arsenic (III) (As^{III}) and arsenic (V) (As^{V}) are toxic inorganic forms in aqueous solution and are responsible for cancer, arsenicosis, vascular diseases and toxicity related to genes, cells, epidemiology and so on. In view of these problems, it is necessary to detect and decontaminate arsenic contamination in potable water. In this paper, brief descriptions are given of the most significant electrochemical methods, due to their advantages such as robustness, speed, accuracy and simplicity. Moreover, techniques such as differential pulse voltammetry, square-wave voltammetry (SWV), stripping chronopotentiometry, anodic stripping voltammetry and cyclic voltammetry (CV) have kept the electrochemical method as a diverse and advanced technique for the sensing process. Furthermore, details of the determination and decontamination of arsenic in potable water through an electrochemical process with a particular focus on SWV and CV are discussed.

Keywords: arsenic/cyclic voltammetry/decontamination/electrochemical method/ground water/heavy metals/square-wave voltammetry/toxicity/UN SDG 3: Good health and well-being/UN SDG 6: Clean water and sanitation

Notation

E_{step}	potential step
I_1, I_2	current
V	potential
ΔE	pulse amplitude
τ	time (s)

Introduction

Water, which covers 70% of the earth's crust, is one of the most important natural resources necessary for the good health and well-being and survival of life on earth. As a wonderful natural component, it can dissolve numerous constituents (organic and inorganic chemicals and various other substances) in varying concentrations (Mudila *et al*., 2018; Obinnaa and Ebere, 2019). The chemicals dissolved in potable water could be beneficial as well as hazardous to the living community consuming that water. A large part of the world is suffering from public health emergencies of incredible proportions due to the scarcity of potable water, while a large community of the world is under threat due to chemical poisoning and contaminants present in groundwater consumed as drinking water (Hussam, 2013; Pooja *et al*., 2020). Contaminants in potable water are undesired and may be foreign particles and so on, which are responsible for influencing the normal functioning of a system, and could be of different forms and can be generated from a variety of sources (Sharma and Bhattacharya, 2017). These contaminants, regardless of the source, are hazardous to the ecosystem and hence to all the forms of life present there, particularly humans (Gleick, 2002). According to the report of the World Health Organization (WHO) on potable water for the year 2022, nearly 2 billion people all over the globe depend on contaminated sources, which leads to various waterborne diseases (cholera, diarrhoea, dysentery and typhoid) and other health hazards (Luvhimbi *et al*., 2022).

A variety of contaminants are present in water coming from different sources. Microbial contamination mainly includes pathogens such as bacteria, parasites, viruses and worms. These pathogens knowingly or unknowingly can reach water sources through human and animal wastes, thus causing distinctive problems in water. Poor water quality, poor hygiene and food sources play a significant role in pathogen exposure leading to the outbreak of waterborne infections such as diarrhoea, dysentery and cholera. Infections caused by

Offprint provided courtesy of www.icevirtuallibrary.com
Author copy for personal use, not for distribution

Escherichia coli bacteria found in contaminated water are still a serious public health concern, as their presence indicates the existence of deadly illnesses such as food poisoning (Gwimbi *et al*., 2019; Khambete, 2019; Sharma and Bhattacharya, 2017). Organic pollutants as contaminants are composed mainly of carbon-containing compounds that are covalently bonded with other elements such as nitrogen, oxygen, sulfur and halogens. These are hydrophilic (polar) and hydrophobic (non-polar) in nature. The problematic and most studied organic pollutants are hydrophobic compounds due to their excess concentration in water; they have bad effects on the aquatic ecosystem (Obinnaa and Ebere, 2019; Schweitzer and Noblet, 2018). These organic chemicals are frequently found in drinking water supplies mainly from major known natural (decomposition of natural organic matter, i.e. humus) and anthropogenic sources – namely, household waste, industrial waste, agricultural run-off and municipal waste water discharge (sewage and sludge) (Shy, 1985). Contamination of water by inorganic pollutants mainly originates from various geogenic and anthropogenic sources. Above all, heavy metals are the major inorganic contaminants of water causing pollution when these are present above their critical value; they constitute the most dangerous group of contaminants in water. Various governing bodies have set certain permissible limits of these heavy metals in drinking water, above which the concentrations of these metals cause serious health hazards. Some metals with their permissible limits as defined by the WHO in potable water are shown in Table 1 (Mudila *et al*., 2018; Palansooriya *et al*., 2019; Wasewar *et al*., 2020). Heavy metal contaminants are found to be non-degradable and tend to bioaccumulate (due to their low solubility in water) and undergo food chain amplification. These heavy metals are toxic even when present at a low concentration, which is more remarkably observed in towns and cities as compared with rural areas (Chioma *et al*., 2021; Mudila *et al*., 2018). The toxicity of these specific heavy metals towards living components is due to their chemical reactivity with the cellular structure of humans and animals, specifically affecting the structure and functioning of proteins, enzymes and membrane systems (Ding *et al*., 2021; Mahurpawar, 2015; Sankhla *et al*., 2016). Although a variety of hazardous heavy metals are a great threat to human health and life, among them, arsenic (As) is one of the major trace elements.

It is thus required that the hazards of arsenic be explored in a scientific way along with its detection and decontamination. This specific review targets the study of the toxicity of arsenic (its different forms) to a variety of living beings. Along with this, a variety of techniques are discussed for effective detection of arsenic in potable water, mainly concentrating on advanced electrochemical techniques. This review will give a deep insight into the studies done on the electrochemical determination of arsenic, which can help researchers further develop novel ideas for arsenic decontamination thereafter.

Arsenic and its toxicity to biota

As an important natural constituent of the earth's crust, arsenic (atomic number 33, atomic weight 74.92) is chiefly found in mineral rocks, which are deposited through natural processes such as desorption and dissolution. It is a member of the nitrogen family, with electronic configuration [Ar] $3d^{10}4s^{2}4p^{3}$. The five valence electrons in arsenic allow it to form covalently bonded compounds, thus stabilising the arsenic (V) (As^{V}) oxidation state, while the presence of three unfilled p orbitals stabilises the arsenic (III) (As^{III}) state when bonded with other atoms. Due to its high oxidation potential, arsenic generates a higher metallic character, while the electronegativity of arsenic is much higher compared with those of nitrogen and phosphorus. Owing to its ability to

Table 1. Heavy metals and their sources, side effects and permissible limits in potable water

Heavy metal	Permissible limit: mg/l (WHO)	Sources from where they contaminate water	Side effects	References
Cadmium (Cd)	0.005	Industries, households, vehicular wastes and so on	Affects the CNS, teratogenesis and carcinogenesis, affects numerous body parts	Mudila *et al*. (2018), Sanyal *et al*. (2020)
Arsenic	**0.01**	**Natural and anthropogenic sources**	**Leucomelanosis, keratosis, skin cancer, CNS disturbance**	Obinnaa and Ebere (2019), Pooja *et al*. (2020), Sanyal *et al*. (2020)
Mercury (Hg)	0.001	Use of fertilisers	Depression, carcinogenic	Mudila *et al*. (2018), Sanyal *et al*. (2020)
Iron (Fe)	0.1	Industrial processes, sewage discharges and so on	Haemorrhagic necrosis, haemochromatosis	Mudila *et al*. (2018), Sanyal *et al*. (2020)
Chromium (Cr)	0.1	Use of fertilisers and industrialisation	Organ failure, liver damage, carcinogenic effects	Puri and Kumar (2012), Obinnaa and Ebere (2019), Sanyal *et al*. (2020)
Lead (Pb)	0.05	Poly(vinyl chloride) pipes, natural and household plumbing systems	Anaemia, learning and behavioural disturbances	Puri and Kumar (2012), Sanyal *et al*. (2020)
Zinc (Zn)	5.0	Weathering and mining of rocks and use of pesticides	Cancer, microcytic anaemia, leucopoenia	Puri and Kumar (2012), Mudila *et al*. (2018), Sanyal *et al*. (2020)

CNS, central nervous system
Bold values represent arsenic toxicity relevant materials

Offprint provided courtesy of www.icevirtuallibrary.com
Author copy for personal use, not for distribution

change its oxidation state and bonding configuration, arsenic forms a variety of compounds (organic and inorganic) that exist in solid, liquid and gaseous states. The oxyanions of arsenic exist in both +3 (reducing environment) and +5 (oxidising environment) oxidation states in an aqueous solution, which is regulated by the pH (6–9) and redox potential. These inorganic forms are much more toxic to living components compared with the organic form of arsenic (Shankar *et al*., 2014).

Like other trace elements, arsenic also plays a significant role in contaminating water sources through both natural sources (forest fire, weathering, sedimentation of rocks and so on) and anthropogenic sources (mining, glass manufacturing, fossil product generation and burning, agrochemicals, wood preservation and others) (Nriagu *et al*., 2007; Shankar *et al*., 2014). Arsenopyrite (FeAsS, most abundant), arsenolite (As_2O_3; oxidised form), realgar (As_4S_4; reduced form) and orpiment (As_2S_3; reduced form) are the natural mineral sources of arsenic (3–10 mg/kg of soil) (Bissen and Frimmel, 2003). Aside from this, factors such as the type of water source, oxygenated water, the degree of microbial activities and the proximity of arsenic-rich sources also regulate its concentration in water (IARC WGECRH, 2012). Factors such as the toxicity, mobility and solubility of arsenic in water sources depend primarily on the oxidation state of the element, while the solubility parameter also depends on the dissolved concentrations of iron (Fe), phosphates and so on. As a nutrient, arsenic is known to have no essential function in plants and other organisms. Many researchers have revealed that arsenic has toxic effects on plants, animals and humans (Farooq *et al*., 2016; Howard, 2003; Shankar *et al*., 2014). Arsenite (arsenic (III)), methylated arsenic (dimethyl arsenic acid, monomethyl arsonic acid) and arsenate (arsenic (V)) are the major forms (Figure 1) of arsenic absorbed by plant roots from the soil solution, which are further translocated and have major effects on plants. A variety of genes are associated with the uptake of each form of arsenic (mentioned earlier) by the plants, apart from various factors that determine the accumulation of arsenic within the plant body. These factors include the concentration of arsenic in soil, soil characteristics, environmental circumstances (discharge from geological constructions and erosion), rate of arsenic accumulation and type of plant (Farooq *et al*., 2016; Tekere, 2019). Minute concentrations of arsenic are responsible for producing certain alterations (physiological, morphological, biochemical. molecular etc.), which can further affect the growth and productivity of plants. An elevated concentration of arsenic has more hazardous effects on floras. Reactive oxygen species such as superoxides, hydroxyl radicals and hydrogen peroxide, which are responsible for the generation of arsenic (III) from arsenic (V), lead to significant toxicity in the plants at the subcellular level (Abbas *et al*., 2018; Farooq *et al*., 2016). Likewise, all forms (inorganic and organic) of arsenic have effects on animals. Depending on the form and the oxidation state (arsenic (III) and arsenic (V)), the severity could be of different levels (acute lethality to chronic). Generally, studies demonstrate inorganic arsenic to be more detrimental compared with organic arsenic. Even in inorganic form, arsenic (III) is more dangerous compared with arsenic (V), which can affect the dermis (e.g. cancer) and various biochemical systems of animals, including the nervous, immune, reproductive, respiratory, cardiovascular and digestive systems. Moreover, arsenic can also lead to some genetic problems (chromosomal aberrations, restricted methylation and repair of deoxyribonucleic acid (DNA) and mutations) (Mandal 2017; Ventura-Lima *et al*., 2011).

According to recent studies, globally, 100 million and more than 45 million people in Asia alone are at risk of being diseased because of consuming arsenic at higher than its permissible limit – that is, more than 5–10 parts per billion (ppb) in drinking water – thus suggesting the severity of arsenic effect on human health (Shankar *et al*., 2014). The elevated atmospheric concentration of arsenic affects a large community through inhalation of contaminated air and smoking of tobacco, while the other chief source of exposure to arsenic is use of contaminated potable water for drinking and preparing food and industrial waste in water (Howard, 2003). Out of all these mentioned sources of arsenic exposure, contaminated groundwater is the most important route of human contact with inorganic arsenic. The exposure of groundwater to inorganic arsenic mainly occurs in areas where arsenic is found in the form of natural minerals. Elevated concentrations of arsenic in drinking water are found to be carcinogenic. Therefore, it is of prime importance to control the concentration of arsenic down to the permissible limit in drinking water as set by the regulating authority (Table 1) (Kapaj *et al*., 2006; Saha *et al*., 2014). Most inorganic arsenic (III) enters the human body through ingestion and inhalation and is further absorbed into the bloodstream through the gastrointestinal and

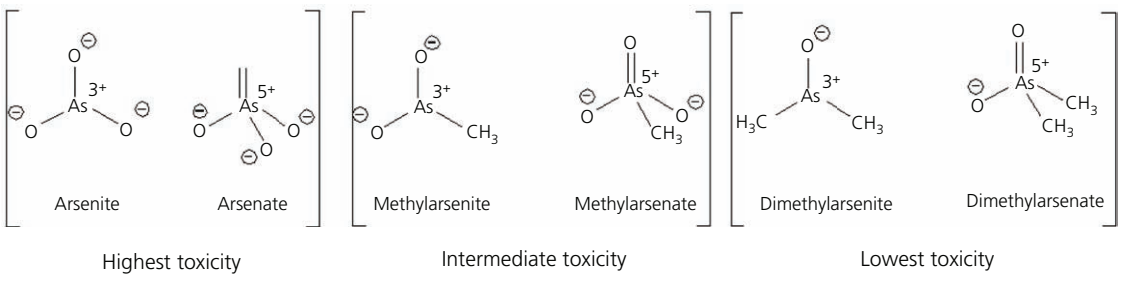

Figure 1. Arsenic species present in aqueous sources and their relative toxicity

Offprint provided courtesy of www.icevirtuallibrary.com
Author copy for personal use, not for distribution

respiratory tracts. This trace element mainly resides in erythrocytes and is further transported to organs by binding with the globin protein chain of haemoglobin (Mazumder *et al*., 2010). Although the effect of arsenic is delayed, certain common symptoms – namely, pigmentation of the skin, skin cancer and keratosis (wart or callus) – mark the presence of arsenic beyond the limit prescribed. Arsenic concentration not only affects the dermis but also leads to issues such as cancers of the lungs, liver and bladder, while prolonged exposure leads to arsenicosis, which is the main reason for complications such as blackfoot disease, skin lesions, peripheral vascular disease, genotoxicity, cytotoxicity and epidemiological toxicity (Figure 2) (Mazumder *et al*., 2010; Shankar *et al*., 2014).

Techniques used for determination of arsenic

The presence of heavy metal ions in aquatic resources is not easily detected simply by taste, smell or sight. Hence, a variety of chemical and spectroscopic techniques are employed for the detection. The results of their detection may vary depending on the type of metal ion and technique employed for individual determination (Mudila *et al*., 2018). Most of the analytical techniques recommended by various government agencies and documented in the literature for the detection of arsenic present in various biological as well as environmental samples have detection limits measured in milligrams per litre (parts per million (ppm)) or micrograms per litre (ppb) or less. Some of the advanced methods employed for efficient detection of arsenic are atomic absorption spectroscopy (AAS) and its advanced forms (e.g. hydride generation (HG-AAS)), neutron activation analysis (NAA), X-ray fluorescence (XRF) and electrochemical sensing (Table 2). There are certain other techniques that involve the coupling of separation techniques with a sensitive detection system such as inductively coupled plasma mass spectrometry (ICP-MS), which is mainly used for the speciation of arsenic species (Behari and Prakash, 2006; Rajakovic and Rajakovic-Ognjanovic, 2018).

AAS

Determination of arsenic by AAS firstly requires reduction of arsenic (V) to arsenic (III), which gives signals/peaks in AAS. AAS with vapour generation assembly (VGA) with an acidic channel (hydrochloric acid (HCl), 10 M) and a reducing channel (containing sodium borohydride ($NaBH_4$)) was employed for the analysis of arsenic in potable water, where a comparative study between the arsenic (arsenic (III) and arsenic (V)) concentrations used and concentrations observed was carried out (Figure 3). The results of the investigation suggest that for effective determination of arsenic (V) by AAS, it must be reduced to arsenic (III), which can be effectively done by using potassium iodide (KI) (Behari and Prakash, 2006). HG-AAS is one of the most reliable methods for the detection of arsenic in a sample. Both arsenic species (arsenic (III) and arsenic (V)) are differentially determined by using this procedure. This method includes the use of tetrahydroborate (reducing reagent), which has a greater tendency to react with arsenic (III) than arsenic (V) at higher pH, thus acting as a source of both hydride and reductant for arsenic (V) (Hung *et al*., 2004).

ICP-MS

The presence of arsenic in water samples can be analysed and detected by various chromatographic techniques coupled with atomic spectrometry. One of the frequently used techniques used for this purpose is online high-performance liquid chromatography (HPLC) coupled with ICP-MS. This method is found to be very advantageous in the determination of trace amounts of arsenic (V) and arsenic (III) in water. Yan *et al*. (1998) used a complex of

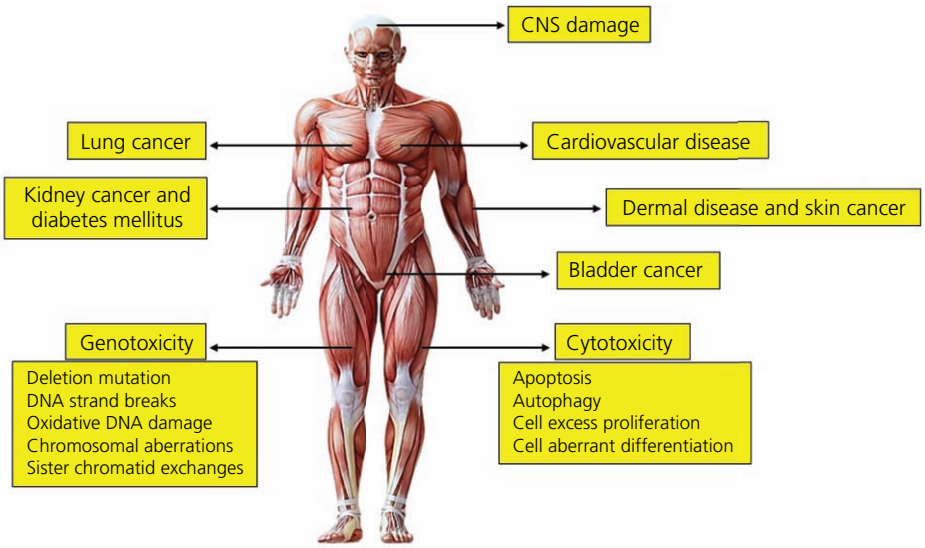

Figure 2. Arsenic poisoning in humans (extracted from Gym Guider (2019))

Offprint provided courtesy of www.icevirtuallibrary.com
Author copy for personal use, not for distribution

Table 2. Techniques for heavy metal detection and their advantages and limitations

Technique	Advantages	Limitations	References
AAS	Highly specific and sensitive, used for a variety of trace elements, high sample output, easy to use and handle, high accuracy, low cost	In a mixture, different lamps are required for different elements; lamps have a short lifespan; solution samples or volatile material is analysed; requires relatively large sample quantities (1–3 ml); is less sensitive towards refractory elements	Hung *et al*. (2004)
ICP	Precise, accurate and sensitive analytical tool with new developments in ICP-MS instrumentation such as a decreased size, a lower detection limit and more user-friendly software for control and hence used for multi-elemental ultra-trace detection and isotopic analysis	Detection of elements by this method may suffer from spectroscopic interference by the isotopes of elements present, which results in a lack of sensitivity. The poor sensitivity of ICP-MS is also due to its sensitivity to matrix effects. It also cannot provide information about the speciation of the sample	Kawabata *et al*. (1994), Larsen and Sturup (1994), Beauchemin (2008)
NAA	Sensitive and accurate analytical technique used for the detection of trace and ultra-trace amounts of elements present in the sample under investigation. Materials difficult to dissolve without sample preparation are easily analysed by using this method. In the absence of interference present in the sample, an LOD of trace elements in nanograms is detected with accuracy	This method is expensive because of its openness to a nuclear reactor. It has a long gyration and slow sample throughput. The sensitivity of NAA decreases in the presence of spectral interference from other elements such as sodium and bromine in the sample	Rajakovic and Rajakovic-Ognjanovic (2018)
XRF	Feasible, useful and non-destructive analytical technique for analysing a variety of hazardous materials and environmental samples (water, powder, soil etc.) due to the availability of efficient radioisotope source excitation combined with highly sensitive detectors and their associated electronics	It is slow, laborious and expensive. Samples taken for analysis are also limited due to the high cost of the laboratory	Melquiades and Appoloni (2004)
Electrochemical method	Versatile, simple, highly sensitive, rapid, repetitive and accurate, easy operation, inexpensive, low detection limit, compatible linear range and output, low power requirements; are of different types such as SWV, SPE, CV and DPSPE	Works in narrow temperature range; affected by humidity and temperature, which reduces the life of the electrode; sometimes other analytes interfere	Ndlovu *et al*. (2014), Stanković *et al*. (2020)

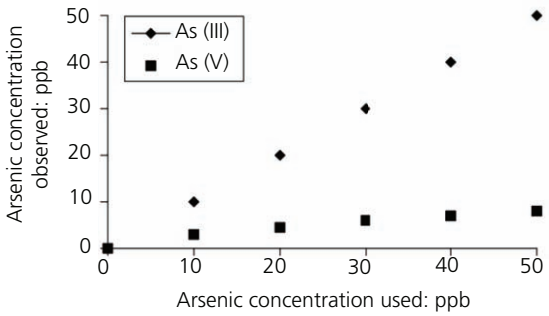

Figure 3. Estimation of arsenic (III) and arsenic (V) by AAS-VGA of water samples (Behari and Prakash, 2006)

arsenic (III) formed with pyrrolidine dithiocarbamate (chelating ligand) in nitric acid (HNO_3) (acidity range 0.01–0.7 M). This complex was found to have a significant role in the detection of arsenic (III). The determination of arsenic (V) is done by calculating the difference between the total inorganic arsenic and arsenic (III).

NAA

Detection of arsenic in various samples is also carried out by one of the most sensitive techniques known as NAA. The presence of other elements such as sodium (Na) and bromine (Br) in the sample under investigation greatly alters the sensitivity of arsenic determination by NAA, but under unhindered conditions – that is, in the absence of other elements – arsenic even in nanograms is detected with accuracy (1 ppb) by using this method (Mok *et al*., 1986).

XRF

Depending on the requirements in the area of analytical chemistry, there are a variety of spectrometric methods based on the principle of XRF, such as energy-dispersive XRF, wavelength-dispersive XRF and total reflection XRF (T-XRF), which differ in advantages and sensitivity (limit of detection (LOD) in ppb). In terms of the detection limits of metals in aqueous samples, the T-XRF technique is analogous or sometimes more effective (having a percentage recovery of >91% of the sample) than the other aforementioned techniques used for trace elemental detection (Sanyal *et al*., 2020).

Offprint provided courtesy of www.icevirtuallibrary.com
Author copy for personal use, not for distribution

Electrochemical methods

As stated earlier, arsenic exists in various organic and inorganic forms in natural water. The major forms of arsenic that primarily exist and have highly toxic effects are arsenic (III) and arsenic (V). Therefore, some methods or techniques are required for their determination. Many analytical techniques as discussed above are employed for their detection, but the results of these techniques are not in easy to process and analyse, practically because of the heavy, complex and expensive instrumentation used. As the operating systems used in these techniques are heavy, they are not carried to the field for analysis (Carrera *et al*., 2017; Jin *et al*., 2020). Alternatives to these methods that are simple, practical and selective and have results that are reliable and obtained in a shorter time and hence are employed largely in the area of research are the electrochemical methods (Carrera *et al*., 2017; Ramalechume *et al*., 2020). Electrochemical analysis has advantages such as low cost, high sensitivity, easy applications, low detection limit, appreciable electrode stability and reproducibility and long shelf life. The electrochemical method is a newer and more advanced technology applied for various purposes in research, energy generation and sensing (biosensing, chemical sensing, medical diagnosis, automotive and environmental monitoring) (Bobacka, 2020; Dziąbowska *et al*., 2018; Gebicki, 2016). Along with the electrolytic solution, the electrode material is an important component of electrochemical studies. The electrode material should be electrochemically active for sensing. Table 3 shows electrochemical techniques that use a variety of proposed electrode materials that are found to be effective for sensing arsenic with a minimum LOD.

Electrochemical methods for determination of arsenic in water

Various forms of electrochemical methods (Table 2) are employed for the successful determination and decontamination of a variety of heavy metals (arsenic in this work) from different strata of the environment including water (Bobacka, 2020; Mudila *et al*., 2018; Pujol *et al*., 2014). These techniques had their own benefits and limitations as discussed in the following sections.

Anodic stripping voltammetry (ASV)

One of the most frequently used analytical methods for measuring the metals present in an aqueous source is ASV, which is also used for the chemical speciation of metals. Many metals, both weakly and strongly complexed, can be determined directly by using this method. Trace metals even at low concentrations can be detected precisely and accurately in a shorter time (Jickells and Baker, 2005; Lan *et al*., 2012a). The basic principle involved in stripping voltammetry techniques for trace metal analysis is

Table 3. Electrode materials and LODs of different electrochemical methods

Electrode used	Electrolyte used	LOD	Concentration	Reference
SWV				
GENC	0.1 M Edta	0.047 ppb	—	Huang and Chen (2013)
EG-Bi	0.1 M acetate buffer solution (pH 5)	5 ppb	1–250 mg/l 1–50 mg/l	Mafa *et al*. (2016)
Gold–manganese ferrite ($MnFe_2O_4$)/GCE	0.1 M NaAc–HAc	3.37 ppb	0–500 ppb	Zhou *et al*. (2016)
EG-Bi/GCE	0.1 M nitric acid	5.0 ppb	—	Melquiades and Appoloni (2004)
Manganese ferrite/GCE	0.1 M HAC–NaAc (pH 5.0)	1.95 ppb	10–100 ppb	Zhou *et al*. (2015)
Tin (IV) oxide (SnO_2)/GCE	0.1 M NaAc–HAc	5.0 ppb	5–300 µg/l	Jiang *et al*. (2016)
Gold disc	1 M nitric acid	0.86 ppb	—	Toor and Bansod (2015)
GCE–AuNPs	0.1 M sulfuric acid	0.28 ppb	—	Idris *et al*. (2017)
ASV				
GCE/gold/CRV	0.1 M sodium chloride (NaCl)	0.8 µM	2.0–22.0 µM	Stanković *et al*. (2020)
Gold/GCE	0.5 M sulfuric acid	1.3 nM	0.05–1 ppb	Lan *et al*. (2012b)
GCE/gold	0.5 M sulfuric acid	0.9 ppb	1–50 ppb	Song and Swain. (2007)
SiNPs/SPCE	1 M potassium chloride (KCl)	6.2 ppb	5–30 µg/l	Ismail *et al*. (2020)
CV				
Ibu–AuPNFs–SPCE	1 M hydrochloric acid	0.018 ppb	—	Bodewig *et al*. (1982)
AuNPs/SPE	—	0.22 ppb	0.5–12 ppb	Trachioti *et al*. (2019)
Gold–copper/GCE	0.1 M HAc–NaAc	5.64 ppb	—	Yang *et al*. (2016)
Platinum/GCE	0.1 M aqueous potassium chloride	2.1 ppb	4.5–753 ppb	Dai and Compton (2006)
NPG-µE	1 M hydrochloric acid	0.62 µ/g	10–200 and 2–30 µg/l	Jaramillo *et al*. (2017)
GO–lead (IV) oxide (PbO_2)	1 M hydrochloric acid	10 nM	1.0 and 50.0 µg/l	Zhao and Liu (2018)
Gold/GO/leucine/Nafion	1 N hydrochloric acid	0.5 ppm	—	Liu *et al*. (2013)

AuPNFs, gold porous nanofibers; Edta, ethylenediaminetetraacetic acid; EG-Bi, exfoliated graphite–bismuth; GCE, glassy carbon electrode; GENC, gold-nanoparticle-embedded nafion composite; HAc, acetic acid; NaAc, sodium acetate; NPG-µE, nanoporous gold microelectrode; SiNPs, silica nanoparticles; SPE, screen-printed electrode

Offprint provided courtesy of www.icevirtuallibrary.com
Author copy for personal use, not for distribution

recording of the oxidation current (stripping current) against the scan potential obtained by electrochemical deposition of the metal on the electrode surface followed by oxidation of the metal back into the solution by a reverse potential scan, which results in a peak in the voltammogram shape as a signal.

ASV is a popular and powerful technique employed for the detection of trace amounts of arsenic in water. This method is based on the principle that, firstly, the trace metal is electrochemically deposited on the electrode surface at a particular reduction potential followed by the oxidation of the metal back into solution by a reverse potential scan. The evolution of hydrogen at the negative potential required for arsenic (III) deposition using a gold (Au) or platinum (Pt) electrode is a problem with ASV, and hence, the detection of arsenic by ASV is performed in highly acidic media. Due to the difference in deposition potential between arsenic (III) and arsenic (V) and due to low hydrogen overvoltage, only arsenic (III) can be subjected to quantitative analysis significantly (Luong *et al*., 2014; Mays and Hussam, 2009). The two prevailing forms of arsenic contamination in groundwater resources are inorganic arsenite (arsenic (III)) and arsenate (arsenic (V)). Most of the total arsenic present in various water resources is in inorganic form, out of which arsenic (III) is more toxic and more mobilised compared with arsenic (V). Luong *et al*. (2014) reported a detection limit of 0.09 ppb for arsenic (III) using a silver (Ag) disc electrode, which is lower than the LOD of 7.5 ppm obtained by using a platinum electrode.

Kopanica and Novotný (1998) studied the use of ASV in the determination of arsenic (III) in water by using gold or gold-plated carbon electrodes, where an LOD of 0.15 µg/l was reported for the gold electrode with a calibration curve in the concentration range of 0.2–250 µg/l arsenic. Carbon fibre ultra-microelectrodes modified with gold nanoparticles (AuNPs) were used to determine the arsenic in natural water by Carrera *et al*. (2017). AuNPs, owing to their small size, not only enhance the efficiency of the used electrode but also generate appreciable interaction between arsenic and gold, thus augmenting sensitivity (0.0176 nA µg/l), analysis and results (LOD = 0.9 µg/l). Because of less reactivity of arsenic (III) as compared with that of arsenic (V), ASV is more frequently used for determination of arsenic (III). Platinum, gold or gold-plated carbon-based electrodes in the presence of electrolytic solutions of hydrochloric acid and nitric acid are employed effectively for the detection of arsenic (III) using the ASV technique. The total concentration of both arsenic (III) and arsenic (V) is also determined by using this method, but this requires the reduction of arsenic (V) before the stripping analysis. A detection limit of 4 ppb for arsenic (III) and arsenic (V) was reported by Viltchinskaia *et al*. (1997) using a gold-plated graphite electrode as a sensor.

A fabricated gold ultra-microelectrode was effectively employed for the determination of arsenic (III) in water by using the linear sweep ASV technique. As the deposition potential increased from −0.2 to −0.5 V, there was also an increase in the value of the peak current due to an increase in the amount of arsenic (0) (As^0) deposited on the gold electrode. It was reported by Duong *et al*. (2015) that −0.5 V would be the optimum deposition potential and 100 s would be the optimum deposition time for the detection of arsenic (III) (LOD of 2 ppb). The ASV technique was used to determine the concentration of arsenic (V) at micrograms per litre levels on gold electrodes. Garlaschelli *et al*. (2017) reported an LOD of 1.1 µg/l and a limit of quantification (LOQ) of 3.7 µg/l for arsenic (V) using gold electrodes. Forsberg *et al*. (1975) reported an LOD of 0.02 ng/ml for arsenic (III) using both the ASV and differential pulse ASV (DPASV) techniques. They preferred gold electrodes over platinum electrodes for arsenic determination and stated that the sensitivity increases with an increase in the concentration of acid taken as a supporting electrolyte.

Lestarini and Ivandini (2019) reported the detection of both arsenic (III) and arsenic (V) on gold electrodes using ASV. From the results of their studies, they concluded that the deposition of arsenic (V) takes place at a very low negative potential because at high negative potentials, the evolution of hydrogen can occur, which can be adsorbed on the electrode surface, inhibiting arsenic (0) deposition. An LOD of 6.07 ppm for arsenic (V) and an LOD of 0.85 for arsenic (III) were reported in their studies using the ASV technique. The failure of previously reported studies to determine arsenic using silver electrodes was due to the oxidation of silver in the presence of the hydrochloric acid solution used in the ASV methods. Simm *et al*. (2005) reported that silver can also be used as a potent electrode for the determination of arsenic. Instead of hydrochloric acid solution, they used nitric acid, which shifts the silver oxidation peak largely to allow the arsenic stripping peak to become visible. The results of their studies are in good agreement with those obtained by using the gold electrodes for the detection of arsenic. They reported an LOD of 6.3×10^{-7} M for arsenic (III) using a silver electrode and ASV. The LOD of 1.8×10^{-7} M for arsenic (III) using a gold electrode was reduced to 1.8×10^{-7} M in the presence of optimised ultrasound while the sensitivity was increased by a factor of 15 for arsenic (III) using ASV.

Differential pulse voltammetry (DPV)

Also known as differential pulse polarography (DPP), this technique comprises applying amplitude potential pulses on a linear ramp potential. A base potential value is selected (applied to the electrode) at which there is no faradaic (redox) reaction taking place. The base potential is allowed to increase with time, between pulses with equal increments. The current generated is immediately measured before and after the pulse application and its end, and the difference between the two is recorded (Simões and Xavier, 2017).

The presence of a supporting electrolyte has been found to affect subjectively the detection of arsenic and other heavy metals by DPV/DPP. A 1 M hydrochloric acid solution is most efficiently used as an electrolyte for arsenic (III) detection by using the DPV method. The obtained polarogram consists of three peaks (−340, −580 and −720 mV) in acidic solutions, raised due to reduction of

Offprint provided courtesy of www.icevirtuallibrary.com
Author copy for personal use, not for distribution

arsenic (III), polarographic maximum and reduction of arsenic (0) to arsine (AsH_3). However, no peak corresponding to arsenic (V) is observed because of its electro-inactiveness in this range of applied potential (Gamboa *et al*., 2013). Another voltammetric method that is selective, sensitive and simple and is rapidly used for the detection of arsenic in natural water is DPASV. Yilmaz *et al*. (2009) used the DPASV technique for the detection of the total arsenic in natural water with a gold electrode in a hydrochloric acid solution. By using a gold electrode and a sample solution of 10 ml, an LOD of 0.5 µg/l was reported. An LOD of 0.02 ng/ml was reported by Bodewig *et al*. (1982) using gold as a working electrode over a platinum electrode for the detection of arsenic by DPASV. An increase in the concentration of acid (1 M solution of either hydrochloric acid or perchloric acid), which acts as the supporting electrolyte, increases the sensitivity of the experiment. This method reports an LOQ and an LOD of 8.9 and 2.7 µg/l, respectively. An LOD of 0.307 µg/l for arsenic (III) in aqueous sources using gold disc electrodes through the DPSAV technique was reported by Dang *et al*. (2019). Gold electrodes are preferred for electroanalysis because of the greater affinity of arsenic (III) towards gold and also because these electrodes have great durability and good reusability and show good sensitivity. These electrodes are also used for the simultaneous detection of both arsenic (III) and mercury (II) (Hg^{II}), and the LOD obtained for both these is below the value set by the WHO. Hema and Sundararajan (2020) reported the sensing of arsenic in water on a glassy carbon electrode (GCE) with nano-gold transformation in 0.5 M sulfuric acid (H_2SO_4) using the DPV technique. The deposition time and concentration of arsenic played a significant role in increasing the output peak current. An LOD of 0.9 ppb for arsenic was reported by Hema and Sundararajan (2020). Detection of inorganic arsenic in both standard and real samples by using gold-coated diamond electrodes is advantageous over the sue of gold and gold-coated carbon electrodes in terms of the peak shape and lower LOD. A comparative study of arsenic detection using gold-coated diamond and gold foil electrodes showed a better response in terms of narrower stripping peaks and a lower LOD for arsenic (III) detection using gold-coated diamond over a gold foil electrode. Song and Swain (2007), in their studies on the detection of the total inorganic arsenic (arsenic (III) and arsenic (V)) using DPASV on gold-coated, boron-doped, diamond thin-film electrodes, reported an LOD of 0.005 ppb for arsenic (III) and 0.08 ppb for arsenic (V).

Long and Nagaosa (2008) developed a method in which bismuth (Bi) is co-deposited onto a basal-plane pyrolytic graphite substrate to obtain a bismuth film electrode with enhanced sensitivity for the arsenic anodic peak. These bismuth film electrodes are employed in arsenic (III) detection using DPASV with an LOD of 0.012 µg/l and deposition time of 180 s. The detection of arsenic is carried out by many working electrodes modified with various types of chemical and biological materials. DNA is one of the most important biological materials fabricated with carbon paste electrodes and used for the detection of arsenic using DPV. However, this method is not frequently used due to the oxidation of DNA, which results in the reduction of the peak current with an increase in the arsenic (III) oxide (As_2O_3) concentration. Microphones at the interface of the gold electrodes are also employed for the detection of arsenic (III), which increases the sensitivity to 14 times greater than that of the bare gold electrodes. An LOD of 8×10^{-4} ppb using microphone-based gold electrodes for detection of arsenic (III) was reported (Gumpu *et al*., 2015). Metallic ruthenium nanoparticles (RuNPs), due to their conducting core and arsenic (III)-selective surface, show a reproducible and highly sensitive response for arsenic (III) detection in an aqueous medium. Gupta *et al*. (2016) reported an LOD of 0.1 ppb and reproducibility of 5.4% using RuNPs/GC electrodes for arsenic (III) using the DPV technique. Saha and Sarkar (2016) detected the presence of arsenic (III) at an LOD of 0.072 ppb with a GCE modified with a chitosan–iron (III) hydroxide ($Fe(OH)_3$) composite and the reducing agent [sc]l[sc]-cysteine by DPV.

Square-wave voltammetry (SWV)

The SWV is a large-amplitude differential technique that works on the principle that a waveform resulting from the superposition of a symmetrical square-wave pulse with the waveform that is constrained to lie between maximum and minimum voltage values is applied to the working electrode. The pulse amplitude, which is the potential of height (ΔE), varies with the potential step (E_{step}, in mV), and the τ duration (period) defines the shape of the potential current curve in SWV. Two currents are measured; the first current (I_1) is measured at the end of the forward square-wave pulse, and the second one (I_2) at the end of the return square-wave pulse. A large peak is obtained because of the differences in their signals, which are opposite in signs (Gamboa *et al*., 2013; Kim *et al*., 2017). In pulse-based voltammetric techniques such as SWV, a better detection limit and a clear signal-to-noise ratio are obtained compared with other expensive spectroscopic techniques used for the same purpose. Working electrodes of different materials (platinum, gold and silver) have been employed for the determination of arsenic (III) by SWV techniques. The most frequently used electrodes in such techniques are carbon electrodes, which include carbon nanotubes (CNTs). However, other metal ions and organic materials present in the sample under investigation have a strong affinity of interaction with the carbon substrate, which results in a decrease in the analytical performance of such electrodes. Therefore, modified electrodes with various materials are preferred over unmodified ones for the better analytical performance of the electrodes. In this regard, gold electrodes are preferred because of their non-toxic nature and strong interaction with arsenic (0) and arsenic (III) during the stripping and deposition processes. Also, they minimise the aforementioned limitation of carbon-based electrodes (Figure 4) (Trachioti *et al*., 2019). Kim *et al*. (2017), in their studies on the determination of arsenic (III) in aqueous solutions by SWV, used porous gold as a working electrode and reported a linear detection range of 0.1–14 ppb and an LOD of 0.1 ppb. Xiao *et al*. (2008), in their studies on the detection of

Offprint provided courtesy of www.icevirtuallibrary.com
Author copy for personal use, not for distribution

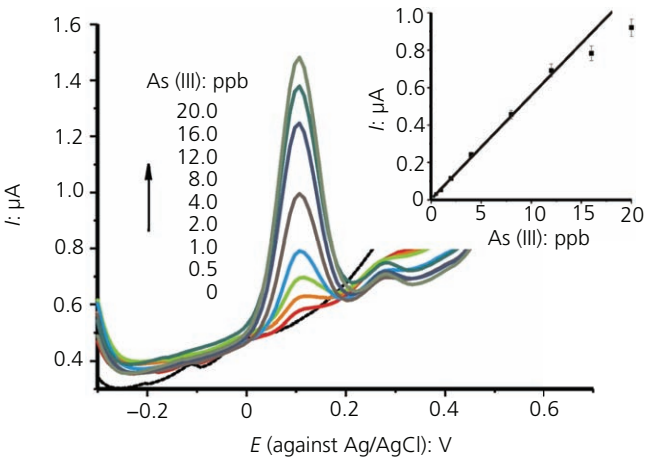

Figure 4. SWASV curve of arsenic (III) in the concentration range 0.5–20 ppb (Trachioti *et al.*, 2019)

arsenic in water by using SWV, reported an LOD of 0.1 ± 0.05 g/l and a sensitivity of 1985 µA/M when using carbon electrodes modified with AuNPs). Carbon-based nanotubes, having a large support area, offer good coverage for AuNPs (Kim *et al.*, 2017; Xiao *et al.*, 2008).

Gold/gold nanotextured electrode (GNE)-based sensors have a wide range of applications in various fields, including electrochemical sensing of heavy metals, because of their low cost, ease of preparation and high reproducibility. Babar *et al.* (2019) used an gold/GNE-based electrode for the electrochemical sensing of ultralow levels of arsenic (III) in water up to a 0.08 ppb concentration. Based on their studies, they reported an LOD of 0.1 ppb and a sensitivity of 39.54 µA/ppb.cm^2 for arsenic (III) using square-wave ASV (SWASV). GCEs modified with AuNPs (AuNPs/GCE) stabilised with novel citrate in 1 M hydrochloric acid are also promising electrodes for the electrochemical detection of arsenic (III) in an aqueous medium. Lan *et al.* (2012b) reported an LOD of 0.025 by SWASV (AuNPs/GCE) electrodes. In the recent era, much work is done on the electrochemical determination of arsenic (III) with increased sensitivity and low LOD. However, its determination still depends on noble metals such as gold in acidic solutions, resulting in an increase in the cost of the experiment and thus reducing its applications. Screen-printed carbon electrodes (SPCEs) modified with an iron (II,III) oxide (Fe_3O_4)–room-temperature ionic liquid (RTIL) composite shows better electrochemical responses than the ordinary used noble metals. An LOD of 8×10^{-4} ppb and a sensitivity of 4.91 µA/ppb were reported with iron (II,III) oxide–RTIL composites using SWASV (Gao *et al.*, 2013). Due to the remarkable adsorption tendency of iron (II,III) oxide towards arsenic (III), Sarnoa *et al.* (2017) developed an iron (II,III) oxide/reduced graphene oxide (rGO) composite fabricated on a GCE for efficient and enhanced sensitivity detection of arsenic (III) using SWASV and cyclic voltammetry (CV) in phosphate buffer solutions. An LOD of 0.38 ppb and a sensitivity of 2.6 µA/ppb were reported for arsenic (III) detection.

CV

CV has been used by researchers as an efficient and advanced tool in energy storage, catalysis and chemical sensing. CV has been employed by researchers for the detection of heavy metal ions and remediation of potable water, and many electrochemical sensors (electrodes) of different electroactive materials and hybrid forms have been employed in this direction. Generally, the electrode materials used in CV are cheap and have a wide potential window, a low LOD, good stability and reproducibility. The quantitative and qualitative information for the electrochemical reactions (reaction mechanisms, electrochemical kinetics etc.) which takes place in the electrochemical cell can be achieved by CV (Zhang *et al.*, 2013). A variety of electrode materials have been studied for the efficient determination of arsenic in aqueous sources using CV. Most studies include gold as a major component of electrodes used for arsenic sensing. AuNPs, owing to their size, shape, non-toxicity, high surface-to-area ratio, surface plasmon resonance and electrical and optical properties, have been used for sensing. Studies show that the detection of arsenic at low levels through a colour change is due to aggregation of AuNPs (Zhang *et al.*, 2013).

Gold/ibuprofen (Ibu) nanostructures were used to determine arsenic (III) using CV, and Nafion was used as a binder to achieve stability of the electrode material. In the concentration range of 0.1–1800 ppb with an LOD of 0.018 ppb (Figure 5), the electrode was found to be highly sensitive (Hassan *et al.*, 2012). Electrochemical detection of various trace elements can be successfully carried out. Determination of arsenic using CV was carried out in a lab, where the water samples from various sources (like spring, minerals, and tap water) were analysed by Nano Au-crystal violet (Au/CRV) film pasted over GCE and indium tin oxide glass electrode (ITO). From the results of the experiments, it was concluded that a weak response in the case of

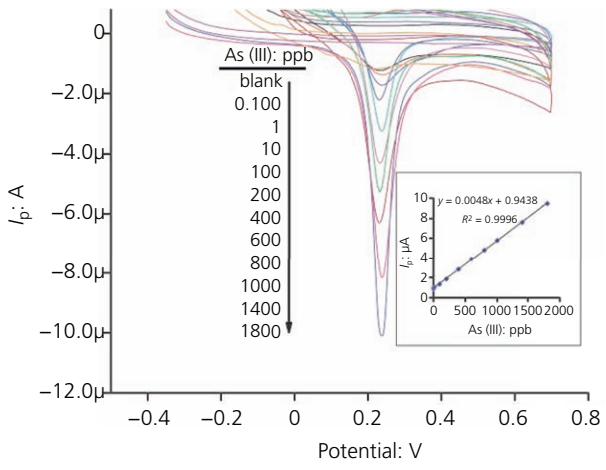

Figure 5. Calibration curves of arsenic (III) in the concentration range 0.1–1800 ppb (Hassan *et al.*, 2012)

Offprint provided courtesy of www.icevirtuallibrary.com
Author copy for personal use, not for distribution

using a CRV film-modified GCE and no response in the case of a bare GCE for arsenic (III) detection were obtained by this method. However, a remarkable response with a signal appearing at 0.5 V for the detection of arsenic (III) using a nano-gold–CRV film-modified GCE was obtained by CV. Detection limits of 0.20 µM in lab water samples, 0.28 µM in river water samples and 0.69 µM in spring water samples were reported by Rajkumar *et al*. (2011) when using a nano-gold-CRV film-modified GCE in CV. Toor *et al*. (2015) developed gold/iron (II,III) oxide nanocomposite-modified electrodes for the determination of trace levels of arsenic by CV. They reported that no oxidation peak was obtained for arsenic in the case of a bare GCE; however, an oxidation peak at 0.1 V was obtained when using gold-modified electrodes. Due to the good conductivity of iron (II,III) oxide, an increase in the oxidation peak (anodic and cathodic) was observed in the case of using iron (II,III) oxide-modified electrodes. In the presence of an electrolyte (1 M hydrochloric acid), modified electrodes with nanocrystals in a 1:1 ratio give two main oxidation peaks. The first peak obtained at 0.086 V is due to the oxidation of arsenic (0) to arsenic (III), and the second peak that appears at 0.740 V arises due to the oxidation of arsenic (III) to arsenic (V). However, the detection (by CV) of arsenic in water is not only limited to gold-based electrodes. Various other electrode materials alone or in combinations have been under investigation. Materials such as graphene, graphene oxide (GO), CNTs, metals and conducting polymers have been significantly employed (Daud *et al*., 2016; Ramesha and Sampath, 2011). Modified electrodes prepared by deposition of cobalt (Co) (shorter deposition time) on the bare surface of silicon-based platinum electrodes are quantitively used for the determination of arsenic. Daud *et al*. (2016) reported the electrochemical determination of arsenic using CV. From their studies, they concluded that due to the high tendency of cobalt to reduce arsenic, an increased peak current of arsenic (III) reduction was obtained in a voltammogram at different concentrations of arsenic (III). R^2 values of 0.9976 and 0.9815 in the regression equation of a modified platinum–cobalt electrode at deposition times of 10 and 20 s were obtained, respectively. The detection of arsenic (III) in real water samples with an LOD of 0.20 ppb using 0.20 M aqueous hydrochloric acid as an electrolyte by electrodepositing a composite film of electro-reduced GO (ErGO) and AuNPs by using CV was reported by Liu *et al*. (2013) (Figure 6). The electroanalysis of arsenic (III) is highly sensitive using ErGO–AuNPs/GCE compared with the electroanalysis using AuNPs/GCE. The high sensitivity using ErGO–AuNPs/GCE is mainly attributed to the high anodic stripping peak obtained at 0.06 V compared with the peak (0.05 V) in the case of AuNPs/GCE. rGO–AuNPs/GCE-based sensors were developed by using the electrodeposition process because of their precise surface area, better electron transfer ability and the low tendency of AuNPs to agglomerate, showing very good sensitivity for the detection of arsenic (III) using CV. The applications of these electrodes are also useful in monitoring the arsenic (III) concentrations in various environmental and food samples where an LOD of 0.08 µg/l was reported (Zhao and Liu, 2018). Platinum rotating disc electrodes were employed for the electrochemical detection of arsenic (III) in aqueous solutions using CV. Within a certain potential range (−0.6 to +1.5 V) an anodic

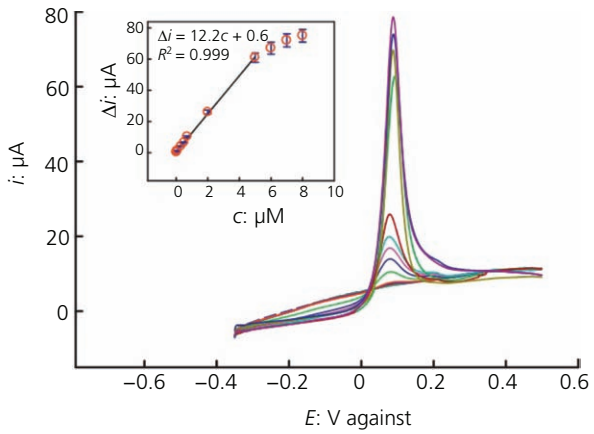

Figure 6. Anodic stripping linear sweep voltammetry responses at ERGO–AuNPs/GCE for arsenic (III) in 0.20 M aqueous hydrochloric acid. SCE, saturated calomel electrode (Liu *et al*., 2013)

stripping peak due to the oxidation of arsenic (III) to arsenic (V) is was obtained at 1.0 V. The current of the peak, which is not affected by the presence of arsenic (V), is directly proportional to the concentration of arsenic (III). Brusciotti and Duby (2007) reported an LOD of 7.5 ppm in their study of the detection of arsenic in acidic solutions. Pujol *et al*. (2014), in their studies of the detection of arsenic (III), reported an LOD of 0.48 µM using gold electrode citrate-capped with AuNPs and immobilised with a thiol group. A cobalt oxide NP-based sensor prepared from aqueous buffer solutions (pH = 7) at a potential of −1.1 to 1.1 V using CV when deposited on the surface of GCE serves as a potent electrode for the analysis of arsenic (III) in real samples containing different reducing compounds and other existing interferences in the sample matrix. Compared with other arsenic (III) sensors, cobalt oxide shows better sensitivity and stability towards the detection of arsenic (III) in an aqueous solution. Salimi *et al*. (2008) reported a detection limit of 11 nM for arsenic (III) using CV.

This review could be beneficial to the readers to gain important insights into detection of arsenic in aqueous sources by using electrochemical methods. Electrochemical techniques are certainly superior, fast, cost effective, accurate and time saving. Studies considered in the section headed 'Electrochemical methods for determination of arsenic in water' and Table 3 suggest that gold-based electrodes are primarily employed for arsenic determination due to their effective and low LOD (as low as 0.22 ppb). However, research indicates that various other materials and composition effectively detect the arsenic present in water sources, which makes them potential materials to achieve the target. Although electrochemical sensing is an advanced technique, it still has a few drawbacks. For example, (*a*) interference by other heavy metals (copper (Cu) mainly) that are oxidised at an equivalent potential as arsenic may intensify the peak current signal, which limits the applicability of electrochemical sensing in real samples (Huang and Chen, 2013).

Offprint provided courtesy of www.icevirtuallibrary.com
Author copy for personal use, not for distribution

(*b*) This technique has narrow sensitivity towards temperature and has a short shelf life.

Conclusion

A variety of contaminants present in potable water, including heavy metals, are responsible for causing numerous health hazards. Arsenic is studied as one of the chief heavy elements hazardous to the different categories of life on earth, including human beings. Arsenic as an important natural constituent of the earth's crust is chiefly found in mineral rocks, which are deposited through various natural processes such as desorption and dissolution, apart from burning of fossil fuels, arsenical agrochemicals, wood preservatives and so on, adding arsenic to groundwater through anthropogenic processes. Arsenic (III) and arsenic (V) are the toxic inorganic forms of arsenic in aqueous solutions, which are regulated at pH of 6–9 and are responsible for cancer, arsenicosis, vascular diseases and toxicity related to genes, cells and epidemiology. Because of these problems, it is necessary to detect and decontaminate arsenic contamination in potable water f. Out of many possible technologies, the electrochemical method of arsenic detection has been considered a significant technique, which is newer, robust, fast, accurate and less complicated. Moreover, techniques such as DPV, SWV, SCP, ASV and CV have kept the electrochemical method as a diverse and the most advanced technique for sensing. However, their performance is restricted with few limitations. Thus, lastly, it can be deduced that electrochemical techniques surely are next-generation techniques that can make the detection of heavy metals easy and rapid but these techniques are still in emerging stages and present a great challenge along with new opportunities for the research fraternity.

REFERENCES

Abbas G, Murtaza B, Bibi I *et al.* (2018) Arsenic uptake, toxicity, detoxification, and speciation in plants: physiological, biochemical, and molecular aspects. *International Journal of Environmental Research and Public Health* **15(1)**: article 59, https://doi.org/10.3390/ijerph15010059.

Babar NUA, Joya KS, Tayyab MA, Ashiq MN and Sohail M (2019) Highly sensitive and selective detection of arsenic using electrogenerated nanotextured gold assemblage. *ACS Omega* **4(9)**: 13645–13657, https://doi.org/10.1021/acsomega.9b00807.

Beauchemin D (2008) Inductively coupled plasma mass spectrometry. *Analytical Chemistry* **80(12)**: 4455–4486.

Behari JR and Prakash R (2006) Determination of total arsenic content in water by atomic absorption spectroscopy (AAS) using vapour generation assembly (VGA). *Chemosphere* **63(1)**: 17–21.

Bissen M and Frimmel FH (2003) Arsenic – a review. Part I: occurrence, toxicity, speciation, mobility. *Acta Hydrochimica et Hydrobiologica* **31(1)**: 9–18.

Bobacka J (2020) Electrochemical sensors for real-world applications. *Journal of Solid State Electrochemistry* **24(9)**: 2039–2040.

Bodewig FG, Valenta P and Nurnberg HW (1982) Trace determination of As(III) and As(V) in natural waters by differential pulse anodic stripping voltammetry. *Fresenius' Zeitschrift für Analytische Chemie* **311(3)**: 187–191.

Brusciotti F and Duby P (2007) Cyclic voltammetry study of arsenic in acidic solutions. *Electrochimica Acta* **52(24)**: 6644–6649.

Carrera P, Espinoza-Montero PJ, Fernández L, Romero H and Alvarado J (2017) Electrochemical determination of arsenic in natural waters using carbon fiber ultra-microelectrodes modified with gold nanoparticles. *Talanta* **166**: 198–206.

Chioma DL, Okechukwu ND and Reminus O (2021) Determination of heavy metals in salt water periwinkle and fresh water periwinkle in Port-Harcourt, Rivers-State. *Scholars International Journal of Chemistry and Material Sciences* **4(1)**: 1–5, https://doi.org/10.36348/sijcms.2021.v04i01.001.

Dai X and Compton RG (2006) Detection of As(iii) *via* oxidation to As(v) using platinum nanoparticle modified glassy carbon electrodes: arsenic detection without interference from copper. *Analyst* **131(4)**: 516–521, https://doi.org/10.1039/B513686E.

Dang VH, Yen PTH, Phong PH, Duy PK and Ha VTT (2019) Simultaneous determination of arsenic and mercury in water at trace levels by differential pulse anodic stripping voltammetry using a simple gold disk electrode. *Vietnam Journal of Chemistry* **57(3)**: 339–342.

Daud N, Kamaruddin NKN, Sulaiman S and Syono MI (2016) Electrochemical detection of arsenic using modified platinum–cobalt electrode. *International Journal of Chemical Engineering and Applications* **7(4)**: 264–268.

Ding R, Cheong YH, Ahamed A and Lisak G (2021) Heavy metals detection with paper-based electrochemical sensors. *Analytical Chemistry* **93(4)**: 1880–1888.

Duong QN, Le NV, Le TD *et al.* (2015) Determination of inorganic arsenic As(III) in water by linear sweep anodic stripping voltammetry using gold ultra-microelectrode array. *ECS Transactions* **66(27)**: 25–32.

Dziąbowska K, Czaczyk E and Nidzworski D (2018) Application of electrochemical methods in biosensing technologies. In *Biosensing Technologies for the Detection of Pathogens – A Prospective Way for Rapid Analysis* (Rinken T and Kivirand K (eds)). IntechOpen, London, UK, https://doi.org/10.5772/intechopen.72175.

Farooq MA, Islam F, Ali B *et al.* (2016) Arsenic toxicity in plants: cellular and molecular mechanisms of its transport and metabolism. *Environmental and Experimental Botany* **132**: 42–52.

Forsberg G, O'Laughlin JW, Megargle RG and Koirtyihann SR (1975) Determination of arsenic by anodic stripping voltammetry and differential pulse anodic stripping voltammetry. *Analytical Chemistry* **47(9)**: 1586–1592.

Gamboa JC, Cornejo L, Acarapi J and Squella JA (2013) Determination of As (III) by differential pulse polarography in waters of Camarones Area, Chile. *Journal of the Chilean Chemical Society* **58(4)**: 2031–2034.

Gao C, Yu XY, Xiong SQ, Liu JH and Huang XJ (2013) Electrochemical detection of arsenic(III) completely free from noble metal: Fe_3O_4 microspheres-room temperature ionic liquid composite showing better performance than gold. *Analytical Chemistry* **85(5)**: 2673–2680.

Garlaschelli F, Alberti G, Fiol N and Villaescusa I (2017) Application of anodic stripping voltammetry to assess sorption performance of an industrial waste entrapped in alginate beads to remove As(V). *Arabian Journal of Chemistry* **10**: S1014–S1021.

Gebicki J (2016) Application of electrochemical sensors and sensor matrixes for measurement of odorous chemical compounds. *TrAC Trends in Analytical Chemistry* **77**: 1–13.

Gleick PH (2002) *Dirty Water: Estimated Deaths from Water-related Disease 2000–2020*. Pacific Institute for Studies in Development, Environment, and Security, Oakland, CA, USA. See https://pacinst.org/wp-content/uploads/2002/08/water_related_deaths_report.pdf (accessed 01/10/2022).

Gumpu MB, Sethuraman S, Krishnan UM and Rayappan JBB (2015) A review on detection of heavy metal ions in water – an electrochemical approach. *Sensors and Actuators B: Chemical* **213**: 515–533.

Gupta R, Gamare JS, Pandey AK, Tyagi D and Kamat JV (2016) Highly sensitive detection of arsenite based on its affinity toward ruthenium nanoparticles decorated on glassy carbon electrode. *Analytical Chemistry* **88(4)**: 2459–2465.

Offprint provided courtesy of www.icevirtuallibrary.com
Author copy for personal use, not for distribution

Gwimbi P, George M and Ramphalile M (2019) Bacterial contamination of drinking water sources in rural villages of Mohale Basin, Lesotho: exposures through neighbourhood sanitation and hygiene practices. *Environmental Health and Preventive Medicine* **24(1)**: article 33, https://doi.org/10.1186/s12199-019-0790-z.

Gym Guider (2019) *Complete Workout Using the Simplicity of Only Your Bodyweight – GymGuider.Com*. Pinterest, San Francisco, CA, USA. See https://www.pinterest.com/pin/66709638217935345 (accessed 02/10/2022).

Hassan SS, Sirajuddin, Solangi AR *et al.* (2012) Nafion stabilized ibuprofen–gold nanostructures modified screen printed electrode as arsenic(III) sensor. *Journal of Electroanalytical Chemistry* **682**: 77–82.

Hema R and Sundararajan M (2020) Development, analysis and evaluation of arsenic (III) sensor. *European Journal of Molecular & Clinical Medicine* **7(4)**: 2533–2551.

Howard G (2003) *Arsenic, Drinking-water and Health Risk Substitution in Arsenic Mitigation: A Discussion Paper*. World Health Organization, Geneva, Switzerland. See https://www.who.int/news-room/fact-sheets/detail/arsenic (accessed 21/09/2022).

Huang JF and Chen HH (2013) Gold-nanoparticle-embedded Nafion composite modified on glassy carbon electrode for highly selective detection of arsenic(III). *Talanta* **116**: 852–859.

Hung DQ, Nekrassova O and Compton RG (2004) Analytical methods for inorganic arsenic in water: a review. *Talanta* **64(2)**: 269–277.

Hussam A (2013) Potable water: nature and purification. In *Monitoring Water Quality: Pollution Assessment, Analysis, and Remediation* (Ahuja S (ed.)). Elsevier. Amsterdam, the Netherlands, pp. 261–283.

IARC WGECRH (International Agency for Research on Cancer Working Group on the Evaluation of Carcinogenic Risks to Humans) (2012) Arsenic and arsenic compounds. In *Arsenic, Metals, Fibres, and Dusts*. IARC, Lyon, France, IARC Monographs on the Evaluation of Carcinogenic Risks to Humans No. 100C, pp. 41–93. See https://www.ncbi.nlm.nih.gov/books/NBK304380/ (accessed 01/10/2022).

Idris AO, Mafa JP, Mabuba N and Arotiba OA (2017) Nanogold modified glassy carbon electrode for the electrochemical detection of arsenic in water. *Russian Journal of Electrochemistry* **53(2)**: 170–177.

Ismail S, Yusof NA, Abdullah J and Abd Rahman SF (2020) Electrochemical detection of arsenite using a silica nanoparticles-modified screen-printed carbon electrode. *Materials* **13(14)**: article 3168, https://doi.org/10.3390/ma13143168.

Jaramillo DXO, Sukeri A, Saravia LPH, Espinoza-Montero PJ and Bertotti M (2017) Nanoporous gold microelectrode: a novel sensing platform for highly sensitive and selective determination of arsenic (III) using anodic stripping voltammetry. *Electroanalysis* **29(10)**: 2316–2322.

Jiang TJ, Guo Z, Liu JH and Huang XJ (2016) Gold electrode modified with ultrathin SnO_2 nanosheets with high reactive exposed surface for electrochemical sensing of As(III). *Electrochimica Acta* **191**: 142–148.

Jickells TD and Baker AR (2005) Seawater – inorganic compounds. In *Encyclopedia of Analytical Science*, 2nd edn. (Worsfold P, Townshend A and Poole C (eds)) Elsevier Amsterdam, the Amsterdam, pp. 283–289.

Jin M, Yuan H, Liu B *et al.* (2020) Review of the distribution and detection methods of heavy metals in environment. *Analytical Methods* **12(48)**: 5747–5766, https://doi.org/10.1039/d0ay01577f.

Kapaj S, Peterson H, Liber K and Bhattacharya P (2006) Human health effects from chronic arsenic poisoning – a review. *Journal of Environmental Science and Health, Part A* **41(10)**: 2399–2428.

Kawabata K, Inoue Y, Takahashi H and Endo G (1994) Determination of arsenic species by inductively coupled plasma mass spectrometry with ion chromatography. *Applied Organometallic Chemistry* **8(3)**: 245–248.

Khambete AK (2019) *When Water Kills*. India Water Portal, Bangalore, India. See https://www.indiawaterportal.org/faqs/waterborne#:~:text=Waterborne%20diseases%20such%20as%20cholera,viral%20hepatitis%2C%20typhoid%20and%20cholera (accessed 21/09/2022).

Kim J, Han S and Kim Y (2017) Electrochemical detection of arsenic(III) using porous gold via square wave voltammetry. *Korean Journal of Chemical Engineering* **34(7)**: 2096–2098.

Kopanica M and Novotný L (1998) Determination of traces of arsenic(III) by anodic stripping voltammetry in solutions, natural waters and biological material. *Analytica Chimica Acta* **368(3)**: 211–218, https://doi.org/10.1016/S0003-2670(98)00220-7.

Lan Y, Luo H, Ren X, Wang Y and Liu Y (2012a) Anodic stripping voltammetric determination of arsenic(III) using a glassy carbon electrode modified with gold–palladium bimetallic nanoparticles. *Microchimica Acta* **178(1–2)**: 153–161.

Lan Y, Luo H, Ren X, Wang Y and Wang L (2012b) Glassy carbon electrode modified with citrate stabilized gold nanoparticles for sensitive arsenic (III) detection. *Analytical Letters* **45(10)**: 1184–1196.

Larsen EH and Sturup S (1994) Carbon-enhanced inductively coupled plasma mass spectrometric detection of arsenic and selenium and its application to arsenic speciation. *Journal of Analytical Atomic Spectrometry* **9(10)**: 1099–1105.

Lestarini DT and Ivandini TA (2019) Electrochemical detection of As^{3+} and As^{5+} by anodic stripping voltammetry at a gold electrode. *IOP Conference Series: Materials Science and Engineering* **496**: article 012030, https://doi.org/10.1088/1757-899x/496/1/012030.

Liu Y, Huang Z, Xie Q *et al.* (2013) Electrodeposition of electroreduced graphene oxide–Au nanoparticles composite film at glassy carbon electrode for anodic stripping voltammetric analysis of trace arsenic (III). *Sensors and Actuators B: Chemical* **188**: 894–901.

Long J and Nagaosa Y (2008) Determination of trace arsenic(III) by differential-pulse anodic stripping voltammetry with *in-situ* plated bismuth-film electrode. *International Journal of Environmental Analytical Chemistry* **88(1)**: 51–60.

Luong JHT, Lam E and Male KB (2014) Recent advances in electrochemical detection of arsenic in drinking and ground waters. *Analytical Methods* **6(16)**: 6157–6169.

Luvhimbi N, Tshitangano TG, Mabunda JT, Olaniyi FC and Edokpayi JN (2022) Water quality assessment and evaluation of human health risk of drinking water from source to point of use at Thulamela municipality, Limpopo Province. *Scientific Reports* **12**: 1–17.

Mafa PJ, Idris AO, Mabuba N and Arotiba OA (2016) Electrochemical co-detection of As(III), Hg(II) and Pb(II) on a bismuth modified exfoliated graphite electrode. *Talanta* **153**: 99–106.

Mahurpawar M (2015) Effects of heavy metals on human health. *International Journal of Research – Granthaalayah* **3(9)**: 1–7.

Mandal P (2017) An insight of environmental contamination of arsenic on animal health. *Emerging Contaminants* **3(1)**: 17–22.

Mays DE and Hussam A (2009) Voltammetric methods for determination and speciation of inorganic arsenic in the environment – a review. *Analytica Chimica Acta* **646(1–2)**: 6–16.

Mazumder DN, Ghosh A, Majumdar K *et al.* (2010) Arsenic contamination of ground water and its health impact on population of district of Nadia, West Bengal, India. *Indian Journal of Community Medicine* **35(2)**: 331–338, https://doi.org/10.4103/0970-0218.66897.

Melquiades FL and Appoloni CR (2004) Application of XRF and field portable XRF for environmental analysis. *Journal of Radioanalytical and Nuclear Chemistry* **262(2)**: 533–541.

Mok WM, Shah NK and Wai CM (1986) Extraction of arsenic(III) and arsenic(V) from natural waters for neutron activation analysis. *Analytical Chemistry* **58(1)**: 110–113.

Mudila H, Prasher P, Kumar M *et al.* (2018) An insight into cadmium poisoning and its removal from aqueous sources by graphene adsorbents. *International Journal of Environmental Health Research* **29(1)**: 1–21, https://doi.org/10.1080/09603123.2018.1506568.

Ndlovu T, Mamba BB, Sampath S, Krause RW and Arotiba OA (2014) Voltammetric detection of arsenic on a bismuth modified exfoliated graphite electrode. *Electrochimica Acta* **128**: 48–53.

Offprint provided courtesy of www.icevirtuallibrary.com
Author copy for personal use, not for distribution

Nriagu J, Bhattacharya P, Mukherjee A *et al.* (2007) Arsenic in soil and groundwater: an overview. In *Arsenic in Soil and Groundwater Environment* (Bhattacharya P, Mukherjee A, Bundschuh J, Zevenhoven R and Loeppert R (eds)). Elsevier, Amsterdam, the Netherlands, pp. 3–60.

Obinnaa IB and Ebere EC (2019) A review: water pollution by heavy metal and organic pollutants: brief review of sources, effects and progress on remediation with aquatic plants. *Analytical Methods in Environmental Chemistry Journal* **2(3)**: 5–38.

Palansooriya KN, Yang Y, Tsang YF *et al.* (2019) Occurrence of contaminants in drinking water sources and the potential of biochar for water quality improvement: a review. *Critical Reviews in Environmental Science and Technology* **50(6)**: 549–611.

Pooja D, Kumar P, Singh P and Patil S (eds) (2020) *Sensors in Water Pollutants Monitoring: Role of Material*. Springer, Singapore.

Pujol L, Evrard D, Groenen-Serrano K *et al.* (2014) Electrochemical sensors and devices for heavy metals assay in water: the French groups' contribution. *Frontiers in Chemistry* **2**: article 19, https://doi.org/10.3389/fchem.2014.00019.

Puri A and Kumar M (2012) A review of permissible limits of drinking water. *Indian Journal of Occupational and Environmental Medicine* **16(1)**: 40–44, https://doi.org/10.4103/0019-5278.99696.

Rajakovic L and Rajakovic-Ognjanovic V (2018) Arsenic in water: determination and removal. *Arsenic – Analytical and Toxicological Studies* (Stoytcheva M and Zlatev R (eds)). IntechOpen, London, UK, https://doi.org/10.5772/intechopen.75531.

Rajkumar M, Thiagarajan S and Chen SM (2011) Electrochemical detection of arsenic in various water samples. *International Journal of Electrochemical Science* **6**: 3164–3177.

Ramalechume C, Keerthana S and Swamidoss CMA (2020) Electrochemical detection of heavy metals using carbon quantum dots modified with metal oxides. *Materials Today: Proceedings*, https://doi.org/10.1016/j.matpr.2020.10.693.

Ramesha GK and Sampath S (2011) In-situ formation of graphene–lead oxide composite and its use in trace arsenic detection. *Sensors and Actuators B: Chemical* **160(1)**: 306–311.

Saha S and Sarkar P (2016) Differential pulse anodic stripping voltammetry for detection of As (III) by chitosan–$Fe(OH)_3$ modified glassy carbon electrode: a new approach towards speciation of arsenic. *Talanta* **158**: 235–245.

Saha JC, Dikshit AK, Bandyopadhyay M and Saha KC (2014) *A Review of Arsenic Poisoning and Its Effects on Human Health*. US Environmental Protection Agency, Washington, DC, USA. See https://www.epa.gov/sites/default/files/2014-03/documents/a_review_of_arsenic_poisoning_and_its_effects_on_human_health_3v.pdf (accessed 21/09/2022).

Salimi A, Mamkhezri H, Hallaj R and Soltanian S (2008) Electrochemical detection of trace amount of arsenic(III) at glassy carbon electrode modified with cobalt oxide nanoparticles. *Sensors and Actuators B: Chemical* **129(1)**: 246–254.

Sankhla MS, Kumari M, Nandan M, Kumar R and Agrawal P (2016) Heavy metals contamination in water and their hazardous effect on human health – a review. *International Journal of Current Microbiology and Applied Sciences* **5(10)**: 759–566.

Sanyal K, Chappa S, Bahadur J, Pandey AK and Mishra NL (2020) Arsenic quantification and speciation at trace levels in natural water samples by total reflection X-ray fluorescence after pre-concentration with *N*-methyl-d-glucamine functionalized quartz supports. *Journal of Analytical Atomic Spectrometry* **35(11)**: 2770–2778.

Sarnoa M, Scudieria C, Longoa A and Ciambellia P (2017) Graphene oxide as a novel nanoplatform for electrochemical detection of arsenic (III). *Chemical Engineering Transactions* **60**: 13–18.

Schweitzer L and Noblet J (2018) Water contamination and pollution. In *Green Chemistry: An Inclusive Approach* (Török B and Dransfield T (eds)). Elsevier, Amsterdam, the Netherlands, pp. 261–290, https://doi.org/10.1016/b978-0-12-809270-5.00011-x.

Shankar S, Shanker U and Shikha (2014) Arsenic contamination of groundwater: a review of sources, prevalence, health risks, and strategies for mitigation. *The Scientific World Journal* **2014**: article 304524, https://doi.org/10.1155/2014/304524.

Sharma S and Bhattacharya A (2017) Drinking water contamination and treatment techniques. *Applied Water Science* **7(13)**: 1043–1067, https://doi.org/10.1007/s13201-016-0455-7.

Shy CM (1985) Chemical contamination of water supplies. *Environmental Health Perspectives* **62**: 399–406, https://doi.org/10.1289/ehp.8562399.

Simm AO, Banks CE and Compton RG (2005) The electrochemical detection of arsenic(III) at a silver electrode. *Electroanalysis* **17(19)**: 1727–1733.

Simões FR and Xavier MG (2017) Electrochemical sensors. In *Nanoscience and Its Applications* (da Róz AL, Ferreira M, Leite FDL and Oliveira ON (eds)). William Andrew, Kidlington, UK, pp. 155–178.

Song Y and Swain GM (2007) Development of a method for total inorganic arsenic analysis using anodic stripping voltammetry and a Au-coated, diamond thin-film electrode. *Analytical Chemistry* **79(6)**: 2412–2420.

Stanković A, Kajinić Z, Turkalj JV *et al.* (2020) Voltammetric determination of arsenic with modified glassy carbon electrode. *Electroanalysis* **32(5)**: 1043–1051, https://doi.org/10.1002/elan.201900666.

Tekere M (2019) Microbial bioremediation and different bioreactors designs applied. *Biotechnology and Bioengineering* (Jacob-Lopes E and Zepka LQ (eds)). IntechOpen, London, UK, https://doi.org/10.5772/intechopen.83661.

Toor SK, Devi P and Bansod BKS (2015) Electrochemical detection of trace amount of arsenic (III) at glassy carbon electrode modified with Au/Fe_3O_4 nanocomposites. *Aquatic Procedia* **4**: 1107–1113.

Trachioti MG, Karantzalis AE, Hrbac J and Prodromidis MI (2019) Low-cost screen-printed sensors on-demand: instantly prepared sparked gold nanoparticles from eutectic Au/Si alloy for the determination of arsenic at the sub-ppb level. *Sensors and Actuators B: Chemical* **281**: 273–280, https://doi.org/10.1016/j.snb.2018.10.112.

Ventura-Lima J, Bogo MR and Monserrat JM (2011) Arsenic toxicity in mammals and aquatic animals: a comparative biochemical approach. *Ecotoxicology and Environmental Safety* **74(3)**: 211–218.

Viltchinskaia EA, Zeigman LL, Garcia DM and Santos PF (1997) Simultaneous determination of mercury and arsenic by anodic stripping voltammetry. *Electroanalysis* **9(8)**: 633–640.

Wasewar KL, Singh S and Kansal SK (2020) Process intensification of treatment of inorganic water pollutants. In *Inorganic Pollutants in Water* (Devi P, Singh P and Kansal SK (eds)). Elsevier, Amsterdam, the Netherlands, pp. 245–271.

Xiao L, Wildgoose GG and Compton RG (2008) Sensitive electrochemical detection of arsenic (III) using gold nanoparticle modified carbon nanotubes via anodic stripping voltammetry. *Analytica Chimica Acta* **620(1–2)**: 44–49.

Yan XP, Kerrich R and Hendry MJ (1998) Determination of (ultra)trace amounts of arsenic(III) and arsenic(V) in water by inductively coupled plasma mass spectrometry coupled with flow injection on-line sorption preconcentration and separation in a knotted reactor. *Analytical Chemistry* **70(22)**: 4736–4742.

Yang M, Guo Z, Li LN *et al.* (2016) Electrochemical determination of arsenic (III) with ultra-high anti-interference performance using Au–Cu bimetallic nanoparticles. *Sensors and Actuators B: Chemical* **231**: 70–78.

Yilmaz S, Baba B, Baba A, Yagmur S and Citak M (2009) Direct quantitative determination of total arsenic in natural hotwaters by anodic stripping voltammetry at the rotating lateral gold electrode. *Current Analytical Chemistry* **5(1)**: 29–34.

Zhang J, Zhang H, Wu J and Zhang J (2013) Techniques for PEM fuel cell testing and diagnosis. In *PEM Fuel Cell Testing and Diagnosis*. Elsevier Science, Burlington, MA, USA, pp. 81–119.

Offprint provided courtesy of www.icevirtuallibrary.com
Author copy for personal use, not for distribution

Zhao G and Liu G (2018) Electrochemical deposition of gold nanoparticles on reduced graphene oxide by fast scan cyclic voltammetry for the sensitive determination of As(III). *Nanomaterials* **9(1)**: article 41.

Zhou SF, Han XJ, Fan HL, Zhang QX and Liu YQ (2015) Electrochemical detection of As(III) through mesoporous $MnFe_2O_4$ nanocrystal clusters by square wave stripping voltammetry. *Electrochimica Acta* **174**: 1160–1166.

Zhou S, Han X, Fan H and Liu Y (2016) Electrochemical sensing toward trace As(III) based on mesoporous $MnFe_2O_4$/Au hybrid nanospheres modified glass carbon electrode. *Sensors* **16(6)**: article 935.

How can you contribute?

To discuss this paper, please submit up to 500 words to the editor at journals@ice.org.uk. Your contribution will be forwarded to the author(s) for a reply and, if considered appropriate by the editorial board, it will be published as a discussion in a future issue of the journal.

Bulgarian Chemical Communications, Volume 55, Special Issue A (pp. 37-43) 2023 DOI: 10.34049/bcc.55.A.0005

Comparative study on the electrochemical performance of PPY/GO binary and PPY-GO/ZnO ternary nanocomposites

G. Singh, Nisha, A. Kumar, H. Mudila*

Department of Chemistry, Lovely Professional University, Phagwara, Punjab-144411, India

Received: April 03, 2023; Revised: April 27, 2023

PPY/GO binary nanocomposites (PGs) and PPY-GO/ZnO ternary nanocomposites (PGZs) as electrode material were synthesized *via* the *ex-situ* method. The PGs, prepared by varying the proportions of GO (%w/w) in PPY, were characterized by FTIR, XRD, TGA, and electrochemical measurements. The PGs were analyzed by cyclic voltammetry (CV) for their electrochemical performance. The binary composite (PG5) having the highest specific capacitance (Cs=391.3 F/g) value was preferred for the preparation of ternary composites, i.e., PGZs with ZnO in different ratios (%w/w) by the *ex-situ* method. The highest specific capacitance of 352.1 F/g was obtained for PGZ-1 at 1 mV/s which is lower than for its binary counterpart (PG5) but was higher than those of ZnO, PPY, and GO. The incorporation of GO has enhanced the electrochemical performance of PGs, however, the encapsulation of ZnO in PG was found to decrease the electrochemical response of PGZs. The result suggested this to occur due to the disorder caused in the PPY chains by ZnO.

Keywords: Conducting polymer; Composites; Capacitance; Graphene oxide; Transition metal oxide, Clean energy.

INTRODUCTION

Conventional energy sources are largely employed to encounter the need for the energy required in various aspects of life. The use of these energy sources at a tremendous rate is the major contributor to climate changes such as air pollution, global warming, etc. [1]. To overcome these issues there is a great need to develop energy techniques that are readily available and environmentally friendly. Among the various energy sources, electrochemical supercapacitors are considered the potent candidates widely used in power inventors, electrochemical actuators, power supplies, etc. The mechanism of charge storage in supercapacitors is based on (a) electrochemical double-layer capacitors (EDLC) or (b) fast and reversible redox reactions that take place on the interface of electrodes and electrolytes (pseudo capacitors) [1, 2]. Various types of electroactive material, *viz*., carbonaceous material, conducting polymers (CPs), and transition metal oxides (TMOs) are employed as the electrode material in supercapacitors. CPs are appropriate as an electrode because of their high porosity, storage ability, and reversibility but they lack cyclic stability and slow charging-discharging rate. These drawbacks can be improved by entering structural changes in CPs by hybridizing them with other electroactive materials [2-4]. CPs with carbonaceous material like graphene oxide (GO) show a synergetic effect and produce an electrode with high capacitance behavior [5]. TMOs having pseudo capacitive behavior act as a filler between the CPs and carbonaceous material that may improve the electrolyte-electrode interaction resulting in the fast diffusion of ions and hence improving the capacitive behavior of the electrode material [3, 6]. However, some studies show a decrease in performance with the addition of TMO in the matrix [4]. Nowadays a variety of CPs (polypyrrole, polyaniline, etc.) are hybridized with carbonaceous material (GO, rGO, etc.), and TMOs (ZnO, V_2O_5, and others) to form ternary composites used in supercapacitors for the storage of the electrochemical energy [7, 8]. This work presents the fabrication of PPY/GO binary nanocomposites (PGs) and PPY-GO/ZnO ternary nanocomposites (PGZs). The as-fabricated PGs and PGZs were further studied for their electrochemical performance by cyclic voltammetry (CV).

MATERIALS AND METHODS

Materials

Monomer pyrrole (PY, >99%, Spectrochem), graphite powder, potassium permanganate ($KMnO_4$), sulfuric acid (H_2SO_4), hydrogen peroxide (H_2O_2), and hydrochloric acid (HCl) were acquired from Loba Chemie. Ferric chloride ($FeCl_3$), and PVDF (polyvinylidene fluoride) were from Sigma Aldrich, N- cetyl -N, N, N- trimethyl ammonium bromide (CTAB), and ascorbic acid were obtained from S D Fine Chem. Ltd.

* To whom all correspondence should be sent:
E-mail: harismudila@gmail.com

© 2023 Bulgarian Academy of Sciences, Union of Chemists in Bulgaria

Preparation of polypyrrole (PPY) and graphene oxide (GO)

Polypyrrole (PPY) was prepared by the chemical oxidative polymerization method mentioned by Mudila *et al. 2013* which involves the use of pyrrole monomer, CTAB surfactant solution, and freshly prepared oxidant solution of $FeCl_3$ [7]. The preparation of GO was carried out by the modified Hummers method as mentioned by Song *et al. 2014* [9].

Preparation of polypyrrole/graphene oxide (PG) binary composites

The preparation of PPY/GO composite in different ratios (wt %, in mg) was carried out by the *ex-situ* method. Requisite amounts of PPY and GO were taken in ethanol (Table 1) followed by mechanical mixing through sonication for 30 minutes to acquire homogeneity. The resultant mixture was then dried in an oven at 60°C.

Table 1. Corresponding ratio, amount, and names of PPY and GO composites

Material	Ratio					
	1: ¼	1: 1/2	1: 3/4	1: 1	1: 2	1: 3
PPY (mg)	100	100	100	100	100	100
GO (mg)	25	50	75	100	200	300
Composite Name (PG)	PG1	PG2	PG3	PG4	PG5	PG6

Preparation of PPY-GO/ZnO (PGZ) ternary composite

Like the method followed for preparation of PGs, the PGZ was prepared (Table 2) with requisite amounts of PPY/GO and ZnO.

Table 2. Corresponding ratio, amount, and codes of PG (PPY-GO) and ZnO composites

Material	Ratio					
	1: 1/4	1: ½	1: 3/4	1: 1	1: 2	1: 3
PPY/GO (mg)	100	100	100	100	100	100
ZnO (mg)	25	50	75	100	200	300
Composite name (PGZ)	PGZ 1	PGZ 2	PGZ 3	PGZ 4	PGZ 5	PGZ 6

Preparation of the working electrodes

Electroactive material (0.05 g), and graphite (0.005 g) were mixed with the binder solution (PVDF in NMP, 5 g/dL), followed by ultra-sonication for 30 minutes and then applied on 1 cm^2 area of stainless steel (304-SS) sheet which was allowed to dry in a vacuum oven for 2 hours at 100°C. This SS sheet with a mass thickness of ~0.01 g on its surface functions as a working electrode [1, 9].

RESULTS AND DISCUSSION

FTIR Spectra

FTIR spectra of the samples were recorded in the range of 400-4000 cm^{-1} (Fig. 1 (a-e)). In the FTIR spectra of PPY the bands at 1631, 1543, and 1415 cm^{-1} are due to stretching of C=N, C=C, and C-N bonds. A broad band at 3300-3500 cm^{-1} is due to stretching of N-H bond. The bands at 1039 cm^{-1}, 1300 $cm^{-1}$and 884 cm^{-1} are due to in-plane and out-of-plane deformation of C-H, C-N and C-H bonds. (Fig. 1a) [10, 11]. In the case of GO, the band at 3272 cm^{-1}corresponds to O-H stretching. The vibrations at 1714 and 1585 cm^{-1} are due to the carbonyl (C=O) and aromatic C=C bonds, respectively. The bands due to stretching of epoxy (C-O-C) and alkoxy (C-O) take place at 1225 and 1045 cm^{-1}(Fig. 1b) [9]. In the FTIR spectrum of PG (Fig. 1c), the peak due to C=O stretching appears at 1705 cm^{-1} which has been shifted towards the lower wavenumber as compared to the same peak of GO. This shifting of the C=O peak may be due to interaction (H-bonding) between the carbonyl (C=O) group of GO and the N-H group of PPY. The bands at 2979 and 1038 cm^{-1} are due to stretching of O-H and epoxy (C-O-C) bonds of GO. The peaks at 1558 and 1210 $cm^{-1}$are ascribed to the C=C and C-N stretching of the PPY ring confirming the presence of PPY in PG composites [12, 13].

FTIR spectra of ZnO (Fig. 1d) show the vibrational mode of ZnO at 560 cm^{-1} [14]. The FTIR spectra of the PGZ composite (Fig. 1e) reflect the characteristic peaks of its individual components with some shifting in peak positions and peak intensities. The peak at1708 cm^{-1} is due to C=O stretching. The shifting of the C=O peak in the case of PGZ may be due to interaction between the carbonyl (C=O) group of GO and the N-H group of PPY. The bands at 3126 and 1059 cm^{-1} are due to stretching vibrations of O-H and epoxy (C-O-C) bonds of GO. The absorption bands at 1562 and 1130 cm^{-1} are ascribed to the C=C and C-N stretching of the PPY ring which further confirms the presence of PPY in PGZ composites. The absorption band at 896 cm^{-1} due to ZnO in PGZ suggests the presence of ZnO in composite material [3, 12-14].

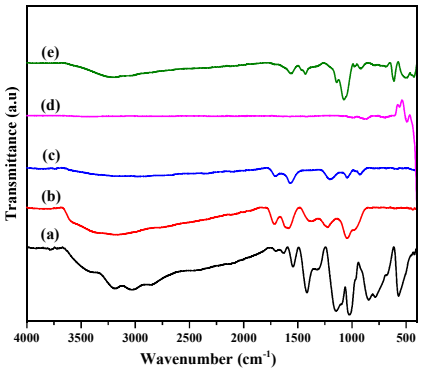

Fig. 1. FT-IR of (a) PPY, (b) GO and (c) PG (d) ZnO (e) PGZ

XRD spectra

The XRD spectra of graphite, PPY, GO, and PG are shown in Fig. 2 (a-f). The XRD spectra of PPY show a broad peak at 2θ=27.52° with interplanar spacing (d spacing) of 0.33 nm suggesting its amorphous nature (Fig. 2b) [4, 10]. The XRD pattern of graphite shows a sharp and intense peak at 2θ=26.38°with spacing (d=0.35 nm) indicating well-defined ordered arrangements of graphite layers (Fig. 2a). GO shows a peak at 2θ = 10.91°with d spacing 0.85 nm (Fig. 2c). The increase in the gallery spacing in case of GO as compared to graphite is ascribed to the encapsulation of oxygen moieties between the carbon layers of GO [7, 15]. The spectra of PG composites show two peaks at 2θ = 11.89^0 due to GO and 2θ = 23.53° due to PPY (Fig. 2d). These peaks signify the integration of GO layers over PPY amorphous nature of composites. [7, 12, 16]. In the XRD spectra of ZnO (Fig. 2e) the peaks at 31°, 34°,36°, 47°, 56°, 63°and 72° signify its crystal behavior. In the XRD spectra of PGZ, Fig. 2f, the peaks of PPY and GO are shifted and the intensity of the peaks increases with the increase of ZnO content suggesting an interaction between the three components in the composite material, which enhances the electrochemical stability of the ternary composite. [15, 17-19]

Thermal analysis

TGA curves of PPY, GO, PG, and PGZ are shown in Fig. 3 (a-e) below. Initially the weight loss at a temperature < 100 °C is due to the removal of moisture content in the prepared samples. In case of PPY the weight loss starts at TG onset of 207 °C with residual weight (W_r %) of 79.22. The weight loss of PPY continuously increases as the temperature rises and it ends at a TG offset of 595 °C indicating the volatilization of PPY (Fig. 3a). In case of GO the weight loss takes place at TG onset 187 °C with W_r % of 76.26 and ends at TG offset of 340 °C. This loss is mainly due to the removal of oxygen functionalities from the surface of GO (Fig. 3b). [8, 12]. In PG the weight loss at 150-170 °C is probably due to the removal of oxygen-containing moieties. The major weight loss in PG after 230 °C arises due to the degradation of PPY from the composite (Fig. 3c). [8, 20]. In the TGA curve of ZnO, the weight loss is due to the removal of moisture content (Fig. 3d) [14]. In case of PGZ, Fig. 3e, the weight loss at TG onset 212 °C and 348 °C is due to the removal of oxygen-containing functional groups and the degradation of the polymer chain from the surface of the composite material. The interaction between PPY and GO functionalities along with the barrier effects of ZnO imparts additional stability to the PGZ in comparison to PPY and GO [14, 21]

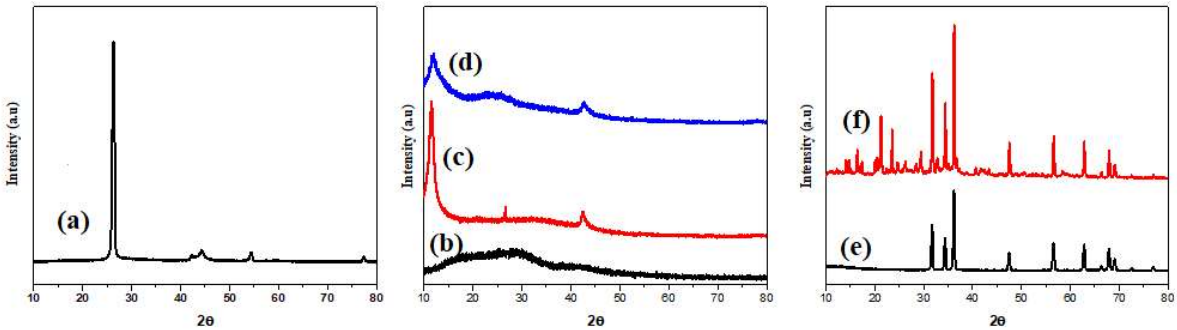

Fig. 2. XRD of (a) graphite (b) PPY, (c) GO (d) PG5 (e) ZnO (f) PGZ1

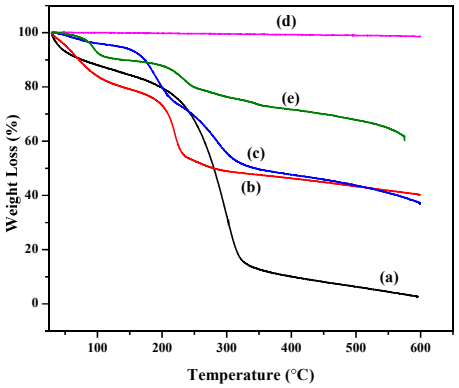

Fig. 3. TGA of (a) PPY (b) GO (c) PG5 (d) ZnO (e) PGZ1

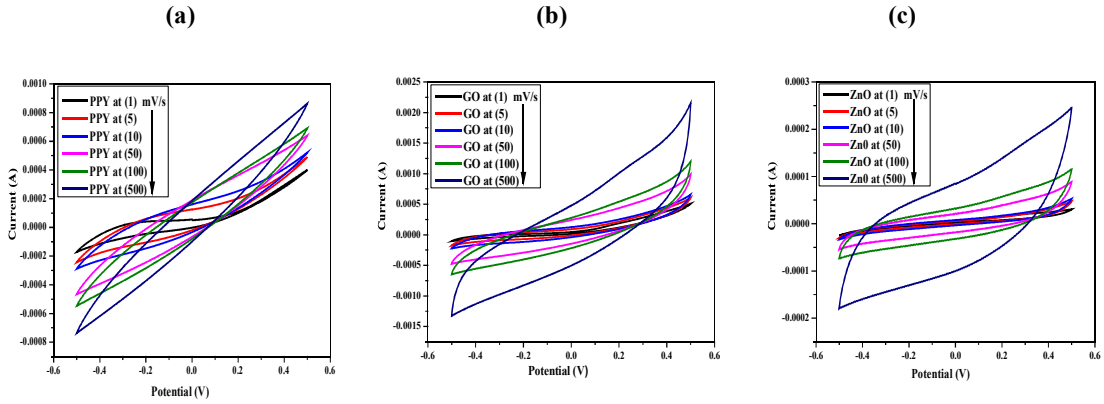

Fig. 4. CV curves of (a) PPY (b) GO (c) ZnO at different scans.

Table 3. Cs values of PPY, GO and ZnO at different scans

Scan mV/s	Cs Values		
	PPY	GO	ZnO
1	102.2	233.0	69.2
5	43.9	121.9	28.1
10	27.6	53.3	11.3
50	16.1	26.1	4.5
100	4.1	8.4	2.2
500	2.0	4.3	1.3

Electrochemical measurement of PPY, GO, and ZnO

ZnO, an *n*-type semiconductor, was found to have much lower Cs as compared to PPY and GO. This may be attributed to the bandgap of ZnO which has been reported to be higher (3.2 eV) as compared to PPY (3.0 eV) and GO (2.2 eV). This higher bandgap of ZnO probably reduces the chances of movement of an electron from the valence to the conduction band. Also, the chances of agglomeration in the case of ZnO can reduce the probability of higher Cs by reducing the surface area (Table 3). [22-23].

Electrochemical measurements

The CV curves of PPY, GO, ZnO, PGs, and PGZs were recorded within the potential window of -0.5 to 0.5V at different scan rates in 1 M KOH electrolytic solution as mentioned earlier [6, 12].

A regular increase in the peak current values with scan rates within the potential window for individual components i.e., PPY, GO, and ZnO, was observed [7]. The low Cs value of PPY is due to its compact structure which does not allow the diffusion of counter-ion readily into its internal matrix. GO gives higher Cs due to increased surface area, porous structure, and large interlayer gaps which makes the

diffusion more feasible as compared to the PPY chains [12, 22].

Electrochemical measurement of PGs

The Cs value of PGs increases with an increase in the amount (%w/w) of GO up to a certain limit and then decreases with the addition of GO in the composite material at all scans (Fig. 5a). This decrease may be due to the assemblage of GO layers with PPY on further addition of GO that results in the decrease of the active surface area of the composite and increase in the resistance that hindered the diffusion of ions on its surface. Therefore, the right amount of GO is necessary for composite material for the effective interaction between PPY and GO which facilitates the transport of ions and decreases the resistance to the movement of ions during the charging/discharging process [24].

The Cs values of different PGs at different %w/w of GO are shown in Table 3 with the highest Cs value for PG5 (Fig. 4b). The Cs value of PG5 is higher than those of PPY, and GO which is because the introduction of GO into the PPY matrix increases the surface area and porosity of the composite material allowing the fast diffusion of counter-ions on its surface, and enhancing its electrochemical behavior [12, 22]. The slope, as well as the area of the CV curve of PGs is higher compared to PPY and GO suggesting the lower resistance< fast ion diffusion rate and good capacitance behavior in the composite material [6].

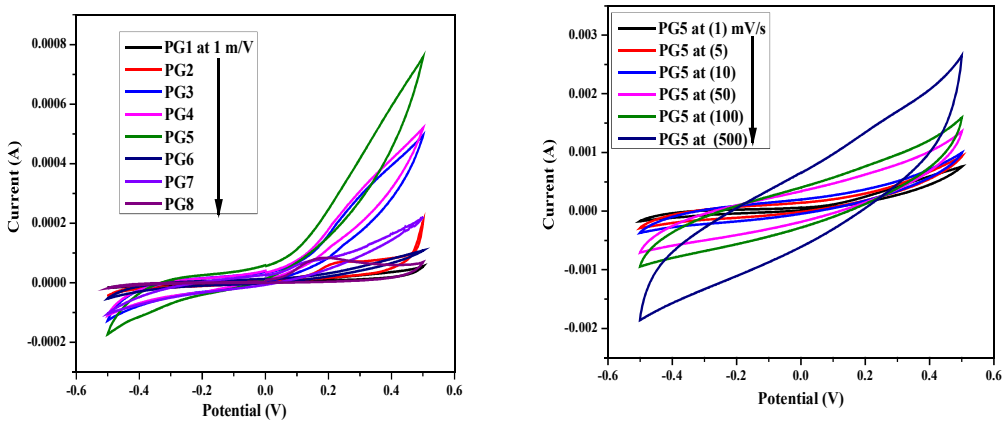

(a) (b)

Fig. 5. CV curves of (a) PG with different %w/w of GO at 1 mV/S (b) PG5 at different scans.

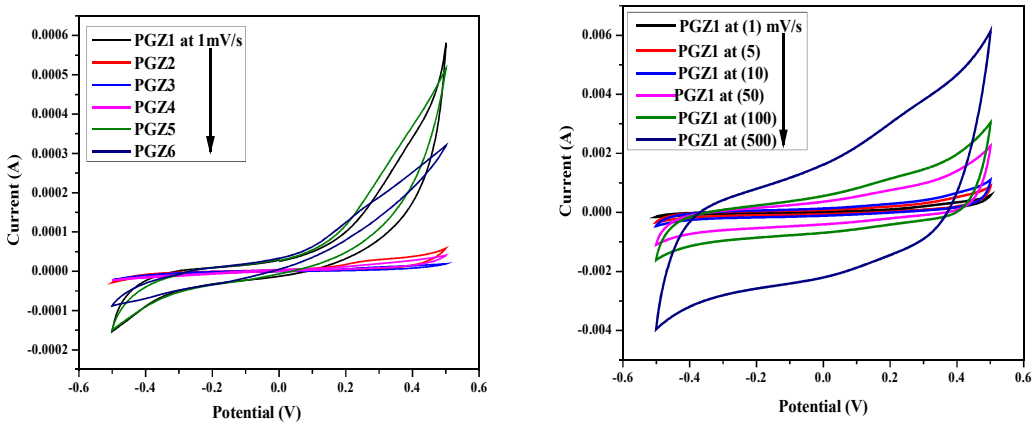

(a) (b)

Fig. 6. CV curves of (a) PGZ with different %w/w of ZnO at 1 mV/S (b) PGZ1 at different scans.

Table 4. Cs values of PGs at different scans

Scan mV/s	Cs values (F/g)							
	PG1	PG2	PG3	PG4	PG5	PG6	PG7	PG8
1	245.8	264.5	295.1	330.1	391.3	311.5	276.9	241.4
5	78.2	87.2	95.1	120.3	137.6	101.6	89.3	76.3
10	52.2	65.2	69.6	83.1	98.1	71.0	69.1	51.1
50	23.9	29.4	33.1	35.1	42.3	32.3	23.4	24.2
100	6.5	10.3	12.0	13.4	27.2	9.6	9.3	6.5
500	4.1	6.4	7.1	8.5	10.0	6.8	7.1	3.9

Table 5. Cs values of PGZs at different scans

Scan rate mV/s	Cs values (F/g)					
	PGZ1	PGZ2	PGZ3	PGZ4	PGZ5	PGZ6
1	352.1	256.5	182.4	47.5	26.3	18.9
5	137.5	121.3	59.9	16.3	10.5	13.5
10	94.5	89.3	38.1	12.6	8.6	7.4
50	39.0	32.3	13.5	8.2	4.4	4.2
100	25.1	21.1	8.3	7.3	3.6	3.1
500	9.4	9.1	3.4	3.8	2.7	2.2

Electrochemical measurement of PGZs

The Cs values of PGZ (Table 3) increase with an increase in the amount of ZnO up to a certain limit and then decrease with further addition of ZnO in the PG composite at a particular scan (Fig. 6a). This decrease may be due to the blockage of the porous surface of PG composite that results in the decrease of the active surface area of the ternary composite and an increase in the resistance that hinders the diffusion of ions on its surface. Thus, a requisite amount of ZnO is necessary for a composite material that decreases the internal resistance and enhances the electrochemical performance of the composite material [24].

The specific capacitance of PPY, GO, PGs, and PGZs decreases as the scan rate increases within a potential window, as shown in Fig. **7.** High Cs value at a low scan rate is due to the fact that electrolyte ions have enough time to attach to the surface of the material resulting in their strong interaction with the active sites of the electrode material and hence, enhancing its capacitive behavior. At higher scan rates the rate of diffusion of ions in the electrolyte is fast but the number of ions on the active sites of the electrode decreases resulting in a decrease in their Cs values**.** The oxidation and reduction peaks due to the internal resistance of the electrode are shifted towards positive and negative potential, respectively, with an increase in scan rate [2, 6].

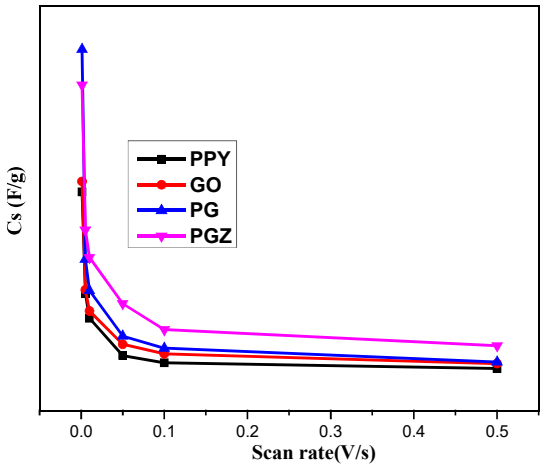

Fig. 7. Effect of scan rate on Cs value of PPY. GO, PG and PGZ

It is significant to note that the Cs of respective PGZs are lower as compared to the Cs of PGs. This relative decrease in the Cs in the case of PGZs may be attributed to the presence of ZnO which itself has a lower Cs due to the presence of a larger bandgap. The presence of ZnO in the matrix of PG brings undesired disorder in the PPY chain thus generating a large polaron bandgap as compared to the PG [4]. Further, it was also observed that with the increase in the amount of ZnO in the matrix of PG (specifically PG5) the Cs were found to get considerably lower (Table 5, Fig. 7).

CONCLUSIONS

A series of nanocomposites were fabricated by mixing PPY and GO (PGs) and PGs and ZnO (PGZs) in certain ratios. The obtained nanocomposites and individual materials were studied for their electrochemical behavior. CV of all the electroactive materials was taken for the earlier purpose, the CV results show that the PG5 was having the highest Cs (391.3 F/g) within all the PGs and individual components. With the addition of ZnO in PGZs, the Cs were found to decrease as compared to the parent PG5, possibly due to a large bandgap and low C_s of ZnO. Additionally, it was proposed that the ZnO may have generated disorder in the PPY chains again effectively reducing the Cs of PGZs. Out of all PGZs, PGZ1 was found to have the highest Cs (352.1 F/g) which continues to decrease with increasing ZnO in the PG matrix.

Conflicts of interest: The authors declared no conflicts of interest.

REFERENCES

1. A. Singh A. Chandra, *J. Appl. Electrochem,* **43**(8), 773 (2013).
2. P. Asen, S. Shahrokhian, A. Irajizad, *Int. J. Hydrog. Energy.,* **42**(33), 21073 (2017)
3. A. Pruna, Q. Shao, M. Kamruzzaman, J. A Zapien, A. Ruotolo, *Electrochim. Acta*. **187**, 517 (2016).
4. S. Dey A. K. Kar, *J. Sol-Gel Sci. Technol.,* **102**, 679 (2021).
5. J. Guerrero-Contreras, F. Caballero-Briones. *Mater. Chem. Phys*, **153**, 209 (2015).
6. W. K. Chee, H. N. Lim, I. Harrison, K. F Chong, Z., Ng, C. H. Zainal, N. M. Huang, *Electrochim. Acta,* **157**, 88 (2015).
7. H. Mudila, M. G. H. Zaidi, S. Rana, V. Joshi, S. Alam. *Int. J. Anal. Chem***. 4**(3), 139 (2013).
8. H. Mudila, V. Joshi, S. Rana, M. G. H. Zaidi, S. Alam, *Carbon Lett.* **15**(3), 171 (2014).
9. J. Song, X. Wang, C. T. Chang. *J. Nanomater*., **2014,** 1. (2014)
10. A. Bisht, R. Sati, K. Singhal, S. Mehtab, M.G.H. Zaidi, *Advances in Solar Power Generation and Energy Harvesting,* 127 (2020)
11. R. Rikhari, B. Saklani, A. Bisht, S. Mehtab, M.G.H, Zaidi, *Sens. Lett.,* **17**, 511 (2019)
12. S. Konwer, R., Boruah, S. K. Dolui. *J. Electron. Mater.,* **40**(11), 2248 (2011).
13. S. Kulandaivalu, N. Suhaimi, Y. Sulaiman, *Sci. Rep.,* **9**(1) (2019).
14. A. Batool, F. Kanwal, M. Imran, T. Jamil, S. A. Siddiqi, *Synth. Met.,* **161** (23-24), 2753 (2012).
15. F. Yin, J., Ren, Y. Zhang, T. Tan, Z. Chen. *Nanoscale Res. Lett.,* **13**(1). (2018).
16. L. Li, K. Xia, L. Li, S. Shang, Q. Guo, G. Yan.*J. Nanopart. Res,* **14**(6) (2012).
17. A. Mostafaei, F. Nasirpouri, *Prog. Org. Coat.,* **77**(1), 146 (2014).
18. N. I. T. Ramli, S. A. Rashid, M. S. Mamat, Y. Sulaiman, S. A. Zobir, S. Krishna. *Electrochim. Acta,* **228**, 259 (2017).
19. P. Patil, G. Gaikwad, D. R. Patil, J. Naik, *Bull. Mater. Sci.,* **39**(3), 655 (2016).
20. S. Bose, T. Kuila, M. E. Uddin, N. H Kim, A. K. T., Lau, J. H. Lee, *Polymer*, **51**(25), 5921 (2010).
21. M. Ates, S. Caliskan, M. Gazi, *Fuller. Nanotub. Carbon Nanostructures,* **26**(10), 631 (2018).
22. P. Joshi, S. Mehtab, M.G.H Zaidi, *Bull. Chem. Soc. Jpn,* **95** (6), 855 (2022)
23. H. Lv, Y. Guo, Z. Yang, Y. Cheng, L.P. Wang, B. Zhang, Y. Zhao, Z. J. Xu, G. Ji, *J. Mater. Chem. C,* **5**(3), 491 (2017).
24. G. Liu, Y. Shi, L. Wang, Y. Song, S. Gao, D. Liu, L. Fan, *Carbon Lett,* **30**(4), 389 (2019).